Observational constraints on the evolution of dust in protoplanetary disks

Martins e Oliveira, I.

Observational Constraints on The Evolution of Dust in Protoplanetary Disks

Observational Constraints on The Evolution of Dust in Protoplanetary Disks

Proefschrift

ter verkrijging van
de graad van Doctor aan de Universiteit Leiden,
op gezag van de Rector Magnificus prof. mr. P. F. van der Heijden,
volgens besluit van het College voor Promoties
te verdedigen op dinsdag 7 juni 2011
klokke 16.15 uur

door

Isabel Martins e Oliveira

geboren te Teresópolis, Brazilië
in 1982

Promotiecommissie

Promotor: Prof. dr. E.F. van Dishoeck

Co-Promotor: Dr. K.M. Pontoppidan (Space Telescope Science Institute, USA)

Overige leden: Dr. J. Bouwman (Max-Planck-Institut für Astronomie, Germany)
                 Prof. dr. C.P. Dullemond (Universität Heidelberg, Germany)
                 Prof. dr. K. Luhman (The Pennsylvania State University, USA)
                 Prof. dr. A.G.G.M. Tielens
                 Prof. dr. K. Kuijken

*"Somos quem podemos ser
Sonhos que podemos ter"*

Humberto Gessinger

TABLE OF CONTENTS

x

1

INTRODUCTION

According to data from the Wilkinson Microwave Anisotropy Probe (WMAP) experiment, the universe came into existence roughly 13.7 billion years ago (Spergel et al. 2003). Modern cosmology suggests that the universe remained a dark place for much of its first billion years, the "dark ages". During this time, the universe consisted of dark matter, as well as clouds of neutral hydrogen gas and little else. The first stars did not form until several hundred million years had passed (Bouwens & Illingworth 2006; Salvaterra et al. 2006). However, once the cosmic star-making machinery ignited, it agitated giant balls of gas into lots of stars that formed the first galaxies. It is now thought that the observable universe contains 10^{21} stars. Cosmic star formation is the dominant mechanism that controls the visible structure of galaxies and the build up of heavy elements in the universe with time. Originally, the only elements were hydrogen, helium, and traces of lithium, beryllium and boron. Heavier elements did not yet exist.

Stars are born, evolve and age, and eventually die. In simple terms, they are born from collapse of molecular clouds and may evolve differently during their lifetime, depending on their masses. During its evolution, a star burns light elements into heavier ones through nuclear fusion, thereby producing the energy necessary to balance the inward gravitational pressure and keep itself alive. During the course of their evolution, stars change mass (through accretion or mass loss), size (expansion or collapse) and luminosity (a change of thermonuclear reactions in their cores). Stars can be single and isolated or, very commonly, live in multiple systems. When a star has used up its nuclear fuel, its radiation pressure can no longer balance its gravity, setting in motion a chain of irreversible processes that eventually lead to its death. Stars of modest mass eject their gaseous envelope and become visible as planetary nebulae, while the more massive ones explode as supernovae. Freshly synthesized heavy elements (including Si, O, C, Mg and Fe, that make up the dust particles from which

planets may eventually form) are thus ejected into space, where they intermingle with the surrounding Interstellar Medium (ISM). This "enriched" ISM subsequently provides the material for the next generation of stars, eventually leading to the creation of the planetary systems in which life in the universe has become possible.

In our own Milky Way, one theory is that a supernova explosion has triggered the formation of our Sun and its protoplanetary disk, around 4.6 billion years ago (e.g., Cameron 1962). Eight planets (Mercury, Venus, Earth, Mars, Jupiter, Saturn, Uranus, and Neptune) and countless smaller bodies (e.g. dwarf planets, comets, asteroids) were formed from the material in this pre-solar nebula. The structure and composition of these Solar System bodies has given the first clues to the development of models of how planets are formed.

This thesis focuses on the interplay of the young star and its protoplanetary disk, on the evolution of the dust particles that make up the protoplanetary disk surrounding the young star, and thus on the very first stage of the formation of planets like those that compose our own Solar system.

1.1   Low-mass Star Formation

The most common type of stellar objects are stars of low mass ($\sim$0.5 $M_\odot$), that dominate both in number and in total mass. Low-mass stars form inside relatively dense concentrations of interstellar gas and dust known as molecular clouds (Stahler & Palla 2004), with the dust making up $\sim$1 % of the mass of the cloud (Tielens 2005). This dust is believed to be sub-μm in size and to consist of almost completely amorphous silicate- and carbon-based grains (Kemper et al. 2004). These regions are mostly self-gravitating, confined by an external pressure, magnetized and extremely cold ($T \sim$ 10 K). Under these conditions, most elements are in molecular form, as revealed by observations of CO emission (Ungerechts & Thaddeus 1987). These dense regions are opaque to visible light due to their high extinction, but translucent at longer wavelengths. Therefore observations at longer wavelengths can probe the internal structure of clouds and study star formation.

Star formation begins when a region in the cloud cools and reaches a sufficient density of matter to satisfy the criteria for Jeans instability, beginning to collapse under its own gravity (Shu et al. 1993; Myers et al. 2000). Matter accretes toward the center at a constant rate. As the gas and dust contract from the inside-out (Shu 1977), gravitational energy is released through radiation and quickly re-absorbed by the opaque envelope of material that is still collapsing. Short wavelength radiation from deep inside the core is then obscured when captured by the dust in the envelope, re-processed and re-emitted at infrared or sub-millimeter wavelengths, thereby providing information on the dusty outer environment. Furthermore, when gravitational energy is transformed into kinetic energy during the collapse, gas particles speed up and collide, increasing the temperature of the forming star and its immediate surroundings. As a result, thermal pressure builds up, which serves to support the cloud structure against further collapse.

As the cloud fragment shrinks due to gravity, conservation of angular momentum leads to a spin-up of the inner parts of the core. Collapse keeps occurring, preferentially along the path of least rotation. Finally, the cloud fragment collapses into a central core surrounded by a rotating disk of material. This central core, a "protostar" and its disk, keeps accreting material from the surrounding envelope. Stellar winds (e.g. X-winds, disk winds) break out along the rotational axis of the system, reversing infall and sweeping up material into two outwardly expanding shells of gas and dust, known as "bipolar outflows" (Snell et al. 1980; Bachiller & Tafalla 1999) while infall still occurs in the equatorial regions. With time, the outflow angle opens up, eventually terminating the infall and revealing the newly-formed star. This pre-main sequence star, surrounded by a circumstellar disk, has now become visible at optical wavelengths. This phase is known as the "T Tauri" phase. The entire star-disk-envelope-outflow system is called a young stellar object (YSO).

At this pre-main sequence stage, the optically visible low-mass star is still contracting toward the main-sequence (MS) on a radiative time scale. With interiors not yet hot enough to burn hydrogen, deuterium burning plays an important role in the early stages of stellar evolution. Due to the stellar contraction, the internal temperature incessantly rises, until it reaches $\sim 10^7$ K, at which point hydrogen fusion begins. At this moment the star is said to be on the *zero-age main-sequence* (ZAMS). The ZAMS marks a locus in the *Hertzsprung-Russell* (H-R) diagram corresponding to a relation between the luminosity of a star and its temperature.

T Tauri stars are known for their excess emission, i.e., beyond that produced by the stellar photosphere. The presence of prominent optical emission lines such as Hα reveal the presence of both outflowing and infalling matter, while their excess continuum radiation at infrared wavelengths furnishes evidence for the existence of circumstellar disks. This infrared excess is understood as reprocessed stellar radiation by the circumstellar disk, which is composed of dust and gas. Actively accreting disks will also produce excess radiation, mostly in the UV regime, and broad emission lines. Because stars and their disks are connected, they evolve together and will affect each other.

Another fundamental characteristic of T Tauri stars is their temporal variability – line and continuum fluctuations that span a range of amplitudes and can be either random or periodic. T Tauri stars are further divided into two subclasses: classical T Tauri stars (CTTS) and weak-line T Tauri stars (WTTS). WTTSs are low-mass pre-MS stars that occupy the same region of the H-R diagram as CTTSs but do not show clear evidence of accretion. The distinction between the two is usually made based on the Hα equivalent width (EW). Since there is a very strong correlation between spectroscopic signatures of gas accretion and the presence of near-IR excess (Hartigan et al. 1995), most CTTSs show near-IR excess while most WTTSs lack such an excess.
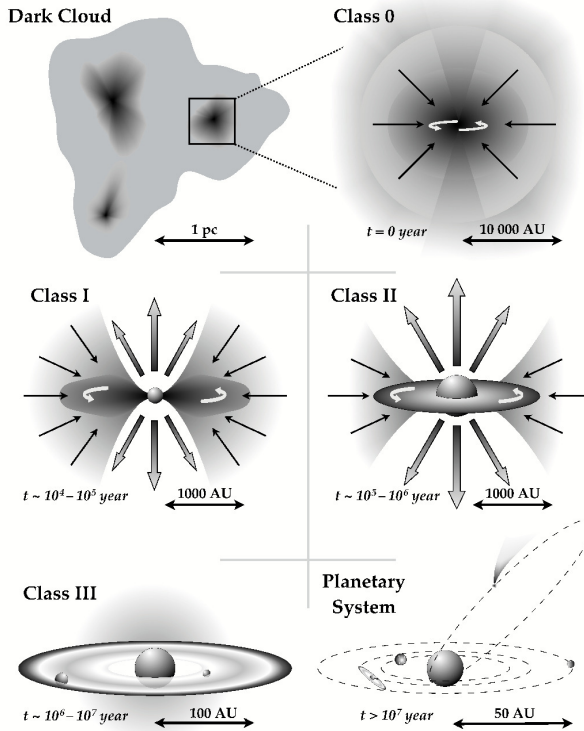
Figure 1.1 – Illustration of the scenario for low-mass star formation, as described in the text (Frieswijk 2008, after Shu et al. 1987). The formation of dense cores occurs in molecular clouds (upper left), and the core collapse under its own gravity (upper right). As the surrounding envelope starts to dissipate, strong bipolar outflows remove angular momentum (middle left) until the newly formed star and its circumstellar disk become visible (middle right). As gas dissipates, giant planets should already be formed (bottom left). By the time the entire disk has dissipated, the possible planetary system around this star should have completely formed (bottom right).

1.2   Stellar Properties

To study the structure and evolution of protoplanetary disks, and how these connect to their host star, it is of prime importance to be able to determine stellar properties. A star of a given temperature emits radiation roughly as a black-body of that temperature. Radiation emitted by massive stars peaks at shorter wavelengths (UV/visible) than that emitted by low-mass stars (visible/near-IR). Consequently, the visible/near-IR regime is the optimal wavelength range to observe T Tauri stars.

By studying the optical spectra of stars of different surface temperatures, it is possible to define temperature-sensitive features that have historically been used to

determine their effective temperature. These absorption bands are more prominent in the spectra of cooler stars and, due to their width, they can be detected even in low-resolution spectra. By comparing the appearance and strength of these temperature-sensitive features with those of stars of different known temperatures (templates), one can determine the spectral type of the star in question. Besides temperature, the analysis of a stellar optical spectrum also allows the determination of its surface gravity, rotational velocity, and metallicity. These quantities, however, are best (and sometimes only) determined with medium- to high-resolution spectroscopy. If the distance to the star is known, the stellar luminosity can be derived directly through flux measurements in different bands. The stellar mass, radius, and age can be estimated based on stellar models. The derivation of stellar parameters from optical spectroscopy is the subject of two chapters in this thesis.

Ages of pre-MS stars, however, are very difficult to determine due to our limited understanding of stellar structure and evolution during the pre-MS stage (Hillenbrand 2009). Different models of stellar evolutionary tracks in the H-R diagram vary considerably, depending on the choice of input physics used. These variations lead to different ages being inferred for the same object, when using different tracks. Furthermore, it has been suggested that the accretion history of an object, which may be episodic, should be taken into consideration when using stellar tracks to age a pre-MS star (Baraffe et al. 2009). This poses a great difficulty for exact age determinations, as no object has been monitored for millions of years. For these reasons, mean cluster ages are often considered to be a better clock than individual ages.

1.3   Protoplanetary Disks and Planet Formation

The origin of planets is naturally connected to the evolution of the protoplanetary disks from which they formed. However, the details of how exactly disks evolve from their initial composition consisting of small dust grains coupled to the gas into complex planetary systems are not yet understood. While virtually all young stars have such disks, most older MS stars show no signs of being surrounded by disks. This constraint implies that disks must evolve, either by accreting or dispersing dust and gas, or by building-up larger bodies.

1.3.1   Disk Properties

Once the envelope surrounding the forming star is dispersed, the now observable circumstellar disk can be studied directly. Observations have shown disks initially to be good mixtures of dust and gas (dust-to-gas mass ratio $\sim$0.01), flared and extending several hundreds of AU in radius. Despite its low abundance, the dust dominates the disk opacity.

1.3.1.1   Disk Observations

The solid material that composes a protoplanetary disk is exposed to the radiation from the central star, and a possible accretion source. The dust, besides absorbing some of the radiation, also re-processes and re-emits a part of it. In fact, the main observational constraint on the existence of protoplanetary disks is the observation of an excess of radiation at IR and (sub-)mm wavelengths that can not be attributed to the star alone. With the current observational facilities, only the few closest disks can be directly imaged. Therefore, the existence of disks is often inferred indirectly from the existence of an IR-excess observed toward a star.

Because the Earth's atmosphere absorbs most of the light in the infrared regime, ground-based infrared observations are impossible at some ranges. For this reason, a lot of effort has been put into launching infrared space telescopes. Most of the data presented in this thesis were obtained using the *Spitzer Space Telescope* (Werner et al. 2004). *Spitzer* was launched in 2003, and operated in full capacity until the summer of 2009, when its cryogenic mission ended. After running out of the Helium supply that kept the telescope cooled, *Spitzer* continues to produce data in its 'warm mission', albeit in only two filters. The telescope is composed of three instruments: the InfraRed Array Camera (IRAC, photometry at 3.6, 4.5, 5.8 and 8 μm), the Multiband Imaging Photometer for Spitzer (MIPS, photometry at 24, 70 and 160 μm), and the InfraRed Spectrograph (IRS, spectroscopy from 5 to 40 μm at $\lambda/\Delta\lambda \sim 50$–$100$ and 600). These wavelengths are used to probe protoplanetary disks at different radii, thereby providing constraints on their structure ranging from the inner to the mid-disk.

1.3.1.2   Star-Disk Interactions

Because stars and their disks are physically connected, a complete understanding of these complex systems can only be gained by studying both objects together. This can be done by studying the spectral energy distribution (SED) of the system. The SED is a plot of flux (λF_λ) versus wavelength, comprising a wide wavelength range. For stars with disks, the stellar photosphere contributes most to the emission at short wavelengths, i.e. in the UV and optical, while the disk is responsible for most radiation at longer wavelengths, i.e. in the IR and (sub-)mm. Although a protoplanetary disk can produce its own energy through accretion, for most cases this amount is small when compared to the stellar luminosity. This way, the discussion presented here can be generalized for passive disks. In this case, the stellar radiation field defines the temperature of the dust in the disk, which can be modeled using dust radiative transfer codes that relate the observed SEDs to the structure of the system. Hence, the SED shape yields the structure of the disk, while the long wavelength flux gives its total mass.

SEDs are an important tool in the study of stars with disks and, together with direct imaging observations, a great deal has been learned about those systems. The warm disk surface layers and disk inner rim, close to the star, are responsible for the

emission at shorter IR wavelengths. Deeper into the disk, probing now a colder dust population, the dominant emission is at longer (far-IR and mm) wavelengths (Figure 1.2). From this basic understanding, it becomes clear what the results would be from suppressing or enhancing any of these components. In reality, however, SEDs are degenerate and interpreting them is neither easy or trivial. Still, SEDs are important tools in the study of protoplanetary disks, and a lot can be learned from them. A disk depleted of dust and gas (that has either accreted toward the star, been blown away by its radiation, or coagulated into big bodies) will present very little or no excess radiation. Additionally, the presence of a gap (star-disk-gap-disk) or hole (star-hole-disk) in the disk will produce very peculiar signatures in the system's SED by suppressing the radiation at short IR wavelengths that the small dust would have produced.
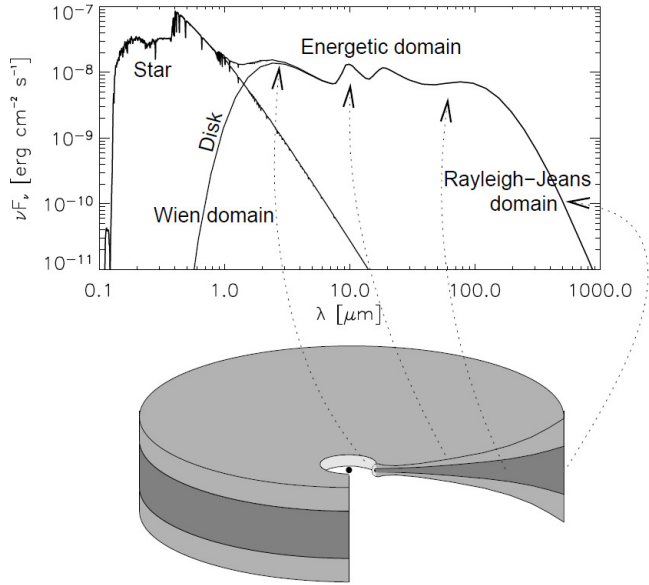
Figure 1.2 – Build-up of the SED of a flaring protoplanetary disk and the origin of its different components: the near-IR emission comes from the inner rim, the mid-IR dust features are emitted by the warm surface layer, and the underlying continuum from the deeper (cooler) disk regions. Typically the near- and mid-IR emission comes from small radii, while the far-IR comes from the outer disk regions. The (sub-)mm emission mostly comes from the midplane of the outer disk (Dullemond et al. 2007).

Furthermore, dust features can be seen overlaid on top of the dust continuum emission. In the IRS regime, polycyclic aromatic hydrocarbon (PAH) and silicate features (at 10 and 20 μm) are very prominent, and can probe the physical and chemical processes affecting the warm dust in the surface layers of the inner regions of the disk, as it is shown in two chapters of this thesis.

1.3.1.3   Processes Affecting the Disk

The evolution of disks is a combination of external and internal processes. Being the main source of radiation of the system, the central star affects the disk dispersal directly. Stellar winds can sweep-up and remove some of the disk material. Furthermore, energetic UV and X-ray photons emitted by the central star (or a massive nearby star) heat the disk surface and cause thermal pressure-driven hydrodynamic mass outflows from the disk. This process is called *photoevaporation* and, in combination with the viscous evolution of disks, has been shown to be a very effective mechanism for the dispersal of disks (Hollenbach et al. 2000; Clarke et al. 2001; Alexander et al. 2006a,b; Ercolano et al. 2009; Górny et al. 2009; Owen et al. 2010). Depending on the energy of the photons, they can be responsible for opening inner gaps in those disks, or inducing mass outflows in the outer disk, where most of the mass resides.

While some material is being expelled from the disk, accretion flows onto the star continue. The inner disk is disrupted by the stellar magnetic field, resulting in magnetospheric accretion, in which disk material is channelled along the magnetic field lines into the star (Koenigl 1991). This material infall produces high temperature optical and UV continuum emission and strong emission lines, the strongest of them being Hα (Calvet & Hartmann 1992).

In addition to the external processes described above, theory, observations and laboratory experiments point to processes that affect the dust inside disks (Weidenschilling 1980; Dominik & Tielens 1997; Blum & Wurm 2008) and thereby also the disk structure (Dullemond & Dominik 2004). The high disk densities facilitate particle collision and dust coagulation. As they grow larger, particles settle gravitationally towards the disk midplane, making it an even denser environment and therefore more prone to further growth into roughly km-sized bodies called *planetesimals*. These steps are the early stages of planet formation. Observationally, particle coagulation is equivalent to the removal of the small dust component, manifesting itself as a flattening of the disk and a decrease of the infrared excess of a disk (Dullemond et al. 2001).

Debris disks, composed of large planetesimal rocks and smaller bodies that are produced in situ by collisions of planetesimals, have been found around both evolved and young stars (Rieke et al. 2005; Su et al. 2006; Gautier et al. 2007; Wyatt 2008; Carpenter et al. 2009). This phase is understood to follow the protoplanetary disk phase, when gas is no longer present.

1.3.2   Planet Formation

Because the very small dust grains that initially compose a disk are coupled to the gas, they move slowly (few cm s^{-1}) in Brownian motion. These low velocities allow grains to grow via pairwise collision in regions of high disk densities (Blum & Wurm 2008). Bigger particles settle faster to the disk mid-plane where, in a similar fashion, particles will continue to coagulate. In this manner particles may grow up to meters in size, at which point their dynamics begin to decouple from the gas. No longer being

coupled to the gas, the motion of these planetesimals is dominated by gravitational forces, following Keplerian orbits and moving faster than the gas. Those particles then feel a headwind from the interaction with the slower moving gas, losing angular momentum. The loss of angular momentum causes the particles to drift inward. This radial drift is very fast, especially for particles of ∼1 meter in size, such that the planetesimals quickly reach the evaporation zone and vaporize (e.g. Dominik et al. 2007). This is a major problem, referred to as *the meter-size barrier*, and any model that relies on aggregational growth from dust to planets must pass this barrier within the timescale that would take for these bodies to drift in.

One way to overcome this problem that has been recently explored in the literature is with streaming instabilities (e.g. Youdin & Goodman 2005; Johansen et al. 2007). In these models the roughly m-sized particles, after concentrating in pressure maxima regions in the turbulent gas in the disk, can grow an order of magnitude by streaming instabilities driven by the relative flow of solids and gas. This collapse is found to be faster than the radial drift timescale, therefore allowing those particles to survive the meter-size barrier and possibly grow further into planets.

The further growth from planetesimals into planets is not yet well understood. To make matters more complicated, objects with sizes in the range $10^{-1} - 10^5$ m cannot be observed directly. Two different models have been introduced to explain the formation of planets (thousands of kilometers in size). The *core-accretion* model (Safronov & Zvjagina 1969; Goldreich & Ward 1973; Pollack et al. 1996) suggests that further growth beyond km size happens gradually, as the coagulation works for small particles. Planetesimals interact gravitationally, accreting onto each other to form a heavy-element core. Once this core is massive enough, its gravitational field captures gas to create a gas giant. Alternatively, the *disk instability* model (Cameron 1978; Boss 1997) suggests that dense clumps will be formed by fragmentation of the disk. These clumps contract to form planets much like the formation of stars by the collapse of a molecular cloud clump. Although the core accretion model is favored by most theorists, both models have advantages and problems. The core accretion model may take too long to form a core massive enough to capture gas, such that by then the gas has already dissipated from the disk. For the disk instability model to work, disks must be more massive than observations seem to suggest.

1.3.3   The Solar System & Exoplanets

Observations of an increasing number of stars have shown that the Solar System is not unique, and that planets and planetary systems come in a variety of forms. The origin of this variety is still unclear, but must be connected to their formation processes.

Planets and planetary systems seem to be a rather common output of disk evolution, and have been observed around hundreds of stars other than the Sun (Udry & Santos 2007). This, however, does not seem to be the only output of disk evolution. Some MS stars present debris disks and, although it is still unclear whether debris disks often also harbor planets (Kóspál et al. 2009), this is true for at least a few

of them (e.g., β Pictoris and Fomalhaut, Lagrange et al. 2010; Kalas et al. 2008). However, most MS stars show no signs of planets or debris within the current observational limitations, meaning that disks around such stars were completely dispersed, leaving no dust behind to tell the story.

Since the landmark discovery of a planet orbiting the solar-like star 51 Peg around 15 years ago (Mayor & Queloz 1995), the ∼500 exoplanets detected to date form a powerful database of the possible end-products of disk evolution. Follow-up studies of planet-host stars have shown that stars that harbor planets are consistently more enriched in metals than those that have shown no sign of orbiting planets (Fischer & Valenti 2005; Udry & Santos 2007). If true, this relation must either be a natural consequence or the direct cause of planet formation. Additionally, the distribution of planet masses and orbital positions in relation to the host stars offer further observational constraints for planet formation models.

Only one planetary system, namely our own Solar System, has been studied to the level of detail necessary to provide reliable information on dynamics and composition of its constituents. Remarkably, our Solar System contains a collection of ancient remnants that have preserved the material that composed the early solar system in virtually unaltered form for over 4.5 Gyr. Analysis of chondritic meteorites and interplanetary dust particles, as well as observations of comets, have revealed their structure and mineralogy, pointing to important physical and chemical processes that took place during the early evolution of the protoplanetary disk around the young Sun. For instance, it has been found that these bodies are composed of considerable fractions of crystalline material (Wooden et al. 2007; Pontoppidan & Brearley 2010, and references therein). Looking for clues on how and when such changes occur in the early stage of protoplanetary disks, when planets are still forming, is a very active field of research, and the subject of Chapter 6 in this thesis.

1.4 Disk Diversity and Evolution

In the following, a more detailed background on the main topics of this thesis is presented: disk and dust evolution.

The launch of *Spitzer* represented a major step forward in the study of circumstellar disks. Although many disks had been successfully observed from the ground and space (e.g., with the *Infrared Space Observatory, ISO*), the sensitivity and mapping capability of *Spitzer* allowed the observation of extremely large numbers of systems. Thanks to the statistically relevant disk samples observed by *Spitzer*, complemented by UV, optical and (sub-)mm data, a previously unknown variety of disk structures and timescales has been revealed.

Before *Spitzer*, the global understanding of disk evolution was very much based on evidence from a small number of sources. Thus models for disk evolution and planet formation were derived from: i) extrapolation of characteristics of the few brightest disks as universal; ii) evidence from our own Solar System, and the "solar nebula" from which it originated; iii) observational evidence for disk dissipation within some

few Myr. The dominant pre-*Spitzer* view was that disks evolve steadily with time, with material either accreting onto the central star, being dissipated by the stellar radiation, or coagulating into bigger and bigger particles that sink to the midplane.

One of the most important parameters for the formation of giant planets is the gaseous disk lifetime. However, since small dust is well coupled to the gas and since dust is an easier observable, disk lifetimes are often derived just from the infrared excess. The clock of circumstellar disks is the age of its central star. Using the mean age of a cluster and measuring the near-IR excess of its members, Haisch et al. (2001) showed that the fraction of stars surrounded by disks decreases steadily with mean age, concluding that time is an essential parameter in disk evolution. Since then, with much more comprehensive disk observations, several authors have revisited this relationship (e.g. Hernández et al. 2008; Magnelli et al. 2009) without much change in the results: by 6 – 8 Myr only less than 10% of stars in a given cluster still have disks. Although this irrefutably presents time as an important parameter, it is not the only one. Within a cluster of a given age (whether a young, 1 Myr cluster, or an older, 7 Myr one), a great diversity in infrared excess (and therefore amount of dust still present in the disk) is seen. It is still not clear why some disks are completely dissipated by 1 or 2 Myr, while others may live up to 10 Myr.

Many other parameters have been suggested to play an important role in the evolution of disks. For instance, Carpenter et al. (2006) and Kennedy & Kenyon (2009) show evidence of different disk lifetimes depending on the mass of the central star (quicker dispersal for disks around higher mass stars). A diversity of stellar temperatures, luminosities and masses among young stars has been known and studied for decades. Indeed, since stars and disks are connected, it is unlikely that differences in the central sources will not be reflected in their surrounding matter. However, to date no strong evidence has been found as to which processes are determinant on setting the timescale in which a disk will dissipate.

Observations of large disk samples have shown that disks in the same cluster, with same assumed age, show very distinct shapes, structures and masses (Furlan et al. 2006; Sicilia-Aguilar et al. 2006; Oliveira et al. 2010). Different amounts of excess infrared radiation, and at different bands, yield different structures for disks. A strong excess is interpreted as a geometrically flared disk, while little excess suggests a flat, almost dissipated disk. A few disks show little or no near-infrared excess, but otherwise a normal disk, with a significant excess at longer wavelengths. These are interpreted as inner gaps or holes (Calvet et al. 2002). Indeed, sub-mm observations of such disks have shown that a gap without small dust really exists, reinforcing the use of the amount of infrared excess as an indicator of disk geometry (Brown et al. 2007). A difference in geometries is demonstrated by a large sample of classical and weak-line T Tauri stars, as well as debris disks, by Cieza et al. (2007). The distribution of excess slope (α_{excess}) changes as a function of the wavelength where the excess starts ($\lambda_{\mathrm{turn-off}}$). If grains were to simply grow and settle, α_{excess} should become increasingly smaller for longer $\lambda_{\mathrm{turn-off}}$. However, Figure 1.3 suggests that a range of possible processes is responsible for inner disk clearing, which could then be

responsible for disks following different paths of evolution.
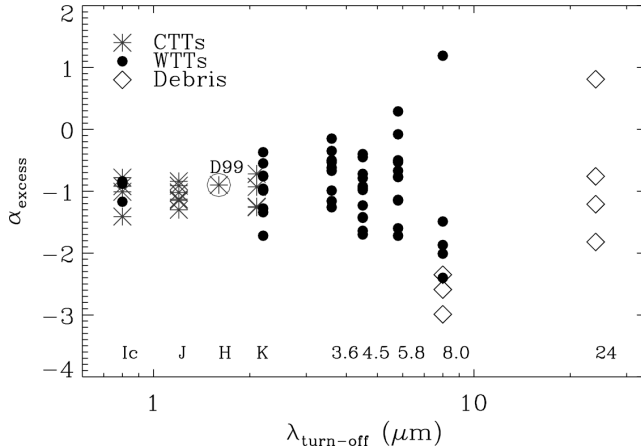
Figure 1.3 – Distribution of excess slopes α_{excess} vs. the wavelength $\lambda_{turn-off}$ at which the infrared excess begins for a sample of WTTSs (filled circles), CTTSs (asterisks) and debris disks (diamonds). The diagram shows a much larger spread in inner disk morphologies of WTTSs with respect of those of CTTSs (Cieza et al. 2007).

As the birthplace of planets, the gas-rich protoplanetary disks have the potential to answer many of the questions related to planet formation. Statistical samples of protoplanetary disks are necessary to identify the environmental and initial conditions of disks, as well as the main processes that affect the evolution of the dust and control the outcome of disk evolution. It has become clear that not all disks evolve in the same manner; however which different paths are possible, and why, is still a mystery.

1.5   Evolution of Dust in Disks

If planetary systems are to be formed, the originally sub-μm-sized, almost completely amorphous ISM dust grains must be transformed into much larger bodies inside protoplanetary disks. A tremendous growth is expected: ∼14–15 orders of magnitude in size, and around 40 orders of magnitude in mass. That is in addition to the complicated chemistry that must take place to create the organic molecules from which life on Earth originated. At least some of these chemical processes happen inside protoplanetary disks, as suggested by observations of primitive Solar System bodies.

1.5.1   Grain Growth

Theoretically, the growth from small to intermediate km-sized planetesimals is fairly well understood. However, these same calculations predict this growth to be a very fast process ($\sim 10^5$ yr, Weidenschilling 1980; Dullemond & Dominik 2005). Therefore, if grains were to grow orderly and uninterruptedly, small dust should no longer be

present in disks that are a few million years old. The observation of hundreds of disks in the 1 – 10 Myr range pleads against such a scenario. Instead, these small dust observations imply that they are also created during the evolution of disks. At the same time that collisions favor coagulation, collisions can also be destructive rather than constructive, if the relative velocity between particles is too high (Paszun & Dominik 2009). This fragmentation of bigger bodies can create particles small enough to be mixed with the gas and be brought to the disk surface by turbulent mixing. Fragmentation can explain the presence of small dust in disks for millions of years.

The shape and strength of the silicate features probed by the IRS spectra at 10 and 20 μm are affected by the composition, size and structure of its emitting dust. Because most protoplanetary disks are optically thick at optical and IR wavelengths, the silicate features observed in the mid-IR are generally emitted by dust in the optically thin disk surface only.

A relationship between the size of the grain and the strength and shape of the 10 μm silicate feature was first shown for Herbig Ae stars (van Boekel et al. 2003). Since then, this relationship was shown to hold for lower mass stars, all the way to the brown dwarf limit (e.g., Kessler-Silacci et al. 2006; Apai et al. 2005). ISM-like grains, $\sim$0.1 μm in size, emit silicate features that are strong and very triangular. As the grain size increases, the emitted silicate features appear more flattened and less peaked. By comparing the observed feature with synthetic features calculated for different grain sizes, it is possible to infer the dominant dust grain size opacity in the surface of disks (Figure 1.4). This process is not without its challenges, since the composition of the dust grain also affects the shape of the silicate features. This discussion, and ways to overcome this degeneracy, is the subject of two chapters in this thesis.

1.5.2   Mineralogy

Changes in composition and lattice structure of dust grains have been inferred from the observation of large fractions of crystalline material in primitive Solar System bodies and in protoplanetary disks. Spectra taken from the ground and from *ISO* gave the first clues of a potential link between crystalline material in protoplanetary disks and comets. A great similarity was noted between the spectra of the disk around the Herbig star HD 100546 and that of comet Hale-Bopp (Crovisier et al. 1997; Malfait et al. 1998). Amorphous silicates show broad smooth mid-IR features, while the opacities of crystalline species, such as forsterite and enstatite, show sharp features due to their large-scale lattice arrangement, such that even small fractions of crystalline grains produce additional structure in the silicate features (van Boekel et al. 2004; Min et al. 2005; Bouwman et al. 2008; Juhász et al. 2009, 2010; Olofsson et al. 2010).

According to our current understanding, the way to re-organize the amorphous lattice of a grain into one that is crystalline is through heating. Two main methods
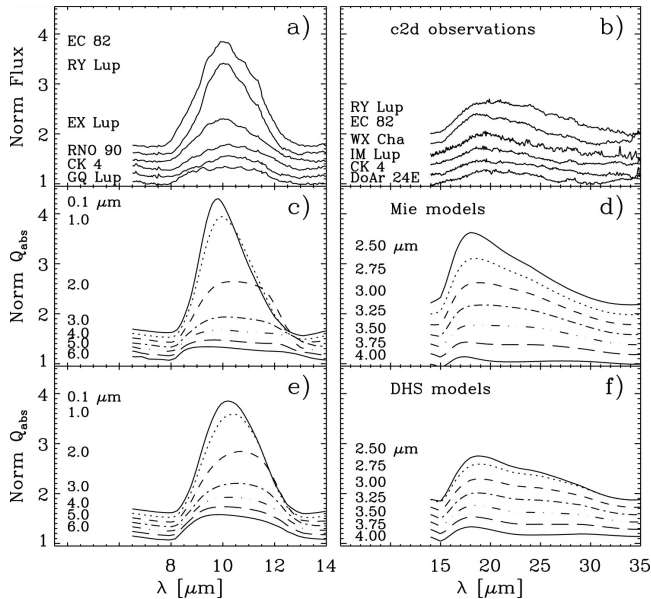
Figure 1.4 – Evidence of grain growth in the Si–O stretching and O–Si–O bending mode features. The top panels show the observed normalized spectra in the (a) 10 μm and (b) 20 μm regions for sub-samples of our sources. The bottom two panels show the normalized absorption efficiencies (Q_{abs}) for models of spherical grains of amorphous olivines with various grain sizes calculated for the 10 and 20 μm regions. Models of filled homogeneous spheres calculated using Mie theory are shown in (c) and (d), and models of hollow spheres calculated using distribution of hollow spheres (DHS) theory are shown in (e) and (f) (Kessler-Silacci et al. 2006).

have been proposed to explain this formation of crystal grains: thermal annealing of amorphous grains or vaporization followed by gas-phase condensation. Both methods require high temperatures (above ∼1000 K, Fabian et al. 2000; Gail 2004), meaning that either method could work in the inner parts of disks, where temperatures are high enough. Yet, observations show crystalline grains over the entire extent of disk surfaces covered by IR observations (van Boekel et al. 2004). Large-scale radial mixing has been invoked to explain the presence of crystals at low temperatures in the outer disk (Bockelée-Morvan et al. 2000; Gail 2004; Ciesla 2009). A third proposed formation mechanism for crystal formation is that of shock waves, which could locally heat amorphous silicates and crystallize them (Desch & Connolly 2002; Harker & Desch 2002).

Mineralogical studies of Solar System bodies show a range of crystallinity fractions. Evidence from primitive chondrites shows that the abundance of crystalline silicate material varies from nearly nothing to up to 20 – 30 % (e.g. Acfer 094 and ALH77307, Pontoppidan & Brearley 2010 and references therein). Oort cloud comets, with long periods and large distances from the Sun, have inferred crystallinity fractions up to 60 – 80 % (e.g. Hale-Bopp, Wooden et al. 1999, 2007). Jupiter-family, or

short period comets, have lower fractions, up to ∼35 % (e.g. 9P/Tempel 1, Harvey et al. 2007b; 81P/Wild 2, Zolensky et al. 2006). This discrepancy in fractions points to the existence of a radial dependence in crystallinity fraction in the protoplanetary disk around the young Sun (Harker et al. 2005). Even when considering the discrepancies, the crystallinity fractions derived for Solar System bodies are appreciably higher than those derived for the ISM dust ($< 2\%$, Kemper et al. 2004). One of the conclusions of this thesis is that the observation of crystalline features in protoplanetary disks suggests that the crystallization occurs early in the disk evolution and is then incorporated into larger solid bodies.

1.6   This Thesis

This thesis presents unbiased surveys of low-mass young stars and their dusty disks in nearby star-forming regions using optical/infrared telescopes to probe the evolution of dust in protoplanetary disks. It addresses the full star-disk system: the stellar characteristics and their effect on disk evolution, as well as the changes taking place in the dust itself by making use of statistically relevant samples. The structure of this thesis is as follows:

Chapter 2 – In this chapter an optical spectroscopic survey designed to characterize the new young stellar population discovered in the Serpens Molecular Cloud by the *Spitzer* c2d program is presented. Spectral types, and therefore effective temperatures, are derived from the spectra. Combined with optical and IR photometry, the stellar luminosities are calculated, which allows the placement of these stars in a H-R diagram. Various methods are devised to distinguish true young stellar objects in the cloud from other reddened sources. The contamination from background objects (reddened stars, galaxies) is found to be quite high (25%), raising caution when using IR colors to identify YSOs in low latitude clouds. Aided by evolutionary stellar tracks, ages in the range of 2–6 Myr and masses of 0.2–1.2 $M_\odot$ are inferred for the stars belonging to the cloud, if its distance is taken to be 259 pc. Furthermore, mass accretion rates are estimated from the full width at 10% of peak intensity of the Hα line in emission, showing that a bit more than half the sample (57%) is actively accreting.

Chapter 3 – Here we report on an optical spectroscopic program similar to that in Chapter 2, but carried out in the Lupus Clouds. A sample of previously selected YSOs is surveyed and spectral types are determined. The sample consists mostly of cooler, late-type M stars (90%). According to theoretical evolutionary models overlaid on H-R diagrams constructed for the sample, the population is ∼2 Myr old, with a mean mass of only 0.2 $M_\odot$. The Hα emission line yields a distribution of mass accretion rates typical of T Tauri stars ($10^{-6} - 10^{-11} M_\odot$ yr^{-1}).

Chapter 4 – This chapter presents a complete sample of flux-limited *Spitzer* IRS mid-IR (5–35 μm) spectra of the young stellar population of Serpens, as studied in Chapter 2. The spectra are presented and classified. In agreement with the findings in Chapter 2, the background population is further characterized into background

stars (due to spectral slope and silicate features in absorption), background galaxies (with redshifted PAH features) and a high ionization object of unknown nature. The bona fide YSOs amount to 115 objects, comprising embedded (class I, 18%) and disk (classes II and III, 82%) sources. Inner disk geometry is inferred from the flux ratio between 30 and 13 μm. The silicate features at 10 and 20 μm are strongly affected by the size of its emitting dust and therefore used as a proxy for dust size. A population of small dust is seen in the surface layers of the disks independent of inner disk geometry, or of a clustered or isolated environment surrounding the stars. Additionally, the results from Serpens are compared with those for the young population in the well-studied Taurus star-forming region and with the c2d IRS sample spread across the sky. The results for Serpens are similar to these two populations of different mean ages and environments. This result implies that the dust population in the surface of disks arises from an equilibrium between particle growth and fragmentation, independent of environment. This equilibrium is maintained for as long as the disks are optically thick at optical and infrared wavelengths.

Chapter 5 – The high ionization object discovered in Chapter 4, OL17, is further studied here. Complimentary spectra are obtained with the X-shooter instrument on the Very Large Telescope (VLT). The wide wavelength range of the X-shooter's three arms (UVB, VIS and NIR) covers several important emission lines that are used to determine the object's nature. Narrow emission lines, combined with low [N II]/Hα and [S II]/Hα line ratios, show that the object is a new very dusty planetary nebula.

Chapter 6 – This chapter presents the grain mineralogy of the dust in disk surfaces for four clusters for which complete IRS samples exist: the young Serpens and Taurus samples discussed in Chapter 4, as well as the Upper Scorpius and η Chamaeleontis clusters which probe the older bin of disk evolution. The data are analyzed with the same techniques, allowing direct comparison of results. A similar distribution of mean mass-averaged grain sizes (few μm) and crystallinity fractions ($\sim$10 – 20%) is observed for the four regions, despite different mean cluster ages and disk fractions. The wide spread in cluster ages ($\sim$1–8 Myr) and disk geometries, without concurrent evolution of the disk surface dust properties, points to a rapid change taking place ($\leq$1 Myr) and an equilibrium such that these properties are statistically the same until disk dissipation.

Chapter 7 – This chapter makes use of the stellar and disk characteristics derived in the previous chapters in the construction of SEDs for the young stars with disks in Serpens. The SEDs allow a correct separation between stellar and disk radiation. Taking into account the new distance of Serpens (415 pc), a younger age distribution is found for the cloud, concentrated in the 1 – 3 Myr range. The distribution of disk fractional luminosities of the Serpens population resembles that of the young Taurus, with most disks consistent with passively irradiated disks. In terms of geometry, no clear separation in fractional disk luminosities is found between the flared and flat disks around T Tauri stars as is the case for the disks around more massive Herbig Ae/Be stars. Furthermore, the mineralogy of the dust in the disk surfaces does not seem to directly correlate with either stellar or disk parameters for the large sample

studied.

Each chapter ends with its conclusions, deduced from the data there presented. Overall the main conclusions from this thesis are:

- Serpens and Lupus are both young regions, with mean ages $\sim$1.5 – 3 Myr (considering the distance to Serpens to be 415 rather than 259 pc). While the distribution of ages is very similar, the distribution of masses is not. Serpens is composed of a few early G and mostly K- and M-type stars, with masses spreading between 0.2 and 1.2 $M_{\odot}$, with a mean value around 0.7 $M_{\odot}$. This distribution is very similar to that of the young stellar population of Taurus. Lupus, however, is almost entirely composed of very low-mass M-type stars, peaking at $\sim$0.2 $M_{\odot}$. This distribution is very similar to the young star-forming regions Chamaeleon I and IC 348. This difference in mass distribution suggests some small deviations of a possible universal IMF.

- For any given region, be it a young $\sim$1 Myr or an old 7–8 Myr cluster, the distribution of the dominant size of the dust in the surface layers of disks is statistically the same. This implies that, besides coagulation and growth, this dust is also a result of destructive collisional processes. An equilibrium of these two processes must be maintained for millions of years, as long as the disk in optically thick at optical/IR wavelengths, to explain the same distributions observed.

- The mineralogical composition of the dust is on average the same for all regions. A considerable level of crystallinity ($\sim$10 – 20 %) must be established in the disk surface early in the disk evolution ($\leq$1 Myr), reaching an equilibrium that is independent of what may be happening in the disk midplane, where planets may be forming.

1.7   Outlook

The work presented in this thesis adds and expands on a large effort in the last decade to characterize the low- and intermediate-mass young stellar populations in the solar neighborhood. The great mapping capabilities and sensitivity of *Spitzer*, enhanced by ground-based surveys from optical to the mm regime, have allowed a thorough census of the disk population within a few hundred pc from the Sun. These observations, combined with large modelling efforts, have been able to set several constraints on how disks evolve. However, due to a lack of sensitivity of past and current facilities, very little is known about more distant star-forming regions. Studying their properties is especially important considering the vastly different initial conditions for regions in distinct parts of the Galaxy. Furthermore, nearby galaxies such as the Magellanic Clouds probe a very low metallicity environment, and their disk population cannot currently be resolved in the same detail as has been done for nearby star-forming regions.

In the upcoming years, the launch of the *James Webb Space Telescope (JWST)* has

the potential to change this picture. With a 6.5-meter primary mirror, the telescope will be sensitive to radiation from 0.6 to 27 μm. These two characteristics combined make this an exceptional telescope for a significant step forward in the study of star and planet formation. The sensitivity of *JWST*, in imaging and low- and medium-resolution spectroscopy, will allow observations of distant environments, like young clusters in the Magellanic Clouds, resolving individual star+disk systems. These very low-metallicity environments could have very strong effects on the disk lifetime and evolution, which in turn could connect with the observed higher likelihood of finding planets around high metallicity stars in the solar neighborhood.

Targeting the dust in the inner $\sim$100 AU of YSOs at a distance of 50, 100, or 200 pc will imply angular sizes of $2''$, $1''$, or $0.5''$, respectively. Given these small angular sizes and their prominence in the near- to mid-IR, the imaging and spectroscopic analysis of protoplanetary disks is among the main science drivers of the *JWST*. In the near-IR, NIRCam will provide virtually diffraction-limited, broad- and narrow-band imaging in the wavelength range of 0.6 to 5 μm (PSF of about $\lesssim 0.1 - 2''$, FWHM). The use of a coronograph can further enhance the contrast for low surface brightness objects (such as disks or planets around their host stars). NIRSpec will allow medium resolution (R $\sim$ 2000-4000) spectroscopy in the 1–5 μm range in any of three modes that are all ideally suited for spatially resolving the spectral properties of the disks. First, the IFU mode will allow full continuous sampling for moderately extended objects over a $3'' \times 3''$ region at a pixel size of $0.''1$. Second, fixed slits (either $0.''1 \times 1.''9$ or $0.''2 \times 3.''3$) can be placed on compact or elongated targets. Third, the microshutter assembly can be used to obtain spectra of arbitrary regions by sampling a single or multiple targets by opening a series of connected or disconnected microshutters each spanning $0.''2 \times 0.''46$ on the sky. These modes thus allow a spatial sampling of the spectral properties of protoplanetary disks up to 5 μm with about ten resolution elements for a 1000 AU disk at 400 pc, and about five resolution elements for a 100 AU disk at 50 pc. In the mid-IR, MIRI covers the 5–29 μm wavelength range for spectroscopy ($R \sim 3000$). Four IFUs will sample the wavelength range using spatial pixels of $0.''18 \times 0.''19$ (at ~ 6 μm), $0.''28 \times 0.''19$ (at ~ 10 μm), $0.''39 \times 0.''24$ (at ~ 15 μm), and $0.''64 \times 0.''27$ (at ~ 23 μm). These spatial samplings were chosen to match the *JWST* PSF at each wavelength, and imply that disks with diameters of about $2''$ will still be resolved with about five $\sim 0.''4$ resolution elements at the central wavelength of MIRI. The number of effective resolution elements for both NIRSpec and MIRI may be further improved by up to a factor of $\sim$2 using clever dithering strategies.

In addition, the Atacama Large Millimeter/submillimeter Array (ALMA), operating in the wavelength range from 0.3 to 3.6 mm at 0.01 to a few arcseconds resolution, has great potential for the study of protoplanetary disks. The combination of sensitivity, angular and spectral resolution allows ALMA to probe the cold gas and dust in protoplanetary disks across almost the entire disk, not just limited to the surface areas. Continuum and lines constrain many of the chemical and physical processes taking place in disks, as well as disk mass and luminosity that are highly uncertain without (sub-)mm points. ALMA will be able to spatially resolve the inner and

outer parts of the closest disks, directly imaging the critical 3 – 30 AU regions of the disk where planets are thought to form, thus complementing mid-IR studies of the innermost ($\sim$1 AU) disk.

References

Alexander, R. D., Clarke, C. J., & Pringle, J. E. 2006, MNRAS, 369, 216

Alexander, R. D., Clarke, C. J., & Pringle, J. E. 2006, MNRAS, 369, 229

Apai, D., Pascucci, I., Bouwman, J., Natta, A., Henning, T., & Dullemond, C. P. 2005, Science, 310, 834

Bachiller, R., & Tafalla, M. 1999, NATO ASIC Proc. 540: The Origin of Stars and Planetary Systems, 227

Baraffe, I., Chabrier, G., & Gallardo, J. 2009, ApJ, 702, L27

Blum, J., & Wurm, G. 2008, ARA&A, 46, 21

Bockelée-Morvan, D., et al. 2000, A&A, 353, 1101

Boss, A. P. 1997, Science, 276, 1836

Bouwens, R. J., & Illingworth, G. D. 2006, Nature, 443, 189

Bouwman, J., et al. 2008, ApJ, 683, 479

Brown, J. M., et al. 2007, ApJ, 664, L107

Calvet, N., & Hartmann, L. 1992, ApJ, 386, 239

Calvet, N., D'Alessio, P., Hartmann, L., Wilner, D., Walsh, A., & Sitko, M. 2002, ApJ, 568, 1008

Cameron, A. G. W. 1962, Icarus, 1, 13

Cameron, A. G. W. 1978, Moon and Planets, 18, 5

Carpenter, J. M., Mamajek, E. E., Hillenbrand, L. A., & Meyer, M. R. 2006, ApJ, 651, L49

Carpenter, J. M., et al. 2009, ApJS, 181, 197

Ciesla, F. J. 2009, Icarus, 200, 655

Cieza, L., et al. 2007, ApJ, 667, 308

Clarke, C. J., Gendrin, A., & Sotomayor, M. 2001, MNRAS, 328, 485

Crovisier, J., Leech, K., Bockelee-Morvan, D., Brooke, T. Y., Hanner, M. S., Altieri, B., Keller, H. U., & Lellouch, E. 1997, Science, 275, 1904

Desch, S. J., & Connolly, H. C., Jr. 2002, Meteoritics and Planetary Science, 37, 183

Dominik, C., & Tielens, A. G. G. M. 1997, ApJ, 480, 647

Dominik, C., Blum, J., Cuzzi, J. N., & Wurm, G. 2007, Protostars and Planets V, 783

Dullemond, C. P., Dominik, C., & Natta, A. 2001, ApJ, 560, 957

Dullemond, C. P., & Dominik, C. 2004, A&A, 421, 1075

Dullemond, C. P., & Dominik, C. 2005, A&A, 434, 971

Dullemond, C. P., Hollenbach, D., Kamp, I., & D'Alessio, P. 2007, Protostars and Planets V, 555

Ercolano, B., Clarke, C. J., & Drake, J. J. 2009, ApJ, 699, 1639

Fabian, D., Jäger, C., Henning, T., Dorschner, J., & Mutschke, H. 2000, A&A, 364, 282

Fischer, D. A., & Valenti, J. 2005, ApJ, 622, 1102

Furlan, E., et al. 2006, ApJS, 165, 568

Frieswijk, W. 2008, Ph.D. Thesis

Gail, H.-P. 2004, A&A, 413, 571

Gautier, T. N., III, et al. 2007, ApJ, 667, 527

Goldreich, P., & Ward, W. R. 1973, ApJ, 183, 1051

Gorti, U., Dullemond, C. P., & Hollenbach, D. 2009, ApJ, 705, 1237

Haisch, K. E., Jr., Lada, E. A., & Lada, C. J. 2001, ApJ, 553, L153

Harker, D. E., & Desch, S. J. 2002, ApJ, 565, L109

Harker, D. E., Woodward, C. E., & Wooden, D. H. 2005, Science, 310, 278

Harker, D. E., Woodward, C. E., Wooden, D. H., Fisher, R. S., & Trujillo, C. A. 2007, Icarus, 190, 432

Hartigan, P., Edwards, S., & Ghandour, L. 1995, ApJ, 452, 736

Hernández, J., Hartmann, L., Calvet, N., Jeffries, R. D., Gutermuth, R., Muzerolle, J., & Stauffer, J. 2008, ApJ, 686, 1195

Hillenbrand, L. A. 2009, IAU Symposium, 258, 81

Hollenbach, D. J., Yorke, H. W., & Johnstone, D. 2000, Protostars and Planets IV, 401

Houck, J. R., et al. 2004, ApJS, 154, 18

Johansen, A., Oishi, J. S., Mac Low, M.-M., Klahr, H., Henning, T., & Youdin, A. 2007, Nature, 448, 1022

Juhász, A., Henning, T., Bouwman, J., Dullemond, C. P., Pascucci, I., & Apai, D. 2009, ApJ, 695, 1024

Juhász, A., et al. 2010, ApJ, 721, 431

Kalas, P., et al. 2008, Science, 322, 1345

Kemper, F., Vriend, W. J., & Tielens, A. G. G. M. 2004, ApJ, 609, 826

Kennedy, G. M., & Kenyon, S. J. 2009, ApJ, 695, 1210

Kessler-Silacci, J., et al. 2006, ApJ, 639, 275

Koenigl, A. 1991, ApJ, 370, L39

Kóspál, Á., Ardila, D. R., Moór, A., & Ábrahám, P. 2009, ApJ, 700, L73

Lagrange, A.-M., et al. 2010, Science, 329, 57

Malfait, K., Waelkens, C., Waters, L. B. F. M., Vandenbussche, B., Huygen, E., & de Graauw, M. S. 1998, A&A, 332, L25

Mamajek, E. E. 2009, American Institute of Physics Conference Series, 1158, 3

Mayor, M., & Queloz, D. 1995, Nature, 378, 355

Min, M., Hovenier, J. W., & de Koter, A. 2005, A&A, 432, 909

Myers, P. C.; Evans, N. J., II; Ohashi, N. 2000, Protostars and Planets IV, 4

Oliveira, I., et al. 2010, ApJ, 714, 778

Olofsson, J., Augereau, J.-C., van Dishoeck, E. F., Merín, B., Grosso, N., Ménard, F., Blake, G. A., & Monin, J.-L. 2010, A&A, 520, A39

Owen, J. E., Ercolano, B., Clarke, C. J., & Alexander, R. D. 2010, MNRAS, 401, 1415

Paszun, D., & Dominik, C. 2009, A&A, 507, 1023

Pollack, J. B., Hubickyj, O., Bodenheimer, P., Lissauer, J. J., Podolak, M., & Greenzweig, Y. 1996, Icarus, 124, 62

Pontoppidan, K. M., & Brearley, A. J. 2010, Protoplanetary Dust: Astrophysical and Cosmochemical Perspectives, 191

Rieke, G. H., et al. 2005, ApJ, 620, 1010

Safronov, V. S., & Zvjagina, E. V. 1969, Icarus, 10, 109

Salvaterra, R., Magliocchetti, M., Ferrara, A., & Schneider, R. 2006, MNRAS, 368, L6

Shu, F. H. 1977, ApJ, 214, 488

Shu, F. H., Adams, F. C., & Lizano, S. 1987, ARA&A, 25, 23

Shu, F., Najita, J., Galli, D., Ostriker, E., & Lizano, S. 1993, Protostars and Planets III, 3

Sicilia-Aguilar, A., Hartmann, L. W., Fürész, G., Henning, T., Dullemond, C., & Brandner, W. 2006, AJ, 132, 2135

Sicilia-Aguilar, A., et al. 2009, ApJ, 701, 1188

Snell, R. L., Loren, R. B., & Plambeck, R. L. 1980, ApJ, 239, L17

Spergel, D. N., et al. 2003, ApJS, 148, 175

Stahler, S. W. & Palla, F. 2004, The Formation of Stars, WILEY-VHC

Su, K. Y. L., et al. 2006, ApJ, 653, 675

Tielens, A. G. G. M. 2005, The Physics and Chemistry of the Interstellar Medium, by A. G. G. M. Tielens, pp. . ISBN 0521826349. Cambridge, UK: Cambridge University Press, 2005

Udry, S., & Santos, N. C. 2007, ARA&A, 45, 397

Ungerechts, H., & Thaddeus, P. 1987, ApJS, 63, 645

van Boekel, R., Waters, L. B. F. M., Dominik, C., Bouwman, J., de Koter, A., Dullemond, C. P., & Paresce, F. 2003, A&A, 400, L21

van Boekel, R., et al. 2004, Nature, 432, 479

Weidenschilling, S. J. 1980, Icarus, 44, 172

Werner, M. W., Gallagher, D. B., & Irace, W. R. 2004, Advances in Space Research, 34, 600

Wooden, D. H., Harker, D. E., Woodward, C. E., Butner, H. M., Koike, C., Witteborn, F. C., & McMurtry, C. W. 1999, ApJ, 517, 1034

Wooden, D., Desch, S., Harker, D., Gail, H.-P., & Keller, L. 2007, Protostars and Planets V, 815

Wyatt, M. C. 2008, ARA&A, 46, 339

Youdin, A. N., & Goodman, J. 2005, ApJ, 620, 459

Zolensky, M. E., et al. 2006, Science, 314, 1735

2

Optical Characterization of a New Young Stellar Population in the Serpens Molecular Cloud

We report on the results of an optical spectroscopic survey designed to confirm the youth and determine the spectral types among a sample of young stellar object (YSO) candidates in the Serpens molecular cloud. We observed 150 infrared (IR) excess objects previously discovered by the *Spitzer* Legacy Program "From Molecular Cores to Planet-Forming Disks" (c2d), bright enough for subsequent *Spitzer*/InfraRed Spectrograph (IRS) spectroscopy. We obtained 78 optical spectra of sufficient signal-to-noise for analysis. Extinctions, effective temperatures and luminosities are estimated for this sample, and used to construct Hertzsprung-Russell (H-R) diagrams for the population. We identified 20 background giants contaminating the sample, based on their relatively high extinction, position in the H-R diagram, the lack of Hα emission and relatively low IR excess. Such strong background contamination (25%) is consistent with the location of Serpens being close to the Galactic plane (5° Galactic latitude). The remaining 58 stars (75%) were all confirmed to be young, mostly K- and M-type stars that are presumed to belong to the cloud. Individual ages and masses for the YSOs are inferred based on theoretical evolutionary models. The models indicate a spread in stellar ages from 1 Myr to 15 Myr, peaking at 2 – 6 Myr, and a mass distribution of 0.2 – 1.2 $M_\odot$ with median value around 0.8 $M_\odot$. Strong Hα emission lines (EW[Hα] > 3 Å) have been detected in more than half of the sample (35 stars). The mass accretion rates as derived from the Hα line widths span a broad distribution over four orders of magnitude with median accretion rate of 10^{-8} $M_\odot$ yr^{-1}. Our analysis shows that the majority of the IR excess objects detected in Serpens are actively accreting, young T-Tauri stars.

Isa Oliveira, B. Merín, K. M. Pontoppidan, E. F. van Dishoeck, R. A. Overzier,
J. Hernández, A. Sicilia-Aguilar, C. Eiroa, B. Montesinos

2.1   Introduction

The Serpens molecular cloud has received considerable attention over the past decade. Because it is an actively star-forming complex containing a substantial mass of molecular gas and young stars within both clustered and diffuse environments, it has become one of our main laboratories for testing theories of low-mass star formation (Djupvik et al. 2006; Eiroa et al. 2005; Klotz et al. 2004; Kaas et al. 2004; Preibisch 2003; Olmi & Testi 2002; Williams & Myers 2000; Hogerheijde et al. 1999; Preibisch 1998; Herbst et al. 1997b).

The Serpens cloud is one of the five clouds selected as part of the *Spitzer* Legacy Program "From Molecular Cores to Planet-Forming Disks" (c2d; Evans et al. 2003), providing images in the $3 - 70$ μm range. The wide wavelength coverage and high sensitivity in the infrared (IR) of *Spitzer* make it possible to easily identify a new, complete, flux-limited (down to luminosities below 0.01 $L_\odot$) young stellar population. This population has been found to be distributed over almost the entire area surveyed, offering an opportunity to determine the stellar content in different regions of the cloud, the distributions of the youngest stars and substellar objects, and the properties of their circumstellar envelopes and disks.

The c2d program has mapped a 0.89 deg^2 portion out of the more than 10 deg^2 area (Kaas et al. 2004) of the Serpens molecular cloud. Assuming a distance of 259 ± 37 pc (Straizys et al. 1996), this corresponds to a covered area of about 2.5 pc $\times$ 9 pc. This region was discovered to be very rich in young stars (Harvey et al. 2007b), some of them previously identified with Infrared Space Observatory (ISO) data (Djupvik et al. 2006). This poorly known cluster of young stars, cluster B, and the previously unknown star-forming region around it, is located about half a degree southwest of the well known Serpens cloud core, containing cluster A (Kaas et al. 2004). It has a high density of young stars, making it a unique target region for obtaining a full and consistent picture of clustered low-mass star formation and compare this with young stars in the surrounding field.

We are currently carrying out a multi-wavelength survey of this region, from X-ray to millimeter wavelengths, in order to create a "template" sample for the study of the evolution of circumstellar disks around stars younger than ~ 10 Myr, within a single, small and well defined region. This work provides the necessary information for anchoring the study of protoplanetary disks to their parent population by means of the optical spectroscopic classification of the central stars. Precise stellar properties are needed to perform an accurate study of the evolutionary stages of the young stellar objects (YSOs) and their disks. Most spectroscopic studies of protoplanetary disk evolution refer to samples of young stars scattered across the sky or to sources in large star-forming clouds like Taurus, making it difficult to separate intrinsic evolutionary effects from those caused by external influences such as environment or star formation history.

In this paper we report on our optical spectroscopic survey designed to confirm the youth and determine spectral types of the newly discovered YSO candidates in

the Serpens region with *Spitzer*. These spectra will also be used to estimate mass accretion rates using the strength of the Hα emission line (Muzerolle et al. 2003; White & Basri 2003, Natta et al. 2004), and the extinction toward each object.

The paper is constructed as follows: Section 2.2 describes the selection criteria for our sample, and in Section 2.3 we describe the observations and data reduction. In Section 2.4 we discuss our spectral classification methods, along with its results for this sample and derive effective temperatures. In Section 2.5, we present our extinction studies based on the *Spitzer* photometry and on our optical spectra. In Section 2.6 we derive luminosities for the objects. This allows us to place each object in a Hertzsprung-Russell (HR) diagram, and derive its age and mass from comparison with evolutionary models. The Hα line and accretion rates are discussed in Section 2.7. Finally, in Section 2.8 we present our conclusions.

2.2   Sample Selection

From the c2d catalog, Harvey et al. (2007b) plotted spectral energy distributions (SEDs; assuming a K7 spectral type for all the sources) and identified 235 YSO candidates – objects with IR excess, interpreted as due to disks or envelopes. These authors discuss the problem that background galaxies and bright background post-AGB stars may show the same color distribution as that of YSOs. Particularly, the post-AGB stars could contaminate the bright end of the luminosity distribution.

To this original sample of 235 objects, a flux threshold of 3mJy at 8μm was applied, resulting in 150 sources bright enough to be observed in follow-up observations with the InfraRed Spectrograph (IRS), onboard *Spitzer*. The IRS observations, carried out to study the evolution of dust in protoplanetary disks of a complete, flux-limited sample will be presented in a future paper (Oliveira et al. 2009). Here, we present optical spectroscopy of 78 stars bright enough to obtain optical spectroscopy with a 4 m class telescope. The remaining objects are too extinct in the optical to be detected, and are being classified in an ongoing near-IR (NIR) spectroscopic survey.

The resulting sample contains objects that span a range in evolutionary stages from embedded Class I (i.e., spectral slope $\alpha_{2-24\mu m} > 0.3$) sources to young stars with protoplanetary disks (Class II sources, $-1.6 < \alpha_{2-24\mu m} < 0.3$) and stars with photospheric fluxes in the Infrared Array Camera (IRAC) bands and excess in the MIPS bands (also called "cold disks", e.g., Brown et al. 2007).

Figure 2.1 shows the spatial distribution of the complete sample of 150 Serpens YSOs observed with *Spitzer*/IRS. The filled and open symbols correspond to detected and undetected objects from the optical survey presented in this paper, respectively.

2.3   Observations and Data Reduction

The spectroscopic data were obtained during observing runs at three telescopes: two runs with the multi-object Wide Field Fiber Optical Spectrograph (*WYFFOS*) at
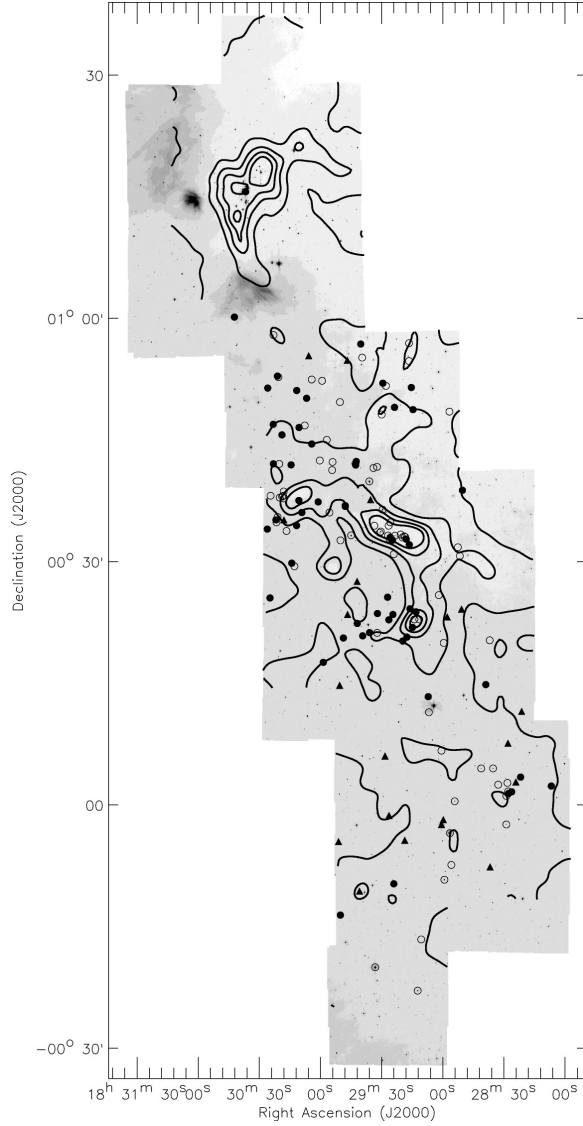
Figure 2.1 − Observed objects shown on the $8.0\mu m$ IRAC map of the Serpens Molecular Cloud, imaged as part of the Spitzer Legacy Program "From Molecular Clouds to Planet-Forming Disks" (c2d) (Harvey et al. 2006). Filled symbols are the 78 objects for which we present optical spectroscopy in this paper: filled circles are confirmed members of the cloud and filled triangles are likely candidate background contaminants (§ 2.6). The open symbols are the remaining young stellar object candidates in the sample, not detected in our survey of 150 YSOs. Overlaid are the contours (5, 10, 15, 20 and 25 mag) of visual extinction derived from the "c2d" extinction maps.

the 4.2m William Herschel Telescope (*WHT*) in 2006 May and 2007 June, and one run with the 3.6m Device Optimized for the LOw RESolution (*DOLORES*) at the Telescopio Nazionale Galileo (*TNG*) in 2006 June, both telescopes are located at the Observatorio del Roque de los Muchachos in La Palma, and one run with the Calar Alto Faint Object Spectrograph (*CAFOS*) at the 2.2m Calar Alto Telescope. Neither absolute flux calibration was performed, nor were telluric absorption features removed. Technical information on each run is specified in Table 2.1. Figure 2.2 shows a representative sample of the spectra of the objects in our sample.

2.3.1   WHT Data

WYFFOS was fed from the AutoFib 2 robotic fiber positioner (Parry et al. 1994) and targets were selected to maximize the number of objects observed in each configuration, using its program `AF2_CONFIGURE`. We used the "small" fiber module of *WYFFOS*, corresponding to fiber aperture of $1''6$. The wavelength range was $\sim$3000 Å, centered at 7000 Å, in order to include the Hα and Li I (6707 Å) lines. The average resolving power was $R \sim 1750$. In order to adequately remove the effects of cosmic-ray hits on the detector, each field was observed using three exposures. Flat fields and bias frames were obtained at the beginning of each night and neon calibration arc lamp spectra at the beginning of the nights, as well as separately for each configuration. Unused fibers were placed on the sky. We obtained *WYFFOS* spectra for 71 objects of our sample.

Data reduction was performed using our own code, based on the instrument reduction guideline[1], within `IRAF` and `IDL`. After bias subtraction and flat fielding, the spectra were extracted and wavelength calibrated with the arc Ne comparison lamp data, to a precision of $\sim$0.5 Å.

2.3.1.1   *Sky subtraction*

The quality of the optical spectra is limited by the accuracy of the sky subtraction, especially for faint stars. As opposed to long-slit spectroscopy, where an adequate sky removal can be performed using the sky background on opposite sides very close to the object spectrum, a precise sky subtraction in multi-object fiber spectroscopy is complicated by the lack of a sky spectrum close to the object spectrum both in position and in time (e.g., see Wyse & Gilmore 1992). In general, the sky background depends mainly on the local sky conditions at the observatory during the time of observations. However, in the case of a molecular cloud, the "sky" may also have a significant contribution from extended continuum and line emission from the cloud itself.

We used the fibers placed on "empty" positions in the field to measure the contribution from the sky. The sky spectra were reduced and extracted in an identical manner to the science data. The sky spectra were visually inspected and a few of bad

---

[1]http://www.ing.iac.es/Astronomy/instruments/af2/index.html
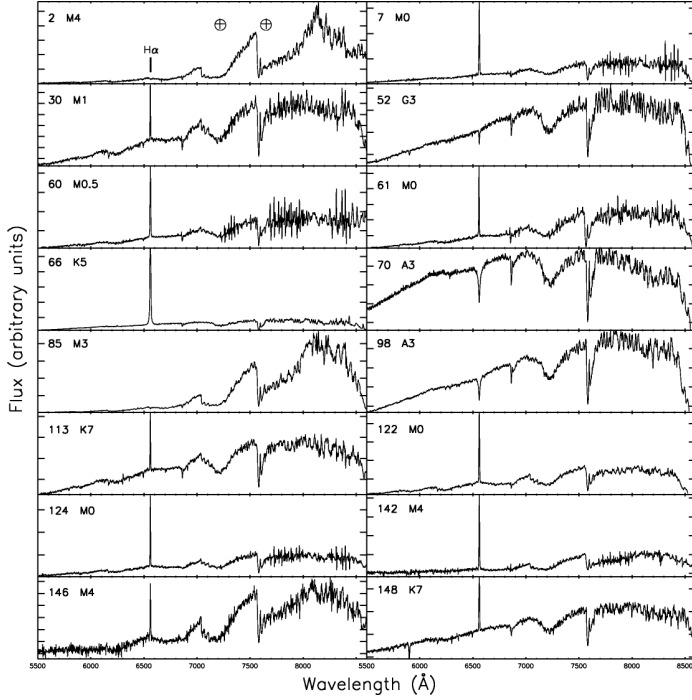
Figure 2.2 – Selected spectra of a representative sample of the observed objects. Along with their numbers from Table 2.1, the extracted spectral types are shown for reference. The strong Hα lines are noticeable in several spectra. The main remaining atmospheric features are indicated with ⊕.

qualities were discarded. None of them showed diffuse Hα in emission from the cloud. To reach optimum results, even for the faintest sources, a single master sky spectrum, built with an average of 12 – 15 sky spectra, was computed for each configuration. During the sky subtraction of each star, we applied small scalings to the master sky spectrum to take into account the fact that the throughput of different fibers shows slight variations. The scalings were typically in the range of 0.95–1.05, and chosen to optimize the sky subtraction.

In several cases, the sky subtraction proved imperfect with residuals being most notable at $\lambda >7700$Å. These residuals are very common in low to intermediate S/N fiber spectra due to the strong OH sky lines beyond 6700 Å. It is very difficult to remove these OH features because the sky lines are usually not well resolved, and also due to the nonlinear variations in throughput and dispersion for different fibers. We have checked, however, that the spectral type classification and Hα equivalent width measurements are not substantially hampered by these effects.

2.3.2   TNG Data

The observations with *DOLORES* used the long-slit mode. Slit rotation was calculated in order to enable more than one object in the slit whenever two targets were closer than the length of the slit (8′). The wavelength range of ∼1600 Å was centered at 7000 Å, again including the Hα and Li I (6707 Å) lines, with resolving power $R \sim 2500$. Exposure times ranged from 12 to 1000 seconds. Flat fields, bias, and argon comparison arc lamp spectra were obtained at the beginning of each night.

After bias subtraction and flat fielding, the spectra were extracted and wavelength calibrated with a combination of the Ar arc lamp data and airglow lines[2], including the OH Meinel bands, using the "doslit" task of the `specred` package in `IRAF`. Sky subtraction was done during the extraction based on the off-source regions along the slit. In total, we obtained *DOLORES* spectra of 18 sources, 15 of which were also observed with *WYFFOS*.

2.3.3   CAFOS Data

CAFOS was used with mask observations in 2008 June. Three masks were taken using the grism R-100. Flat fields, bias, and HgCd/He/Rb comparison arc lamp spectra were obtained at the beginning of each night. The wavelength coverage (3500 Å, centered on 7750 Å) for each source varies slightly depending on their position on the CCD, with resolving power $R \sim 3523$. The exposure time of 2400 seconds for each mask was divided into two for cosmic-ray rejection.

After bias subtraction and flat fielding, the fields were divided so that each source would be in an image by itself and then further reduced as standard slit observations: the spectra were extracted and wavelength calibrated using the "doslit" task of the `specred` package in `IRAF`, performing sky subtraction during the extraction based on the off-source regions along each slit.

The low resolution of these instruments, combined with low signal-to-noise (S/N) for most faint objects, did not allow us to detect or put meaningful upper limits on the Li I (6707 Å) line.

2.4   Spectral Classification

Two methods were used in the spectral classification of the sources and are explained below.

2.4.1   Method I

The objects were classified following the spectral classification scheme of Hernández et al. (2004) optimized to classify early type stars (up to early G). For stars with spectral type later than G, the scheme was extended by incorporating spectral indices for the

---

[2]http://astro.u-strasbg.fr/∼koppen/divers/AirGlow.html
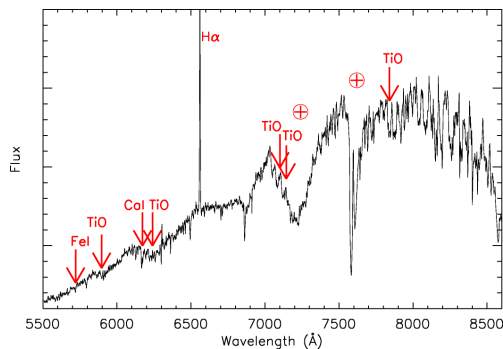
Figure 2.3 − Features used in the spectral type classification scheme of Hernández et al. (2004) are shown on the spectrum of source # 113. (A color version of this figure is available in the online journal)

ranges G0–K5 and K5–M6 (Sicilia-Aguilar et al. 2005, Briceño et al. 2005[3]). More information about this classification scheme can be found in the references above. In short, it is based on strong spectral features that are sensitive to T_{eff} but insensitive to reddening in a specific luminosity class (dwarf in this case), since it uses local continua for the determination of the feature's equivalent widths (EW). It is also designed to avoid problems caused by non-photospheric contributions (e.g. emission lines). The wavelength range of the *WYFFOS* spectra covers 12 of these features for all spectral types, while *DOLORES* covers 6 and the range of *CAFOS* covers 15 features. On average, 6 features for *WYFFOS*, 5 features for *DOLORES*, and 7 features for *CAFOS* were used for each classification, as exemplified in Figure 2.3.

The spectral types calculated from each feature result in a weighted mean spectral type. The errors in the estimated spectral types have two contributions: the error in the measurement of each feature and the error of its fit to the standard (see Hernández et al. 2004 for more details). A few objects were observed in both runs (as can be seen in Table 2.1). For these objects, both spectra were ran separately through the spectral classification code. Their spectral classifications were found to be consistent with each other, typically within one subclass.

2.4.2   Method II

Due to telluric absorption features not corrected for in the spectra presented here, care needs to be taken when using automatic fitting of features very close to these telluric bands. To make sure that the spectral types derived in Method I are correct, an additional spectral typing procedure was applied to the data.

The library of standard spectra from Mora et al. (2001), covering the wavelength range of 5800–7000Å, was used in this method. In this region, different lines and bands

---

[3]Information about the code can be found at
http://www.astro.lsa.umich.edu/∼hernandj/SPTclass/sptclass.html
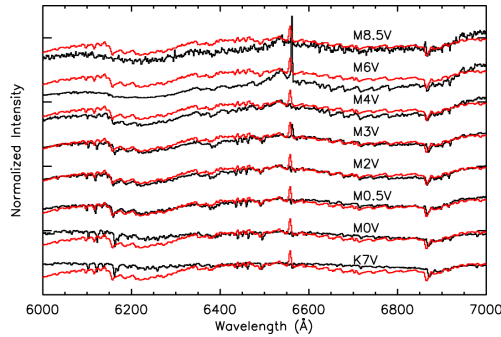
Figure 2.4 – Correlation between science spectrum of source #115 (gray) and standard spectra for different spectral types (black; spectral types indicated on the top right of each standard spectrum from the library of Mora et al. (2001)). (A color version of this figure is available in the online journal)
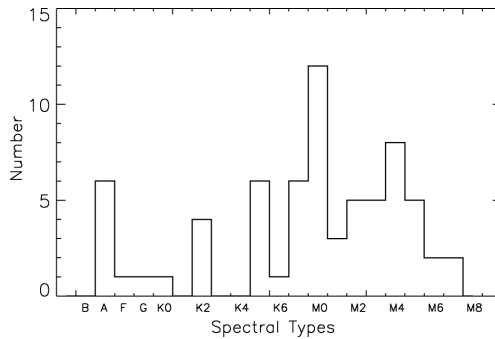
Figure 2.5 – Distribution of spectral types of YSO candidates in the Serpens molecular cloud based on the classification scheme described in Section 2.4.

are found for specific spectral types, making them unique. Each science spectrum was normalized and compared to normalized standards of different spectral types. The spectral classification procedure was based on finding the best correlation between observed and standard spectra, combined with a visual inspection of each match. Figure 2.4 shows an example of the correlation.

2.4.3   Results

The two methods agree in their classification (within 1 subclass) for about 80% of the sources. When in disagreement, Method II is judged to be more reliable because of the visual inspections, whereas Method I may be contaminated by the aforementioned telluric absorption features. The spectral types obtained for our sample are given in Table 2.2. Figure 2.5 shows the distribution of spectral types, which is clearly dominated by K- and M-type stars.

2.4.4   Effective Temperature

Effective temperatures (T_{eff}) were determined using calibrations relating them to spectral types. For stars earlier than M0, the relationship established by Kenyon & Hartmann (1995) was adopted, while for later type stars that by Luhman et al. (2003) was used. This method was also used in the determination of T_{eff} for similar study on another of the clouds observed by the c2d, Cha II (Spezzi et al. 2008). The errors in T_{eff} come directly from the errors in the spectral type determination.

2.5   Visual Extinction

Once the spectral types are known, we used synthetic NEXTGEN spectra (Hauschildt et al. 1999) and the extinction law by Weingartner & Draine (2001) to compute the observed extinction toward our targets (A_VObs). The appropriate synthetic spectrum for each spectral type was extincted with A_V ranging from 0 to 20 mag (with increments of 0.5 mag) and a χ^2 minimization was performed between the observed and synthetic extincted spectra to estimate the extinction. We estimate an intrinsic error in our A_VObs determinations of 1.0-1.5 mag by comparing our source 98 (spectral type A3) with the A3 V absolute flux standard star Kopff 27 (Stone 1977), from the ING list of spectro-photometric standard stars. This error includes the uncertainty in the total extinction determination and the fact that the fiber-fed spectra are not flux calibrated.

Table 2.2 compares our extinction values from the optical spectra (A_VObs) with those from the "c2d" extinction maps (A_VCloud). The "c2d" map was constructed using the average extinction toward background stars within a $5'$ beam. Thus, these values give an indication of the average amount of extinction that the cloud produces in a given area, albeit with a large beam. More information about this extinction determination and its uncertainties can be found in the "c2d" delivery documentation (Evans et al. 2007), and in Harvey et al. (2006).

Figure 2.6 compares the two estimates of extinction for our targets described above. A large spread around the line of equal extinction is seen. This dispersion is useful to pinpoint objects with peculiar extinction characteristics. Taking into account a typical error of 2 mag in both extinction determinations and the large beam sizes for the "c2d" extinction values, the larger differences might be explained by two effects:

1. For the sources with A_VObs $\lesssim A_V$Cloud, an indication of their depth in the cloud can be obtained. Specifically, such sources are likely embedded in the cloud, or located in front of it.

2. If A_VObs $>> A_V$Cloud (shaded area in Figure 2.6), the molecular cloud by itself is unlikely to explain such extinction. On the one hand, for young stars embedded in their parent envelopes, an extra extinction compared to the local average in the cloud is naturally expected. Such embedded sources, however, are also expected to show a strong IR excess. On the other hand, stars at distances much larger than that of the cloud are also likely to have an enhanced extinction. We argue that
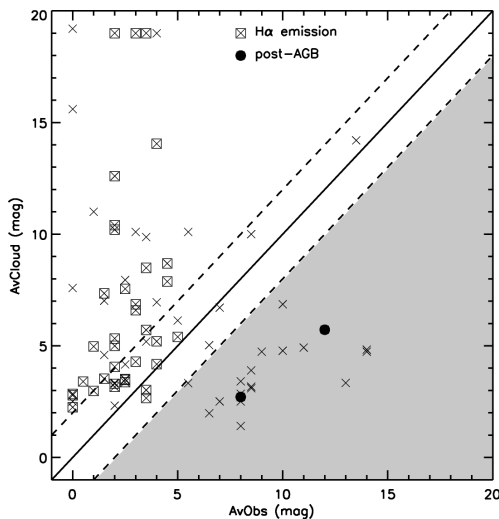
Figure 2.6 – Relationship between the extinction values estimated from our optical spectra (A_V Obs) and the extinction values from the "c2d" Spitzer data averaged over a $5'$ radius (A_V Cloud) is shown with crosses. The solid line indicates A_V Obs $= A_V$ Cloud, with typical errors of 2 mag (dashed lines). Objects marked with a square are accreting stars according to the definition of White & Basri (2003), while objects marked with a filled circle are confirmed post-AGB stars. The shaded region is where we propose background stars should lie.

this is the dominant category of sources in the shaded area of Figure 2.6, though confirmation through another method is needed.

Indeed, none of the objects in the shaded area was found to have a strong IR excess, as evidenced by the low *Spitzer*-derived slope ($\alpha_{2-24\mu m}$) values, shown in Table 2.2. This suggests that those objects are not surrounded by large amounts of circumstellar dust but rather by tenuous dust layers, consistent with them being post-AGB stars at distances of several kpc. Follow-up c2d observations of bright YSO candidates in the Serpens cloud with *Spitzer* IRS confirmed that two of the sources with A_V Obs $\gg A_V$ Cloud are post-AGB stars, seen through the cloud (filled circles in Figure 2.6). Post-AGB stars are so bright that, at a farther distance, their colors and magnitudes can be comparable to those of YSOs in the cloud. They can, however, be distinguished by the presence of spectral features at 13 and 21 μm, not seen in YSOs (Waters et al. 1999).

2.6   H-R Diagram

Given the spectral type, effective temperature (derived in Section 2.4.4), and luminosity of a source, individual age and mass can be estimated by comparing its position in the H-R diagram with evolutionary tracks.

2.6.1   Luminosities

Stellar luminosities were calculated by integrating the NEXTGEN stellar photosphere for each object, scaled to dereddened optical (from the literature) or Two Micron All Sky Survey (2MASS) fluxes, depending on their availability. The errors are derived from the uncertainty in the distance to the cloud and the error on the extinction (± 2 mag). Similar methods for luminosity estimation have been widely used in the literature (van den Ancker et al. 1997, van den Ancker et al. 1998, Alcalá et al. 2008, Merín et al. 2008). The extinction law of Weingartner & Draine (2001) was used to correct for the reddening, to be consistent with the analysis in Section 2.5. A careful inspection of all the resulting SEDs was performed to find the best-fit extinction from the two A_V values discussed above plus the best-fit A_V from the spectral type and the optical or NIR photometry. The resulting best-fit extinctions (A_V Final) and luminosities are shown in Table 2.3. Objects # 44 and 47 were not detected by 2MASS and, therefore, no J, H, and K magnitudes are available for them. For this reason, we could not determine their luminosities and they are not included in the H-R diagram. Objects # 41 and 117 are rising sources (likely due to an edge-on disk or envelope), resulting in an unrealistically low luminosity and were marked with a different symbol (square) in the H-R diagram.

2.6.2   Results

The H-R diagram of the sample is shown in Figure 2.7. The stars are compared with evolutionary tracks from Baraffe et al. (1998) and Siess et al. (2000). Twenty objects are outside the range of the isochrones in the H-R diagram (gray circles in Figure 2.7). These objects are too luminous to be at a distance of 259 pc even in the extreme case of having vanishing extinction. As discussed above, their SEDs indeed show very little IR excess, only at the longest wavelengths, and therefore they likely do not belong to the cloud. Obviously for these objects, no ages or masses could be determined.

Sixteen of these outliers have A_V Obs $>> A_V$ Cloud and therefore appear in the shaded area of Figure 2.6. Thus, there is a 92% correspondence of both methods to identify background sources. The 20 background stars are removed from the sample, leaving the remainder as a purer YSO sample in Serpens.

These remaining objects, shown with black circles in Figure 2.7, are found to be consistent along the 1–10 Myr isochrones and between the 0.2 and 1.2 $M_\odot$ mass tracks in both diagrams, indicating a possibly coeval population of YSOs dominated by very low-mass stars. Early type ($T_{\rm eff} > 6000$K) stars fall outside the Baraffe et al. (1998) tracks, but are in the range of the Siess et al. (2000) models. In these cases, ages and masses could only be derived from the latter.

Individual ages and masses of the YSOs in Serpens were derived from the models and are shown in Table 2.3 and Figure 2.8. The Baraffe et al. (1998) tracks tend to produce larger masses and ages than those found with the Siess et al. (2000) tracks for the same position in the diagram. We also find that, for the different models, the
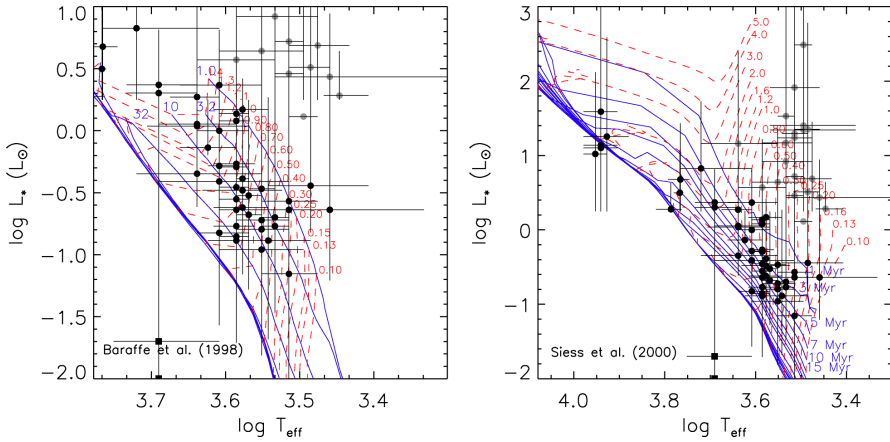
Figure 2.7 − H-R diagrams of the objects in this sample. Overlaid are the isochrones (solid lines) and mass tracks (dashed lines) from Baraffe et al. (1998) (left) and Siess et al. (2000) (right), with their corresponding age (in Myr) and mass (in $M_\odot$) indicated. Black circles correspond to objects in the Serpens Cloud, while gray circles are background sources (see text for details). Note the different scales in the two plots. (A color version of this figure is available in the online journal)

differences in ages are within the luminosity errors, while the differences in masses are slightly larger than those due to the errors. In spite of the differences between models, we find similar mass and age distributions in both cases. Both sets of tracks imply a population of YSOs concentrated between 1 Myr and 15 Myr with a few sources older than 15 Myr, and strongly peaked at $2-6$ Myr. The inferred median age is 7.5 Myr with the Baraffe et al. (1998) and 4.7 Myr with the Siess et al. (2000) tracks. Individual masses range from 0.2 $M_\odot$ to 2.2 $M_\odot$, with median values of 0.8 $M_\odot$ and 0.6 $M_\odot$ for the Baraffe et al. (1998) and Siess et al. (2000) models, respectively. The objects more massive than 2.0 $M_\odot$ (#62, 70, 98, 108, 120, 139, 141) do not lie in the more clustered regions of the cloud, and are also separate from each other. The main uncertainty is caused by the uncertainty in extinction: higher (lower) extinction values by 2 mag can shift the Siess et al. (2000) median age by a factor of 2 to younger (older) ages. It is also important to stress that this is not a complete IMF study–we observe a bias toward a larger mean age due to the bias in the selection of the sources (i.e., lack of very young, deeply embedded, Class 0 objects). Nevertheless, given that some of the stellar ages are clearly larger than the theoretical median age of a molecular cloud (Bary et al. 2007), we cannot rule out from the current age distribution that several star-forming events have taken place in the observed Serpens cloud. This is also consistent with the studied region in Serpens being larger than other coeval star-forming clusters, where less disperse age distributions have been found, e.g., IC 348 (Muench et al. 2007) or Chamaeleon I (Luhman 2007).

Some basic tests for environmental trends were performed using our current data set consisting of 78 stars. No strong correlations between the main parameters derived
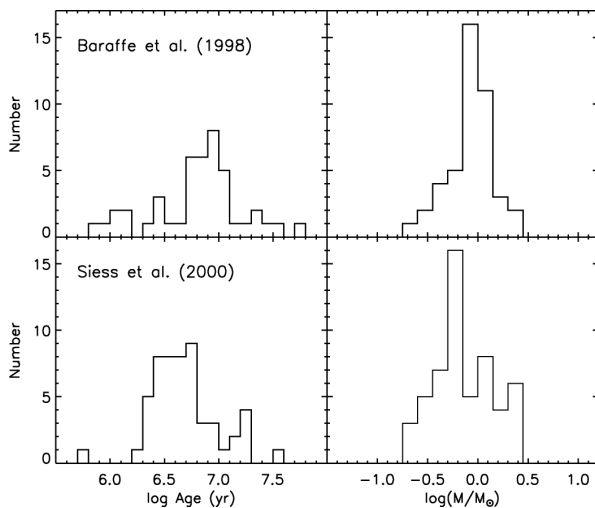
Figure 2.8 – Histograms of masses and ages for the sample of YSOs in Serpens, derived from the models of Baraffe et al. (1998) (top) and Siess et al. (2000) (bottom).

from the stellar spectra (ages and masses) and their positions in the cloud were found. This analysis will be revisited once the entire sample of 150 YSOs will be available.

Recent analysis suggests that the distance to Serpens may be as low as 193 ± 13 pc (J. Knude, private communication), rather than the distance of 259 pc assumed here. The smaller distance would imply a notable increase in individual ages due to the decrease in luminosities, with median ages of 15.9 Myr and 10.1 Myr with the Baraffe et al. (1998) and Siess et al. (2000) tracks, respectively. Median masses are not so strongly affected due to the mass tracks being almost vertical in the low-mass regime, yielding median masses of 0.8 $M_\odot$ and 0.6 $M_\odot$ according to the Baraffe et al. (1998) and Siess et al. (2000) tracks, respectively.

2.7   Accretion Based on Hα Emission

A relation between the Hα line-to-continuum ratio and evolution of its emitting source has been widely explored (Bertout 1989, Hartmann 1998, Muzerolle et al. 2003, White & Basri 2003, Stahler & Palla 2004, Natta et al. 2004). It is argued that the strength of the Hα line decreases with evolutionary stage. A similar decline is seen in the strength of the prominent Ca II H and K lines (3968 Å and 3934 Å, respectively) and in the surface rotational velocity, reinforcing the motivation for a chromospheric origin for main-sequence Hα emission. However, active T Tauri stars have Hα fluxes much larger than those predicted by chromospheric models (Stahler & Palla 2004), meaning that for these objects Hα is unlikely to originate primarily in a chromosphere. Mass accretion from a circumstellar disk is thought to be responsible for the excess

emission of classical T Tauri stars (CTTS) (Lynden-Bell & Pringle 1974). The inner disk is disrupted by the stellar magnetic field, resulting in magnetospheric accretion, where disk material is channelled along the magnetic field lines into the star (Koenigl 1991). Prominent emission lines originate in the free-falling gas (Calvet & Hartmann 1992). Hα is one of the strongest emission lines in CTTSs, and has been extensively studied as an indicator of accretion (e.g., White & Basri 2003, Muzerolle et al. 2003, Natta et al. 2004).

We use the Hα line, covered by our optical spectra and present in emission in 35 objects of this sample, to obtain an indication of accretion activities according to two different methods from the literature: the Hα EW and its full width at 10% of the peak intensity. The non-detection of Hα is not uncommon for pre-main-sequence (PMS) stars. The sources could either be more evolved weak-line T Tauri stars (WTTSs; see Section 2.7.1), or the non-detection could also be explained by the known temporal variability of T Tauri stars (Stahler & Palla 2004).

2.7.1   Hα Equivalent Width

According to White & Basri (2003), there is no unique EW[Hα] value to distinguish between accreting CTTSs and WTTSs. For instance, Hα emission from equally saturated chromospheres will appear much more prominently in a late-M star than in an early-K star due to the former's substantially diminished photospheric continuum near 6500 Å.

Taking into account this spectral type dependence, White & Basri (2003) proposed that a T Tauri star is classical if EW[Hα] $\geq$ 3 Å for K0–K5 stars, EW[Hα] $\geq$ 10 Å for K7–M2.5 stars, EW[Hα] $\geq$ 20 Å for M3–M5.5 stars, and EW[Hα] $\geq$ 40 Å for M6–M7.5 stars. These values were determined empirically from the maximum values of EW[Hα] for nonveiled T Tauri stars within each spectral type, from high-resolution spectra. Stars with values of EW[Hα] below these levels are not necessarily WTTSs, for which confirmation depends upon the Li abundance or other youth indicators, such as variability.

We have determined the equivalent width of Hα with the usual fitting of Gaussian profiles to the lines and the results are given in Table 2.4. The Hα feature lies near the 6567 Å TiO band head, a strong feature in mid- and late-M stars. In low-resolution spectra, the edge of this band becomes blended with the Hα emission feature, leading to an underestimate of the continuum on the redward side and thus an overestimate of the EW[Hα]. Also, self-absorption is missed in these unresolved data. For these reasons, our EW[Hα] values are likely somewhat overestimated. Nonetheless, we identify 35 stars with large EW[Hα] to be classified as CTTSs. The remaining four stars present marginal detections.
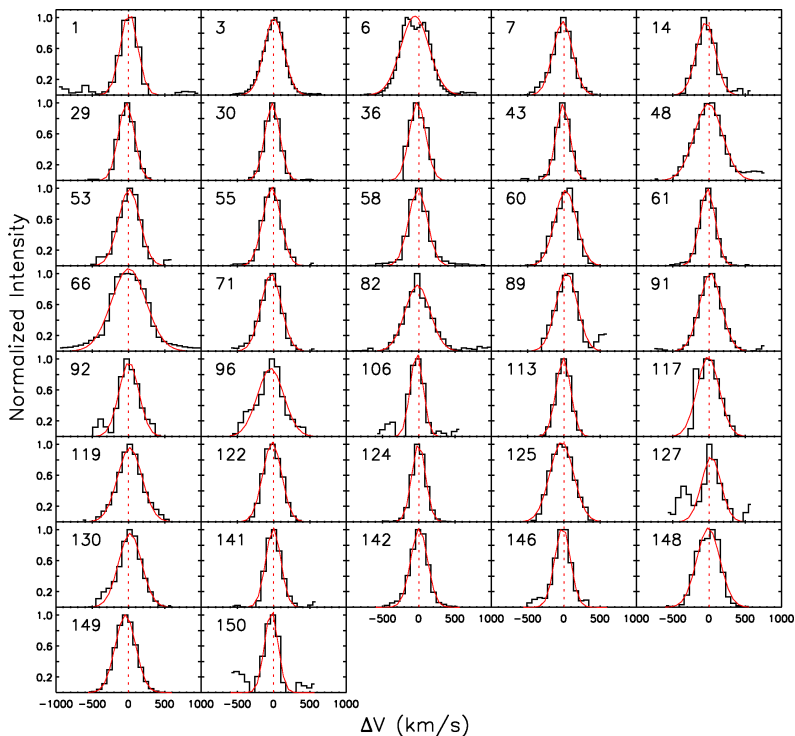
Figure 2.9 – Continuum-subtracted profiles of Hα emission lines. The solid gray lines are the Gaussian fit to each profile; dashed gray lines mark the center of the Gaussian. (A color version of this figure is available in the online journal)

2.7.2   Full Width of Hα at 10%

Due to the uncertainties in the determination of EW[Hα] in low-resolution spectra, White & Basri (2003) proposed the full width of Hα at 10% of the peak intensity (Hα[10%]) as an alternative to distinguish CTTSs from WTTSs. They found that stars with Hα[10%] greater than 270 km s^{-1} are CTTSs, independent of spectral types.

We fitted Gaussian profiles to the Hα lines (shown in Figure 2.9) in order to determine the Hα[10%]. The errors were calculated by propagating the error on the spectral resolution and the error of the Gaussian fit to the Hα line. The measured FWHM of each profile was deconvolved assuming a Gaussian instrumental profile. Because of the low resolution of our spectra (183.6 km s^{-1} for *WYFFOS*, 126 km s^{-1} for *DOLORES*, and 100 km s^{-1} for *CAFOS*), very narrow profiles (e.g., objects 106 and 150) are unresolved.

In spite of the low resolution, the Hα profiles found are broad enough in most cases to allow the extraction of velocity information, although with low accuracy.
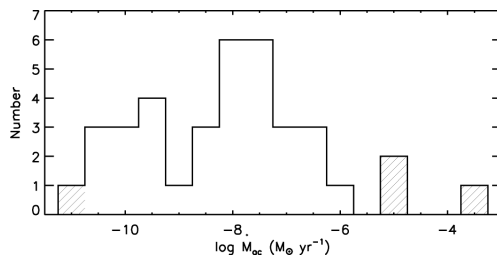
Figure 2.10 – Histogram of mass accretion rates derived from Eq. (2.1) for the sample of sources in Serpens with Hα in emission. The shaded areas show objects out of the range for which the relationship between Hα[10%] and $\dot{M}_{ac}$ was calibrated by Natta et al. (2004).

These results are shown in Table 2.4. According to this criterion, 33 objects are CTTSs, while the remaining four stars are consistent with being CTTSs, given their uncertainties, showing a good agreement between both methods described.

Studying accretion properties in low mass objects, Natta et al. (2004) found that Hα can be used not only as a qualitative indicator of the accreting nature of low mass objects, but also to obtain a quantitative estimate of the mass accretion rate $\dot{M}_{ac}$. They found an empirical relationship between the mass accretion rate, $\dot{M}_{ac}$ (from Hα profile model fittings or veiling measurements) and Hα[10%] from high-resolution spectra (Figure 3 in their paper):

$$\log \dot{M}_{ac} = -12.89(\pm 0.3) + 9.7(\pm 0.7) \times 10^{-3} \text{H}\alpha[10\%] \tag{2.1}$$

where Hα[10%] is in km s^{-1} and $\dot{M}_{ac}$ is in M$_{\odot}$ yr^{-1}. We use Eq. 2.1 to derive $\dot{M}_{ac}$ for the objects showing Hα in emission (see Table 2.4).

The $\dot{M}_{ac}$ values derived here (presented in Figure 2.10) are largely consistent with the range typical for T Tauri stars. Exception are objects 109, 50, 7, and 68 (Hα[10%] = 175, 762, 805, and 966 km s^{-1}, respectively). These Hα[10%] values are out of the range over which relationship (2.1) was calibrated, which may result in erroneous accretion rates (shaded areas in Figure 2.10). The distribution of mass accretion rates versus ages shows a large scatter, although for the 7 strongest accreters ($\log \dot{M}_{ac} \gtrsim -7$) a weak trend is seen, in the sense of a decreasing accretion rate as a function of stellar age.

2.8   Conclusions

We have presented a spectroscopic survey at optical wavelengths designed to determine spectral types and confirm the PMS nature of a sample of YSO candidates in the Serpens molecular cloud, selected on the basis of the "c2d" *Spitzer* Legacy Program (Harvey et al. 2007b). This sample will subsequently be used to study disk evolution, making use of *Spitzer* IR photometry and spectra, obtained by our group.

- We have determined spectral types for 78 stars in the cloud, finding mostly K and M stars (88%), a late-type young stellar population. However, the high optical extinction toward this region makes it impossible to detect about half of the original sample of 150 stars with optical spectroscopy. NIR spectroscopy will be used to classify the remaining objects in the sample (Oliveira et al. 2009).
- Comparison of extinction values determined from our optical spectra with those calculated from the contribution of the cloud at each point (averaged over a 5′ radius) is a powerful method for identifying candidate background sources with IR excess from *Spitzer* selected samples of YSO candidates. The effectiveness of this method has been confirmed for two objects by follow-up IRS spectra.
- Effective temperatures and luminosities were derived and the objects were placed in a H-R diagram, compared with theoretical isochrones and mass tracks from models of Baraffe et al. (1998) and Siess et al. (2000). Twenty objects are too luminous to be at the distance of Serpens. These objects have a nearly one-to-one correspondence with those identified by the extinction method and are therefore very likely background objects. They amount to 25% of the detected sample, a relatively large amount likely due to the position of the Serpens molecular cloud at very low Galactic latitude. Two of these background sources were confirmed to be post-AGB stars through IRS spectra.
- The theoretical models by Baraffe et al. (1998) and Siess et al. (2000) imply a population of YSOs concentrated in the age range between 1 and 15 Myr, strongly peaked at 2 – 6 Myr. The median age was found to be 7.5 and 4.7 Myr with the Baraffe et al. (1998) and Siess et al. (2000) tracks, respectively. Individual masses range from 0.2 to 2.2 $M_\odot$, with median values of 0.8 and 0.6 $M_\odot$ for the Baraffe et al. (1998) and Siess et al. (2000) models, respectively.
- The optical spectra cover the Hα line, an important indicator of accretion. We explored this relationship through two different approaches: qualitatively, the accreting nature of low-mass objects has been determined by either the equivalent width of Hα, or its full width at 10% of Hα peak intensity. This confirms 37 objects (or 55% of the YSO sample) to be actively accreting objects classified as new classical T Tauri stars in Serpens. The quantitative estimate of $\dot{M}_{ac}$ based on the full width of Hα at 10% of the peak intensity yields a median of $\sim 10^{-8}$ $M_\odot$ yr^{-1}, with a broad distribution of values.

References

Adams, F. C., Lada, C. J., & Shu, F. H. 1987, ApJ, 312, 788

Alcalá, J. M., et al. 2008, ApJ, 676, 427

André, P., Ward-Thompson, D., & Barsony, M. 1993, ApJ, 406, 122

André, P., & Montmerle, T. 1994, ApJ, 420, 837

Ballesteros-Paredes, J., & Hartmann, L. 2007, Revista Mexicana de Astronomia y Astrofisica, 43, 123

Baraffe, I., Chabrier, G., Allard, F., & Hauschildt, P. H. 1998, A&A, 337, 403

Bertout, C. 1989, ARA&A, 27, 351

Briceño, C., Calvet, N., Hernández, J., Vivas, A. K., Hartmann, L., Downes, J. J., & Berlind, P. 2005, AJ, 129, 907

Brown, J. M., et al. 2007, ApJ, 664, L107

Calvet, N., & Hartmann, L. 1992, ApJ, 386, 239

Cambrésy, L. 1999, A&A, 345, 965

Djupvik, A. A., André, P., Bontemps, S., Motte, F., Olofsson, G., Gålfalk, M., & Florén, H.-G. 2006, A&A, 458, 789

Dullemond, C. P., & Dominik, C. 2004a, A&A, 417, 159

Dullemond, C. P., & Dominik, C. 2004b, A&A, 421, 1075

Eiroa, C., Torrelles, J. M., Curiel, S., & Djupvik, A. A. 2005, AJ, 130, 643

Eiroa, C., Djukvip, A. A., & Casali, M. M. 2006, Astron. Nachr., 327, 14

Enoch, M. L., Glenn, J., Evans, N. J., II, Sargent, A. I., Young, K. E., & Huard, T. L. 2007, ApJ, 666, 982

Evans, N. J., II, et al. 2003, PASP, 115, 965

Evans, N. J., II, et al. 2007, delivery documentation[4]

Giardino, G., Favata, F., Silva, B., Micela, G., Reale, F., & Sciortino, S. 2006, A&A, 453, 241

Gorlova, N., et al. 2004, ApJS, 154, 448

Haisch, K. E., Jr., Lada, E. A., & Lada, C. J. 2001, ApJ, 553, L153

Hartmann, L. 1998, Accretion Processes in Star Formation (Cambridge: Cambridge Univ. Press)

Harvey, P. M., et al. 2006, ApJ, 644, 307

Harvey, P. M., et al. 2007, ApJ, 663, 1139

Harvey, P., Merín, B., Huard, T. L., Rebull, L. M., Chapman, N., Evans, N. J., II, & Myers, P. C. 2007, ApJ, 663, 1149

Hauschildt, P. H., Allard, F., Ferguson, J., Baron, E., & Alexander, D. R. 1999, ApJ, 525, 871

Herbst, T. M., Beckwith, S. V. W., & Robberto, M. 1997, ApJ, 486, L59

Hernández, J., Calvet, N., Briceño, C., Hartmann, L., & Berlind, P. 2004, AJ, 127, 1682

Hillenbrand, L. A. 1995, PhD thesis, Univ. Massachussetts

Hogerheijde, M. R., van Dishoeck, E. F., Salverda, J. M., & Blake, G. A. 1999, ApJ, 513, 350

Kaas, A. A., et al. 2004, A&A, 421, 623

Kenyon, S. J., & Hartmann, L. 1995, ApJS, 101, 117

Kessler-Silacci, J., et al. 2006, ApJ, 639, 275

Klotz, A., Caux, E., Monin, J.-L., & Lodieu, N. 2004, A&A, 425, 927

Koenigl, A. 1991, ApJ, 370, L39

Lada, C. J., & Wilking, B. A. 1984, ApJ, 287, 610

Lada, C. J. 1987, in IAU Symp. 115: Star Forming Regions, ed M. Peimbert & J. Jugaka (Dordrecht: Kluwer), 1

Luhman, K. L., Stauffer, J. R., Muench, A. A., Rieke, G. H., Lada, E. A., Bouvier, J., & Lada, C. J. 2003, ApJ, 593, 1093

Luhman, K. L. 2007, ApJS, 173, 104

Lynden-Bell, D. & Pringle, J. E. 1974, MNRAS, 168, 603

Marengo, M., Reiter, M., & Fazio, G. G. 2008, in AIP Conf. Proc. 1001, IXth Torino Workshop on Evolution and Nucleosynthesis in AGB Stars and the IInd Perugia Workshop

---

[4]http://ssc.spitzer.caltech.edu/legacy/c2dhistory.html

on Nuclear Astrophysics, 331-338 (arXiv:0802.2292)

Meeus, G., Waters, L. B. F. M., Bouwman, J., van den Ancker, M. E., Waelkens, C., & Malfait, K. 2001, A&A, 365, 476

Merín, B., et al. 2008, ApJS, 177, 551

Mora, A., et al. 2001, A&A, 378, 116

Muench, A. A., Lada, C. J., Luhman, K. L., Muzerolle, J., & Young, E. 2007, AJ, 134, 411

Muzerolle, J., Hillenbrand, L., Calvet, N., Briceño, C., & Hartmann, L. 2003, ApJ, 592, 266

Natta, A., Testi, L., Muzerolle, J., Randich, S., Comerón, F., & Persi, P. 2004, A&A, 424, 603

Olmi, L., & Testi, L. 2002, A&A, 392, 1053

Parry, I. R., Lewis, I. J., Sharples, R. M., Dodsworth, G. N., Webster, J., Gellatly, D. W., Jones, L. R., & Watson, F. G. 1994, Proc. SPIE, 2198, 125

Preibisch, T. 1998, A&A, 338, L25

Preibisch, T. 2003, A&A, 410, 951

Randich, S., Pallavicini, R., Meola, G., Stauffer, J. R., & Balachandran, S. C. 2001, A&A, 372, 862

Rieke, G. H., & Lebofsky, M. J. 1985, ApJ, 288, 618

Shu, F. H., Adams, F. C., & Lizano, S. 1987, ARA&A, 25, 23

Sicilia-Aguilar, A., Hartmann, L. W., Hernández, J., Briceño, C., & Calvet, N. 2005, AJ, 130, 188

Siess, L., Dufour, E., & Forestini, M. 2000, A&A, 358, 593

Spezzi, L., Alcalá, J. M., Covino, E., Frasca, A., Gandolfi, D., Oliveira, I., Chapman, N., Evans, N. J., II, Huard, T. L., Jørgensen, J. K., Merín, B., Stapelfeldt, K. R. 2008, ApJ, in press

Stahler, S. W. & Palla, F. 2004, The Formation of Stars, Wiley-VHC

Steenman, H., & The, P. S. 1991, Ap&SS, 184, 9

Stone, R. P. S. 1977, ApJ, 218, 767

Straizys, V., Cernis, K. & Bartasiute, S. 1996, Baltic Astron., 5, 125

Trumpler, R. J. 1930, Lick Obs. Bull., 14, 154

van den Ancker, M. E., The, P. S., Feinstein, A., Vazquez, R. A., de Winter, D., & Perez, M. R. 1997, A&AS, 123, 63

van den Ancker, M. E., de Winter, D., & Tjin A Djie, H. R. E. 1998, A&A, 330, 145

van Boekel, R., et al. 2004, Nature, 432, 479

Waters, L. B. F. M., et al. 1999, The Universe as Seen by ISO, 427, 219

Weingartner, J. C., & Draine, B. T. 2001, ApJ, 548, 296

White, R. J., & Basri, G. 2003, ApJ, 582, 1109

Whitney, B. A., Wood, K., Bjorkman, J. E., & Cohen, M. 2003, ApJ, 598, 1079

Wild, V., & Hewett, P. C. 2005, MNRAS, 358, 1083

Wilking, B. A. 1989, PASP, 101, 229

Williams, J. P., & Myers, P. C. 2000, ApJ, 537, 891

Wyse, R. F. G., & Gilmore, G. 1992, MNRAS, 257, 1

Date	Telescope + Instrument	Wavelength Blaze (Å)	Resolution (Å)	Spectral Coverage (Å)	Object ID (as in Table 2.2)
2006 May 4	WHT+WYFFOS	7000	4.0	3000	16, 34, 44, 47, 48, 87, 89, 91, 93, 96, 97, 113, 119, 123, 125, 128, 130, 145, 148
2006 June 29, 30	TNG+DOLORES	7000	2.8	1600	2, 3, 4, 6, 35, 52, 70, 76, 85, 86, 108, 118, 120, 122, 131, 139, 146, 150
2007 June 9, 10, 11	WHT+WYFFOS	7000	4.0	3000	2, 4, 5, 7, 14, 16, 18, 22, 23, 29, 30, 35, 36, 40, 43, 52, 53, 55, 60, 61, 62, 66, 70, 71, 76, 77, 81, 82, 84, 85, 86, 87, 88, 92, 93, 96, 98, 99, 106, 110, 112, 113, 114, 117, 118, 119, 120, 121, 122, 124, 125, 127, 130, 131, 138, 139, 141, 142, 146, 148, 149, 150
2008 June 29, 30	Calar Alto+CAFOS	7750	2.2	3500	1, 41, 58, 70, 82, 93, 99, 115, 120, 130, 139, 141, 149, 150

Table 2.1 – Observation log

#	ID[a]	c2d ID SSTc2dJ	$\alpha_{2\mu m - 24\mu m}$ [b]	Spectral Type (±subtype)	A_V Obs[c] (mag)	A_V Cloud[d] (mag)	A_V Final (mag)
1	1	18275383−0002335	−1.26	K2±3	1.0	2.98	9.0
2	2	18280503+0006591	−2.29	M4±1	6.5	1.98	2.0
3	3	18280845−0001064	−0.70	M0±1	0.0	2.85	2.0
4	4	18281100−0001395	−2.13	M5±1	8.0	2.85	6.0
5		18281315+0003128	−1.80	M3±3	14.0	4.83	9.0
6	5	18281350−0002491	−1.08	K5±2	2.0	5.33	3.0
7	6	18281501−0002588	−0.05	M0±1	2.0	5.33	7.0
14	13	18282143+0010411	−1.44	M2±2	3.5	2.66	3.0
16	15	18282432+0034545	−2.01	M0±1	8.0	3.41	6.0
18	16	18282738−0011499	−1.98	M5±4	10.0	4.78	11.0
22		18283000+0020147	−1.60	M4±3	14.0	4.74	12.0
23		18283736+0019276	−2.19	M7.5±1	0.0	7.59	11.0
29	25	18284481+0048085	−1.01	M2±3	3.0	4.29	6.0
30	27	18284497+0045239	−1.35	M1±1	2.5	7.55	2.0
34		18284828−0005300	−2.43	M5.5±1.5	11.0	4.92	10.0
35[e]		18284938−0006046	−2.01	M5±1	12.0	5.72	13.0
36	32	18285020+0009497	−0.24	K5±4	5.0	5.40	10.0
40	36	18285249+0020260	−0.15	M7±4	8.5	10.00	12.0
41	37	18285276+0028466	0.06	K2±3	0.0	19.20	10.0
43	39	18285395+0045530	−1.16	M0.5±3	3.5	8.49	7.0
44	40	18285404+0029299	1.35	M6±5	0.0	15.60	
47	43	18285489+0018326	0.88	M5±4	13.5	14.20	
48	44	18285529+0020522	−0.29	M5.5±3	3.0	6.86	14.0
52	48	18285808+0017244	−2.11	G3±5	3.5	9.87	6.0
53	49	18285860+0048594	−1.06	M2.5±3	2.5	3.37	6.0
55	51	18290025+0016580	−1.01	K2±3	4.5	7.88	12.0
58	54	18290088+0029315	−0.42	K7±2	3.5	19.00	5.0
60	56	18290122+0029330	−0.39	M0.5±0.5	3.0	19.00	7.0
61	58	18290175+0029465	−0.84	M0±1	2.0	19.00	5.0
62	59	18290184+0029546	−0.77	K0±7	4.0	19.00	8.0
66	62	18290393+0020217	−0.82	K5±2	1.5	3.53	7.0
70	65	18290575+0022325	−2.12	A3±3	2.5	4.17	5.0
71	66	18290615+0019444	−1.52	M3±1	2.0	4.06	6.0
76	72	18290775+0054037	−1.06	M1±1	2.0	2.32	6.0
77	73	18290808−0007371	−2.22	M4±1	8.5	3.10	8.0
81	77	18290980+0034459	−0.97	M5±4	1.0	11.00	15.0
82	78	18291148+0020387	−1.34	M0±2	2.0	3.30	6.0
84	81	18291407+0002589	−2.19	M3±3	9.0	4.74	9.0
85[e]		18291477−0004237	−2.29	M3±1	8.0	2.71	9.0
86	83	18291508+0052124	−1.89	M5.5±1.5	8.0	2.51	8.0
87	84	18291513+0039378	−1.50	M4±3	2.5	7.95	7.0
88	85	18291539−0012519	−1.72	M0.5±2	7.0	2.51	7.0
89	86	18291557+0039119	−0.56	K5±5	2.0	10.20	12.0
91	88	18291617+0018227	0.45	K7±3	1.0	4.97	18.0
92	89	18291969+0018031	−1.23	M0±1	2.5	3.51	7.0
93	90	18292001+0024497	−2.04	M2±3	8.5	3.17	9.0
96	94	18292184+0019386	−0.99	M1±1	2.0	3.16	7.0
97		18292250+0034118	−1.65	M2±2	3.0	10.10	10.1
98		18292253+0034176	−2.48	A3±5	5.5	10.10	5.0
99	95	18292616+0020518	−2.26	M4±2	13.0	3.34	8.0
106	102	18292927+0018000	−1.24	M3±1	2.5	3.48	7.5
108	105	18293254−0013233	−2.58	K5±5	0.0	2.51	1.0
110	107	18293319+0012122	−1.81	M6±2	8.5	3.90	5.0
112	109	18293381+0053118	−2.06	M7±4	1.5	4.59	8.0
113	110	18293561+0035038	−1.53	K7±1	2.0	12.60	4.0
114	111	18293619+0042167	−0.92	F9±5	7.0	6.71	11.0
115	114	18293672+0047579	−1.08	M0.5±2	6.5	5.03	8.0
117	118	18294020+0015131	0.87	K2±5	0.5	3.40	2.0
118		18294067−0007033	−2.53	M4±1.5	8.0	1.41	8.0
119	119	18294121+0049020	−1.39	K7±2	4.0	5.20	5.5
120	123	18294168+0044270	−1.42	A2±2	5.0	6.13	8.5
121		18294301−0016083	−2.18	K7±5	5.5	3.33	7.0
122	126	18294410+0033561	−1.68	M0±1.5	1.5	7.35	5.0
123	129	18294503+0035266	−1.26	M0±1	1.5	7.02	10.0
124	132	18294725+0039556	−1.32	M0±1.5	2.0	10.40	5.5
125	133	18294726+0032230	−1.31	M0±1	3.0	6.59	7.0
127	143	18295001+0051015	−1.68	M2±1	4.0	4.18	6.5
130	145	18295041+0043437	−1.32	K6±1	4.5	8.69	8.5
131	148	18295130+0027479	−2.42	A3±3	2.0	3.34	5.5
138	161	18295322+0033129	−1.99	M0±3	10.0	6.86	11.0
139	165	18295422+0045076	−2.35	A4±4	4.0	6.95	6.5

#	ID[a]	c2d ID SSTc2dJ	$\alpha_{2\mu m-24\mu m}$[b]	Spectral Type (±subtype)	A_V Obs[c] (mag)	A_V Cloud[d] (mag)	A_V Final (mag)
141	169	18295531+0049393	-0.74	A3±3	3.5	3.02	9.0
142	172	18295592+0040150	-0.85	M4±2	3.5	5.71	3.5
145	178	18295714+0033185	-0.82	G2.5±2.5	3.5	5.19	10.0
146	182	18295772+0114057	0.44	M4±2	4.0	14.05	3.0
148	206	18300178+0032162	-1.25	K7±1	2.0	5.00	7.0
149	210	18300350+0023450	-1.22	M0±1	0.0	2.25	3.5
150	222	18300861+0058466	-0.70	K5±3	0.0	2.79	5.0

Table 2.2 − Stellar parameters for the YSO candidates in Serpens

[a] From Harvey et al. (2007b).

[b] Obtained from a linear fit to the logarithm of the fluxes between the 2MASS K (2µm) and the MIPS1 (24µm) bands (Harvey et al. 2007b).

[c] Extinction found in this work.

[d] Extinction found by "c2d" over 5′ region.

[e] Post-AGB stars confirmed with Spitzer IRS spectra.

#	T_{eff} (K)	L_* ($L_\odot$)	Age_B (Myr)	$Mass_B$ ($M_\odot$)	Age_S (Myr)	$Mass_S$ ($M_\odot$)
1	4900^{+510}_{-550}	$2.01^{+2.39}_{-1.13}$	$11.60^{+13.91}_{-10.01}$	$1.56^{+0.63}_{-0.48}$	$6.10^{+11.00}_{-4.15}$	$1.57^{+0.43}_{-0.44}$
2†	3270 ± 145	$5.24^{+6.26}_{-2.95}$				
3	3850^{+210}_{-145}	$0.51^{+0.61}_{-0.29}$	$5.42^{+10.98}_{-3.67}$	$0.92^{+0.13}_{-0.16}$	$2.76^{+5.58}_{-1.98}$	$0.57^{+0.22}_{-0.11}$
4†	3125^{+145}_{-135}	$1.30^{+1.55}_{-0.73}$				
5†	3415^{+435}_{-425}	$14.78^{+17.64}_{-8.31}$				
6	4350^{+380}_{-290}	$1.13^{+1.35}_{-0.64}$	$5.98^{+13.19}_{-4.28}$	$1.38^{+0.18}_{-0.34}$	$3.41^{+8.77}_{-2.10}$	$1.13^{+0.19}_{-0.37}$
7	3850^{+210}_{-145}	$0.23^{+0.27}_{-0.13}$	$16.25^{+35.98}_{-10.56}$	$0.81^{+0.11}_{-0.15}$	$8.26^{+21.22}_{-5.45}$	$0.59^{+0.19}_{-0.12}$
14	3560 ± 290	$0.19^{+0.22}_{-0.10}$	$6.87^{+14.79}_{-4.99}$	0.52 ± 0.25	$4.37^{+7.90}_{-2.00}$	$0.37^{+0.22}_{-0.12}$
16	3850^{+210}_{-145}	$1.20^{+1.44}_{-0.68}$	$1.56^{+3.64}_{-1.36}$	$1.03^{+0.16}_{-0.17}$	$0.52^{+2.19}_{-4.64}$	$0.55^{+0.20}_{-0.09}$
18†	3125^{+580}_{-725}	$25.26^{+30.15}_{-14.21}$				
22†	3270^{+435}_{-390}	$81.97^{+97.83}_{-46.11}$				
23†	2795^{+140}_{-240}	$1.92^{+2.29}_{-1.08}$				
29	3560^{+500}_{-435}	$0.11^{+0.14}_{-0.06}$	$12.51^{+62.38}_{-11.01}$	$0.50^{+0.16}_{-0.35}$	$7.80^{+46.64}_{-4.83}$	$0.36^{+0.29}_{-0.19}$
30	3705 ± 145	$0.30^{+0.36}_{-0.17}$	$6.57^{+13.95}_{-4.33}$	$0.71^{+0.15}_{-0.16}$	$3.41^{+6.76}_{-1.63}$	$0.46^{+0.12}_{-0.09}$
34†	3057^{+212}_{-177}	$3.24^{+3.87}_{-1.82}$				
35[a],†	3125^{+145}_{-135}	$306.47^{+365.79}_{-172.40}$				
36	4350^{+730}_{-645}	$1.09^{+1.30}_{-0.61}$	$6.34^{+19.20}_{-5.33}$	$1.36^{+0.20}_{-0.51}$	$3.68^{+14.43}_{-3.46}$	$1.13^{+0.03}_{-0.67}$
40	2880^{+535}_{-730}	$0.23^{+0.27}_{-0.13}$			$2.86^{+2.86}_{-2.80}$	$0.31^{+0.31}_{-0.30}$
41	4900^{+510}_{-550}	0.01 ± 0.01				
43	3777^{+500}_{-435}	$0.33^{+0.39}_{-0.18}$	$7.47^{+19.56}_{-6.17}$	$0.80^{+0.11}_{-0.44}$	$3.79^{+14.75}_{-2.02}$	$0.52^{+0.39}_{-0.23}$
44[b]	2990^{+715}_{-840}					
47[b]	3125^{+580}_{-725}					
48	3057^{+430}_{-502}	$0.36^{+0.42}_{-0.20}$			$2.47^{+2.47}_{-2.40}$	$0.35^{+0.35}_{-0.30}$
52	5830^{+370}_{-260}	$4.76^{+5.68}_{-2.68}$	$8.70^{+15.63}_{-8.02}$	$2.53^{+0.64}_{-1.16}$	$12.00^{+9.69}_{-6.27}$	$1.50^{+0.46}_{-0.28}$
53	3487^{+537}_{-430}	$0.13^{+0.16}_{-0.07}$	$7.52^{+49.36}_{-6.95}$	$0.44^{+0.27}_{-0.31}$	$5.35^{+34.68}_{-3.54}$	$0.33^{+0.35}_{-0.17}$
55	4900^{+510}_{-550}	$2.34^{+2.79}_{-1.31}$	$9.45^{+12.25}_{-8.31}$	$1.60^{+0.53}_{-0.45}$	$4.98^{+9.13}_{-3.47}$	$1.66^{+0.41}_{-0.53}$
58	4060^{+290}_{-355}	$1.00^{+1.19}_{-0.56}$	$3.15^{+7.30}_{-2.20}$	$1.18^{+0.15}_{-0.34}$	$2.39^{+3.91}_{-2.33}$	$0.76^{+0.37}_{-0.30}$
60	3777 ± 72	$0.41^{+0.48}_{-0.23}$	$5.73^{+11.95}_{-3.81}$	$0.82^{+0.08}_{-0.09}$	$2.89^{+6.01}_{-1.71}$	$0.52^{+0.06}_{-0.05}$
61	3850^{+210}_{-145}	$1.37^{+1.63}_{-0.77}$	$1.24^{+3.01}_{-1.12}$	$1.05^{+0.17}_{-0.16}$	2.07 ± 0.41	0.66 ± 0.09
62	5250^{+580}_{-1190}	$6.70^{+7.99}_{-3.77}$	$2.08^{+4.18}_{-2.07}$	$2.19^{+1.17}_{-0.56}$	$3.87^{+4.94}_{-3.63}$	$2.09^{+0.49}_{-1.52}$
66	4350^{+380}_{-290}	$1.87^{+2.23}_{-1.05}$	$4.26^{+4.79}_{-3.72}$	$1.44^{+0.25}_{-0.19}$	$2.13^{+3.49}_{-2.13}$	$1.12^{+0.42}_{-0.39}$
70	8720^{+800}_{-695}	$12.64^{+15.09}_{-7.11}$			8.18 ± 2.21	2.09 ± 0.19
71	3415 ± 145	$0.20^{+0.24}_{-0.11}$	$2.86^{+5.90}_{-1.64}$	$0.38^{+0.14}_{-0.11}$	$2.94^{+3.96}_{-0.93}$	0.31 ± 0.06
76	3705 ± 145	$0.21^{+0.25}_{-0.12}$	$9.62^{+21.62}_{-6.22}$	$0.68^{+0.11}_{-0.16}$	$5.40^{+11.80}_{-2.90}$	$0.46^{+0.13}_{-0.09}$
77†	3270 ± 145	$2.88^{+3.44}_{-1.62}$				
81†	3125^{+580}_{-725}	$22.08^{+26.35}_{-12.42}$				
82	3850^{+355}_{-290}	$0.13^{+0.15}_{-0.07}$	$32.64^{+56.97}_{-22.59}$	$0.72^{+0.13}_{-0.22}$	$19.65^{+57.48}_{-13.69}$	$0.58^{+0.09}_{-0.22}$
84†	3415^{+435}_{-425}	$8.33^{+9.94}_{-4.68}$				
85[a],†	3415 ± 145	$33.83^{+40.37}_{-19.03}$				
86†	3057^{+212}_{-177}	$22.52^{+26.89}_{-12.67}$				
87	3270^{+435}_{-390}	$0.23^{+0.28}_{-0.13}$	$1.36^{+7.32}_{-1.36}$	$0.28^{+0.41}_{-0.21}$	$2.57^{+2.13}_{-2.57}$	$0.25^{+0.21}_{-0.08}$
88	3777^{+355}_{-290}	$1.48^{+1.77}_{-0.83}$	$0.74^{+2.08}_{-0.64}$	$0.97^{+0.31}_{-0.14}$	$1.76^{+0.27}_{-0.27}$	$0.66^{+0.15}_{-0.15}$
89	4350^{+900}_{-790}	$0.45^{+0.54}_{-0.25}$	$21.77^{+449.61}_{-19.55}$	$1.00^{+0.13}_{-0.42}$	$13.98^{+35.23}_{-13.10}$	$1.00^{+0.13}_{-0.61}$
91	4060^{+530}_{-500}	$2.33^{+2.79}_{-1.31}$	$0.82^{+2.26}_{-0.80}$	$1.28^{+0.59}_{-0.24}$	2.53 ± 0.20	1.13 ± 0.37
92	3850^{+210}_{-145}	$0.28^{+0.34}_{-0.16}$	$10.82^{+23.60}_{-6.86}$	$0.85^{+0.10}_{-0.15}$	$5.82^{+14.61}_{-3.42}$	$0.58^{+0.22}_{-0.12}$
93†	3560^{+500}_{-435}	$4.39^{+5.24}_{-2.47}$				
96	3705 ± 145	$0.21^{+0.26}_{-0.12}$	$9.46^{+21.21}_{-6.18}$	$0.68^{+0.11}_{-0.16}$	$5.23^{+11.50}_{-2.76}$	$0.46^{+0.13}_{-0.09}$
97	3560 ± 290	$0.16^{+0.19}_{-0.09}$	$8.01^{+17.71}_{-5.82}$	$0.51^{+0.24}_{-0.25}$	$4.94^{+9.43}_{-2.37}$	$0.37^{+0.22}_{-0.12}$
98	8720^{+3180}_{-1140}	$5.44^{+6.49}_{-3.06}$			$3.79^{+3.79}_{-3.79}$	$2.73^{+2.73}_{-2.73}$

#	T_{eff} (K)	L_* ($L_\odot$)	Age_B (Myr)	$Mass_B$ ($M_\odot$)	Age_S (Myr)	$Mass_S$ ($M_\odot$)
99†	3270^{+290}_{-280}	$17.27^{+20.61}_{-9.72}$				
106	3415 ± 145	$0.17^{+0.20}_{-0.09}$	$3.48^{+7.76}_{-1.86}$	$0.37^{+0.14}_{-0.10}$	$3.63^{+5.22}_{-1.31}$	0.30 ± 0.06
108†	4350^{+900}_{-790}	$14.48^{+17.28}_{-8.15}$				
110†	2990 ± 280	$4.87^{+5.81}_{-2.74}$				
112†	2880^{+535}_{-880}	$2.72^{+3.24}_{-1.53}$				
113	4060^{+145}_{-210}	$0.52^{+0.61}_{-0.29}$	$8.64^{+19.10}_{-5.88}$	$1.06^{+0.13}_{-0.22}$	$4.78^{+14.01}_{-2.65}$	$0.79^{+0.16}_{-0.22}$
114	6115^{+475}_{-315}	$1.89^{+2.25}_{-1.06}$			19.37 ± 3.64	1.30 ± 0.09
115	3777^{+355}_{-290}	$0.24^{+0.29}_{-0.14}$	$10.28^{+23.83}_{-7.21}$	$0.77^{+0.08}_{-0.32}$	$5.70^{+15.08}_{-3.25}$	$0.52^{+0.30}_{-0.17}$
117	4900^{+736}_{-840}	$0.02^{+0.02}_{-0.01}$				
118†	3270^{+217}_{-212}	$19.67^{+23.47}_{-11.06}$				
119	4060^{+290}_{-355}	$0.15^{+0.18}_{-0.08}$	$51.52^{+46.77}_{-51.52}$	$0.73^{+0.20}_{-0.07}$	$36.46^{+26.56}_{-36.40}$	$0.70^{+0.11}_{-0.25}$
120	8970^{+550}_{-510}	$10.48^{+12.51}_{-5.89}$			$7.22^{+7.22}_{-7.17}$	$2.19^{+2.19}_{-2.14}$
121	4060^{+840}_{-790}	$0.39^{+0.47}_{-0.22}$	$12.68^{+76.74}_{-12.21}$	$0.99^{+0.15}_{-0.69}$	$7.38^{+40.69}_{-5.73}$	$0.81^{+0.06}_{-0.55}$
122	3850^{+282}_{-217}	$0.54^{+0.64}_{-0.30}$	$5.06^{+10.19}_{-3.44}$	$0.93^{+0.17}_{-0.25}$	$2.68^{+5.04}_{-2.07}$	$0.57^{+0.31}_{-0.15}$
123	3850^{+210}_{-145}	$0.35^{+0.42}_{-0.20}$	$8.54^{+18.18}_{-5.66}$	$0.88^{+0.11}_{-0.15}$	$4.34^{+10.41}_{-2.43}$	$0.58^{+0.23}_{-0.11}$
124	3850^{+282}_{-217}	$0.17^{+0.21}_{-0.10}$	$23.46^{+52.63}_{-15.55}$	$0.76^{+0.12}_{-0.17}$	$12.65^{+33.50}_{-8.73}$	$0.59^{+0.15}_{-0.18}$
125	3850^{+210}_{-145}	$0.28^{+0.34}_{-0.16}$	$10.98^{+23.96}_{-6.97}$	$0.85^{+0.10}_{-0.15}$	$5.89^{+14.82}_{-3.47}$	$0.58^{+0.22}_{-0.12}$
127	3560 ± 145	$0.34^{+0.41}_{-0.19}$	$2.87^{+5.76}_{-1.83}$	$0.56^{+0.17}_{-0.13}$	$2.62^{+2.87}_{-1.55}$	$0.38^{+0.09}_{-0.07}$
130	4205^{+385}_{-355}	$0.73^{+0.87}_{-0.41}$	$7.88^{+16.91}_{-5.44}$	$1.19^{+0.18}_{-0.27}$	$4.39^{+12.07}_{-2.68}$	$0.95^{+0.20}_{-0.38}$
131	8720^{+800}_{-695}	$13.75^{+16.42}_{-7.74}$			$6.06^{+3.67}_{-6.00}$	$1.94^{+0.42}_{-0.18}$
138†	3850^{+500}_{-435}	$3.73^{+4.46}_{-2.10}$				
139	8460^{+1060}_{-880}	$17.96^{+21.44}_{-10.10}$			$8.88^{+40.03}_{-8.80}$	$2.01^{+0.51}_{-0.27}$
141	8720^{+800}_{-695}	$38.80^{+46.31}_{-21.83}$			$4.51^{+5.16}_{-1.84}$	$2.51^{+0.54}_{-0.51}$
142	3270^{+290}_{-280}	$0.07^{+0.09}_{-0.04}$	$5.70^{+19.62}_{-4.92}$	$0.24^{+0.26}_{-0.14}$	$6.06^{+8.12}_{-2.96}$	$0.21^{+0.13}_{-0.10}$
145	5845^{+185}_{-75}	$3.15^{+3.77}_{-1.77}$	$180.47^{+511.90}_{-178.57}$	$2.01^{+1.34}_{-0.81}$	$16.48^{+44.83}_{-7.78}$	$1.33^{+0.36}_{-0.17}$
146	3270^{+290}_{-280}	$0.27^{+0.33}_{-0.15}$	$1.05^{+2.82}_{-1.05}$	$0.28^{+0.25}_{-0.13}$	$2.35^{+1.75}_{-59.44}$	$0.25^{+0.12}_{-0.04}$
148	4060^{+145}_{-210}	$0.52^{+0.62}_{-0.29}$	$8.54^{+18.89}_{-5.82}$	$1.06^{+0.13}_{-0.22}$	$4.72^{+13.78}_{-2.62}$	$0.79^{+0.16}_{-0.22}$
149	3850^{+210}_{-145}	$0.14^{+0.17}_{-0.08}$	$29.53^{+66.82}_{-19.81}$	$0.74^{+0.13}_{-0.17}$	$17.36^{+48.16}_{-12.23}$	$0.59^{+0.10}_{-0.13}$
150	4350^{+550}_{-500}	$1.13^{+1.35}_{-0.63}$	$6.04^{+13.30}_{-4.31}$	$1.37^{+0.18}_{-0.35}$	$3.46^{+9.21}_{-2.69}$	$1.13^{+0.12}_{-0.57}$

Table 2.3 − Stellar parameters for the YSO candidates in Serpens

[a] Post-AGB stars, confirmed with Spitzer IRS spectra.

[b] Objects without 2MASS J, H and K magnitudes.

† background objects.

Subscript B corresponds to values derived from the Baraffe et al. (1998) models, while S corresponds to values derived from Siess et al. (2000).

#	EW[Hα][a] (6563 Å)	CTTS (EW[Hα])	Hα[10%] (km/s)	CTTS (Hα[10%])	log M_{ac} (M$_\odot$/yr)
1	4.6	✓	469 ± 88	✓	-8.34 ± 0.96
3	61.5	✓	539 ± 59	✓	-7.66 ± 0.75
6	23.9	✓	805 ± 110	✓	-5.08 ± 1.24
7	55.5	✓	464 ± 87	✓	-8.39 ± 0.95
14	23.9	✓	448 ± 112	✓	-8.54 ± 1.17
16	–				
29	104.9	✓	333 ± 84	✓	-9.66 ± 0.90
30	11.2	✓	284 ± 61	✓	-10.13 ± 0.69
36	128.1	✓	340 ± 292	✓	-9.59 ± 2.86
40	–				
41	-0.7				
43	19.1	✓	241 ± 94		-10.55 ± 0.97
44	–				
47	–				
48	332.3	✓	762 ± 127	✓	-5.50 ± 1.37
52	-2.2				
53	92.7	✓	529 ± 112	✓	-7.76 ± 1.19
55	11.2	✓	413 ± 70	✓	-8.88 ± 0.80
58	71.6	✓	507 ± 63	✓	-7.97 ± 0.77
60	44.8	✓	545 ± 104	✓	-7.60 ± 1.12
61	28.5	✓	311 ± 57	✓	-9.87 ± 0.67
62	–				
66	127.4	✓	966 ± 138	✓	-3.52 ± 1.53
70	-15.1				
71	68.1	✓	490 ± 84	✓	-8.14 ± 0.93
76	-9.7				
82	25.2	✓	656 ± 123	✓	-6.53 ± 1.31
87	–				
88	–				
89	22.2	✓	532 ± 174	✓	-7.73 ± 1.75
91	108.9	✓	549 ± 65	✓	-7.56 ± 0.80
92	24.8	✓	478 ± 138	✓	-8.25 ± 1.41
96	22.0	✓	704 ± 168	✓	-6.06 ± 1.73
97	–				
98	-7.8				
106	15.8	✓	175 ± 186		-11.19 ± 1.83
113	10.9	✓	273 ± 73	✓	-10.24 ± 0.79
114	–				
115	–				
117	91.9	✓	559 ± 152	✓	-7.47 ± 1.55
119	8.8		639 ± 94	✓	-6.69 ± 1.06
120	-11.0				
121	–				
122	37.1	✓	444 ± 76	✓	-8.58 ± 0.85
123	–				
124	34.7	✓	225 ± 64		-10.71 ± 0.71
125	49.0	✓	618 ± 95	✓	-6.89 ± 1.06
127	5.6		460 ± 213	✓	-8.43 ± 2.11
130	123.2	✓	590 ± 114	✓	-7.17 ± 1.22
131	-9.6				
139	-6.4				
141	9.0	✓	289 ± 100	✓	-10.09 ± 1.03
142	116.6	✓	367 ± 75	✓	-9.33 ± 0.83
145	-1.5				
146	23.4	✓	318 ± 102	✓	-9.80 ± 1.06
148	18.6	✓	598 ± 122	✓	-7.09 ± 1.29
149	226.1	✓	502 ± 36	✓	-8.02 ± 0.58
150	3.4	✓	213 ± 198		-10.82 ± 1.95

Table 2.4 − Hα equivalent widths and line widths, and mass accretion rates for YSOs in Serpens
[a] Positive values denote emission.

3

Spectroscopic properties of Young Stellar Objects in the Lupus Molecular Clouds

The results of an optical spectroscopic survey of a sample of young stellar objects (YSOs) and pre-main sequence (PMS) stars in the Lupus Clouds are presented. 92 objects were observed with VLT/FLAMES. All of those objects show IR excess as discovered by the *Spitzer* Legacy Program "From Molecular Cores to Planet-Forming Disks" (c2d). After reduction, 54 spectra with good signal-to-noise ratio are spectrally classified. Effective temperatures and luminosities are derived for these objects, and used to construct H-R diagrams for the population. The sample consists mostly of M-type stars, with 10% K-type stars. Individual ages and masses are inferred for the objects according to theoretical evolutionary models. The mean population age is found to be between 3.6 and 4.4 Myr, depending on the model, while the mean mass is found to be $\sim$0.3 $M_\odot$ for either model. Together with literature data, the distribution of spectral types is found to be similar to that in Chamaeleon I and IC348. The Hα line in emission, found in 49% of the sample, is used to distinguish between classical and weak-line T Tauri stars. 56% of the objects show Hα in emission and are accreting T Tauri stars. Mass accretion rates between 10^{-8} and 10^{-11} M$_\odot$ yr^{-1} are determined from the full width at 10% of the Hα peak intensity.

Annelies Mortier, Isa Oliveira and Ewine F. van Dishoeck
Submitted to Monthly Notices of the Royal Astronomical Society

3.1   Introduction

Lupus Molecular Clouds is the generic denomination of a loosely connected concentration of dark clouds and low-mass pre-main sequence stars located in the Scorpius-Centaurus OB association at $16^h20^m < \alpha < 15^h30^m$ and $-43° < \delta < -33°$. Due to its large size, close distance ($d = 150$–200 pc) and substantial mass of molecular gas, the Lupus Clouds have been subject of many studies at all wavelengths over the years (e.g. Hughes et al. 1994; Merín et al. 2008; see Comerón 2008 for a review; Comerón et al. 2009; Tothill et al. 2009).

Lupus is one of the five clouds selected by the *Spitzer* Legacy Program *"From Molecular Cores to Planet-Forming Disks"*, also referred to as c2d (Cores to Disks, Evans et al. 2003). Using 400 hours of observations and all three instruments of *Spitzer*, the c2d program studies the process of star and planet formation from the earliest stages of molecular cores to the epoch of planet-forming disks. The five observed clouds cover a range of cloud types broad enough to study all modes of low-mass star formation, and large enough to allow statistical conclusions. A rich population of low-mass young stellar objects (YSOs) still surrounded by their circumstellar material has been discovered by *Spitzer* in these clouds (Harvey et al. 2007a,b; Merín et al. 2008; Evans et al. 2009).

Disks around YSOs, called protoplanetary disks, consist mainly of dust and gas. Dust particles of sub-μm size dominate the disk opacity, making it easily observable at infrared and (sub-)millimeter wavelengths by re-emitting some of the received stellar radiation. Dust emission is also temperature dependent with colder dust emitting at longer wavelengths than warm dust. Protoplanetary disks evolve in time, ending up in different scenarios like a planetary system or a debris disk, that may or may not also harbor planets.

The stellar radiation spectrum depends on the effective temperature of the star. Because of the properties of dust emission, the IR excess in a spectral energy distribution (SED) of this star+disk system provides information about the geometry and properties of the dusty disk. To separate star and disk emission, the stellar characteristics need to be known. The inner regions of the circumstellar disk are disrupted by the stellar magnetosphere. The stellar magnetic field creates channels through which material can flow from the disk onto the star. This produces atomic lines from hydrogen, calcium, oxygen, etc. The strongest emission line is Hα at 6562.8 Å.

The Lupus complex is one of the largest low-mass star forming regions on the sky, with four main star forming sites, referred to as Lupus I-II-III-IV. Furthermore, Lupus III contains one of the richest associations of T Tauri stars (see Comerón 2008 for a review). The work presented here concentrates on data from Lupus I, III and IV because those were the regions observed by the c2d program. Their star formation rates are 4.3, 31 and 4.5 M$_\odot$ Myr^{-1}, respectively (Evans et al. 2009). Distances of 150 ± 20 pc for Lupus I and IV and 200 ± 20 pc for Lupus III are assumed in this work (Comerón 2008).

We present an optical spectroscopic survey designed to characterize the young

stellar population of Lupus I, III and IV, as observed by the c2d program. Section 3.2 describes the selection criteria for the sample and Section 3.3 the observations and data reduction. Using libraries of standards from the literature, spectral types and effective temperatures are obtained in Section 3.4. Combined with additional photometric data, the SEDs of the objects can be built. In Section 3.5, the stellar and disk luminosities are calculated from the SEDs. In Section 3.6, the stars are placed in Hertzsprung-Russell diagrams and individual masses and ages are derived based on theoretical tracks. The mass accretion rates, determined through the Hα line, are presented in Section 3.7. In Section 3.8 the young stellar population of Lupus is discussed in context with other regions. Finally, in Section 3.9, the conclusions from this work are stated.

3.2   Sample Selection

Merín et al. (2008) used the *Spitzer* c2d point source catalog to identify the YSO population in the Lupus clouds. Objects are classified as YSO if they show an IR excess in the SED. To obtain an optimal separation between young stars, background galaxies and Galactic post-AGB stars, Merín et al. (2008) used the selection criteria developed by the c2d team on its official point source catalog (Evans et al. 2007). The method relies on an empirical probability function that depends on the relative position of any given source in several color-color and color-magnitude diagrams where diffuse boundaries have been determined.

The list of YSOs from Evans et al. (2007) was then adapted by Merín et al. (2008). Visual inspection was performed to subtract suspected galaxies or binaries, leaving the list with 94 YSOs. The final list of Merín et al. (2008) was merged with 65 pre-main sequence (PMS) stars and PMS candidates. Here, the term PMS star is used for other objects added to the list whose youth had already been confirmed using other observational techniques, mainly optical spectroscopy. If an object has not been spectroscopically confirmed as young but it was selected by its optical and near-IR photometry as such, it is labeled as a PMS candidate. This final list of 159 young objects is used for the observations presented here.

3.3   Observations and Data Reduction

The data presented here were taken in the second half of the nights of 20 – 25 February 2008 with the Very Large Telescope (VLT) and the instrument FLAMES/GIRAFFE (ID: 080C.0473-A, PI: Oliveira). The instrument was used in the MEDUSA mode, with wavelength coverage of 6437 – 7183 Å, and spectral resolution of 0.2 Å. This wavelength range was chosen for containing temperature sensitive features, useful for spectral classification. Additionally, it covers the Hα line, an accretion diagnostic. MEDUSA has 135 fibers available, each with an aperture of 1.2″. In total, 250 stars in 19 fields were observed (on average: 14 stars per field). Of those, 158 are field stars, leaving the Lupus science sample with 92 objects. An overview of the observations

can be found in Table 3.1. The different exposure times are adjusted to the mean magnitude of the objects in a given field to avoid saturation of the brightest sources.

The VLT data pipeline, GASGANO, was used for the data reduction. For each observation night, a set of 5 dark frames, 3 flat-fields and 1 arc frame are produced. GASGANO performs bias subtraction, flat-fielding and wavelength calibration. Further spectral extraction was performed within IDL. In each observed field, unused fibers were placed in random "empty" sky positions. Those positions are not really "empty" sky, since the cloud itself can contribute to the sky with a lot of emission lines. In each field, all the sky spectra are combined within IDL into one master sky spectrum, with a 2σ clipping. This combined sky is then subtracted from the science spectra to obtain spectra that are ready for analysis.

The spectra are sorted into four categories: good spectra, non-detection with a mean flux around zero, featureless spectra and not useful spectra (marked as G, U, F and O respectively in Table 3.1). The two spectra classified as not useful for our science purpose are objects # 14 and 53. Object 14 was discovered to be a galaxy (see section 3.4.2) while object 53 was observed with a broken fibre, resulting in an unclassifiable spectrum. The non-detections (marked 'U', 23 objects) and featureless (marked 'F', 13 objects) spectra could also not be spectrally classified. This leads to 54 good classifiable spectra, out of which 27 have very good signal-to-noise ratio.

3.4   Spectral Classification

3.4.1   Method

From the obtained spectra, the YSOs were classified by comparing their spectral features with libraries of standard stars. To match the high resolution of the FLAMES spectra, high resolution standards from Montes (1998) were used. However, standards for all spectral types are not available in this library, so that only a range of spectral types can be derived from it. To further the analysis and narrow down the spectral type, a low resolution (3.58 Å) library was used as well (G. Herczeg, private communication, 2010). Once a spectral type range has been determined from the high resolution standards, the low resolution library is used for a finer determination due to the availability of standards of nearly all spectral types in this library.

The most prominent features in late type stars are the Titanium Oxide (TiO) absorption lines at 7050 – 7150 Å. Mostly K-type and M-type stars have these features because they are cold enough for TiO to exist. The TiO feature at these wavelengths shows three absorption bands, which are deeper for colder objects. The Li I line in absorption at 6707 Å is also a common feature in young stars. This line could, however, not be clearly detected in these objects, due to the often low signal-to-noise ratio and limited spectral resolution.

To compare with the high resolution standards, the science spectra are normalized (divided by the continuum) and overplotted on the normalized standard spectra of different spectral types (see Figure 3.1). A spectral range is visually determined by
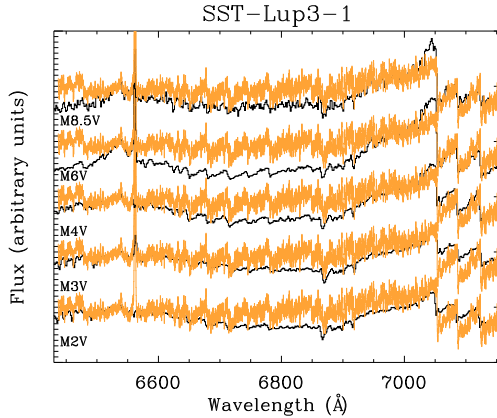
Figure 3.1 − Example of the classification method of SST-Lup3-1 with high resolution standards. The black curves represent the high resolution standard models and the gray curves the science spectrum. At the left of each standard its spectral type is indicated. The range of plausible spectral types is determined to be M4 - M8.5

the best match for the TiO bands. The method for the low resolution standards is somewhat different because that library is not normalized. First, the resolution of the science spectra is lowered to that of the standard (3.59Å). This is done by convolving the spectrum with a Gaussian profile. The comparison of the spectra with the low resolution standards then happens in two ways. One way consists of scaling the spectra to the standards by anchoring their fluxes at certain wavelengths (6500, 7020 and 7050 Å). An example is shown in Figure 3.2 (top left, top right and bottom left). In the alternative method a scale factor is determined by first dividing both spectra and then taking the mean of those values, ignoring extreme features (like Hα emission lines) in the process. This factor is then used to scale the original spectra to the standards (see bottom right panel of Figure 3.2). Both methods agree very well, producing four different plots for each spectral type within the determined range. The correct spectral type is again visually determined by the best match at the TiO bands. The typical uncertainty in the spectral classification is one sub-class.

3.4.2   Special Spectra

Some spectra present special features besides the temperature sensitive ones used for spectral classification. These objects were inspected more closely and are differentiated in three special types of spectra:

- Ten spectra show [He I] emission lines at 6677.6 and 7064.6 Å (objects # 7, 52, 76, 82, 83, 84, 85, 87, 91, 93 - see examples in Figure 3.3). All of these objects also show strong Hα in emission. Strongly accreting objects produce emission lines other than Hα, such as this line. It is concluded that these lines are a sign
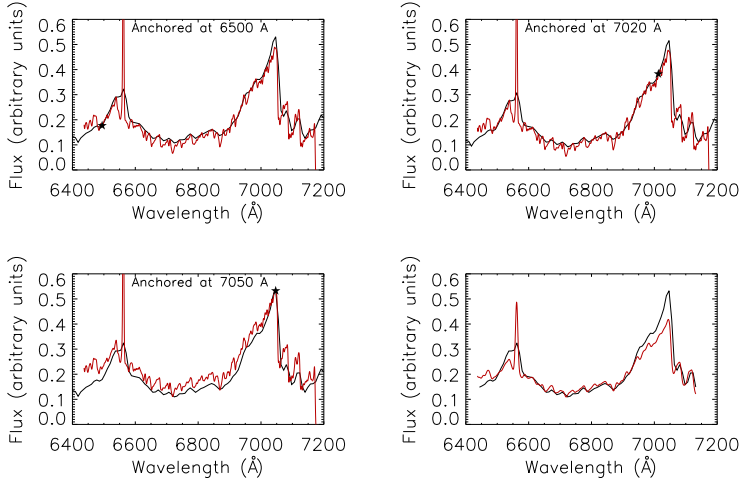
Figure 3.2 – Example of the classification methods of SST-Lup3-1 with the low resolution standard of a M6 main sequence star. The first three panels show the first method where the spectra are anchored at different wavelengths (wavelength explicitly mentioned in each plot, and marked to guide the eye). The last panel shows the second method. In all plots, the model is shown in black and the science spectrum in gray.
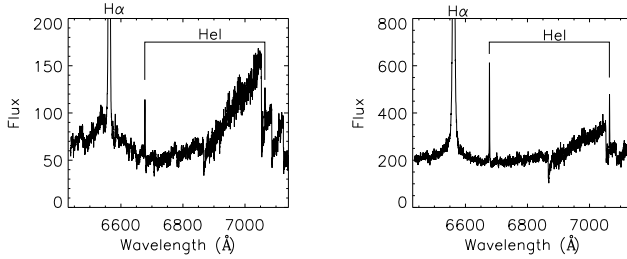
Figure 3.3 – Sample of spectra (#82 on left panel and #7 on right panel) with strong Hα (6562.8 Å), and He I (6677.6 and 7064.6 Å) emission lines.

of accretion, as is Hα (see Section 3.7 for more information on this subject).

- Four spectra (objects #50, 59, 78 and 88) show the [N II] doublet at 6548.4 and 6583.4 Å and the [S II] doublet at 6715.8 and 6729.8 Å (see examples in Figure 3.4). These lines are indicative of ionised gas. Par-Lup3-4 (#50) and Sz102 (#78) are related to Herbig-Haro (HH) objects HH600 and HH228 respectively (Wang & Henning 2009). They classified these objects to be HHs with the [S II] doublet line at 6717/6731 Å. The two other objects that show similar spectra, SSTc2dJ160708.6-391407 (#59) and Sz133 (#88), are not yet classified
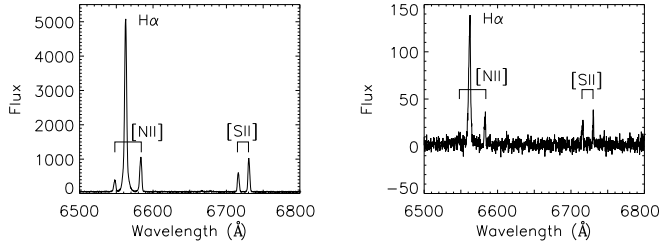
Figure 3.4 – Sample of spectra (#78 on left panel and #59 on right panel) with [NII] and [SII] doublets (at 6548.4 and 6583.4, and 6715.8 and 6729.8 Å respectively). Those sources may be associated with Herbig-Haro objects.
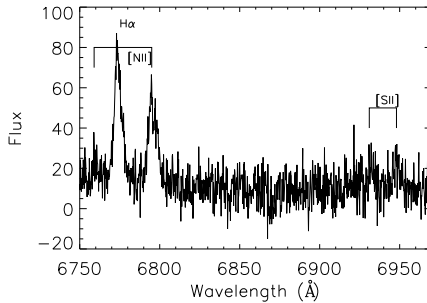
Figure 3.5 – Spectrum of IRAS15589-4132. The emission lines correspond with the spectral lines [N II] (at 6548.4 and 6583.4 Å) and [S II] (at 6715.8 and 6729.8 Å). This object is identified as a galaxy at redshift $z = 0.0324$.

as Herbig-Haro, and are thus designated as Herbig-Haro candidates.

- One spectrum, IRAS15589-4132 (#14), shows lines at 6757.95, 6774, 6794.8, 6931.5 and 6947.8 Å, and no other features (see Figure 3.5). These lines are identified as the doublets [N II] (at 6548.4 and 6583.4 Å) and [S II] (at 6715.8 and 6729.8 Å) and the strongest Hα line (at 6562.8 Å) at a redshift $z = 0.032$. This suggests that the object is a red-shifted galaxy rather than a YSO in the Lupus Cloud. In the NASA/IPAC Extragalactic Database (NED), there is a galaxy classified at the position of this object: 2MASSJ16022165-4140536. For further analysis, this object will no longer be considered part of the sample, leaving 91 sources in total.

3.4.3   Spectral Types

Following the method described above, the resulting spectral types with their error ranges are listed in Table 3.2. The objects are mostly M-type stars, but 10% are
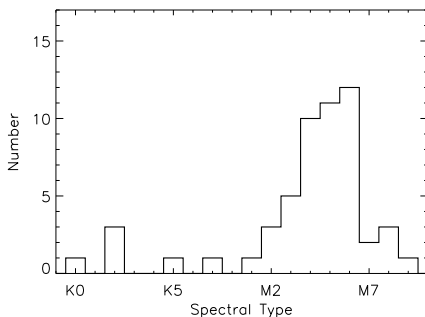
Figure 3.6 – Distribution of spectral types found in this work. The distribution peaks at M4–M6.

K-type. The histogram in Figure 3.6 shows the spectral type distribution, peaking at M6.

40 of these 54 objects were designated by Merín et al. (2008) as YSOs. Spectral classification is found in the literature for 31 of the 54 objects (57%). The literature classifications match well (within one sub-class) with those derived here. One object, however, differs: object # 26 is classified by López Martí et al. (2005) as M5, but as K0 (range from K0 to K2) here. For further analysis, our derived values are used.

3.4.4   Effective Temperature

Because spectral types are directly related to effective temperature T_{eff}, the temperatures of the stars classified here can be obtained (see Table 3.3). For spectral types in the range K – M0, the relationship adopted by Kenyon & Hartmann (1995) was used, while the relationship from Luhman et al. (2003) was adopted for types later than M0. The uncertainties in the temperature are determined directly from the spectral type uncertainties.

3.5   Spectral Energy Distributions

For a given star with known spectral type (and therefore T_{eff}), an SED can be constructed using the correct stellar atmosphere model and additional photometric data. The templates for stellar atmospheres used here are the NextGen Model Atmospheres (Hauschildt et al. 1999; Allard et al. 2000). In addition, various photometric datasets are available for the objects in Lupus. Optical and near-IR photometry in the R_C, I_C and Z_{WFI} bands (at 0.6517, 0.7838 and 0.9648 μm, respectively) was obtained from Comerón et al. (2010, private communication). The data were taken with the Wide Field Imager (WFI) at the La Silla 2.2 m Telescope in Chile. Near-infrared Two Micron All-Sky Survey (2MASS) photometry at J, H and K (at 1.235, 1.662 and 2.159 μm, respectively) is publicly available. Finally, *Spitzer* mid-infrared data at the

IRAC and MIPS bands (at 3.6, 4.5, 5.8, 8.0, 24 and 70 μm, respectively) are also available online [1] (Evans et al. 2003).

For each object, its photometric data and corresponding NextGen model atmosphere are used (matching its spectral type and the gravitational acceleration for a pre-main-sequence star). The observed photometric data are corrected for extinction at all wavelengths from the object's visual extinction (A_V), using the extinction law by Weingartner & Draine (2001) with $R_V = 5.5$. Subsequently, the NextGen atmosphere is scaled to the extinction corrected photometric data at a given band. The scaling band used is either the z_{WFI} or J band, depending on the availability of the photometry and the quality of the fit. In Table 3.2, the extinction values and normalization bands are presented for all fitted objects.

Figure 3.7 shows the constructed SEDs for 41 out of 54 objects. Here, the solid black line is the NextGen model atmosphere, the open squares are the observed photometry while filled circles show the extinction corrected data. SEDs could not be produced for 13 out of the 54 spectrally classified objects. Either not enough infrared (both 2MASS as Spitzer) photometry is available, or the different photometric data (optical, 2MASS and Spitzer) did not match well with each other.

A wide variety of SEDs can be seen in Figure 3.7. Consequently, a wide variety in disk types is inferred. The infrared spectral index slope can be used as a characteristic to distinguish between Class I, II and III objects, as defined by Lada. For the 39 objects with available data in K and MIPS1, the slope can be calculated as:

$$\alpha_{2-24\mu m} = \frac{(\lambda F_\lambda)_{24\mu m} - (\lambda F_\lambda)_{2\mu m}}{\lambda_{24\mu m} - \lambda_{2\mu m}}$$

These values are shown in Table 3.2. One object has $\alpha_{2-24\mu m}$ consistent with a Class I source ($\alpha > 0$) and 15 consistent with Class III sources ($\alpha < -2$), the majority of them are Class II, disk sources. Additionally, object #67 is a confirmed cold disk, as studied by Merín et al. (2010). Cold disks are disks with large inner dust holes (i.e. lack of warm dust). Objects # 27, 79 and 80 have SEDs consistent with inner dust holes. Although confirmation of their nature as cold disks requires SED modelling that is out of the scope of this work, 4 out of 41 objects with SEDs in Figure 3.7 amount to ∼10% of cold disks in the sample, which is consistent with the range of 4 – 12% of cold disk frequency derived by Merín et al. (2010).

3.5.1   Luminosities

Stellar and disk luminosities can be derived for the objects for which SEDs could be plotted. Stellar luminosity is calculated with the formula:

$$L_* = 4\pi D^2 \int F_\lambda d\lambda$$

---

[1] htpp://ssc.spitzer.caltech.edu/spitzerdataarchives/
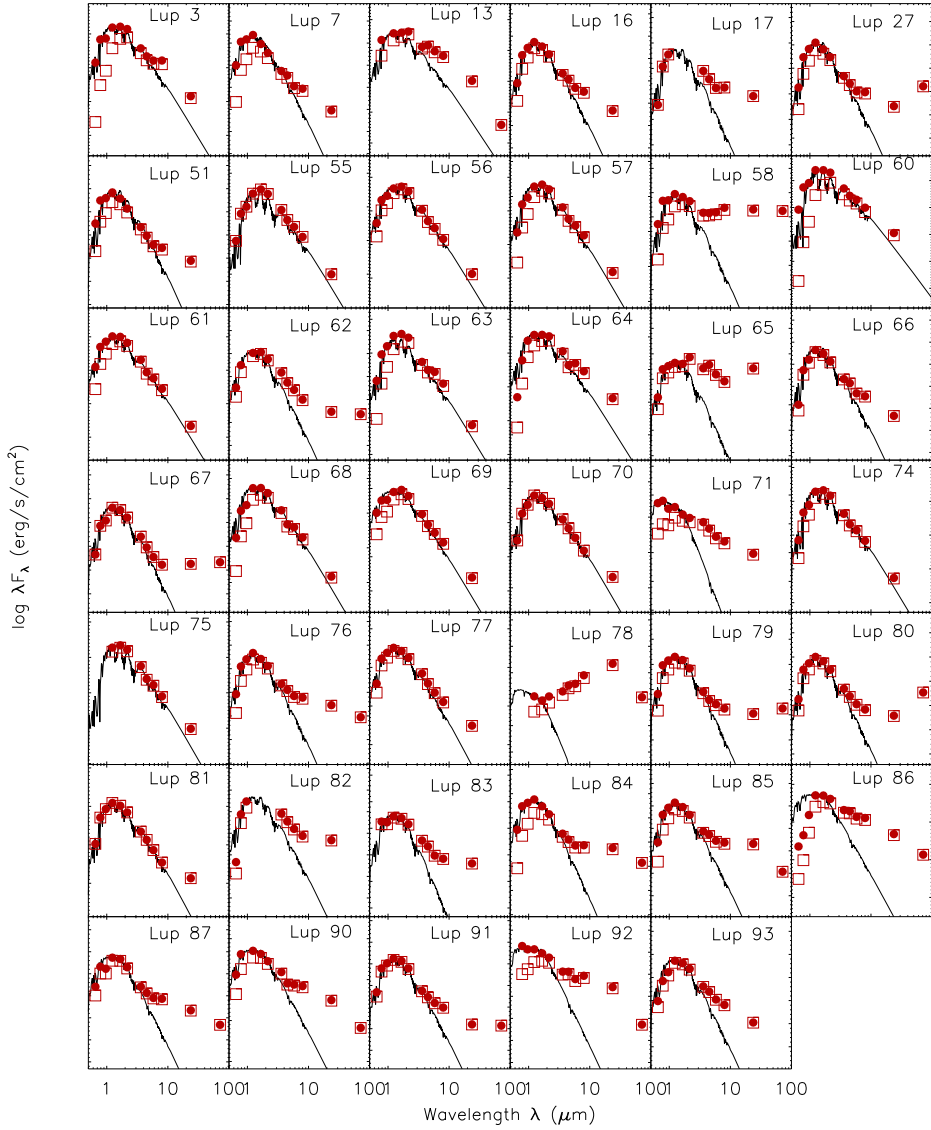
Figure 3.7 – SEDs of all the objects. The thick black curve is the model atmosphere of a star at its given temperature. The open points are the observed optical, 2MASS and *Spitzer* data. The closed points are the extinction corrected data. Notice the wide variety in SEDs (and thus disk shapes).

where D is the distance to the source and F_λ is the stellar flux – an integration of the NextGen model atmosphere scaled and normalized to the dereddened photometric data. Errors are derived from the uncertainty in the distance and flux, which includes an error in A_V of ± 0.5 mag. The disk luminosity is the integrated excess emission above the stellar photosphere. Errors are derived from the stellar luminosity errors. Those two values are shown in Table 3.3.

3.6   H-R Diagram

The age and mass of a star can be derived from theoretical tracks, overlaid on physical H-R diagrams. The position of an object in the H-R diagram is determined by its temperature (derived in Section 3.4.4) and luminosity (derived in Section 3.5.1).

3.6.1   Results

The pre-main sequence evolutionary tracks of Baraffe et al. (1998, 2001) and Siess et al. (2000) are overlaid in the H-R diagrams where the objects in this sample are placed (Figure 3.8). Thirteen objects are outside the range of the tracks (red and yellow circles in Figure 3.8).

Three objects (marked in red) are below the tracks: ID # 65, 71 and 78. By looking at their SEDs in Figure 3.7, it can be seen that objects 65 and 78 have substantial IR excess. The stellar fluxes are also not that high. These may be objects still surrounded by envelopes, which could be responsible for their low luminosity. Another explanation is that the objects are seen edge-on, such that the dust in the disk blocks some of the light of the star. In both cases, the calculated luminosity will be too low, resulting in an incorrect placement in the HR diagram. Object 71 does not to have a lot of IR excess. The reason of its misplacement in the HR diagram could be that it is a background source and is in fact at a larger distance, which will increase the calculated luminosity.

Ten objects (marked in yellow) are above the tracks: ID 3, 13, 55, 60, 61, 63, 64, 68, 74 and 75. An easy explanation would be that the assumed distance is wrong and that the objects are actually closer to us. However, even with very small distances (e.g. 60 pc), the objects are still above the tracks. Other effects have to play a role. One option is that they are part of a binary system that is unresolved, resulting in a stellar luminosity that is too high. Another option is that they are evolved AGB-stars. The working assumption is that these objects, however, do not belong to the Lupus Clouds.

For those 13 objects, no ages and masses were derived. For the other objects, the effective temperature, stellar and disk luminosity, age and mass can be found Table 3.3. As can be seen from Figure 3.9, the two models agree on the range of ages and masses, albeit with a different distribution. The mean age is 3.6 Myr for the Baraffe models and 4.4 Myr for the Siess models. For the masses, both models determine a mean stellar mass of only 0.3 M$_\odot$. This result is in agreement with that derived
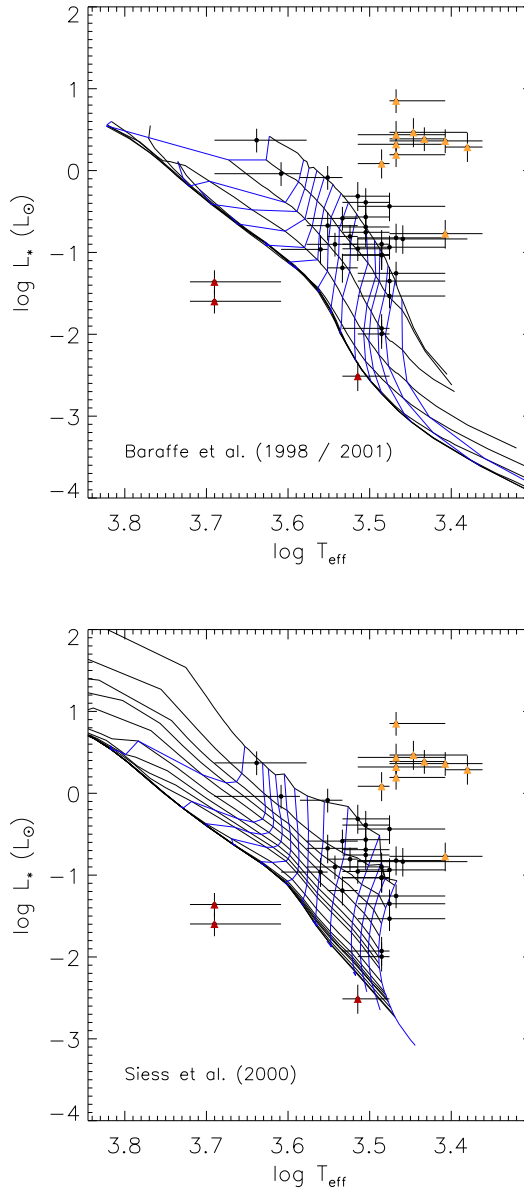
Figure 3.8 – HR diagram of the objects. Overlaid are the isochrones (black) and mass tracks (gray). The top panel shows the tracks from Baraffe et al. (1998, 2001) and the bottom panel the tracks from Siess et al. (2000). The corresponding ages (in Myr) and masses (in $M_\odot$) are marked. The red and yellow circles are objects that do not follow the tracks.
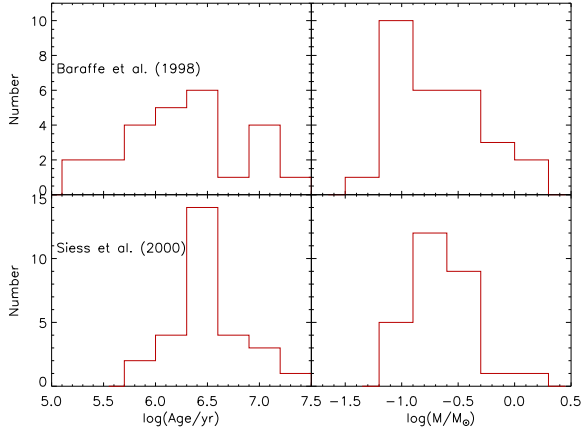
Figure 3.9 – Histograms of the ages and masses as derived from the two models.

by Merín et al. (2008). When deriving a luminosity function for the young stellar population in Lupus, the authors found it to peak at 0.2 $L_\odot$, which corresponds to 0.2 $M_\odot$ according to the PMS evolutionary tracks of Baraffe et al. (1998).

3.7   Accretion Based on Hα in Emission

From the data presented here, 45 of the objects (48 %) show the Hα line in emission. The strength of the Hα emission line is often used to distinguish between two classes of pre-MS stars: classical T Tauri stars (CTTS) and weak-line T Tauri stars (WTTS). CTTS are believed to correspond to stars that are actively accreting and WTTS are not, respectively. To this end, different methods have been proposed in the literature. Here, two methods are explored: the equivalent width and the full width of Hα at 10% of its peak intensity.

3.7.1   Hα Equivalent Width

The value of equivalent width (EW) can be used to distinguish between accreting and non-accreting objects, with the dividing threshold depending on the spectral type of the star. White & Basri (2003) proposed that a star is a CTTS if EW[Hα] $\geq$ 3 Å for K0–K5 stars, EW[Hα] $\geq$ 10 Å for K7–M2.5 stars, EW[Hα] $\geq$ 20 Å for M3–M5.5 stars and EW[Hα] $\geq$ 40 Å for M6–M7.5 stars. It is important to note that stars with EW[Hα] values lower than these proposed levels are not necessarily WTTS. Extra confirmation is needed from other diagnostics such as the Lithium abundance.

Following this criterion, 24 of the 45 objects (53.3%) are considered to be actively accreting (values can be found in Table 3.4). For objects # 22, 49, 50 and 59, no spectral type is available. However, since the EWs of these 4 objects are greater than 40 Å, they are considered accreters anyway.

3.7.2 Full Width of Hα at 10% of Peak Intensity

White & Basri (2003) proposed the use of another quantity to distinguish accreting and non-accreting objects: the full width of the line at 10% of the peak intensity, Hα[10%]. Lines with Hα[10%] > 270 km s^{-1} are, according to their measurements, assumed to be accreting. Based on physical reasoning as well as empirical findings, Jayawardhana et al. (2003) adopted 200 km s^{-1} as a more reasonable accretion cut-off, especially for low-mass stars. This is the cut-off value used in this work.

By performing a Gaussian fit (see Figure 3.10), Hα[10%] values can be obtained. To account for the resolution, the measured FWHM of each profile must be deconvolved assuming a Gaussian instrumental profile. For this sample, the Hα[10%] values can be found in Table 3.4. The errors are propagated from the error in the Gaussian fit to the error on the spectral resolution. According to the criterion of Jayawardhana et al. (2003), 25 of the 45 objects (55.5%) are considered accreters. The other 20 objects are not consistent with CTTS, even within their uncertainties. They are classified as non-accreters.

Some line profiles show broad wings at the bottom, which cannot be properly fitted by a Gaussian. In order to reproduce those lines, Voigt profiles were fitted to all the lines. In most cases, the fit is either the same or slightly better at the wings as can be see in Figure 3.11. However, this correction has no significant effect on the full width at 10%. Due to this insignificant difference, only the values from the Gaussian fits are further considered in this work.

The EW and Hα[10%] methods are generally consistent in the classification of sources. Only for three objects (#65, 80, 81) do the two methods give discrepant results.

3.7.3 Mass Accretion Rate

The Hα[10%] value can not only be used as an indicator of accretion, but also allows a quantitative estimate of the mass accretion rate. Natta et al. (2004) derived a correlation between Hα[10%] and mass accretion rate $\dot{M}_{ac}$ (derived from veiling and Hα profile model fittings):

$$\log \dot{M}_{ac} = -12.89(\pm 0.3) + 9.7(\pm 0.7) \cdot 10^{-3} \text{H}\alpha[10\%]$$

where $\dot{M}_{ac}$ is in M$_\odot$ yr^{-1} and Hα[10%] in km s^{-1}. The relation derived by Natta et al. (2004) was only calibrated for $-11 < \log \dot{M} < -6$. The cut-off of 200 km s^{-1} agrees with a cut-off of $10^{-10.95}$ M$_\odot$ yr^{-1} for $\dot{M}$. With this relation, mass accretion rates can be calculated for the objects in this sample with Hα in emission (see Table 3.4). In Figure 3.12 the distribution of the mass accretion rates is shown. Typical uncertainties are an order of magnitude. Most of the accreters have mass accretion rates that are consistent with the typical range for classical T Tauri stars.
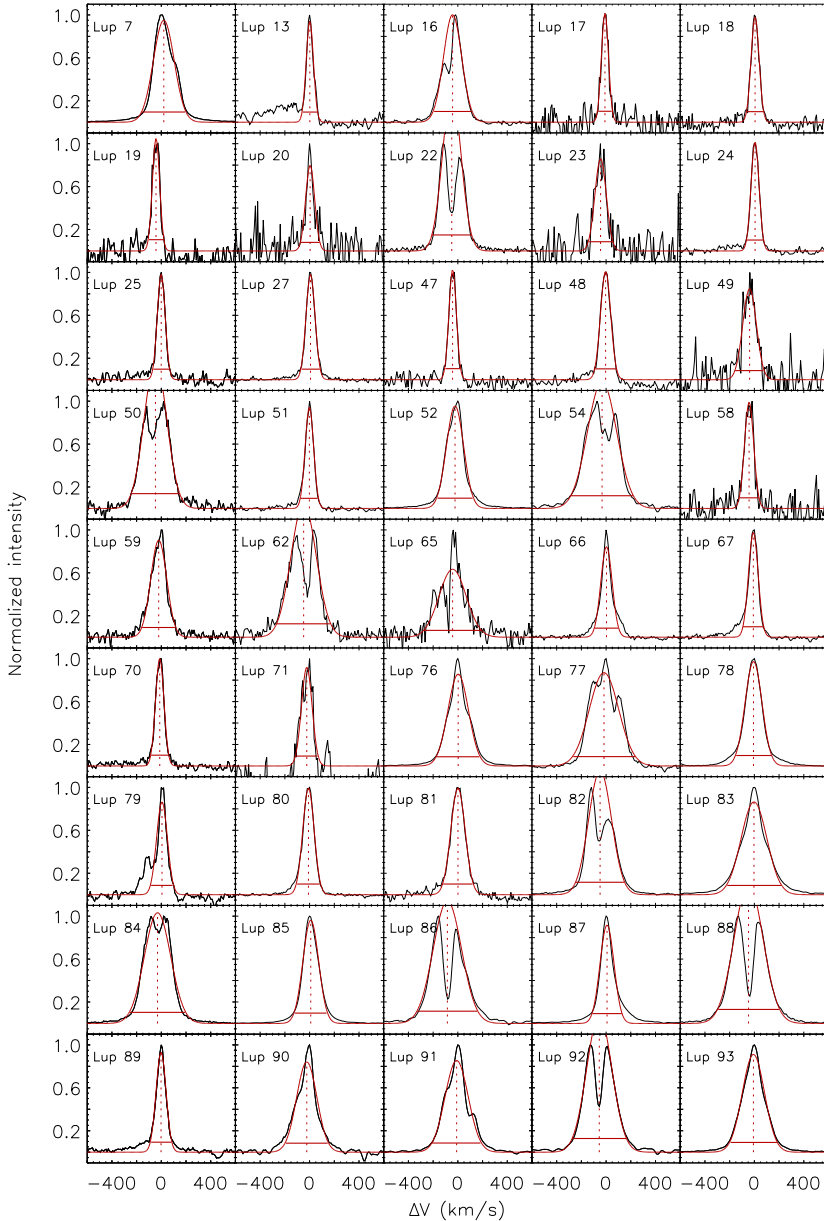
Figure 3.10 − Continuum subtracted, normalized profiles of the Hα emission lines (black line) overplotted with a Gaussian fit (gray solid line). The red dotted line marks the centre of the Gaussian fit and the horizontal gray line marks the width at 10% intensity.
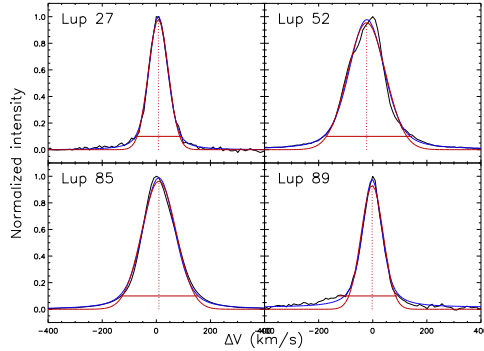
Figure 3.11 − Sample of continuum subtracted, normalized profiles of the Hα emission lines over-plotted with a Gaussian fit (light gray solid line) and a Voigt fit (dark gray solid line). The red dotted line marks the center of the Gaussian fit.
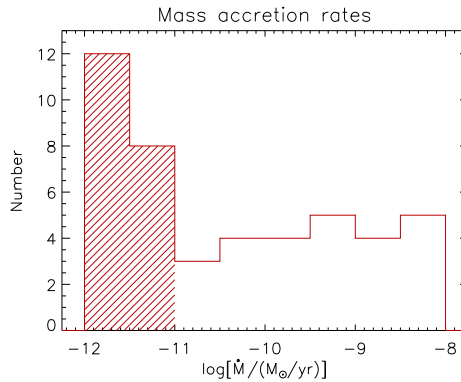
Figure 3.12 − Histogram of the mass accretion rates derived from the Hα[10%] value. The shaded area are objects out of the range for which the relationship of Natta et al. (2004) was calibrated. Those objects are generally classified as non-accreters.
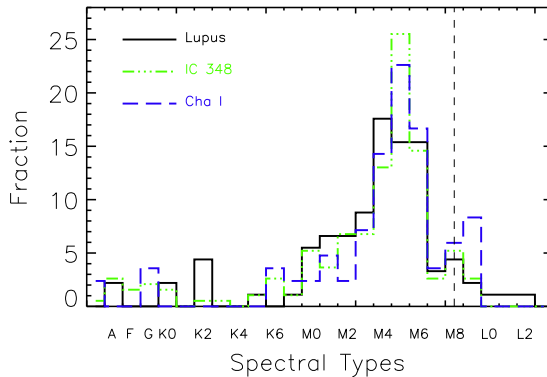
Figure 3.13 – Distribution of spectral types in Lupus (black solid line), IC 348 (light gray dot-dashed line) and Chamaeleon I (dark gray dashed line).

3.8   Discussion

Our work can be added to some of the objects classified as young stars by Merín et al. (2008) that have previously been spectrally classified in the literature in different studies (López Martí et al. 2005; Allers et al. 2006; Allen et al. 2007; Merín et al. 2007; Comerón 2008). This amounts to 91 of the 159 IR excess sources in the sample of Merín et al. (2008) to have known spectral types. This fairly complete sample can be compared to other nearby star-forming regions with equally complete stellar characterization.

Luhman et al. (2003) studied the young cluster IC348. Spectral types are determined with low-resolution optical spectroscopy for 169 objects. Similarly, Luhman (2007) determined spectral types for the 85 targets in the star forming region Chamaeleon I. Figure 3.13 shows the distribution of spectral types in Lupus (this work + literature), in IC 348 and Chamaeleon I. The vertical dashed line shows the completeness of the IC 348 and Cha I samples, which is comparable to the limit achieved by Merín et al. (2008). It can be seen that the three regions show very similar distributions of stellar types, from which is inferred that the IMF of Lupus is very similar to those of IC 348 and Cha I.

It is important to note that the sample of Merín et al. (2008) is selected on the basis of IR excess and it is, by definition, biased against young stars without disks (i.e. no IR excess). A similar study characterizing the young stellar population without disks in Lupus is still lacking.

3.9   Conclusions

We have presented a spectroscopic survey at optical wavelengths designed to determine spectral types and confirm the pre-main sequence nature of a sample of young

stellar objects in the Lupus Clouds found in the *Spitzer* c2d survey.

- Spectral types were determined for 54 stars belonging to Lupus I, III or IV. The sample consists mostly of M-type stars (90%), but also a few K-type stars. No early type object was found in this sample. The distribution of spectral types peaks at M4–M6. The distribution of spectral types is very similar to that of well studied star-forming regions like IC 348 and Chamaeleon I.
- The objects were placed in a H-R diagram after effective temperatures and luminosities were derived. Comparison with theoretical isochrones and mass tracks from models of Baraffe et al. (1998) and Siess et al. (2000) yield individual ages and masses for the objects. 10 objects are too luminous to belong to the clouds, while 3 objects are too faint. The very faint objects could still belong to the clouds by having a remnant envelope or an edge-on disk dimming some of the stellar luminosity.
- The theoretical models by Baraffe et al. (1998) and Siess et al. (2000) imply a population of YSOs concentrated in the age range between 1 and 5 Myr. The mean age is found to be 3.6 and 4.4 Myr with the Baraffe et al. (1998) and Siess et al. (2000) tracks, respectively. Individual masses range from 0.1 to 1.0 $M_\odot$, with mean values of 0.3 $M_\odot$ for both models.
- About half of the sample shows the Hα line in emission, an important indicator of accretion. This relationship was explored in two different ways: the equivalent width of Hα, and its full width at 10% of peak intensity. This confirms 25 objects (or 56% of the YSO sample) to be actively accreting objects classified as classical T Tauri stars. The quantitative estimate of the mass accretion rate $\dot{M}_{ac}$ based on the full width of Hα at 10% of the peak intensity yields a broad distribution of values ($\sim 10^{-11} - 10^{-8}$ $M_\odot \mathrm{yr}^{-1}$), typical of T Tauri stars.

References

Allard, F., Hauschildt, P. H., Alexander, D. R., Ferguson, J. W., & Tamanai, A. 2000, From Giant Planets to Cool Stars, 212, 127

Allen, P. R., Luhman, K. L., Myers, P. C., Megeath, S. T., Allen, L. E., Hartmann, L., & Fazio, G. G. 2007, ApJ, 655, 1095

Allers, K. N., Kessler-Silacci, J. E., Cieza, L. A., & Jaffe, D. T. 2006, ApJ, 644, 364

Baraffe, I., Chabrier, G., Allard, F., & Hauschildt, P. H. 1998, A&A, 337, 403

Baraffe, I., Chabrier, G., Allard, F., & Hauschildt, P. 2001, From Darkness to Light: Origin and Evolution of Young Stellar Clusters, 243, 571

Comerón, F. 2008, Handbook of Star Forming Regions, Volume II, 295

Comerón, F., Spezzi, L., & López Martí, B. 2009, A&A, 500, 1045

Evans, N. J., II, et al. 2003, PASP, 115, 965

Evans, N. J., et al. 2007, Final Delivery of Data from the c2d Legacy Project: IRAC and MIPS (Pasadena: SSC)[2]

Evans, N. J., et al. 2009, ApJS, 181, 321

Harvey, P. M., et al. 2007, ApJ, 663, 1139

---

[2]http://ssc.spitzer.caltech.edu/spitzermission/observingprograms/legacy/c2dhistory.html

Harvey, P., Merín, B., Huard, T. L., Rebull, L. M., Chapman, N., Evans, N. J., II, & Myers, P. C. 2007, ApJ, 663, 1149

Hauschildt, P. H., Allard, F., Ferguson, J., Baron, E., & Alexander, D. R. 1999, ApJ, 525, 871

Hughes, J., Hartigan, P., Krautter, J., & Kelemen, J. 1994, AJ, 108, 1071

Jayawardhana, R., Mohanty, S., & Basri, G. 2003, ApJ, 592, 282

Kenyon, S. J., & Hartmann, L. 1995, ApJS, 101, 117

López Martí, B., Eislöffel, J., & Mundt, R. 2005, A&A, 440, 139

Luhman, K. L., Stauffer, J. R., Muench, A. A., Rieke, G. H., Lada, E. A., Bouvier, J., & Lada, C. J. 2003, ApJ, 593, 1093

Luhman, K. L. 2007, ApJS, 173, 104

Merín, B., et al. 2007, ApJ, 661, 361

Merín, B., et al. 2008, ApJS, 177, 551

Merín, B., et al. 2010, ApJ, 718, 1200

Montes, D. 1998, Ap&SS, 263, 275

Natta, A., Testi, L., Muzerolle, J., Randich, S., Comerón, F., & Persi, P. 2004, A&A, 424, 603

Oliveira, I., et al. 2009, ApJ, 691, 672

Siess, L., Dufour, E., & Forestini, M. 2000, A&A, 358, 593

Tothill, N. F. H., et al. 2009, ApJS, 185, 98

Wang, H., & Henning, T. 2009, AJ, 138, 1072

Weingartner, J. C., & Draine, B. T. 2001, ApJ, 548, 296

White, R. J., & Basri, G. 2003, ApJ, 582, 1109

Table 3.1 − ID, name, cloud, position, observing dates and exposure times of the objects.

ID	Name	Cloud	RA (deg)	Dec (deg)	Observing Date	t_{exp} (s)	M[1]
1	2MASSJ16075475-3915446	Lupus III	16 : 07 : 54.72	−39 : 15 : 44.27	2008-02-21	630.0	U
2	2MASSJ16080175-3912316	Lupus III	16 : 08 : 01.68	−39 : 12 : 31.31	2008-02-21	630.0	U
3	2MASSJ16080618-3912225	Lupus III	16 : 08 : 06.24	−39 : 12 : 22.32	2008-02-21	630.0	S
4	2MASSJ16081497-3857145	Lupus III	16 : 08 : 14.88	−38 : 57 : 14.77	2008-02-21	630.0	U
5	2MASSJ16084747-3905087	Lupus III	16 : 08 : 47.52	−39 : 05 : 08.17	2008-02-21	630.0	U
6	2MASSJ16085373-3914367	Lupus III	16 : 08 : 53.76	−39 : 14 : 36.96	2008-02-21	630.0	U
7	2MASSJ16085529-3848481	Lupus III	16 : 08 : 55.20	−38 : 48 : 48.24	2008-02-22	1000.0	X
8	2MASSJ16085953-3856275	Lupus III	16 : 08 : 59.52	−38 : 56 : 27.96	2008-02-21	630.0	U
9	AKC2006-17	Lupus I	15 : 39 : 27.36	−34 : 48 : 43.56	2008-02-23	800.0	U
10	IRACJ16083010-3922592	Lupus III	16 : 08 : 30.00	−39 : 22 : 59.15	2008-02-26	1000.0	U
11	IRACJ16084679-3902074	Lupus III	16 : 08 : 46.80	−39 : 02 : 07.44	2008-02-21	630.0	U
12	IRACJ16093418-3915127	Lupus III	16 : 09 : 34.08	−39 : 15 : 12.61	2008-02-26	1000.0	U
13	IRAS15567-4141	Lupus IV	16 : 00 : 07.44	−41 : 49 : 48.72	2008-02-21	550.0	X
14	IRAS15589-4132	Lupus IV	16 : 02 : 21.60	−41 : 40 : 53.76	2008-02-24	1000.0	W
16	Lup604s	Lupus III	16 : 08 : 00.24	−39 : 02 : 58.93	2008-02-21	630.0	X
17	Lup607	Lupus III	16 : 08 : 28.08	−39 : 13 : 09.83	2008-02-21	630.0	S
18	Lup608s	Lupus III	16 : 09 : 08.40	−39 : 03 : 42.84	2008-02-21	630.0	S
19	Lup617	Lupus III	16 : 08 : 48.24	−39 : 09 : 19.44	2008-02-21	630.0	S
20	Lup650	Lupus III	16 : 09 : 49.92	−38 : 49 : 02.65	2008-02-22	1000.0	S
21	Lup654	Lupus III	16 : 07 : 23.52	−39 : 05 : 09.97	2008-02-21	630.0	N
22	Lup706	Lupus III	16 : 08 : 37.44	−39 : 23 : 11.03	2008-02-26	1000.0	N
23	Lup710	Lupus III	16 : 09 : 17.04	−39 : 27 : 09.73	2008-02-23	1000.0	S
24	Lup714	Lupus III	16 : 07 : 58.80	−39 : 24 : 34.91	2008-02-26	1000.0	X
25	Lup802s	Lupus III	16 : 11 : 51.12	−38 : 51 : 05.03	2008-02-26	1000.0	X
26	Lup810s	Lupus III	16 : 09 : 54.48	−39 : 12 : 03.24	2008-02-22	1000.0	S
27	Lup818s	Lupus III	16 : 09 : 56.40	−38 : 59 : 51.00	2008-02-22	1000.0	X
28	Lupus3MMS	Lupus III	16 : 09 : 18.00	−39 : 04 : 53.40	2008-02-24	10.0	N
					2008-02-26	1000.0	
29	NTO2000-0526.9-5630	Lupus III	16 : 08 : 28.08	−39 : 04 : 24.61	2008-02-21	630.0	U
30	NTO2000-0532.1-5616	Lupus III	16 : 08 : 53.52	−39 : 04 : 09.11	2008-02-21	630.0	U
31	NTO2000-0536.7-5943	Lupus III	16 : 08 : 58.32	−39 : 07 : 35.40	2008-02-24	1000.0	N
32	NTO2000-0536.7-5956	Lupus III	16 : 08 : 58.32	−39 : 07 : 49.45	2008-02-24	10.0	N
					2008-02-26	1000.0	
33	NTO2000-0537.4-5653	Lupus III	16 : 08 : 59.04	−39 : 04 : 45.84	2008-02-21	630.0	U
34	NTO2000-0540.9-5757	Lupus III	16 : 09 : 02.40	−39 : 05 : 49.20	2008-02-21	630.0	N
35	NTO2000-0546.4-5934	Lupus III	16 : 09 : 07.92	−39 : 07 : 26.76	2008-02-24	10.0	N
					2008-02-26	1000.0	
36	NTO2000-0554.9-5651	Lupus III	16 : 09 : 16.32	−39 : 04 : 43.68	2008-02-24	1000.0	N
37	NTO2000-0558.8-5610	Lupus III	16 : 09 : 20.40	−39 : 04 : 01.56	2008-02-24	10.0	N
					2008-02-26	1000.0	
38	NTO2000-0601.7-5616	Lupus III	16 : 09 : 23.04	−39 : 04 : 07.32	2008-02-24	10.0	N
					2008-02-26	1000.0	
39	NTO2000-0605.1-5606	Lupus III	16 : 09 : 26.64	−39 : 03 : 57.61	2008-02-26	1000.0	U
40	NTO2000-0605.6-5437	Lupus III	16 : 09 : 27.12	−39 : 02 : 28.32	2008-02-21	630.0	U
41	NTO2000-0614.0-5414	Lupus III	16 : 09 : 35.52	−39 : 02 : 05.64	2008-02-21	630.0	U
42	NTO2000-0615.6-5616	Lupus III	16 : 09 : 37.20	−39 : 04 : 06.96	2008-02-24	1000.0	U
43	NTO2000-0615.6-5953	Lupus III	16 : 09 : 37.20	−39 : 07 : 44.76	2008-02-24	1000.0	U
44	NTO2000-0615.8-5734	Lupus III	16 : 09 : 37.44	−39 : 05 : 25.80	2008-02-24	1000.0	U
45	NTO2000-0617.7-5641	Lupus III	16 : 09 : 39.36	−39 : 04 : 31.80	2008-02-24	1000.0	U
46	NTO2000-0619.6-5414	Lupus III	16 : 09 : 41.04	−39 : 02 : 05.64	2008-02-21	630.0	U
47	Par-Lup3-1	Lupus III	16 : 08 : 16.08	−39 : 03 : 03.97	2008-02-21	630.0	S
48	Par-Lup3-2	Lupus III	16 : 08 : 35.76	−39 : 03 : 47.53	2008-02-21	630.0	X
49	Par-Lup3-3	Lupus III	16 : 08 : 49.44	−39 : 05 : 39.12	2008-02-21	630.0	N
50	Par-Lup3-4	Lupus III	16 : 08 : 51.36	−39 : 05 : 30.13	2008-02-21	630.0	N
51	SST-Lup3-1	Lupus III	16 : 11 : 59.76	−38 : 23 : 38.40	2008-02-25	1000.0	X
52	SSTc2dJ155925.2-423507	Lupus IV	15 : 59 : 25.20	−42 : 35 : 07.08	2008-02-26	1000.0	S
53	SSTc2dJ160000.6-422158	Lupus IV	16 : 00 : 00.48	−42 : 21 : 57.23	2008-02-26	1000.0	W
54	SSTc2dJ160002.4-422216	Lupus IV	16 : 00 : 02.40	−42 : 22 : 14.88	2008-02-26	1000.0	X
55	SSTc2dJ160111.6-413730	Lupus IV	16 : 01 : 11.52	−41 : 37 : 30.00	2008-02-21	550.0	X
56	SSTc2dJ160143.3-413606	Lupus IV	16 : 01 : 43.20	−41 : 36 : 05.76	2008-02-21	550.0	X
57	SSTc2dJ160229.9-415111	Lupus IV	16 : 02 : 30.00	−41 : 51 : 10.80	2008-02-24	1000.0	S
58	SSTc2dJ160703.9-391112	Lupus III	16 : 07 : 03.84	−39 : 11 : 11.40	2008-02-21	630.0	S
59	SSTc2dJ160708.6-391407	Lupus III	16 : 07 : 08.64	−39 : 14 : 07.44	2008-02-21	630.0	N
60	SSTc2dJ160755.3-390718	Lupus III	16 : 07 : 55.20	−39 : 07 : 17.39	2008-02-21	630.0	S
61	SSTc2dJ160803.0-385229	Lupus III	16 : 08 : 03.12	−38 : 52 : 29.64	2008-02-24	1000.0	X
62	SSTc2dJ160901.4-392512	Lupus III	16 : 09 : 01.44	−39 : 25 : 11.99	2008-02-23	1000.0	S
63	SSTc2dJ160934.1-391342	Lupus III	16 : 09 : 34.08	−39 : 13 : 42.24	2008-02-21	630.0	S
64	SSTc2dJ161000.1-385401	Lupus III	16 : 10 : 00.00	−38 : 54 : 00.36	2008-02-22	1000.0	X
65	SSTc2dJ161013.1-384617	Lupus III	16 : 10 : 12.96	−38 : 46 : 16.31	2008-02-22	1000.0	S
66	SSTc2dJ161019.8-383607	Lupus III	16 : 10 : 19.92	−38 : 36 : 06.48	2008-02-23	1000.0	X

ID	Name	Cloud	RA (deg)	Dec (deg)	Observing Date	t_{exp} (s)	M[1]
67	SSTc2dJ161029.6-392215	Lupus III	16 : 10 : 29.52	−39 : 22 : 14.52	2008-02-23	1000.0	X
68	SSTc2dJ161034.5-381450	Lupus III	16 : 10 : 34.56	−38 : 14 : 50.28	2008-02-25	1000.0	X
69	SSTc2dJ161131.9-381110	Lupus III	16 : 11 : 31.92	−38 : 11 : 09.96	2008-02-25	1000.0	S
70	SSTc2dJ161144.9-383245	Lupus III	16 : 11 : 44.88	−38 : 32 : 44.88	2008-02-23	1000.0	X
71	SSTc2dJ161148.7-381758	Lupus III	16 : 11 : 48.72	−38 : 17 : 57.84	2008-02-25	1000.0	S
72	SSTc2dJ161204.5-380959	Lupus III	16 : 12 : 04.56	−38 : 09 : 58.69	2008-02-25	1000.0	U
73	SSTc2dJ161211.2-383220	Lupus III	16 : 12 : 11.28	−38 : 32 : 20.03	2008-02-22	1000.0	U
74	SSTc2dJ161219.6-383742	Lupus III	16 : 12 : 19.68	−38 : 37 : 41.88	2008-02-22	1000.0	S
75	SSTc2dJ161251.7-384216	Lupus III	16 : 12 : 51.60	−38 : 42 : 15.84	2008-02-22	1000.0	S
76	Sz100	Lupus III	16 : 08 : 25.68	−39 : 06 : 01.08	2008-02-21	300.0	X
					2008-02-23	200.0	
					2008-02-26	200.0	
77	Sz101	Lupus III	16 : 08 : 28.32	−39 : 05 : 31.92	2008-02-21	630.0	X
78	Sz102	Lupus III	16 : 08 : 29.76	−39 : 03 : 10.81	2008-02-21	630.0	S
79	Sz103	Lupus III	16 : 08 : 30.24	−39 : 06 : 10.80	2008-02-21	630.0	X
80	Sz104	Lupus III	16 : 08 : 30.72	−39 : 05 : 48.49	2008-02-21	630.0	X
81	Sz107	Lupus III	16 : 08 : 41.76	−39 : 01 : 36.84	2008-02-21	630.0	S
82	Sz108B	Lupus III	16 : 08 : 42.96	−39 : 06 : 14.40	2008-02-21	630.0	X
					2008-02-23	200.0	
					2008-02-26	200.0	
83	Sz110	Lupus III	16 : 08 : 51.60	−39 : 03 : 17.64	2008-02-21	300.0	S
					2008-02-23	200.0	
					2008-02-26	200.0	
84	Sz113	Lupus III	16 : 08 : 57.84	−39 : 02 : 22.56	2008-02-21	630.0	X
85	Sz114	Lupus III	16 : 09 : 01.92	−39 : 05 : 12.12	2008-02-21	300.0	X
					2008-02-23	200.0	
					2008-02-26	200.0	
86	Sz118	Lupus III	16 : 09 : 48.72	−39 : 11 : 16.80	2008-02-22	1000.0	S
87	Sz130	Lupus IV	16 : 00 : 30.96	−41 : 43 : 36.83	2008-02-21	550.0	X
88	Sz133	Lupus IV	16 : 03 : 29.52	−41 : 40 : 02.28	2008-02-24	1000.0	S
89	Sz94	Lupus III	16 : 07 : 49.68	−39 : 04 : 28.56	2008-02-21	630.0	S
90	Sz96	Lupus III	16 : 08 : 12.48	−39 : 08 : 33.01	2008-02-21	630.0	S
91	Sz97	Lupus III	16 : 08 : 21.84	−39 : 04 : 21.36	2008-02-21	630.0	X
					2008-02-23	200.0	
					2008-02-26	200.0	
92	Sz98	Lupus III	16 : 08 : 22.56	−39 : 04 : 45.84	2008-02-21	300.0	S
					2008-02-23	200.0	
					2008-02-26	200.0	
93	Sz99	Lupus III	16 : 08 : 24.00	−39 : 05 : 49.20	2008-02-21	630.0	X
					2008-02-23	200.0	
					2008-02-26	200.0	

[1] G means good spectra, U non-detections, F featureless spectra, and O not useful spectra. See Section 3.4.3 for more details.

Table 3.2 – Spectral types, visual extinction (A_V), normalization bands and the spectral index, calculated between the 2MASS K-band (2 μm) and the MIPS1 band (24 μm), for the classifiable objects. Objects for which SEDs could not be produced do not have all values.

ID	SpT	Range	A_V (mag)	Band	$\alpha_{2-24\mu m}$	Class
3	M6.5	M4 - M8.5	5.30	J	-1.91	III
7	M3	M2 - M4	2.50	Z	-1.25	II
13	M6.5	M4 - M8.5	2.00	J	-1.54	II
16	M5.5	M4 - M6	1.20	Z	-1.21	II
17	M5.5	M4 - M6	0.00	Z		
18	M5.5	M4 - M8.5				
19	M6	M4 - M8.5				
20	M3.5	M2 - M4				
23	M4.5	M3 - M6				
24	M6	M4 - M8.5				
25	M5.5	M4 - M6				
26	K0	K0 - K2				
27	M6	M4 - M8.5	1.40	Z	-1.01	II
47	M5.5	M4 - M6				
48	M5	M4 - M6				
51	M6	M4 - M8.5	1.80	J	-1.08	II
52	M4.5	M3 - M6				
54	M3.5	M2 - M4				
55	M8.5	M6 - M9.5	0.00	J	-2.30	III
56	M6	M4 - M8.5	1.20	J	-2.36	III
57	M7	M4 - M9	2.60	J	-2.27	III
58	M5.5	M3 - M6	2.20	Z	-0.17	II
60	M9	M8.5 - M9.5	8.00	Z	-2.16	III
61	M5.5	M4 - M6	2.00	Z	-2.39	III
62	M3.5	M2 - M4	0.60	J	-1.10	II
63	M7.5	M6 - M9	3.40	Z	-2.49	III
64	M6.5	M6 - M8.5	2.80	J	-1.82	III
65	M4	M3 - M6	0.70	Z	-0.21	II
66	M6	M4 - M8.5	0.40	J	-1.18	II
67	M5.5	M3 - M6	0.00	J	-0.93	II
68	M6.5	M6 - M8.5	2.90	J	-2.31	III
69	M2.5	M0.5 - M4	1.90	J	-2.30	III
70	M6.5	M4 - M8.5	0.00	J	-1.99	III
71	K2	K0 - K7	1.60	J	-0.60	II
74	M8	M6 - M8.5	1.60	J	-2.34	III
75	M8.5	M6 - M9.5	1.00	J	-2.15	III
76	M4.5	M3 - M6	1.20	Z	-0.80	II
77	M4.5	M3 - M6	0.70	Z	-1.68	III
78	K2	K0 - K7	2.50	J	0.59	I
79	M4.5	M3 - M6	1.00	Z	-0.86	II
80	M5.5	M3 - M6	0.70	Z	-0.91	II
81	M6.5	M4 - M8.5	0.00	Z	-1.64	III
82	M5.5	M3 - M6	0.80	Z		
83	M3	M0.5 - M4	0.20	J	-0.71	II
84	M1.5	K7 - M2	2.40	Z	-0.67	II
85	M4	M3 - M6	1.30	Z	-0.62	II
86	K7	K2 - M0	2.60	J	-0.90	II
87	M2	M0.5 - M4	0.60	J	-0.94	II
88	K2	K0 - K7				
89	M4.5	M3 - M6				
90	M2	M0 - M3	1.43	J	-0.91	II
91	M4.5	M3 - M6	0.30	Z	-1.24	II
92	K5	K2 - M0.5	2.50	J	-0.64	II
93	M4	M3 - M6	0.40	J	-1.12	II

Note: Sources without ages and masses do not follow the evolutionary tracks.

Table 3.3 – Effective temperature T_{eff}, stellar and disk luminosity, L_* and L_{disk}, age and mass for Baraffe et al. (1998 - 2001) and Siess et al. (2000).

ID	T_{eff} (K)	L_* ($L_\odot$)	L_{disk} ($L_\odot$)	Age_B (Myr)	$Mass_B$ ($M_\odot$)	Age_S (Myr)	$Mass_S$ ($M_\odot$)
3	$2935.0^{+335.0}_{-380.0}$	$2.09^{+0.80}_{-0.61}$	$0.61^{+0.45}_{-0.31}$				
7	$3415.0^{+145.0}_{-145.0}$	$0.06^{+0.03}_{-0.02}$	$0.01^{+0.01}_{-0.01}$	$13.64^{+14.82}_{-7.21}$	$0.35^{+0.15}_{-0.12}$	$9.90^{+6.37}_{-3.46}$	$0.27^{+0.07}_{-0.06}$
13	$2935.0^{+335.0}_{-380.0}$	$2.74^{+1.28}_{-0.94}$	$1.93^{+1.05}_{-0.74}$				
16	$3057.5^{+212.5}_{-67.5}$	$0.09^{+0.05}_{-0.03}$	$0.02^{+0.02}_{-0.02}$	$1.17^{+2.79}_{-0.78}$	$0.12^{+0.13}_{-0.02}$	$3.85^{+0.96}_{-3.85}$	$0.14^{+0.08}_{-0.02}$
17	$3057.5^{+212.5}_{-67.5}$	$0.01^{+0.00}_{-0.00}$	$0.00^{+0.01}_{-0.00}$	$12.75^{+42.27}_{-4.13}$	$0.09^{+0.09}_{-0.02}$	$16.25^{+48.83}_{-7.41}$	$0.09^{+0.09}_{-0.02}$
27	$2990.0^{+280.0}_{-435.0}$	$0.04^{+0.02}_{-0.02}$	$0.01^{+0.01}_{-0.01}$	$1.87^{+7.16}_{-1.87}$	$0.09^{+0.13}_{-0.09}$	$4.43^{+4.99}_{-2.82}$	$0.09^{+0.10}_{-0.09}$
51	$2990.0^{+280.0}_{-435.0}$	$0.12^{+0.04}_{-0.03}$	$0.01^{+0.02}_{-0.01}$	$0.19^{+2.79}_{-0.19}$	$0.11^{+0.15}_{-0.11}$	$3.62^{+0.59}_{-0.59}$	$0.17^{+0.06}_{-0.06}$
55	$2555.0^{+435.0}_{-255.0}$	$0.17^{+0.08}_{-0.06}$	$0.05^{+0.05}_{-0.02}$				
56	$2990.0^{+280.0}_{-435.0}$	$0.37^{+0.17}_{-0.13}$	$0.06^{+0.08}_{-0.04}$	$0.00^{+0.57}_{-0.00}$	$0.18^{+0.12}_{-0.18}$	$1.81^{+-1.81}_{-1.81}$	$0.26^{+-0.26}_{-0.26}$
57	$2880.0^{+390.0}_{-480.0}$	$0.15^{+0.07}_{-0.05}$	$0.03^{+0.03}_{-0.02}$	$0.00^{+2.44}_{-0.00}$	$0.06^{+5.02}_{-0.00}$	$3.40^{+-3.40}_{-3.40}$	$0.24^{+-0.24}_{-0.24}$
58	$3057.5^{+357.5}_{-67.5}$	$0.01^{+0.01}_{-0.00}$	$0.02^{+0.01}_{-0.01}$	$9.83^{+131.97}_{-2.07}$	$0.09^{+0.20}_{-0.02}$	$13.83^{+101.47}_{-5.94}$	$0.09^{+0.16}_{-0.02}$
60	$2400.0^{+155.0}_{-100.0}$	$1.94^{+0.95}_{-0.66}$	$0.80^{+0.61}_{-0.40}$				
61	$3057.5^{+212.5}_{-67.5}$	$1.22^{+0.60}_{-0.42}$	$0.19^{+0.33}_{-0.19}$				
62	$3342.5^{+217.5}_{-72.5}$	$0.16^{+0.06}_{-0.05}$	$0.06^{+0.03}_{-0.03}$	$2.86^{+5.43}_{-0.69}$	$0.31^{+0.20}_{-0.05}$	$3.49^{+1.67}_{-0.67}$	$0.27^{+0.09}_{-0.03}$
63	$2795.0^{+195.0}_{-395.0}$	$2.93^{+1.43}_{-1.00}$	$1.14^{+0.94}_{-0.61}$				
64	$2935.0^{+55.0}_{-380.0}$	$1.56^{+0.60}_{-0.45}$	$0.45^{+0.34}_{-0.23}$				
65	$3270.0^{+145.0}_{-280.0}$	$0.00^{+0.00}_{-0.00}$	$0.00^{+0.01}_{-0.00}$				
66	$2990.0^{+280.0}_{-435.0}$	$0.03^{+0.01}_{-0.01}$	$0.00^{+0.01}_{-0.00}$	$3.07^{+12.27}_{-3.07}$	$0.09^{+0.12}_{-0.09}$	$5.02^{+9.65}_{-2.91}$	$0.08^{+0.10}_{-0.08}$
67	$3057.5^{+357.5}_{-67.5}$	$0.09^{+0.04}_{-0.03}$	$0.02^{+0.02}_{-0.01}$	$1.17^{+7.21}_{-0.78}$	$0.12^{+0.24}_{-0.02}$	$3.85^{+2.80}_{-3.85}$	$0.14^{+0.14}_{-0.02}$
68	$2935.0^{+55.0}_{-380.0}$	$7.12^{+2.72}_{-2.07}$	$0.99^{+1.27}_{-0.82}$				
69	$3487.5^{+290.0}_{-217.5}$	$0.13^{+0.05}_{-0.04}$	$0.02^{+0.02}_{-0.02}$	$7.98^{+19.47}_{-5.19}$	$0.44^{+0.26}_{-0.18}$	$5.74^{+8.90}_{-1.79}$	$0.33^{+0.19}_{-0.09}$
70	$2935.0^{+335.0}_{-380.0}$	$0.06^{+0.02}_{-0.02}$	$0.00^{+0.01}_{-0.00}$	$0.44^{+7.07}_{-0.44}$	$0.08^{+0.15}_{-0.08}$	$3.57^{+4.02}_{-2.32}$	$0.08^{+0.12}_{-0.08}$
71	$4900.0^{+350.0}_{-840.0}$	$0.04^{+0.02}_{-0.01}$	$0.02^{+0.01}_{-0.01}$				
74	$2710.0^{+280.0}_{-155.0}$	$2.44^{+0.93}_{-0.71}$	$0.38^{+0.43}_{-0.29}$				
75	$2555.0^{+435.0}_{-255.0}$	$2.30^{+0.88}_{-0.67}$	$0.57^{+0.47}_{-0.31}$				
76	$3197.5^{+217.5}_{-207.5}$	$0.27^{+0.13}_{-0.09}$	$0.10^{+0.09}_{-0.05}$	$0.53^{+1.73}_{-0.53}$	$0.20^{+0.20}_{-0.04}$	$1.94^{+0.75}_{-1.94}$	$0.23^{+0.08}_{-0.02}$
77	$3197.5^{+217.5}_{-207.5}$	$0.41^{+0.20}_{-0.14}$	$0.06^{+0.10}_{-0.06}$	$0.15^{+1.25}_{-0.15}$	$0.19^{+0.26}_{-0.01}$	$0.82^{+1.34}_{-0.82}$	$0.25^{+0.07}_{-0.02}$
78	$4900.0^{+350.0}_{-840.0}$	$0.03^{+0.01}_{-0.01}$	$0.13^{+0.04}_{-0.03}$				
79	$3197.5^{+217.5}_{-207.5}$	$0.20^{+0.10}_{-0.07}$	$0.06^{+0.06}_{-0.04}$	$0.99^{+1.86}_{-0.98}$	$0.20^{+0.18}_{-0.07}$	$2.48^{+0.67}_{-2.48}$	$0.22^{+0.09}_{-0.04}$
80	$3057.5^{+357.5}_{-67.5}$	$0.13^{+0.06}_{-0.04}$	$0.04^{+0.04}_{-0.02}$	$0.64^{+5.03}_{-0.51}$	$0.13^{+0.24}_{-0.01}$	$2.82^{+1.96}_{-2.82}$	$0.15^{+0.14}_{-0.02}$
81	$2935.0^{+335.0}_{-380.0}$	$0.15^{+0.07}_{-0.05}$	$0.01^{+0.04}_{-0.01}$	$0.00^{+2.36}_{-0.00}$	$0.10^{+0.16}_{-0.10}$	$3.28^{+-3.28}_{-3.28}$	$0.24^{+-0.24}_{-0.24}$
82	$3057.5^{+357.5}_{-67.5}$	$0.09^{+0.05}_{-0.03}$	$0.03^{+0.03}_{-0.02}$	$1.18^{+7.23}_{-0.79}$	$0.12^{+0.24}_{-0.02}$	$3.86^{+2.82}_{-3.86}$	$0.14^{+0.14}_{-0.02}$
83	$3415.0^{+362.5}_{-145.0}$	$0.26^{+0.10}_{-0.08}$	$0.09^{+0.06}_{-0.04}$	$2.35^{+7.10}_{-1.20}$	$0.40^{+0.38}_{-0.12}$	$2.73^{+2.25}_{-0.38}$	$0.31^{+0.20}_{-0.06}$
84	$3632.5^{+427.5}_{-72.5}$	$0.11^{+0.05}_{-0.04}$	$0.04^{+0.03}_{-0.03}$	$19.64^{+59.62}_{-9.80}$	$0.58^{+0.08}_{-0.08}$	$9.95^{+50.10}_{-3.95}$	$0.40^{+0.24}_{-0.04}$
85	$3270.0^{+145.0}_{-280.0}$	$0.49^{+0.24}_{-0.17}$	$0.22^{+0.16}_{-0.11}$	$0.26^{+0.81}_{-0.26}$	$0.32^{+0.16}_{-0.10}$	$1.12^{+0.96}_{-1.12}$	$0.27^{+0.05}_{-0.01}$
86	$4060.0^{+840.0}_{-210.0}$	$0.92^{+0.35}_{-0.27}$	$0.56^{+0.27}_{-0.21}$	$3.72^{+20.71}_{-1.37}$	$1.16^{+0.04}_{-0.16}$	$2.54^{+13.53}_{-1.09}$	$0.76^{+0.39}_{-0.20}$
87	$3560.0^{+217.5}_{-290.0}$	$0.21^{+0.10}_{-0.07}$	$0.06^{+0.06}_{-0.03}$	$5.77^{+7.30}_{-4.20}$	$0.52^{+0.23}_{-0.25}$	$3.74^{+3.02}_{-1.03}$	$0.37^{+0.14}_{-0.12}$
90	$3560.0^{+290.0}_{-145.0}$	$0.82^{+0.31}_{-0.24}$	$0.27^{+0.19}_{-0.13}$	$0.88^{+1.79}_{-0.56}$	$0.67^{+0.32}_{-0.08}$	$0.81^{+0.94}_{-0.81}$	$0.39^{+0.18}_{-0.06}$
91	$3197.5^{+217.5}_{-207.5}$	$0.18^{+0.09}_{-0.06}$	$0.04^{+0.05}_{-0.03}$	$1.29^{+1.86}_{-1.27}$	$0.21^{+0.16}_{-0.08}$	$2.70^{+1.00}_{-2.70}$	$0.22^{+0.09}_{-0.05}$
92	$4350.0^{+550.0}_{-572.5}$	$2.35^{+0.90}_{-0.68}$	$1.18^{+0.66}_{-0.47}$	$2.42^{+3.02}_{-2.24}$	$1.53^{+0.39}_{-0.45}$	$1.49^{+3.46}_{-1.49}$	$1.12^{+0.54}_{-0.65}$
93	$3270.0^{+145.0}_{-280.0}$	$0.11^{+0.04}_{-0.03}$	$0.03^{+0.02}_{-0.02}$	$3.07^{+3.72}_{-2.85}$	$0.26^{+0.11}_{-0.15}$	$4.34^{+1.22}_{-4.34}$	$0.23^{+0.06}_{-0.10}$

Table 3.4 − Hα line widths and mass accretion rates.

ID	EW[Hα] (Å)	CTTS?	Hα [10%] (km s^{-1})	CTTS?	log $\dot{M}_{ac}$ (M$_\odot$ yr^{-1})	Double peak?
7	201.3	yes	351.0 ± 5.0	yes	-9.5 ± 0.4	
13	4.1		98.0 ± 11.0		-11.9 ± 0.3	
16	27.2	yes	306.0 ± 4.0	yes	-9.9 ± 0.4	yes
17	4.7		94.0 ± 11.5		-12.0 ± 0.3	
18	7.1		116.0 ± 7.5		-11.8 ± 0.3	
19	2.2		100.0 ± 11.0		-11.9 ± 0.3	yes
20	8.2		137.0 ± 16.5		-11.6 ± 0.3	
22	327.3	yes	312.0 ± 4.5	yes	-9.9 ± 0.4	yes
23	5.2		183.0 ± 16.0		-11.1 ± 0.4	yes
24	10.6		115.0 ± 6.0		-11.8 ± 0.3	
25	7.0		112.0 ± 7.0		-11.8 ± 0.3	
27	36.6		137.0 ± 5.5		-11.6 ± 0.3	
47	9.8		104.0 ± 8.0		-11.9 ± 0.3	yes
48	3.4		159.0 ± 7.0		-11.3 ± 0.3	
49	44.7	yes	224.0 ± 19.5	yes	-10.7 ± 0.4	yes
50	147.2	yes	385.0 ± 6.5	yes	-9.2 ± 0.4	yes
51	11.5		125.0 ± 6.0		-11.7 ± 0.3	
52	130.8	yes	289.0 ± 4.0	yes	-10.1 ± 0.4	
54	26.8	yes	501.0 ± 6.0	yes	-8.0 ± 0.5	yes
58	10.7		139.0 ± 11.0		-11.5 ± 0.3	yes
59	255.6	yes	264.0 ± 8.0	yes	-10.3 ± 0.4	
62	22.3	yes	431.0 ± 10.5	yes	-8.7 ± 0.4	yes
65	17.7		463.0 ± 27.5	yes	-8.4 ± 0.5	yes
66	23.6		181.0 ± 6.0		-11.1 ± 0.3	
67	9.4		149.0 ± 6.0		-11.4 ± 0.3	
70	11.9		123.0 ± 6.5		-11.7 ± 0.3	
71	−0.7		167.0 ± 24.0		-11.3 ± 0.4	
76	97.8	yes	348.0 ± 4.5	yes	-9.5 ± 0.4	
77	23.7	yes	504.0 ± 9.0	yes	-8.0 ± 0.5	
78	333.6	yes	283.0 ± 7.0	yes	-10.1 ± 0.4	
79	6.4		171.0 ± 9.5		-11.2 ± 0.3	
80	26.8	yes	182.0 ± 4.5		-11.1 ± 0.3	
81	10.5		236.0 ± 6.0	yes	-10.6 ± 0.3	
82	68.8	yes	389.0 ± 6.0	yes	-9.1 ± 0.4	yes
83	71.8	yes	440.0 ± 5.5	yes	-8.6 ± 0.4	
84	267.2	yes	450.0 ± 6.5	yes	-8.5 ± 0.4	yes
85	139.2	yes	261.0 ± 3.5	yes	-10.4 ± 0.3	
86	41.0	yes	486.0 ± 6.0	yes	-8.2 ± 0.5	yes
87	58.3	yes	229.0 ± 5.0	yes	-10.7 ± 0.3	
88	121.7	yes	498.0 ± 4.0	yes	-8.1 ± 0.5	yes
89	7.5		156.0 ± 6.0		-11.4 ± 0.3	
90	11.4	yes	344.0 ± 6.5	yes	-9.5 ± 0.4	
91	38.7	yes	395.0 ± 6.5	yes	-9.1 ± 0.4	
92	26.4	yes	432.0 ± 4.0	yes	-8.7 ± 0.4	yes
93	117.0	yes	379.0 ± 3.0	yes	-9.2 ± 0.4	

4

A *Spitzer* Survey of Proto-planetary Disk Dust in the Young Serpens Cloud: How do Dust Characteristics Evolve with Time?

We present *Spitzer* InfraRed Spectrograph (IRS) mid-infrared (5–35 μm) spectra of a complete flux-limited sample (≥ 3 mJy at 8 μm) of young stellar object (YSO) candidates selected on the basis of their infrared colors in the Serpens Molecular Cloud. Spectra of 147 sources are presented and classified. Background stars (with slope consistent with a reddened stellar spectrum and silicate features in absorption), galaxies (with redshifted polycyclic aromatic hydrocarbon (PAH) features), and a planetary nebula (with high ionization lines) amount to 22% of contamination in this sample, leaving 115 true YSOs. Sources with rising spectra and ice absorption features, classified as embedded Stage I protostars, amount to 18% of the sample. The remaining 82% (94) of the disk sources are analyzed in terms of spectral energy distribution shapes, PAHs, and silicate features. The presence, strength, and shape of these silicate features are used to infer disk properties for these systems. About 8% of the disks have 30/13 μm flux ratios consistent with cold disks with inner holes or gaps, and 3% of the disks show PAH emission. Comparison with models indicates that dust grains in the surface of these disks have sizes of at least a few μm. The 20 μm silicate feature is sometimes seen in the absence of the 10 μm feature, which may be indicative of very small holes in these disks. No significant difference is found in the distribution of silicate feature shapes and strengths between sources in clusters and in the field. Moreover, the results in Serpens are compared with other well-studied samples: the c2d IRS sample distributed over five clouds and a large sample of disks in the Taurus star-forming region. The remarkably

similar distributions of silicate feature characteristics in samples with different environment and median ages – if significant – imply that the dust population in the disk surface results from an equilibrium between dust growth and destructive collision processes that are maintained over a few million years for any YSO population irrespective of environment.

Isa Oliveira, Klaus M. Pontoppidan, Bruno Merín, Ewine F. van Dishoeck,
Fred Lahuis, Vincent C. Geers, Jes K. Jørgensen, Johan Olofsson,
Jean-Charles Augereau, Joanna M. Brown

4.1   Introduction

Newly formed stars are observed to have infrared (IR) excess due to their circumstellar disk composed of dust and gas (Strom 1992; Hillenbrand 2008). Most older main-sequence (MS) stars, on the other hand, have photospheric emission with no excess in the IR. It is intuitive to conclude that the circumstellar disk evolves with time, gradually getting rid of the IR excess. One of the main questions in stellar astrophysics is how this happens.

Observational studies, as well as theoretical simulations, have demonstrated the interaction between star and disk. The stellar radiation facilitates disk evolution in terms of photoevaporation (e.g., Richling & Yorke 2000; Alexander et al. 2006; Alexander 2008; Gorti & Hollenbach 2009) or dust growth and settling (e.g., Weidenschilling 1980; Sterzik et al. 1995; Dominik & Tielens 1997; Dullemond & Dominik 2005; Johansen et al. 2008). In the other direction, mass is accreted from the disk to the star following magnetic field lines (e.g., Muzerolle et al. 2003; White & Basri 2003; Natta et al. 2004). A diversity of stellar temperatures, luminosities, and masses among young stars has been known and studied for decades. Facilitated by new IR and (sub-)millimeter observations, a great variety of disk shapes, structures, and masses is now being actively studied. The next step is to try to connect stellar and disk characteristics in order to understand the evolution of these systems.

The study of a single object, however, is unlikely to provide unambiguous information regarding the evolutionary stage of the associated disk. Most studies to date refer to samples of young stars scattered across the sky, or to sources distributed across large star-forming clouds like Taurus. In addition to evolutionary stage, the specific environment in which the stars are formed may influence the evolution of disks by dynamical and radiative interaction with other stars or through the initial conditions of the starting cloud, making it difficult to separate the evolutionary effects (e.g., Richling & Yorke 1998, 2000). For this reason, clusters of stars are very often used as laboratories for calibrating the evolutionary sequence (e.g., Lada & Lada 1995; Haisch et al. 2001). The power of this method, to gain statistical information on disk composition in coeval samples, was found to be very successful for loose associations of older, pre-MS stars such as the 8 Myr old η Cha (Bouwman et al. 2006) and the 10 Myr old TW Hydrae association (Uchida et al. 2004). Identifying clusters of even younger disk populations is a natural step toward the completion of the empirical calibration of the evolution of disks surrounding young low-mass stars. This paper analyzes the inner disk properties of a flux-limited, complete unbiased sample of young stars with IR excess in the Serpens Molecular Cloud ($d = 259 \pm 37$ pc; Straizys et al. 1996) which has a mean age ~ 5 Myr (Oliveira et al. 2009) with an YSO population in clusters and also in isolation. It has been recently argued (L. Loinard, private communication) that the distance to Serpens could be considerably higher than previously calculated. This would imply a rather younger median age for this cloud.

The *Spitzer* Legacy Program "From Molecular Cores to Planet-Forming Disks" (c2d) has uncovered hundreds of objects with IR excess in five star-forming clouds

(Cha II, Lupus, Ophiuchus, Perseus, and Serpens), and allowed statistical studies within a given cloud (Evans et al. 2009). The c2d study of Serpens with Infrared Array Camera (IRAC, 3.6, 4.5, 5.8 and 8.0 μm, Fazio et al. 2004) and MIPS (24 and 70 μm; Rieke et al. 2004) data has revealed a rich population of mostly previously unknown young stellar objects (YSOs) associated with IR excess, yielding a diversity of disk spectral energy distributions (SEDs; Harvey et al. 2006, 2007a,b). Because of the compact area in Serpens mapped by *Spitzer* (0.89 deg^2), this impressive diversity of disks presents itself as an excellent laboratory for studies of early stellar evolution and planet formation. Indeed, the Serpens core (Cluster A, located in the northeastern part of the area studied by c2d) has been well studied in this sense (e.g., Zhang et al. 1988; Eiroa & Casali 1992; Testi & Sargent 1998; Kaas et al. 2004; Eiroa et al. 2005; Winston et al. 2007, 2009), whereas only some of the objects in Group C (formerly known as Cluster C) were studied with ISOCAM data (Djupvik et al. 2006).

Because of its wavelength coverage, sensitivity, and mapping capabilities, the *Spitzer Space Telescope* has offered an opportunity to study many of these systems (star+disk) in unprecedented detail. *Spitzer*'s photometry in the mid-IR, where the radiation reprocessed by the dust is dominant, gives information on the shape of the disks and, indirectly, its evolutionary stage (assuming an evolution from flared to flat disks). Follow-up mid-IR spectroscopic observations with the InfraRed Spectrograph (IRS, 5 – 38 μm; Houck et al. 2004) on-board *Spitzer* probe the physical and chemical processes affecting the hot dust in the surface layers of the inner regions of the disk. The shapes and strengths of the silicate features provide information on dust grain size distribution and structure (e.g., van Boekel et al. 2003; Przygodda et al. 2003; Bouwman et al. 2008; Kessler-Silacci et al. 2006, 2007; Geers et al. 2006; Watson et al. 2009; Olofsson et al. 2009). These, in turn, reflect dynamical processes such as radial and vertical mixing, and physical processes such as annealing. A smooth strong Si–O stretching mode feature centered at 9.8 μm is indicative of small amorphous silicates (like those found in the interstellar medium (ISM)) while a structured weaker and broader feature reveals bigger grains or the presence of crystalline silicates. Polycyclic aromatic hydrocarbon (PAH) features are a probe of the UV radiation incident on the disk, whereas their abundance plays a crucial role in models of disk heating and chemistry (e.g., Geers et al. 2006; Dullemond et al. 2007; Visser et al. 2007). The shape and slope of the mid-infrared excess provides information on the flaring geometry of the disks (Dullemond & Dominik 2004), while ice bands may form for highly inclined sources (edge-on) where the light from the central object passes through the dusty material in the outer parts of the disk (Pontoppidan et al. 2005). Thus, the wavelength range probed by the IRS spectra enables analysis of the geometry of individual disks. It also probes the temperature and dust size distributions as well as crystallinity of dust in the disk surface at radii of 0.1 – few AU. Statistical results from a number of sources help the understanding of the progression of disk clearing and possibly planet formation.

Our group has been conducting multi-wavelength observing campaigns of Serpens. Optical and near-IR wavelength data, where the stellar radiation dominates, are be-

ing used to characterize the central sources of these systems (Oliveira et al. 2009). Effective temperatures, luminosities, extinctions, mass accretion rates, as well as relative ages and masses are being determined. In this paper, we present a complete flux-limited set of *Spitzer* IRS spectra for this previously unexplored young stellar population in Serpens. We analyze these spectra in terms of common and individual characteristics and compare the results to those of Taurus, one of the best studied molecular clouds to date and dominated by isolated star formation. A subsequent paper will deal with the full SED fitting for the disk sources in Serpens and their detailed analyses. Our ultimate goal is to statistically trace the evolution of young low-mass stars by means of the spectroscopic signatures of disk evolution, discussed above.

Section 4.2 describes our *Spitzer* IRS data. In Section 4.3, we divide our sample into categories based on their IRS spectra: the background contaminants are presented in Section 4.3.1 separated according to the nature of the objects; embedded sources are presented in Section 4.3.2, and disk sources in Section 4.3.3 (with emphasis on PAH and silicate emission). In Section 4.4, we discuss disk properties in relation to environment and to another cloud, Taurus, for comparison. In Section 4.5, we present our conclusions.

4.2 *Spitzer* IRS Data

4.2.1 Sample Selection

Harvey et al. (2007b) describe the selection criteria used by the c2d team to identify YSO candidates based on the *Spitzer* IRAC and MIPS data, band-merged with the Two Micron All Sky Survey (2MASS) catalog. They used a number of color–color and color–magnitude diagrams to separate YSOs (both embedded YSOs and young stars with disks) from other types of sources, such as background galaxies and stars. In this manner, a set of 235 YSOs was identified in Serpens, in both clusters and in isolation, as described in Section 4.4.1. These criteria, however, are not fail-proof. Harvey et al. (2007b) treated this problem very carefully in a statistical sense, but the locus region for YSOs and, for instance, background galaxies overlap somewhat in color–color diagrams with *Spitzer* photometry. Therefore, some contamination may well still be present in the sample which was impossible to disentangle from photometry alone.

An additional criterion was applied to this sample in order to guarantee IRS spectra with sufficient quality to allow comparative studies of solid-state features, namely signal-to-noise (S/N) ≥ 30 on the continuum. A lower limit flux cutoff of 3 mJy at 8μm was imposed. This flux limit ensures coverage down to the brown dwarf limit ($L \sim 0.01\ L_{\odot}$) and leads to a final sample of 147 objects, the same as in Oliveira et al. (2009). This is a complete flux-limited sample of IR excess sources in the c2d mapped area, except in the Serpens core. It is also important to note that this sample, by definition, does not include young stars without IR excess (Class III).

Figure 4.1 shows the distribution of our observed objects in the Serpens Molecular Cloud. Table 4.1 lists the sample together with their 2–24 μm spectral slope.

4.2.2   Observations and Data Reduction

Out of the 147 objects in this sample, 22 were observed between 2004 September and 2006 June, as part of the c2d IRS 2nd Look campaign. The reduced high resolution spectra ($R = \lambda/\Delta\lambda = 600$; Short High (SH), 9.9 – 19.6 μm and Long High (LH), 18.7 – 37.2 μm), complemented with Short Low spectra (SL, $R = 50 - 100$; 5.2 – 14.5 μm) are public to the community through the c2d delivery web Site (Evans et al. 2007). The other 125 targets were observed as part of a *Spitzer Space Telescope*'s cycle 3 program (GO3 30223, PI: Pontoppidan) in the low resolution module (SL and Long Low (LL), 14.0 – 38.0 μm) in 35 AORs, between 2006 October and 2007 April.

All objects were observed in IRS staring mode and extracted from the SSC pipeline (version S12.0.2 for the c2d IRS 2nd look program, and version S15.3.0 for the GO3 program) basic calibration data (BCD) using the c2d reduction pipeline (Lahuis et al. 2006). This process includes bad-pixel correction, optimal point-spread function (PSF) aperture extraction, defringing and order matching. Technical information about each object can be found in Table 4.1.

4.3   Results

The large number of objects studied here allows statistical studies of each stage of disk evolution in a single star-forming region. By simply looking at the spectra, a diversity of spectral shapes can be noted immediately. This diversity of objects can be divided into several categories, each of which is thought to be related to a different evolutionary stage of the star+disk system, described below.

4.3.1   Background Sources

Due to the low galactic latitude of Serpens (l=030.4733, b=+05.1018) the contamination by galactic background sources is expected to be higher for this region than for other studied star-forming regions (e.g., Taurus, Lupus, Chamaeleon). With the help of the IRS spectra, background contaminants can readily be identified, even when seen through a large column density of molecular cloud material. These are presented and discussed in Appendix A.

To further study the YSOs, the 32 contaminants are removed from the sample, which then consists of 115 objects for further analysis.

4.3.2   Embedded Sources

A newly formed protostar, still embedded in an envelope of gas and dust, will show an excess in the mid-IR that rises with wavelength. In this cold environment, a significant fraction of the molecules are found in ices. Many of these ices are observed
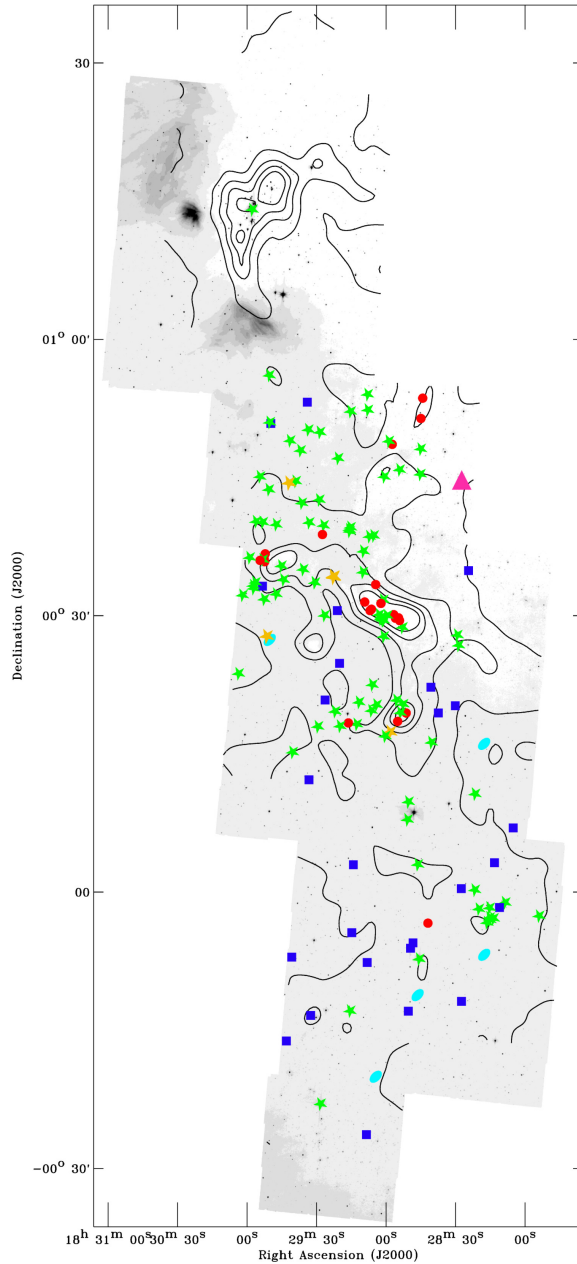
Figure 4.1 – Observed objects over-plotted on the c2d IRAC4 (8.0 μm) map of Serpens. The contours (5, 10, 15, 20, and 25 mag) of visual extinction are derived from the c2d extinction maps (Evans et al. 2007). Squares are background stars, ellipses are redshifted galaxies, circles are embedded sources, and stars represent disks. The triangle is the PN candidate (see Section A.3 for details). (A color version of this figure is available in the online journal)
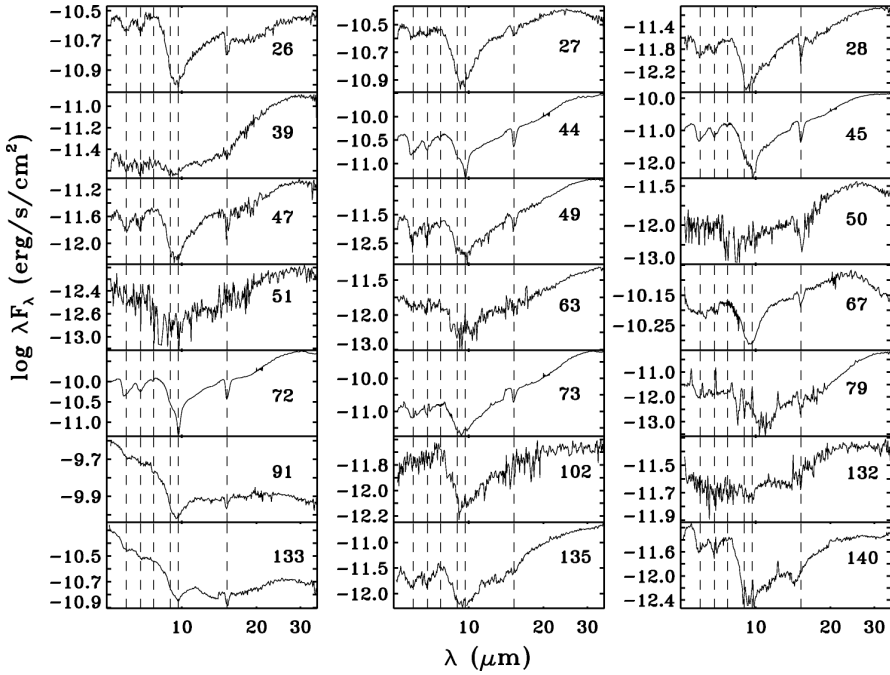
Figure 4.2 − IRS spectra of the embedded sources in Serpens with rising mid-IR spectra. The prominent ice absorption features (at 6.0, 6.85, 7.7, 9.0 and 15.2 μm) are marked, together with the silicate absorption feature at 9.7 μm. The object number is indicated at the top right of each panel.

as absorption features in the wavelength range of the IRS instrument (e.g., Boogert et al. 2004).

Of our sample, 21 sources have spectra consistent with embedded sources. These spectra are shown in Figure 4.2. The most prominent ice feature, CO_2 at 15.2 μm, can readily be seen in all spectra. Weaker features, such as H_2O at 6.0 and 6.85 μm and CH_3OH at 9.7 μm, need high S/N. Those features are detected in objects 26, 27, 28, 44, 45, 47, 49, 67, 72, 73, 135 and 140. As can be seen in Figure 4.1, the embedded objects seem to be concentrated in high extinction regions ($A_V \sim 10 - 15$ mag).

The embedded objects observed as part of the c2d IRS 2nd Look Program have been studied in detail in a series of papers on ices around YSOs (H_2O in Boogert et al. 2008; CO_2 in Pontoppidan et al. 2008; CH_4 at 7.7 μm in Öberg et al. 2008; and NH_3 at 9.0 μm and CH_3OH in Bottinelli et al. 2010) and are not discussed further in this paper.
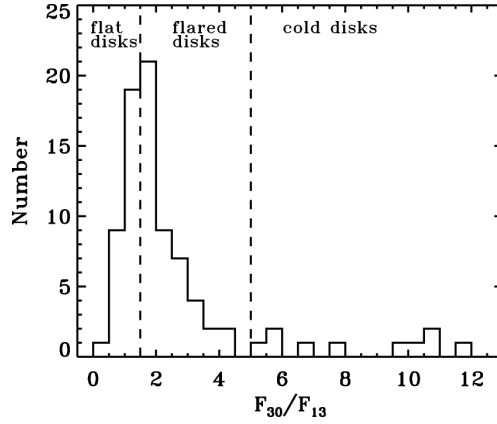
Figure 4.3 – Distribution of the flux ratio between 30 and 13 μm, used as a proxy for disk geometry.

4.3.3 Disk Sources

YSOs with IR excess that have a flat or negative slope in the near- to mid-IR are identified as disk sources. Following Greene et al. 1994 and Evans et al. 2009, flat sources have $-0.3 \leq \alpha_{2\mu m - 24\mu m} \leq 0.3$, Class II sources have $-1.6 \leq \alpha_{2\mu m - 24\mu m} \leq -0.3$, and Class III sources have $\alpha_{2\mu m - 24\mu m} \leq -1.6$. Many of these sources also have silicate emission bands and a few show PAH features. In the following, these different features are analyzed and discussed in detail for the total of 94 disk sources.

4.3.3.1 Disk Geometry: F_{30}/F_{13} and Cold Disks

Disk geometry is inferred from the flux ratio between 30 and 13 μm (F_{30}/F_{13}). High ratios ($F_{30}/F_{13} \gtrsim 15$) yield edge-on disks, intermediate values ($5 \lesssim F_{30}/F_{13} \lesssim 15$ and $1.5 \lesssim F_{30}/F_{13} \lesssim 5$) identify cold disks and flared disks with considerable excess in the IR, respectively, and low ratios ($F_{30}/F_{13} \lesssim 1.5$) select flat, settled disks with little IR excess (Brown et al. 2007; Merín et al. 2010). Figure 4.3 shows the distribution of F_{30}/F_{13} for the disk population in Serpens.

Cold disks, sometimes referred to as transitional disks, as studied in Brown et al. (2007) and Merín et al. (2010), present a peculiar SED, with inner gaps or holes producing a region with no IR excess in the near- to mid-IR but a substantial excess at mid- to far-IR wavelengths. Binaries (Ireland & Kraus 2008), planet formation (Quillen et al. 2004; Varnière et al. 2006) and photoevaporation (Clarke et al. 2001; Alexander et al. 2006) are some of the suggested mechanisms for this removal of warm dust.

Following Brown et al. (2007), F_{30}/F_{13} is used to differentiate cold disks from the general disk population. Those wavelengths were chosen to avoid the silicate features and to probe the spectra steeply rising at mid- to far-IR following a deficit at shorter

Figure 4.4 – IRS spectra of the cold disks in Serpens. Object number is indicated in each panel. In gray are the original spectra, while in black a binned version is overplotted. The dotted line represents the stellar photosphere, for comparison.

wavelengths, characteristic of cold disks. Eight objects (9, 21, 69, 82, 90, 113, 114, and 122) in this sample are classified as cold disks based on $5 \lesssim F_{30}/F_{13} \lesssim 15$, corresponding to 8.5% of the disk population. These spectra are shown in Figure 4.4. For clarity, the original spectra are shown in gray, while in black a binned version is overplotted. The binning was done using a Savitzky-Golay (Savitzky & Golay 1964) filter of order 0 and degree 3, for illustrative purposes only. This is the most unbiased survey of cold disks to date, based entirely on spectroscopy in the critical mid-IR range, and should thus give a representative fraction of such disks. These objects are also part of a larger cold disk sample, studied by Merín et al. (2010), where the authors have selected cold disks from photometric criteria in all five c2d clouds.

4.3.3.2   PAH Emission

PAHs are large molecules whose emission is excited by UV radiation out to large distances from the star. Thus, these features are good diagnostics of the amount of stellar UV intercepted by the disk surface.

Almost half of the sample of Herbig Ae/Be stars (young stars of intermediate masses) studied by Meeus et al. (2001) and Acke & van den Ancker (2004) show PAH emission. Geers et al. (2006), on the other hand, show that PAH emission is not as common among low-mass YSOs as it is for more massive stars. The authors argue that the lack of features is not only due to their weaker UV radiation fields, but also to a lower PAH abundance compared with the general ISM.

In the current sample, five sources have clear PAH emission, presented in Figure 4.5. Although a great variation in shapes and strengths is seen, all sources show the features at 6.2, 7.7, 8.6, 11.2 and 12.8 μm. Objects 52, 97, and 131 also show a feature that could be the PAH band at 16.4 μm, although the feature does not match perfectly in position.

The central stars in these five sources were studied with optical spectroscopy in Oliveira et al. (2009). Spectral types and luminosities were derived, yielding ages and
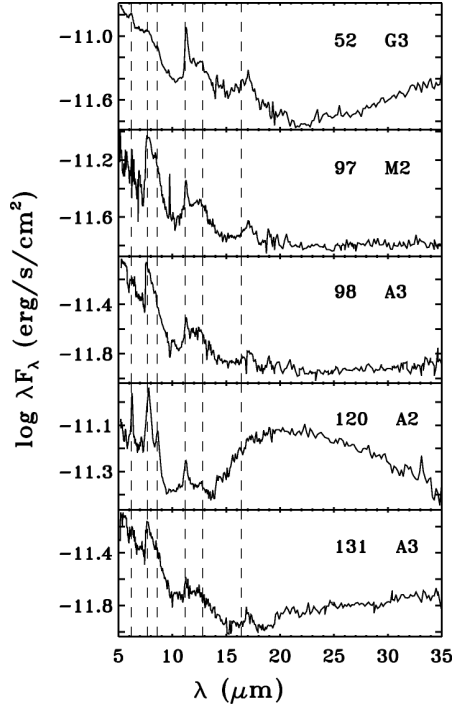
Figure 4.5 − IRS spectra of the disk sources which show clear PAH features. The dashed lines indicate the positions of the most prominent bands (at 6.2, 7.7, 8.6, 11.2, 12.8 and 16.4 μm). The object number and its spectral type (from Oliveira et al. 2009) are indicated at the top right of each panel. Note that the ratios of different line strengths differ between sources.

masses for each object. Objects 52, 98, 120, and 131 have masses between 1.9 and 2.7 $M_\odot$ (spectral type G3 to A2), while object 97 has lower mass, of around 0.45 $M_\odot$ (M2). Objects 97 and 98 are spatially very close to each other and have very similar PAH features. IRAC Band 4 (8 μm) images show that there is extended nebulosity surrounding both positions so that the PAHs are likely associated with this nebula rather than the disks.

Discarding these 2 sources, this sample indicates that PAHs are present in 3.2% of the disk population studied, which is below the 11%–14% of PAH detection rate found by Geers (2007). This discrepancy could be due to the two samples being differently selected, with the current sample having a larger fraction of late-type stars. The percentage of PAHs present in disks in Serpens is, however, very comparable with that in Taurus (4% of the disk population, Section 4.4.3).

Interestingly, none of the cold disks show PAHs, different from expected if grain settling enhances PAH features (Dullemond et al. 2007) and observed for other cold disk samples studied which do show PAHs (Brown et al. 2007; Merín et al. 2010). In

addition, the objects with PAH emission have standard F_{30}/F_{13} flux ratios, falling in the 'flat' and 'flared' regions of Figure 4.3.

Only object 120 shows a silicate feature (at 20 μm, as discussed in Section 4.3.3.3), in addition to PAHs. This alludes to an anti-correlation between PAHs and silicates that could be simply explained in terms of contrast, i.e., it is hard to detect PAH features when a strong 10 μm silicate feature is present (Geers et al. 2006). In this sense, PAHs should be more easily detected in disks without silicates, since the falling spectrum provides an increase in the feature to continuum ratio improving contrast.

4.3.3.3   Silicate Emission

Silicate emission has been observed around numerous circumstellar disks (e.g., van Boekel et al. 2003; Przygodda et al. 2003; Kessler-Silacci et al. 2006; Furlan et al. 2006; Bouwman et al. 2008; Olofsson et al. 2009). Some of this material has different characteristics in disks compared to primitive interstellar material. The strength and the shape of silicate features (at 10 and 20 μm) contain important information on the dust sizes in the surface layer of the disk. The 89 disk sources in this sample were inspected for their silicate characteristics. Their spectra can be seen in Figures 4.6–4.8 (completed with Figures 4.4 and 4.5), arranged in order of decreasing strength of the 10 μm feature and decreasing $\alpha_{2-24\mu m}$ spectral slope. No extinction correction has been applied to these spectra (see Section 4.3.3.5).

Five of these sources (5% of the disk population) have spectra that are featureless, i.e., they have neither the 10 nor the 20 μm silicate features in emission, although they present IR excess (objects 38, 42, 59, 83, and 87). It is found that when the 10 μm feature appears, the 20 μm band is also present (by visual inspection of the continuum-subtracted spectra, see Section 4.3.3.4). The contrary is not true, as objects 13, 20, 24, 32, 62, 64, 69, 70, 109, 116, 127, 139, 143 and 145 have an observed 20 μm feature but no apparent 10 μm feature (also reported by Kessler-Silacci et al. (2006) for T Cha, SR21 and HD 135344B). Also, object 120 shows the 20 μm band and no 10 μm feature, as this region is dominated by PAH features in this source (see Section 4.3.3.2). When present, the 10 μm feature ($S_{\mathrm{peak}}^{10\mu m}$) is usually stronger than the 20 μm ($S_{\mathrm{peak}}^{20\mu m}$) one as is common in disk sources.

Crystalline silicate features (as discussed by, e.g., Bouwman et al. 2001, 2008; Acke & van den Ancker 2004; van Boekel et al. 2004; Apai et al. 2005; Olofsson et al. 2009; Sargent et al. 2009) are seen in several sources. A detailed analysis in terms of statistics and crystalline fraction of these features is non-trivial and beyond the scope of this paper, but will be subject of a future publication.

4.3.3.4   The Silicate Strength-Shape Relation

As first shown for Herbig Ae stars (van Boekel et al. 2003), there is a dependence between grain size and silicate shape and strength for both 10 and 20 μm features: as the sizes of the grains grow, the silicate features appear more and more flattened
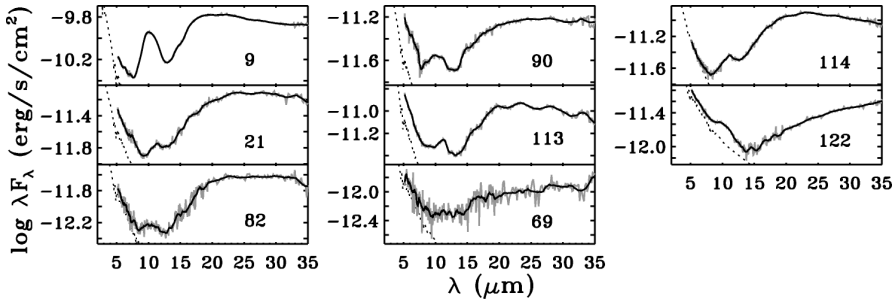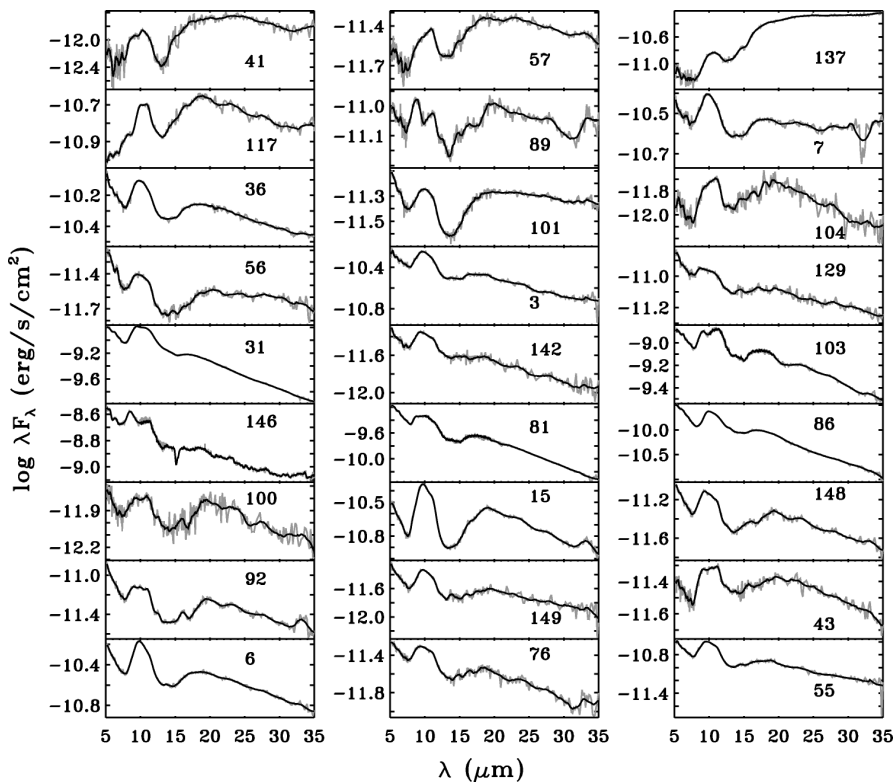
Figure 4.6 – IRS spectra of the disk sources in Serpens. Object number is indicated in each panel. In gray are the original spectra, while in black a binned version (using a Savitzky–Golay (Savitzky & Golay 1964) filter of order 0 and degree 3) is overplotted.

and shift to longer wavelengths.

A statistical analysis of these two features can be done using the following quantities: $S_{\text{peak}}^{10\mu m}$ is a measure of the strength of the feature centered at 10 μm and $S_{11.3}/S_{9.8}$ is a proxy for the shape of the feature (the smaller this value, the more peaked the feature is); $S_{\text{peak}}^{20\mu m}$ measures the strength of the 20 μm feature, while $S_{23.8}/S_{19}$ is a proxy for this feature shape. Following Kessler-Silacci et al. (2006), S_λ is defined as:

$$S_\lambda = 1 + \frac{1}{2\delta} \int_{\lambda-\delta}^{\lambda+\delta} \frac{F_\lambda - C_\lambda}{C_\lambda} \, d\lambda. \tag{4.1}$$

In this paper, we use $\delta = 0.1 \, \mu$m.

Kessler-Silacci et al. (2006) found a global trend (best fit to observations) for both features (Figure 9 in their paper and Figure 4.9 in this one), indicating that the feature shape and strength are physically related, as expected if the silicate features
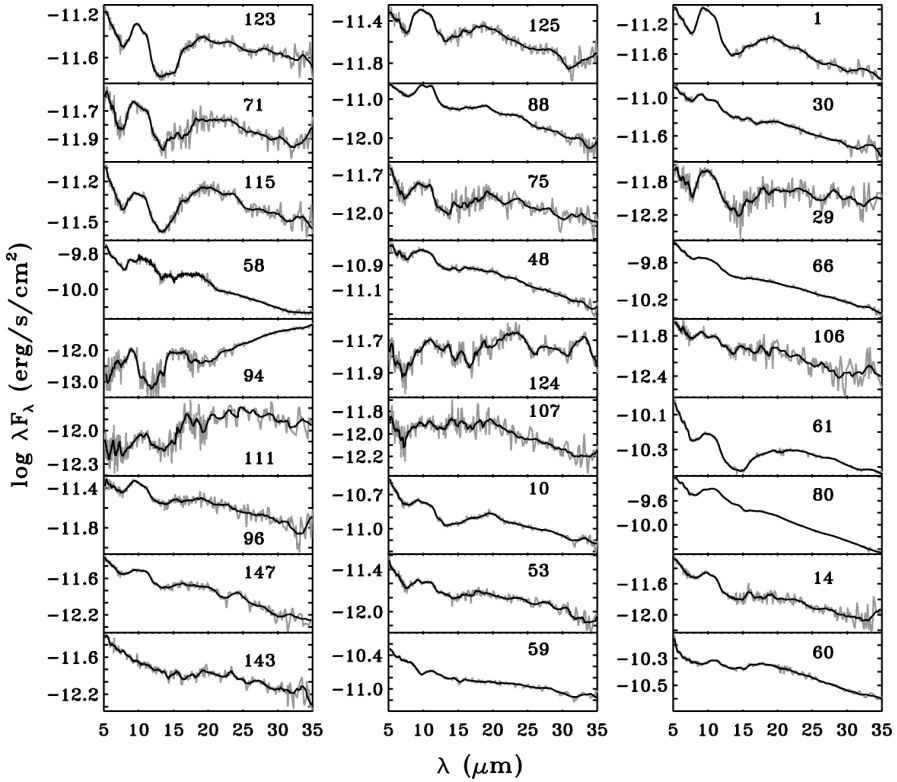
Figure 4.7 − IRS spectra of the disk sources in Serpens, contd.

are indeed tracers of grain size. The relationship is much tighter for the 10 μm feature, as also seen by the great spread in the correlation for the 20 μm feature.

Following their procedure, we first subtracted the continuum of each spectrum by fitting a second-order polynomial to the following regions: blueward of the 10 μm feature, between the 10 and the 20 μm features, and redward of the 20 μm feature (6.8–7.5, 12.5–13.5 and 30–36 μm). The peak fluxes at 9.8, 10, 11.3, 19, 20, and 23.8 μm were then determined (see Table 4.2). Figure 4.9 shows the results for our sample of disks, excluding those with PAH emission. The best fit found by Kessler-Silacci et al. (2006) for the c2d IRS first look sample of YSOs has been indicated for comparison (solid line). The agreement of the Serpens data with the best fit of Kessler-Silacci et al. (2006) is excellent, and more evident for the 10 μm than for the 20 μm feature due to the larger scatter in the latter group.

Olofsson et al. (2009) generated synthetic 10 μm features calculated for different grain sizes and compositions. Their models are generated for amorphous silicates of olivine and pyroxene stoichiometry and a 50:50 mixture, with grain size varying
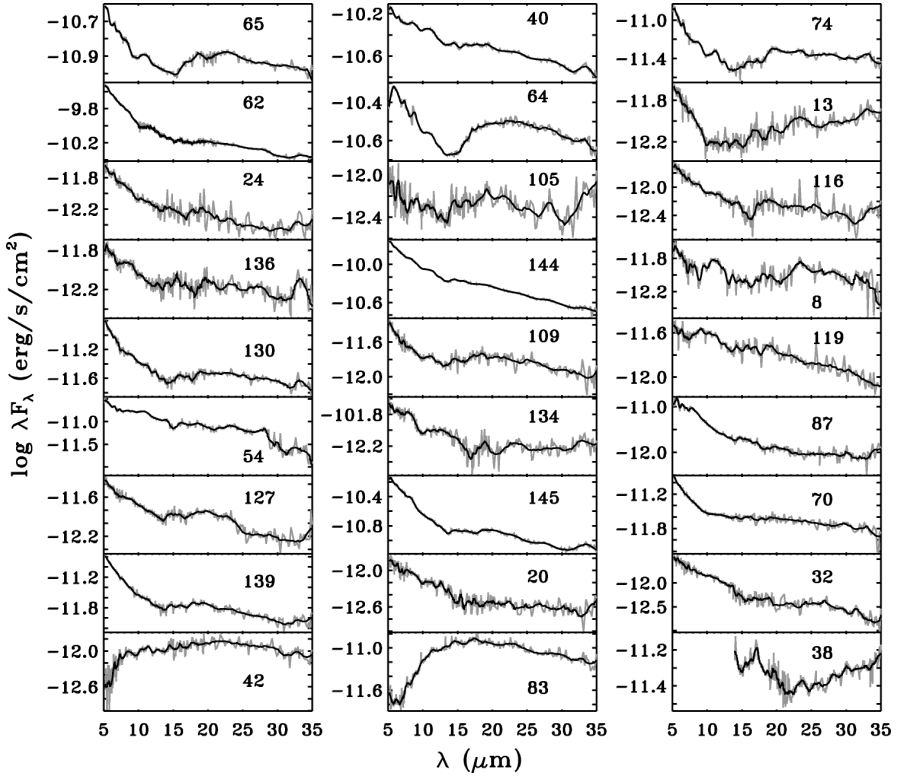
Figure 4.8 – IRS spectra of the disk sources in Serpens, contd.

between 0.1 and ∼6 μm. Those models are overplotted in the left panel of Figure 4.9, with open symbols corresponding to different grain sizes. The comparison of the data presented here with these models shows that the majority of our sample lies in a region consistent with an opacity dominated by grains with sizes larger than 2.0 μm, having no features consistent with grain sizes smaller than 1.5 μm. A considerable fraction of the sample is consistent with grains as large as 6 μm (the largest grain size modeled). The precise sizes depend on composition and treatment of the opacities, but sizes of a few μm are clearly implicated. It is important to note that crystallinity also affects the shape of silicate features. However, as shown by Apai et al. (2005) and Olofsson et al. (2009), the effect of crystallinity is orthogonal to that of grain sizes in the strength versus shape plot (Figure 4.9). Grain sizes are found to be the dominant parameter changing the shape of the 10 μm silicate feature, whereas crystallinity introduces scatter (Figure 13 of Olofsson et al. 2009).

All cold disks present silicate features in emission. According to the models of grain sizes (the left panel of Figure 4.9), the cold disks in this sample have grains bigger than 2.7 μm, with the bulk of the sample presenting grains as big as 6.0 μm,
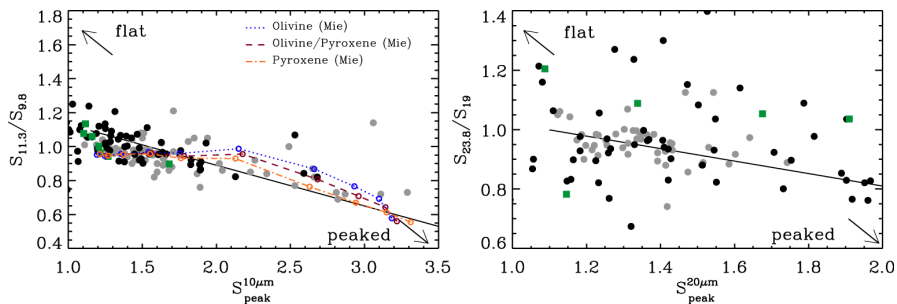
Figure 4.9 – In the left panel, black dots show the ratio of peaks at 11.3 to 9.8 μm ($S_{11.3}/S_{9.8}$) plotted against the peak at 10 μm ($S_{\mathrm{peak}}^{10\mu m}$). In the right panel, the ratio of peaks at 23.8 to 19 μm ($S_{23.8}/S_{19}$) is plotted against the peak at 20 μm ($S_{\mathrm{peak}}^{20\mu m}$). The best fit found by Kessler-Silacci et al. (2006) for the c2d IRS first look sample of YSOs (gray dots) has been indicated for comparison (solid black line). Dark gray squares are the cold disks in this sample (see Section 4.3.3.1). Colored curves are derived from theoretical opacities for different mixtures by Olofsson et al. (2009). The open circles correspond to different grain sizes, from left to right 6.25, 5.2, 4.3, 3.25, 2.7, 2.0, 1.5, 1.25, 1.0 and 0.1 μm. Typical uncertainties for peak strengths are ∼0.1, while typical uncertainties for the peak ratios are ∼0.12. (A color version of this figure is available in the online journal)

according to these models.

4.3.3.5   Effects of Extinction

The amount of foreground extinction is, for some sources, substantial enough to affect the appearance of silicate emission features in the mid-infrared. Because the extinction law has strong resonances from silicates, the strength and shape of any silicate emission feature may be significantly affected if a large column of cloud material is present in front of a given source. Here, the potential effects of extinction on statistical results, such as those presented in Figure 4.9, are discussed.

The model presented by Weingartner & Draine (2001) for an absolute to selective extinction of $R_V = 5.5$ has been found to be a reasonable match to the observed dark cloud extinction law (Chapman et al. 2009; McClure 2009; Chapman & Mundy 2009), and it is assumed that this law holds for Serpens. One caveat is the lack of resonances due to ices in this model, but given other uncertainties in the determination of extinction laws, this is probably a minor contribution for the purposes of this work.

The opacity caused by a silicate resonance is defined as (e.g., Draine 2003)

$$\Delta\tau_\lambda = \tau_\lambda - \tau_C, \qquad (4.2)$$

where τ_C is the optical depth of the "continuum" opacity without the silicate resonance. The relation between optical extinction and $\Delta\tau$ is, using the fact that the optical depth is proportional to the extinction coefficient C^{ext}:
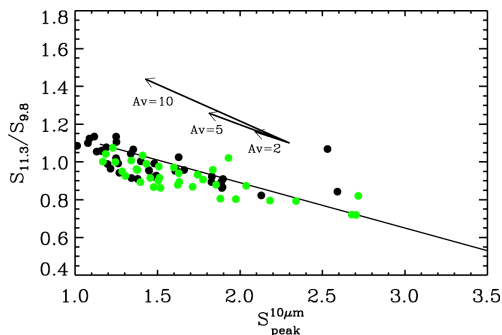
Figure 4.10 − Comparison between the observed values (in black) and the extinction corrected values (in gray) for the 10 μm silicate feature. The arrows give an indication of the effects of extinction on the feature, however their length depends on the starting point (see the text for details). (A color version of this figure is available in the online journal)

$$\frac{A_V}{\Delta\tau_\lambda} = \frac{\tau_V}{0.921\Delta\tau_\lambda} = \frac{C_V^{\mathrm{ext}}}{0.921\Delta C_\lambda^{\mathrm{ext}}} \equiv X_\lambda \,\mathrm{mag}. \tag{4.3}$$

Using Equations 4.1 and 4.3 and by approximating $\delta \to 0$, the silicate strength corrected for extinction is

$$S_\lambda^{\mathrm{corr}} \sim \frac{S_\lambda}{\exp(-\Delta\tau_\lambda)} = \frac{S_\lambda}{\exp(-A_V/X_\lambda)} \tag{4.4}$$

For the $R_V = 5.5$ extinction law of Weingartner & Draine (2001), the relevant values for X_λ are 19.6, 20.9, and 41.6 mag for 9.8, 10.0, and 11.3 μm, respectively.

Using this relationship, it is possible to correct the position of sources with known values for A_V in Figure 4.9. Oliveira et al. (2009) measured A_V values for 49 of the 89 disks studied here albeit with some uncertainty. The resulting extinction-corrected strength-shape distribution is shown in Figure 4.10 (in green) and compared with the uncorrected distribution (in black). It is seen that extinction moves points along curves that are almost parallel to the relation between shape and strength. Most points, having $A_V < 5$ mag, are not changed enough to alter the slope of the relation, and the median strength is unaffected. However, a few highly extincted disks are corrected by large amounts, as can be seen by the extinction arrows in Figure 4.10.

There are 40 YSOs in the sample for which Oliveira et al. (2009) do not estimate A_V. Some of these may be highly extincted ($A_V \gtrsim 10$ mag) sources (not being bright enough for optical spectroscopy using a 4-m class telescope). The correction for extinction, as derived above, would be greater for such objects, possibly introducing a displacement between the distributions of extinction corrected and uncorrected features. However, it is important to note that this assumes that the $R_V = 5.5$ extinction law is valid for the densest regions of molecular clouds. Chiar et al. (2007) recently

found that at $A_V > 10$ mag, the relationship between optical depth and extinction derived for diffuse ISM is no longer valid, possibly due to grain growth, and that $X_{9.7\,\mu m}$ is significantly larger in this regime. If true, then the Weingartner & Draine (2001) extinction law represents a "worst case" scenario. Since most of the measured extinctions are small, and given the uncertainty in extinction laws and the lack of A_V data for a significant fraction of the sample, the uncorrected silicate feature strengths are used in the remainder of the paper.

4.3.3.6   *Statistical Analysis of Silicate Features*

Figure 4.11 shows the strengths of the observed 10 and 20 μm features with no apparent correlation. To quantify a correlation, a Kendall τ rank correlation coefficient is used to measure the degree of correspondence between two populations and to assess the significance of said correspondence. In other words, if there is a correlation (anti-correlation) between two data sets, the Kendall τ rank coefficient is equal to 1 (-1). If the data sets are completely independent, the coefficient has value 0. For the strengths of the 10 and 20 μm silicate features, $\tau = 0.26$, meaning at best a weak correlation.

The lack of apparent correlation between the 10 and the 20 μm features, in both strength and appearance, suggests that they are emitted by different regions in the disk. Indeed, several authors have shown that the 10 μm feature is emitted by warm dust in the inner region, while the 20 μm feature originates from a colder component, further out and deeper into the disk (e.g., Kessler-Silacci et al. 2007; Merín et al. 2007; Bouwman et al. 2008; Olofsson et al. 2009). Therefore, the absence of the 10 μm feature but presence of the 20 μm band for a given source implies that such disk lacks warmer small dust grains close to the star. This reminisce the disk around the Herbig Ae star HD 100453 studied by Meeus et al. (2002) and Vandenbussche et al. (2004), who find that the absence of the 10 μm silicate feature can be fitted with a model deprived in warm small grains. 16% of the disk sources shown in this sample fit this scenario. A possible explanation for such a scenario is that those disks have holes or gaps on such a small scale ($\lesssim 1$ AU) that the holes do not produce a strong signature in the spectra probed by our data, as the cold disks do.

4.4   Discussion

In this section we discuss the properties of the YSO sample presented in sections 4.3.2 and 4.3.3 with respect to environment, and compare the results with those for another nearby star-forming region, Taurus (Furlan et al. 2006), as well as the full c2d IRS sample (Kessler-Silacci et al. 2006; Olofsson et al. 2009).

4.4.1   Cluster Versus Field Population

Comparison of the disk properties between the cluster and field populations determines the importance of environment in the evolution of these systems. If the evo-
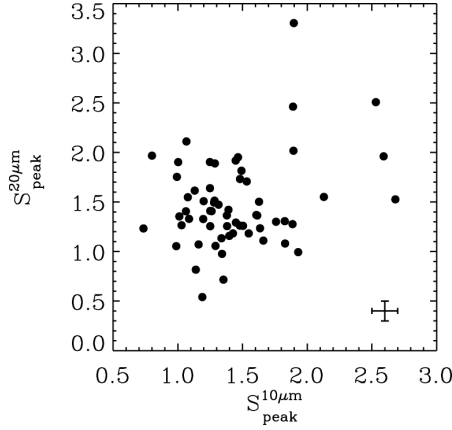
Figure 4.11 − Relative strength of the 10 vs. 20 μm silicate features. Typical error bars are shown in the bottom right corner. No obvious correlation is found.

lution of the disks in clusters is found to follow a different pace than that for more isolated stars, this can set important constraints on disk evolution theories.

As discussed in Harvey et al. (2006), the brightest YSOs in Serpens appear to be concentrated in clusters, but a more extended young stellar population exists outside these clusters. For the determination of clusters and their boundaries, we follow the method developed by Jørgensen et al. (2008) for Ophiuchus and Perseus. Using volume density and number of YSOs as criteria, the method consists of a nearest neighbor algorithm, and has as input the complete sample of YSOs in Serpens (Harvey et al. 2007b). The associations are divided into loose (volume density of 1 $M_\odot pc^{-3}$, blue contour in Figure 4.12) and tight (volume density of 25 $M_\odot pc^{-3}$, yellow contours in Figure 4.12). Furthermore, the associations are divided into clusters (more than 35 members) and groups (less than 35 members). The results of this method in Serpens yield 2 clusters (A and B) and 3 groups (C, D, and E), that can be seen in Figure 4.12. Individual memberships are marked in Table 4.2. With the exception of one, virtually all YSOs in Serpens are within the blue contour, i.e., all YSOs belong to, at least, a loose association. This differs, for instance, from Ophiuchus and Perseus (Jørgensen et al. 2008), where some YSOs are completely isolated. For number statistics of clustering in all c2d clouds, see Evans et al. (2009).

Table 4.3 lists the number of objects in each tight association. It appears that the ratio of disk to embedded sources in a given cluster increases with distance from the densest part of the cluster, where Group C is located (see Figure 4.12).

To compare the populations, all objects belonging to any of the tight associations were grouped into the "cluster population", for better number statistics. Objects not belonging to any cluster were grouped into the "field population". Figure 4.13 shows the comparison between these two populations for three quantities derived from the
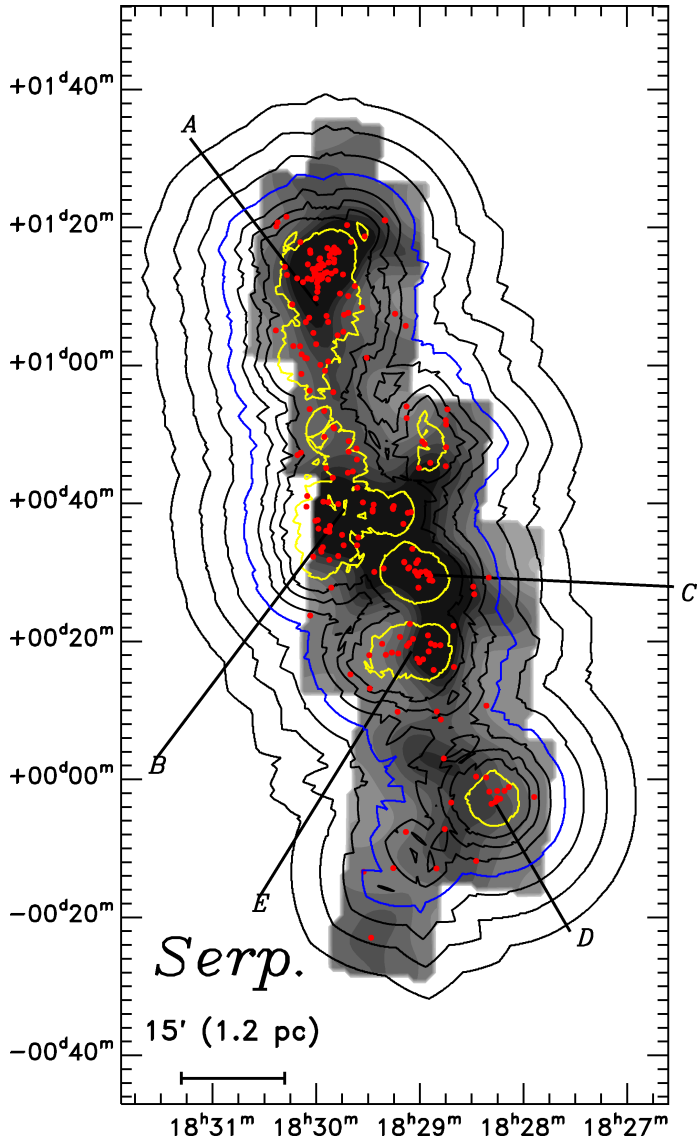
Figure 4.12 – Clusters and groups in Serpens as defined according to the criteria in Jørgensen et al. (2008). The volume density contours are overlaid on the Serpens extinction map (Evans et al. 2007). The red dots are the YSOs in Serpens from Harvey et al. (2007b). Black contours indicate volume densities of 0.125, 0.25, 0.5, 2.0 and 4.0 $M_\odot$ pc^{-3}, gray contour corresponds to volume density of 1 $M_\odot$ pc^{-3} and white contours to a volume density of 25 $M_\odot$ pc^{-3}. (A color version of this figure is available in the online journal)
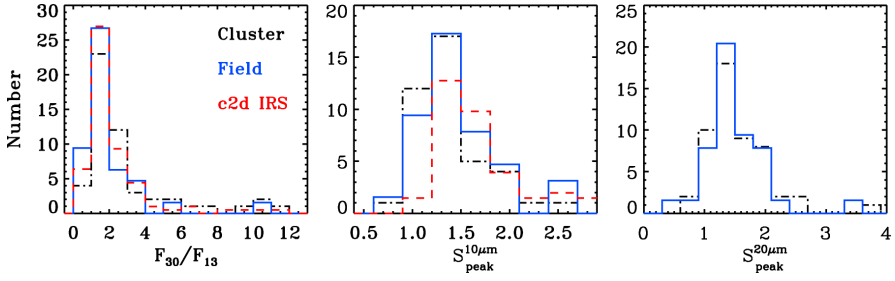
Figure 4.13 – Comparison between the clustered (dot-dashed black line) and field populations (solid dark gray line) of Serpens, with data from the c2d IRS program (dashed light gray line, Olofsson et al. 2009). In the left panel, the flux ratio between 30 and 13 μm (F_{30}/F_{13}) is an indication of the disk geometry. The middle and right panels show the strength of the silicate features at 10 and 20 μm, respectively. (A color version of this figure is available in the online journal)

IRS spectra. In the left panel, the flux ratio between 30 and 13 μm (F_{30}/F_{13}) is an indication of disk geometry. The middle and right panels show the peak intensity of the silicate features at 10 and 20 μm, respectively. For all three quantities, the two populations (cluster and field) are statistically indistinguishable. A two sample Kolmogorov–Smirnov test (KS test) was performed for each quantity and the results show that the null hypothesis that the two distributions come from the same parent population cannot be rejected to any significance (18%, 13%, and 79% for F_{30}/F_{13}, $S_{\text{peak}}^{10\mu m}$, and $S_{\text{peak}}^{20\mu m}$, respectively).

Differences between the cluster versus field populations will be further investigated with ancillary data (e.g., relative stellar ages and masses) and modeling (e.g., disk sizes). However, the IRS spectra allow the conclusion that no significant differences are found for disk geometry or the grain size distribution in the upper layers of circumstellar disks in clustered compared with field stars. The latter result only applies to the inner disk, as traced by silicate features. The outer disk may still be different between cluster and field populations.

4.4.2   Comparison with Other Samples

The young stars with disks observed by the c2d team with IRS spectroscopy (c2d IRS sample) are scattered across the sky in the five molecular clouds studied (Olofsson et al. 2009). The other four clouds studied by the c2d are Chamaeleon II, Lupus, Perseus and Ophiuchus. All clouds are nearby (within 300 pc), span a range of star-formation activity, have typical median ages of a few Myr and have a spread between more (Perseus and Ophiuchus) and less (Cha II and Lupus) clustered YSO populations (Evans et al. 2009). The results from this sample are also compared to the results in Serpens in Figures 4.9 and 4.13. A conspicuous similarity is seen between the samples. Note that Olofsson et al. (2009) do not analyze the 20 μm silicate feature in this same manner and, therefore, $S_{\text{peak}}^{20\mu m}$ for the c2d IRS sample is missing from the right panel in Figure 4.13.
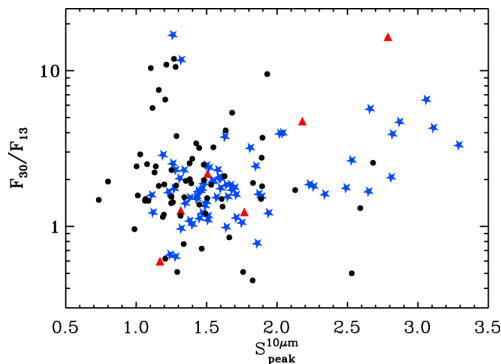
Figure 4.14 – Flux ratio between 30 and 13 μm (F_{30}/F_{13}) plotted against the peak at 10 μm ($S_{peak}^{10\mu m}$, black dots), compared against the T Tauri FEPS sample (gray triangles; Bouwman et al. 2008) and the c2d IRS sample (gray stars; Olofsson et al. 2009). Typical uncertainties for the 10 μm peak strength are $\sim$0.1, while typical uncertainties for the flux ratio are $\sim$0.12. (A color version of this figure is available in the online journal)

The models of Dullemond & Dominik (2008) conclude that, if sedimentation is the unique reason for the variety of observed strength and shape of the 10 μm silicate feature, then this feature is strong for weak excess in mid- to far-IR (as probed by F_{30}/F_{13}), and vice-verse. However, when studying a small sample of T Tauri stars from the Spitzer Legacy Program "The Formation and Evolution of Planetary Systems: Placing Our Solar System in Context" (FEPS) sample, Bouwman et al. (2008) found the opposite: a trend in which weak F_{30}/F_{13} correlates with a weak feature. A confirmation of this trend for a larger sample implies that sedimentation alone cannot be the sole cause for the diversity of observed silicate features. Dullemond & Dominik (2008) argue that dust coagulation must then play a vital role in producing different silicate profiles. In Figure 4.14, we populate this diagram with the Serpens sample (black dots) and the c2d IRS sample (blue stars), as well as the Bouwman FEPS sample (red triangles). This large combined sample shows no correlation between the strength of the 10 μm silicate feature and F_{30}/F_{13} ($\tau = 0.07$) and therefore does not support either the correlation (as seen by Bouwman et al. 2008) or the anti-correlation (as modeled by Dullemond & Dominik (2008) for sedimentation alone) between the IR flux excess and the strength of the 10 μm silicate feature.

4.4.3   Comparison with Taurus

The Taurus Molecular Cloud is the best characterized star-forming region to date, due to its proximity and relatively low extinction. With young stars and their surrounding disks studied for more than two decades (e.g., Kenyon & Hartmann 1987, 1995), its members have been well characterized at a wide range of wavelengths. Taurus has thus become the reference for comparison of star-forming regions. Compared to Serpens, Taurus seems to be a somewhat younger (2.0 Myr median age, Hartmann et

al. 2001 versus 4.7 Myr Oliveira et al. 2009) and has a lower star-forming rate. Due to uncertainties in pre-main sequence age determinations (e.g., Baraffe et al. 2009; Hillenbrand 2009; Naylor 2009), this difference may not be significant. However, cluster ages are statistically more likely to be different than the same.

In a campaign similar to that presented here, IRS spectra were obtained for a sample of 139 YSOs in Taurus, as part of a larger IRS guaranteed-time observing program. These data were presented in two separate papers: Furlan et al. (2006) treated the disk sources, while Furlan et al. (2008) presented the embedded population in Taurus.

Because the young stellar population in Serpens has been discovered and characterized using IR observations, this sample does not include young stars without disks (and therefore no IR excess, also called Class III sources, as defined in Lada (1987)). For this reason, a comparison between the Class III sources of the two clouds does not make sense. Twenty-six Class III objects were studied in Taurus. These objects present featureless spectra with very little IR excess at longer wavelengths. It is, however, possible to compare the IR excess populations of both regions. Out of the entire YSO sample studied in Taurus, embedded sources (or Class I) amount to 20% while in Serpens they amount to 18%, a very comparable number. This also matches the typical percentage of Class I sources in the global YSO statistics of the five clouds from the c2d photometric sample (Evans et al. 2009). In Serpens only five objects have featureless spectra.

Excluding the embedded sources to analyze the disk population alone, objects having both 10 and 20 μm silicate features amount to 72% in Taurus, comparable to 73% of the Serpens disk population. Also comparable is the percentage of disks with PAH emission: 3% in Serpens and 4% in Taurus.

In both regions, all disks with a 10 μm silicate feature also show the 20 μm one. However, a difference is found for disks with only the 20 μm feature in emission: they amount to 17% of the disk population in Serpens and only 4.5% in Taurus. These statistics are summarized in Table 4.4.

IRS data on the 85 disk sources presented in Furlan et al. (2006) were obtained from the Spitzer archive and reduced in the same manner as our Serpens data. The same method described in Section 4.3.3.4 was applied to these data in order to compare the processes affecting the dust in both regions. Figure 4.15 (bottom) shows the strength versus shape of the 10 μm silicate feature for both Serpens (black dots) and Taurus (red dots), as well as the distribution of peak strength for both regions (top). Serpens and Taurus present remarkably similar distributions, with populations clustered around flatter features and bigger grains, and almost no strongly peaked silicate emission sources. A KS test shows that the hypothesis that the distributions are drawn from the same population cannot be rejected (82%).
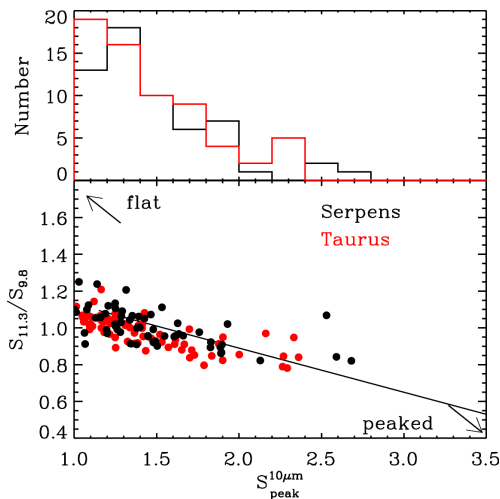
Figure 4.15 – Top: distribution of the 10 μm peak strength for Serpens (black) and Taurus (gray). Bottom: strength and shape of the 10 μm silicate feature for both Serpens (black) and Taurus (gray). (A color version of this figure is available in the online journal)

4.4.4   Implications

Comparisons between disks around stars that were formed in clusters or in isolation in the Serpens Cloud, explored in Section 4.4.1, indicate very similar populations. Thus, statistically no differences are found in terms of both disk geometry (probed by the ratio F_{30}/F_{13}) and processes affecting the dust (probed by the silicate features). This suggests that local environment does not affect the evolution path and timescale of disks.

Even more remarkable is the agreement between the YSO populations of Serpens and Taurus, as well as the c2d IRS sample spread over five clouds, in terms of silicate features, as shown in Sections 4.4.2 and 4.4.3. Even though there are clear differences in silicate features from source to source within a cloud, the overall *distribution* of feature shapes is statistically indistinguishable: in all three samples, each containing of the order of 100 disks, the bulk of the sources has a rather flat silicate profile, and a tail of peaked shapes.

If the difference in median ages is significant, the similarity seen in Figure 4.15 indicates that a 2-3 Myr difference in age is not reflected in a concurrent evolution of the average disk surface dust properties. This indicates that the dust population in the disk surface is an equilibrium between dust growth and destruction processes, which is maintained at least as long as the disk is optically thick.

The process of grain growth through coagulation and settling to the midplane has been shown to be much too short to be consistent with disk observations (Weidenschilling 1980; Dullemond & Dominik 2005). That means that the small grain

population must be replenished somehow, which could happen by fragmentation of bigger aggregates and turbulent mixing. It is widely accepted in the literature that the 10 μm silicate feature is representative of the dust in the surface layers of the disk at a few AU from the star (Kessler-Silacci et al. 2007). Significant evolution could still take place in the disk mid-plane, which is not traced with these observations. Indeed, millimeter observations have indicated that disk midplanes are abundant in grains with mm/cm sizes (Natta et al. 2004; Rodmann et al. 2006; Lommen et al. 2007). That means that, if this population of small grains in the disk surface must be replenished by fragmentation of bigger grains followed by turbulent mixing, the surface dust is an indirect tracer of midplane grains.

If the age difference between Serpens and Taurus is significant, then there exists a statistical equilibrium of processes of dust coagulation and fragmentation in the disk lasting at least a few million years that is independent of which YSO population is being studied. The observable IR dust characteristics of a cluster population of protoplanetary disks do not appear to depend on cluster properties (age, density) within the first 5 Myr, for relatively low-mass clusters. No specific property or event that may influence the infrared dust signatures of a single disk (stellar luminosity, spectral type, presence of a companion, disk-planet interactions, disk instabilities, etc.) produces detectable temporal or spatial evolutionary effects visible in the distribution of disk properties of an entire cluster within this time frame.

This is consistent with a picture in which a specific disk may change its appearance on short time-scales (much less than 1 Myr), but in a *reversible* way. That is, the properties of disk surfaces may oscillate between different states (Bary et al. 2007; Muzerolle et al. 2009). If some evolution of the disk surface is *irreversible*, and happens at a given rate, a stable distribution of surface properties would not be seen over time. This requires that the effect on the disk surface of any reprocessing events has to be erased.

Another option is that the disk surface properties are determined by a single parameter, such as the initial conditions of the formation of such disks. In this scenario those properties should be kept "frozen" over the observed time scale of ~few Myr. However, this cannot be the case for objects like EX Lup, where real time changes of the disk surface properties after the initial formation of the disk have been observed on time scales of just a few years (namely crystallization through thermal annealing of the dust in the disk surface, Ábrahám et al. 2009).

For this theory to work, the putative oscillation of states proposed here must be stable over disk lifetimes of ~5 Myr. As long as the disks are gas-rich and optically thick, as in the three samples studied here, we do not see a distinguishable evolution. It will be important to search for surface evolution indicators in even older clusters. Such comparisons will yield constraints on the global time scale of disk evolution, which in turn will help constrain the importance of the processes that play a vital role in the dissipation of the disks.

The scenario in which a considerable population of small particles is still present af-

ter bigger aggregates are formed and altered through multiple events is consistent with evidence from primitive chondrites in our own solar system. Chondritic meteorites are observed to contain fine-grained dust-like matrices formed after coarse-grained materials such as chondrules and calcium–aluminum-rich inclusions (CAIs). This indicates that the solar nebula underwent violent reprocessing events in the feeding zones of parent bodies at 3-4 AU (see Pontoppidan & Brearley (2010) for a recent review on solar system dust in an astrophysical context). These events included systemic melting of large dust aggregates and possibly even evaporation and re-condensation of silicate grains. In fact, presolar material is present in primitive chondrites only at the trace level: ~100 ppm (Lodders & Amari 2005; Zinner et al. 2007), testifying to the complete evaporative destruction of ISM dust at a few AU in protoplanetary dust.

4.5   Conclusions

We present *Spitzer*/IRS spectra from a complete and unbiased flux limited sample of IR excess sources found in the Serpens Molecular Cloud, following the c2d mapping of this region.

- Among our total of 147 IRS spectra, 22% are found to be background contamination (including background stars, redshifted galaxies, and a planetary nebula candidate). This high number is not surprising given the position of Serpens, close to the galactic plane.
- Excluding the background objects from the sample, the bona fide set of YSOs amounts to 115 objects. The embedded-to-disk source ratio is 18%, in agreement with the ratios derived from photometry (Evans et al. 2009) for the five c2d clouds.
- Disks with PAH in emission amount to 2% of the YSO population, but 3% of the disk population. Only G and A star show PAH emission. In the disk population, 73% show both silicate emission features, at 10 and 20 μm, while 17% show only the 20 μm feature. 4% of the disks show featureless mid-IR spectra. Only one source, 120, shows both PAH and silicate in emission.
- Our YSO population in Serpens is very similar to that in Taurus, also studied with IRS spectra. In both regions about 70% of the disk sources present both 10 and 20 μm silicate features in emission and the 10 μm feature is never seen without the 20 μm feature. The only significant difference between the two populations is in the number of sources lacking the 10 μm feature but showing the 20 μm feature. This may be indicative of small holes ($\lesssim$ 1 AU) in these sources.
- The silicate features in the IRS spectra measure the grain sizes that dominate the mid-IR opacity. The relationships between shape and strength of these features present distributions very similar to those obtained from other large samples of young stars. Comparison with the models of Olofsson et al. (2009) yields grains consistent with sizes larger than a few μm.
- No significant differences are found in the disk geometry or the grain size distri-

bution in the upper layers of circumstellar disks (probed by the silicate features) in clustered or field stars in the cloud, indicating that the local environment where a star is born does not influence the evolution of its harboring disk.

- Quantitatively, the shape and strength of the 10 μm silicate feature were used to compare both Serpens and Taurus as well as a large sample of disks across five clouds, indicating remarkably similar populations. This implies that the dust population in the disk surface results from an equilibrium between dust growth and destruction processes that are maintained over a few million years.

References

Ábrahám, P., et al. 2009, Nature, 459, 224

Acke, B., & van den Ancker, M. E. 2004, A&A, 426, 151

Alexander, R. D., Clarke, C. J., & Pringle, J. E. 2006, MNRAS, 369, 216

Alexander, R. D. 2008, MNRAS, 391, L64

Apai, D., Pascucci, I., Bouwman, J., Natta, A., Henning, T., & Dullemond, C. P. 2005, Science, 310, 834

Baraffe, I., Chabrier, G., Allard, F., & Hauschildt, P. H. 1998, A&A, 337, 403

Baraffe, I., Chabrier, G., & Gallardo, J. 2009, ApJ, 702, L27

Bary, J. S., Leisenring, J. M., & Skrutskie, M. F. 2007, BAAS, 38, 1007

Bernard-Salas, J., Peeters, E., Sloan, G. C., Gutenkunst, S., Matsuura, M., Tielens, A. G. G. M., Zijlstra, A. A., & Houck, J. R. 2009, ApJ, 699, 1541

Boogert, A. C. A., et al. 2004, ApJS, 154, 359

Boogert, A. C. A., et al. 2008, ApJ, 678, 985

Bottinelli, S., et al. 2010, ApJ, 718, 1100

Bouwman, J., Meeus, G., de Koter, A., Hony, S., Dominik, C., & Waters, L. B. F. M. 2001, A&A, 375, 950

Bouwman, J., Lawson, W. A., Dominik, C., Feigelson, E. D., Henning, T., Tielens, A. G. G. M., & Waters, L. B. F. M. 2006, ApJ, 653, L57

Bouwman, J., et al. 2008, ApJ, 683, 479

Brauer, F., Dullemond, C. P., Johansen, A., Henning, T., Klahr, H., & Natta, A. 2007, A&A, 469, 1169

Brauer, F., Dullemond, C. P., & Henning, T. 2008a, A&A, 480, 859

Brauer, F., Henning, T., & Dullemond, C. P. 2008b, A&A, 487, L1

Brown, J. M., et al. 2007, ApJ, 664, L107

Chabrier, G. 2003, PASP, 115, 763

Chapman, N. L., Mundy, L. G., Lai, S.-P., & Evans, N. J. 2009, ApJ, 690, 496

Chapman, N. L., & Mundy, L. G. 2009, ApJ, 699, 1866

Chiar, J. E., et al. 2007, ApJ, 666, L73

Clarke, C. J., Gendrin, A., & Sotomayor, M. 2001, MNRAS, 328, 485

Condon, J. J. 1992, ARA&A, 30, 575

Condon, J. J., Cotton, W. D., Greisen, E. W., Yin, Q. F., Perley, R. A., Taylor, G. B., & Broderick, J. J. 1998, AJ, 115, 1693

Djupvik, A. A., André, P., Bontemps, S., Motte, F., Olofsson, G., Gålfalk, M., & Florén, H.-G. 2006, A&A, 458, 789

Dominik, C., & Tielens, A. G. G. M. 1997, ApJ, 480, 647

Draine, B. T. 2003, ARA&A, 41, 241

Dullemond, C. P., & Dominik, C. 2004, A&A, 421, 1075

Dullemond, C. P., & Dominik, C. 2005, A&A, 434, 971

Dullemond, C. P., Henning, T., Visser, R., Geers, V. C., van Dishoeck, E. F., & Pontoppidan, K. M. 2007, A&A, 473, 457

Dullemond, C. P., & Dominik, C. 2008, A&A, 487, 205

Eiroa, C., & Casali, M. M. 1992, A&A, 262, 468

Eiroa, C., Torrelles, J. M., Curiel, S., & Djupvik, A. A. 2005, AJ, 130, 643

Evans, N. J., II, et al. 2003, PASP, 115, 965

Evans, N. J., II, et al. 2007[1]

Evans, N. J., et al. 2009, ApJS, 181, 321

Fazio, G. G., et al. 2004, ApJS, 154, 10

Furlan, E., et al. 2006, ApJS, 165, 568

Furlan, E., et al. 2008, ApJS, 176, 184

Forrest, W. J., et al. 2004, ApJS, 154, 443

Geers, V. C., et al. 2006, A&A, 459, 545

Geers, V. C. 2007, Ph.D. thesis

Ghavamian, P., Raymond, J. C., Blair, W. P., Long, K. S., Tappe, A., Park, S., & Winkler, P. F. 2009, ApJ, 696, 1307

Gorti, U., & Hollenbach, D. 2009, ApJ, 690, 1539

Greene, T. P., Wilking, B. A., Andre, P., Young, E. T., & Lada, C. J. 1994, ApJ, 434, 614

Haisch, K. E., Jr., Lada, E. A., & Lada, C. J. 2001, ApJ, 553, L153

Hartmann, L., Ballesteros-Paredes, J., & Bergin, E. A. 2001, ApJ, 562, 852

Harvey, P. M., et al. 2006, ApJ, 644, 307

Harvey, P. M., et al. 2007, ApJ, 663, 1139

Harvey, P., Merín, B., Huard, T. L., Rebull, L. M., Chapman, N., Evans, N. J., II, & Myers, P. C. 2007, ApJ, 663, 1149

Hillenbrand, L. A. 2008, Phys. Scr. T, 130, 014024

Hillenbrand, L. A. 2009, in IAU Symp. 258, The Ages of Stars (Cambridge: Cambridge Univ. Press), 81

Houck, J. R., et al. 2004, ApJS, 154, 18

Ireland, M. J., & Kraus, A. L. 2008, ApJ, 678, L59

Johansen, A., Brauer, F., Dullemond, C., Klahr, H., & Henning, T. 2008, A&A, 486, 597

Jørgensen, J. K., Johnstone, D., Kirk, H., Myers, P. C., Allen, L. E., & Shirley, Y. L. 2008, ApJ, 683, 822

Kaas, A. A., et al. 2004, A&A, 421, 623

Kenyon, S. J., & Hartmann, L. 1987, ApJ, 323, 714

Kenyon, S. J., & Hartmann, L. 1995, ApJS, 101, 117

Kessler-Silacci, J., et al. 2006, ApJ, 639, 275

Kessler-Silacci, J. E., et al. 2007, ApJ, 659, 680

Lada, C. J. 1987, Star Forming Regions, 115, 1

Lada, E. A., & Lada, C. J. 1995, AJ, 109, 1682

Lahuis, F., et al. 2006, c2d Spectroscopy Explanatory Supplement, Techical Report (Pasadena, CA: Spitzer Science Center)

Lodders, K., & Amari, S. 2005, Geochemistry, 65, 93

Lommen, D., et al. 2007, A&A, 462, 211

Magnelli, B., Elbaz, D., Chary, R. R., Dickinson, M., Le Borgne, D., Frayer, D. T., &

---

[1] Delivery Documentation, http://ssc.spitzer.caltech.edu/legacy/c2dhistory.html

Willmer, C. N. A. 2009, A&A, 496, 57

McClure, M. 2009, ApJ, 693, L81

Meeus, G., Waters, L. B. F. M., Bouwman, J., van den Ancker, M. E., Waelkens, C., & Malfait, K. 2001, A&A, 365, 476

Meeus, G., Bouwman, J., Dominik, C., Waters, L. B. F. M., & de Koter, A. 2002, A&A, 392, 1039

Merín, B., et al., ApJ, submitted

Merín, B., et al. 2010, ApJ, 718, 1200

Merín, B., et al. 2007, ApJ, 661, 361

Muzerolle, J., Hillenbrand, L., Calvet, N., Briceño, C., & Hartmann, L. 2003, ApJ, 592, 266

Muzerolle, J., et al. 2009, ApJ, 704, L15

Natta, A., Testi, L., Muzerolle, J., Randich, S., Comerón, F., & Persi, P. 2004, A&A, 424, 603

Natta, A., Testi, L., Neri, R., Shepherd, D. S., & Wilner, D. J. 2004, A&A, 416, 179

Naylor, T. 2009, MNRAS, 1142

Öberg, K. I., Boogert, A. C. A., Pontoppidan, K. M., Blake, G. A., Evans, N. J., Lahuis, F., & van Dishoeck, E. F. 2008, ApJ, 678, 1032

Oliveira, I., et al. 2009, ApJ, 691, 672

Olofsson, J., et al. 2009, A&A, 507, 327

Papovich, C., et al. 2004, ApJS, 154, 70

Pascucci, I., Apai, D., Luhman, K., Henning, T., Bouwman, J., Meyer, M. R., Lahuis, F., & Natta, A. 2009, ApJ, 696, 143

Pontoppidan, K. M., Dullemond, C. P., van Dishoeck, E. F., Blake, G. A., Boogert, A. C. A., Evans, N. J., II, Kessler-Silacci, J. E., & Lahuis, F. 2005, ApJ, 622, 463

Pontoppidan, K. M., et al. 2008, ApJ, 678, 1005

Pontoppidan, K. M., & Brearly, A. J. 2010, Book by D. Apai

Prantzos, N., & Aubert, O. 1995, A&A, 302, 69

Przygodda, F., van Boekel, R., Àbrahàm, P., Melnikov, S. Y., Waters, L. B. F. M., & Leinert, C. 2003, A&A, 412, L43

Quillen, A. C., Blackman, E. G., Frank, A., & Varnière, P. 2004, ApJ, 612, L137

Richling, S., & Yorke, H. W. 1998, A&A, 340, 508

Richling, S., & Yorke, H. W. 2000, ApJ, 539, 258

Rieke, G. H., et al. 2004, ApJS, 154, 25

Rieke, G. H., Alonso-Herrero, A., Weiner, B. J., Pérez-González, P. G., Blaylock, M., Donley, J. L., & Marcillac, D. 2009, ApJ, 692, 556

Rodmann, J., Henning, T., Chandler, C. J., Mundy, L. G., & Wilner, D. J. 2006, A&A, 446, 211

Sanders, D. B., & Mirabel, I. F. 1996, ARA&A, 34, 749

Sandstrom, K., Bolatto, A., Stanimirović, S., Smith, J. D., Simon, J. D., & Leroy, A. 2009, The Evolving ISM in the Milky Way and Nearby Galaxies,

Sargent, B. A., et al. 2009, ApJS, 182, 477

Savitzky, A., & Golay, M. J. E. 1964, Anal. Chem., 36, 1627

Siess, L., Dufour, E., & Forestini, M. 2000, A&A, 358, 593

Smith, J. D. T., et al. 2007, ApJ, 656, 770

Sterzik, M. F., Morfill, G. E., & Dubrulle, B. 1995, Ap&SS, 224, 567

Straizys, V., Cernis, K. & Bartasiute, S. 1996, Baltic Astron., 5, 125

Strom, S.W. 1992, Nature, 359, 360

Testi, L., & Sargent, A. I. 1998, ApJ, 508, L91

Tielens, A. G. G. M. 2008, ARA&A, 46, 289

Uchida, K. I., et al. 2004, ApJS, 154, 439

van Boekel, R., Waters, L. B. F. M., Dominik, C., Bouwman, J., de Koter, A., Dullemond, C. P., & Paresce, F. 2003, A&A, 400, L21

van Boekel, R., Waters, L. B. F. M., Dominik, C., Dullemond, C. P., Tielens, A. G. G. M., & de Koter, A. 2004, A&A, 418, 177

van Boekel, R., Min, M., Waters, L. B. F. M., de Koter, A., Dominik, C., van den Ancker, M. E., & Bouwman, J. 2005, A&A, 437, 189

Vandenbussche, B., Dominik, C., Min, M., van Boekel, R., Waters, L. B. F. M., Meeus, G., & de Koter, A. 2004, A&A, 427, 519

Varnière, P., Blackman, E. G., Frank, A., & Quillen, A. C. 2006, ApJ, 640, 1110

Visser, R., Geers, V. C., Dullemond, C. P., Augereau, J.-C., Pontoppidan, K. M., & van Dishoeck, E. F. 2007, A&A, 466, 229

Watson, D. M., et al. 2009, ApJS, 180, 84

Weidenschilling, S. J. 1980, Icarus, 44, 172

Weingartner, J. C., & Draine, B. T. 2001, ApJ, 548, 296

White, R. J., & Basri, G. 2003, ApJ, 582, 1109

Winston, E., et al. 2007, ApJ, 669, 493

Winston, E., et al. 2009, AJ, 137, 4777

Zhang, C. Y., Laureijs, R. J., & Clark, F. O. 1988, A&A, 196, 236

Zinner, E., et al. 2007, Geochim. Cosmochim. Acta, 71, 4786

Table 4.1 − Observed Objects in Serpens

#[a]	ID[b]	c2d ID (SSTc2dJ)	$\alpha_{2\mu m-24\mu m}$[c]	Program[d]	AOR	Obs. Date	$\frac{F_{30}}{F_{13}}$[e]	Type
1	1	18275383-0002335	−1.42	GO3	17891072	2007-04-19	1.31	Disk
2	2	18280503+0006591	−2.29	GO3	17883648	2007-04-24	0.35	BG star
3	3	18280845-0001064	−0.70	GO3	17883136	2007-04-24	1.52	Disk
4	4	18281100-0001395	−2.13	GO3	17888256	2007-04-29	0.27	BG star
5		18281315+0003128	−1.84	c2d	13210368	2005-05-20	0.27	BG star
6	5	18281350-0002491	−1.08	GO3	17883136	2007-04-24	1.71	Disk
7	6	18281501-0002588	−0.05	GO3	17883136	2007-04-24	2.54	Disk
8	7	18281519-0001407	−1.25	GO3	17889536	2007-04-30	2.43	Disk
9	8	18281525-0002434	−0.85	GO3	17882368	2007-04-25	5.37	Cold disk
10	9	18281629-0003164	−1.13	GO3	17884160	2007-04-19	1.83	Disk
11		18281757-0006474	0.65	GO3	17890560	2007-04-28	3.36	Galaxy
12		18281757+0016065	0.53	GO3	17888768	2007-05-05	4.72	Galaxy
13	11	18281981-0001475	−0.89	GO3	17889792	2007-04-30	4.09	Disk
14	13	18282143+0010411	−1.44	GO3	17888000	2007-04-30	1.38	Disk
15	14	18282159+0000162	−0.99	GO3	17883136	2007-04-24	2.56	Disk
16	15	18282432+0034545	−2.01	GO3	17887744	2007-04-24	0.32	BG star
17		18282720+0044450	1.82	GO3	17884928	2007-04-29	11.04	PN cand.
18	16	18282738-0011499	−1.98	GO3	17883136	2007-04-24	0.32	BG star
19	17	18282741+0000239	−1.97	GO3	17887744	2007-04-24	0.43	BG star
20	18	18282849+0026500	−1.12	GO3	17890048	2007-04-29	1.13	Disk
21	19	18282905+0027560	−1.06	GO3	17884928	2007-04-29	10.38	Cold disk
22		18283000+0020147	−1.60	c2d	13210624	2005-05-20	0.29	BG star
23		18283736+0019276	−2.19	GO3	17887744	2007-04-24	0.27	BG star
24	20	18284025+0016173	−0.96	GO3	17890048	2007-04-29	1.20	Disk
25	21	18284053+0022144	−1.91	GO3	17887744	2007-04-24	0.42	BG star
26	22	18284187-0003215	0.53	GO3	17883136	2007-04-24	3.39	Emb
27	23	18284403+0053379	0.70	GO3	17882880	2007-04-28	3.37	Emb
28	24	18284479+0051257	1.04	GO3	17885184	2007-04-24	10.18	Emb
29	25	18284481+0048085	−1.01	GO3	17888512	2007-05-05	2.76	Disk
30	27	18284497+0045239	−1.35	GO3	17886720	2007-04-24	0.77	Disk
31	38	18284559-0007132	−0.77	GO3	17882368	2007-04-25	0.51	Disk
32	29	18284614+0003016	−0.64	GO3	17889024	2007-04-25	0.66	Disk
33		18284632-0011103	0.53	GO3	17890560	2007-04-28	11.17	Galaxy

#[a]	ID[b]	c2d ID (SSTc2dJ)	$\alpha_{2\mu m-24\mu m}$[c]	Program[d]	AOR	Obs. Date	$\frac{F_{30}}{F_{13}}$[e]	Type
34		18284828-0005300	−2.43	GO3	17888256	2007-04-29	0.47	BG star
35		18284938-0006046	−2.01	c2d	13210624	2005-05-20	0.28	BG star
36	32	18285020+0009497	−0.24	c2d	13461505	2006-04-31	1.98	Disk
37	33	18285039-0012552	−1.40	GO3	17884160	2007-04-19	0.32	BG star
38		18285060+0007540	−2.31	c2d	13460736	2005-09-09	–	Disk
39	34	18285122+0019271	0.45	GO3	17883904	2007-04-29	8.98	Emb
40	36	18285249+0020260	−0.15	GO3	17883136	2007-04-24	1.46	Disk
41	37	18285276+0028466	0.07	GO3	17887232	2007-04-27	9.50	Disk
42	38	18285362+0019302	−0.64	GO3	17887488	2007-04-25	2.09	Disk
43	39	18285395+0045530	−1.16	GO3	17886208	2007-09-30	1.96	Disk
44	40	18285404+0029299	1.35	c2d	13461249	2006-04-20	18.21	Emb
45	42	18285450+0029520	0.15	c2d	13460993	2006-04-19	35.49	Emb
47	43	18285489+0018326	0.88	GO3	17883392	2007-04-29	7.58	Emb
48	44	18285529+0020522	−0.29	GO3	17884160	2007-04-19	1.43	Disk
49	45	18285582+0029444	1.81	GO3	17883392	2007-04-29	99.75	Emb
50	46	18285660+0030080	1.84	GO3	17889792	2007-04-30	21.37	Emb
51	47	18285718+0048359	−0.32	GO3	17888718	2007-05-05	11.27	Emb
52	48	18285808+0017244	−2.11	GO3	17888000	2007-04-30	1.23	Disk
53	49	18285860+0048594	−1.06	GO3	17887488	2007-04-25	1.55	Disk
54	50	18285946+0030029	−0.59	c2d	13461249	2006-04-20	0.62	Disk
55	51	18290025+0016580	−1.01	GO3	17884416	2007-04-30	1.50	Disk
56	52	18290057+0045079	−0.94	GO3	17886208	2007-09-30	3.22	Disk
57	53	18290082+0027467	−0.36	GO3	17885440	2007-04-24	3.41	Disk
58	54	18290088+0029315	−0.37	c2d	13210112	2005-04-17	1.82	Disk
59	55	18290107+0031451	−0.49	c2d	13461249	2006-04-20	1.14	Disk
60	56	18290122+0029330	−0.39	c2d	13461505	2006-04-21	1.58	Disk
61	58	18290175+0029465	−0.84	c2d	13461249	2006-04-20	2.30	Disk
62	59	18290184+0029546	−0.77	c2d	13210112	2005-04-17	1.32	Disk
63	60	18290210+0031210	0.29	GO3	17887232	2007-04-27	32.23	Emb
64		18290215+0029400	−0.86	GO3	17885184	2007-04-24	2.89	Disk
65	61	18290286+0030089	−0.23	c2d	13460993	2006-04-21	2.43	Disk
66	62	18290393+0020217	−0.82	GO3	17883136	2007-04-24	1.19	Disk
67	63	18290436+0033237	0.95	c2d	13461505	2006-06-21	2.54	Emb
68		18290442+0020018	0.52	GO3	17890560	2007-04-28	5.61	Galaxy
69	64	18290518+0038438	−1.24	GO3	17889792	2007-04-30	5.64	Cold disk
70	65	18290575+0022325	−2.12	GO3	17886720	2007-04-29	1.76	Disk
71	66	18290615+0019444	−1.52	GO3	17888512	2007-05-05	2.49	Disk
72	67	18290620+0030430	1.69	c2d	13461249	2006-04-21	17.07	Emb
73	68	18290680+0030340	1.67	c2d	13460993	2006-04-21	75.97	Emb
74	69	18290699+0038377	−0.63	GO3	17884416	2007-04-30	2.90	Disk
75	71	18290765+0052223	−1.01	GO3	17888512	2007-05-05	2.01	Disk
76	72	18290775+0054037	−1.06	GO3	17888000	2007-04-30	1.34	Disk
77	73	18290804+0007371	−2.22	GO3	17888256	2007-04-29	0.27	BG star
78		18290843-0026187	−2.28	GO3	17885696	2007-04-28	0.31	BG star
79	75	18290910+0031300	0.24	GO3	17884928	2007-04-29	51.02	Emb
80	76	18290956+0037016	−1.13	GO3	17882368	2007-04-25	0.51	Disk
81	77	18290980+0034459	−0.97	c2d	13210624	2005-05-20	0.85	Disk
82	78	18291148+0020387	−1.34	GO3	17887232	2007-04-27	11.90	Cold disk
83	79	18291249+0018152	−1.06	GO3	17889536	2007-04-30	2.06	Disk
84	81	18291407+0002589	−2.19	GO3	17885696	2007-04-28	0.30	BG star
85		18291477-0004237	−2.29	c2d	13210112	2005-04-17	0.24	BG star
86	83	18291518+0052124	−1.89	GO3	17882880	2007-04-28	0.45	Disk
87	84	18291513+0039378	−1.50	GO3	17889024	2007-04-25	1.01	Disk
88	85	18291539-0012519	−1.72	GO3	17885952	2006-10-23	0.50	Disk
89	86	18291557+0039119	−0.56	GO3	17884416	2007-04-30	2.51	Disk
90	87	18291563+0039228	−0.89	GO3	17885184	2007-04-24	6.52	Cold disk
91	88	18291617+0024227	0.45	c2d	13210617	2005-04-17	2.11	Emb
92	89	18291969+0018031	−1.23	GO3	17885440	2007-04-24	2.10	Disk
93	90	18292001+0024497	−2.04	GO3	17886720	2007-04-24	0.29	BG star
94		18292050+0047080	1.29	GO3	17888768	2007-05-05	25.76	Disk
95	93	18292094+0030345	−1.73	GO3	17882880	2007-04-28	0.40	BG star
96	94	18292184+0019386	−0.99	GO3	17886976	2007-04-29	1.54	Disk
97		18292250+0034118	−1.65	GO3	17889280	2007-04-24	0.29	Disk
98		18292253+0034176	−2.48	GO3	17889024	2007-04-25	1.34	Disk
99	95	18292616+0020518	−2.26	GO3	17883648	2007-04-24	0.37	BG star
100	96	18292640+0030042	−0.98	GO3	17888768	2007-05-05	1.89	Disk
101	97	18292679+0039497	−0.60	GO3	17885440	2007-04-24	4.13	Disk
102	99	18292736+0038496	0.29	GO3	17886464	2007-04-29	3.95	Emb
103	100	18292824-0022574	−0.41	c2d	13210368	2005-05-20	1.17	Disk
104		18292833+0049569	−0.48	GO3	17887488	2007-04-25	1.85	Disk
105		18292864+0042369	−0.97	GO3	17890024	2007-04-29	1.94	Disk
106	102	18292927+0018000	−1.24	GO3	17889792	2007-04-30	1.15	Disk
107		18293056+0033377	−0.60	GO3	17889536	2007-04-30	1.46	Disk

#[a]	ID[b]	c2d ID (SSTc2dJ)	$\alpha_{2\mu m-24\mu m}$[c]	Program[d]	AOR	Obs. Date	$\frac{F_{30}}{F_{13}}$[e]	Type
108	105	18293254-0013233	−2.58	GO3	17884672	2007-04-28	1.36	BG star
109	106	18293300+0040087	−1.35	GO3	17888512	2007-05-05	2.16	Disk
110	107	18293319+0012122	−1.81	GO3	17883648	2007-04-24	0.34	BG star
111		18293337+0050136	−0.26	GO3	17888768	2007-05-05	3.80	Disk
112	109	18293381+0053118	−2.06	GO3	17886720	2007-04-24	0.29	BG star
113	110	18293561+0035038	−1.53	GO3	17883904	2007-04-29	5.76	Cold disk
114	111	18293619+0042167	−0.92	GO3	17883904	2007-04-29	7.52	Cold disk
115	114	18293672+0047579	−1.00	GO3	17886976	2007-04-29	3.19	Disk
116	116	18293882+0044380	−1.23	GO3	17890048	2007-04-29	1.55	Disk
117	118	18294020+0015131	0.87	GO3	17883392	2007-04-29	2.72	Disk
118		18294067-0007033	−2.53	GO3	17884672	2007-04-28	0.38	BG star
119	119	18294121+0049020	−1.39	GO3	17889280	2007-04-24	1.55	Disk
120	123	18294168+0044270	−1.42	GO3	17884416	2007-04-30	3.13	Disk
121		18294301-0016083	−2.18	GO3	17890304	2006-10-25	0.33	BG star
122	126	18294410+0033561	−1.68	GO3	17886464	2007-04-29	10.92	Cold disk
123	129	18294503+0035266	−1.26	GO3	17886976	2007-04-29	3.71	Disk
124	132	18294725+0039556	−1.32	GO3	17887232	2007-04-27	2.22	Disk
125	133	18294726+0032230	−1.31	GO3	17886976	2007-04-29	1.50	Disk
126	140	18294962+0050528	−2.00	GO3	17890816	2007-04-24	0.35	BG star
127	143	18295001+0051015	−1.68	GO3	17889280	2007-04-24	1.23	Disk
128		18295012+0027229	0.14	GO3	17888768	2007-05-05	2.60	Galaxy
129	144	18295016+0056081	−0.76	GO3	17886208	2007-09-30	1.86	Disk
130	145	18295041+0043437	−1.32	GO3	17886720	2007-04-24	2.14	Disk
131	148	18295130+0027479	−2.42	GO3	17889024	2007-04-25	2.09	Disk
132	149	18295206+0036436	−0.06	GO3	17886464	2007-04-29	4.04	Emb
133		18295240+0035527	−0.33	GO3	17884416	2007-04-30	3.07	Emb
134	153	18295244+0031496	−0.59	GO3	17889244	2007-04-30	1.48	Disk
135	154	18295252+0036116	0.78	GO3	17883392	2007-04-29	24.39	Emb
136	156	18295304+0040105	−1.16	GO3	17889536	2007-04-30	1.50	Disk
137	157	18295305+0036065	0.07	GO3	17882624	2006-10-23	10.57	Disk
138	161	18295322+0033129	−1.99	GO3	17886720	2007-04-24	2.35	BG star
139	165	18295422+0045076	−2.35	GO3	17889024	2007-04-25	1.03	Disk
140	166	18295435+0036015	−0.19	GO3	17887232	2007-04-27	9.65	Emb
142	172	18295592+0040150	−0.85	GO3	17888000	2007-04-30	1.21	Disk
143	173	18295620+0033391	−0.54	GO3	17889024	2007-04-25	1.21	Disk
144	177	18295701+0033001	−1.15	GO3	17882880	2007-04-28	0.96	Disk
145	178	18295714+0033185	−0.82	GO3	17883648	2007-04-24	1.26	Disk
146	182	18295772+0114057	−0.44	c2d	9828352	2004-09-02	1.41	Disk
147	189	18295872+0036205	−1.11	GO3	17888000	2007-04-30	0.72	Disk
148	206	18300178+0032162	−1.25	GO3	17886976	2007-04-29	1.90	Disk
149	210	18300350+0023450	−1.22	GO3	17888000	2007-04-30	1.81	Disk

[a] As in Oliveira et al. (2009).

[b] From Harvey et al. (2007b).

[c] $\frac{d \log(\lambda F_\lambda)}{d \log(\lambda)}$ between the 2MASS K (2μm) and the MIPS1 (24μm) bands (Harvey et al. 2007b).

[d] "GO3" means the object was observed as part of the *Spitzer Space Telescope*'s cycle 3 program 30223, PI: K. Pontoppidan; 'c2d' means the object was observed as part of the c2d 2nd Look program, PI: N. Evans.

[e] Flux ratio between 30 and 13 μm.

Table 4.2 – Characteristics of YSOs in Serpens

No.	Emb	PAH^a	$S_{9.8}$	$S_{11.3}$	$S_{\text{peak}}^{10\mu m}$	$S_{19.0}$	$S_{23.8}$	$S_{\text{peak}}^{20\mu m}$	Cluster	Spectral Type
1	–	–	2.53	2.13	2.59	2.00	1.52	1.96		K2
3	–	–	1.49	1.35	1.50	1.33	1.23	1.26	D	M0
6	–	–	2.12	1.73	2.13	1.61	1.33	1.55	D	K5
7	–	–	1.38	1.25	1.38	1.39	1.34	1.36	D	M0
8	–	–	1.15	1.43	1.14	1.21	1.45	0.82	D	
9	–	–	1.64	1.48	1.68	2.24	1.97	2.27	D	
10	–	–	1.25	1.29	1.28	1.47	1.29	1.51	D	
13	–	–	–	–	–	1.33	1.87	1.29	D	
14	–	–	1.45	1.38	1.45	1.65	1.43	1.53		M2
15	–	–	2.67	2.19	2.68	2.59	2.07	2.46	D	
20	–	–	–	–	–	0.90	0.85	1.13		
21	–	–	1.09	1.17	1.10	1.45	1.57	1.34		
24	–	–	–	–	–	1.69	1.29	1.30		
26	Y	–	–	–	–	–	–	–		
27	Y	–	–	–	–	–	–	–		
28	Y	–	–	–	–	–	–	–		
29	–	–	1.84	1.59	1.89	1.56	2.03	1.73		M2
30	–	–	1.32	1.38	1.34	1.22	1.18	1.33		M1
31	–	–	1.76	1.72	1.76	0.99	0.92	0.99		
32	–	–	–	–	–	0.89	1.13	0.72		
36	–	–	1.47	1.35	1.48	1.41	1.31	1.41		K5
38	–	–	–	–	–	–	–	–		
39	Y	–	–	–	–	–	–	–	E	
40	–	–	1.06	1.20	1.09	1.29	1.26	1.25	E	M7
41	–	–	1.73	1.77	1.93	3.45	4.18	3.74	C	K2
42	–	–	–	–	–	–	–	–	E	
43	–	–	1.32	1.40	1.35	1.18	1.18	1.28		M0.5
44	Y	–	–	–	–	–	–	–	C	M6
45	Y	–	–	–	–	–	–	–	C	
47	Y	–	–	–	–	–	–	–	E	M5
48	–	–	1.22	1.21	1.26	1.12	1.05	1.18	E	M5.5
49	Y	–	–	–	–	–	–	–	C	
50	Y	–	–	–	–	–	–	–	C	
51	Y	–	–	–	–	–	–	–		
52	–	Y	–	–	–	–	–	–	E	G3
53	–	–	1.19	1.32	1.25	1.26	1.04	1.18		M2.5
54	–	–	1.13	1.26	1.21	1.19	1.47	1.07	C	
55	–	–	1.88	1.68	1.89	1.53	1.18	1.35	E	K2
56	–	–	1.56	1.49	1.55	1.32	1.23	1.41		
57	–	–	1.39	1.47	1.43	2.01	1.81	1.90	C	
58	–	–	1.09	1.15	1.16	1.13	1.20	1.33	C	K7
59	–	–	–	–	–	–	–	–	C	
60	–	–	1.00	1.08	1.01	1.27	1.25	1.26	C	M0.5
61	–	–	1.24	1.25	1.25	1.28	1.32	1.26	C	M0
62	–	–	–	–	–	1.21	1.31	1.26	C	K0
63	Y	–	–	–	–	–	–	–	C	
64	–	–	–	–	–	1.41	1.27	1.36	C	
65	–	–	1.00	1.10	1.00	1.21	1.12	1.06	C	
66	–	–	1.19	1.18	1.20	1.15	1.07	1.11	E	K5
67	Y	–	–	–	–	–	–	–	C	
69	–	–	–	–	–	2.14	2.17	2.27	B	
70	–	–	–	–	–	1.29	1.36	1.31	E	A3
71	–	–	1.50	1.49	1.48	2.48	2.86	2.51	E	M3
72	Y	–	–	–	–	–	–	–	C	
73	Y	–	–	–	–	–	–	–	C	
74	–	–	0.99	1.24	1.03	1.44	1.33	1.55	B	
75	–	–	1.37	1.37	1.38	1.64	1.35	1.50		
76	–	–	1.58	1.51	1.61	1.83	1.78	1.75		M1
79	Y	–	–	–	–	–	–	–	C	
80	–	–	1.27	1.39	1.29	0.96	0.92	0.98	B	
81	–	–	1.59	1.52	1.66	1.50	1.28	1.42		M5
82	–	–	1.31	1.23	1.27	1.14	0.90	1.15	E	M0
83	–	–	–	–	–	–	–	–	E	
86	–	–	1.80	1.61	1.83	1.28	0.98	1.23		M5.5
87	–	–	–	–	–	–	–	–	B	M4
88	–	–	2.58	2.75	2.53	1.70	1.41	1.47		M0.5
89	–	–	1.10	1.21	1.08	1.62	1.68	1.71	B	K5
90	–	–	1.19	1.19	1.21	1.54	1.62	1.67	B	
91	Y	–	–	–	–	–	–	–	E	K7
92	–	–	1.56	1.60	1.63	1.92	1.66	1.97	E	M0
94	–	–	1.14	0.85	0.99	0.46	0.53	0.54		

#	Emb	PAH[a]	$S_{9.8}$	$S_{11.3}$	$S^{10\mu m}_{peak}$	$S_{19.0}$	$S_{23.8}$	$S^{20\mu m}_{peak}$	Cluster	Spectral Type
96	–	–	1.35	1.23	1.34	1.53	1.48	1.41	E	M1
97	–	Y	–	–	–	–	–	–		M2
98	–	Y	–	–	–	–	–	–		A3
100	–	–	1.39	1.47	1.39	1.90	1.56	1.89		
101	–	–	1.60	1.55	1.63	1.95	1.65	1.92	B	
102	Y	–	–	–	–	–	–	–	B	
103	–	–	1.27	1.53	1.31	1.30	1.28	1.16		
104	–	–	1.50	1.67	1.53	1.96	1.70	1.90		
105	–	–	0.87	0.87	0.80	3.84	3.15	3.30		
106	–	–	1.19	1.28	1.19	1.22	1.42	1.61		M3
107	–	–	1.07	1.04	1.06	1.24	1.16	1.37		
109	–	–	–	–	–	1.58	1.31	1.51	B	
111	–	–	1.24	1.32	1.29	0.61	1.11	1.23		
113	–	–	1.10	1.25	1.12	1.76	1.82	1.91		K7
114	–	–	1.14	1.21	1.16	1.90	1.99	2.05	B	F9
115	–	–	1.43	1.36	1.45	2.22	2.06	2.11		M0.5
116	–	–	–	–	–	1.56	1.51	1.49	B	
117	–	–	1.37	1.38	1.40	1.87	1.68	1.81		K2
119	–	–	1.20	1.23	1.25	1.22	0.82	1.05	B	K7
120	–	Y	–	–	–	1.70	1.52	1.64	B	A2
122	–	–	1.22	1.17	1.21	0.90	1.08	1.09	B	M0
123	–	–	1.87	1.70	1.90	1.97	1.63	1.95	B	M0
124	–	–	1.09	1.15	1.13	1.06	1.15	1.08	B	M0
125	–	–	1.57	1.50	1.61	2.06	1.86	2.02	B	M0
127	–	–	–	–	–	1.85	1.71	2.00	B	M2
129	–	–	1.19	1.16	1.20	1.11	0.95	1.15		
130	–	–	–	–	–	1.39	1.24	1.23		K6
131	–	Y	–	–	–	–	–	–		A3
132	Y	–	–	–	–	–	–	–	B	
133	Y	–	–	–	–	–	–	–	B	
134	–	–	0.76	0.88	0.73	1.25	1.33	0.89	B	
135	Y	–	–	–	–	–	–	–	B	
136	–	–	1.08	0.98	1.07	1.30	1.38	1.54	B	
137	–	–	1.27	1.24	1.28	1.99	2.06	2.01	B	
139	–	–	–	–	–	1.88	1.50	1.76		A4
140	Y	–	–	–	–	–	–	–	B	
142	–	–	1.50	1.39	1.49	1.26	1.13	1.16	B	M4
143	–	–	–	–	–	1.42	1.26	1.47	B	
144	–	–	0.98	1.11	0.99	1.30	1.23	1.32	B	
145	–	–	–	–	–	1.27	1.26	1.32	B	G2.5
146	–	–	1.23	1.39	1.25	1.28	1.15	1.22	A	M4
147	–	–	1.41	1.51	1.46	1.40	1.23	1.42	B	
148	–	–	1.81	1.67	1.83	1.76	1.51	1.79	B	K7
149	–	–	1.90	1.65	1.89	1.47	1.31	1.43		M0

[a] All disk sources with PAH in emission show the features at 6.2, 7.7, 8.6, 11.2 and 12.8 μm.

Table 4.3 – Number of Objects in Tight Groups and Associations

	Embedded	Disks	Total
Cluster A	0	1	1^a
Cluster B	5	26	31
Group C	9	10	19
Group D	0	8	8
Group E	3	12	15

[a] The Serpens Core, or Cluster A, is not complete in these observations.

Table 4.4 – Statistics of the YSO Populations in Serpens and Taurus

	Embedded	Disks			
		PAH	Both 10 and 20 μm	Only 20 μm	Featureless
Serpens	18.3%	2.6%	60.0%	13.9%	4.3%
Taurus	20.1%	2.9%	57.6%	3.6%	18.7%

A.   Background Sources

Here the background contamination discussed in Section 4.3.1 is presented in three categories.

A.1   Background Stars

The IRS spectra of bright background stars, when seen through a molecular cloud, show the silicate feature at 10 μm in absorption and not in emission as for disk sources (see Section 4.3.3.3), on top of a falling infrared spectrum. Oliveira et al. (2009) identified candidate background stars based on optical spectra for 78 objects in this sample. After determining spectral types, extinctions and luminosities, those objects were placed in a Hertzsprung–Russell diagram (HRD) and compared with two sets of isochrones and mass tracks (Baraffe et al. 1998, Siess et al. 2000). 20 out of those 78 objects proved to be much too luminous to be at the distance of Serpens ($d = 259 \pm 13$pc, Straizys et al. 1996). Those objects were then classified as background sources, typically asymptotic giant branch (AGB) stars with dusty shells. Interestingly, 18 of the 20 objects classified as background in Oliveira et al. (2009) have IRS spectra characteristic of background sources; the other two objects, 81 and 86, show silicates in emission (just like those seen in circumstellar disks) and were then re-classified as YSOs.
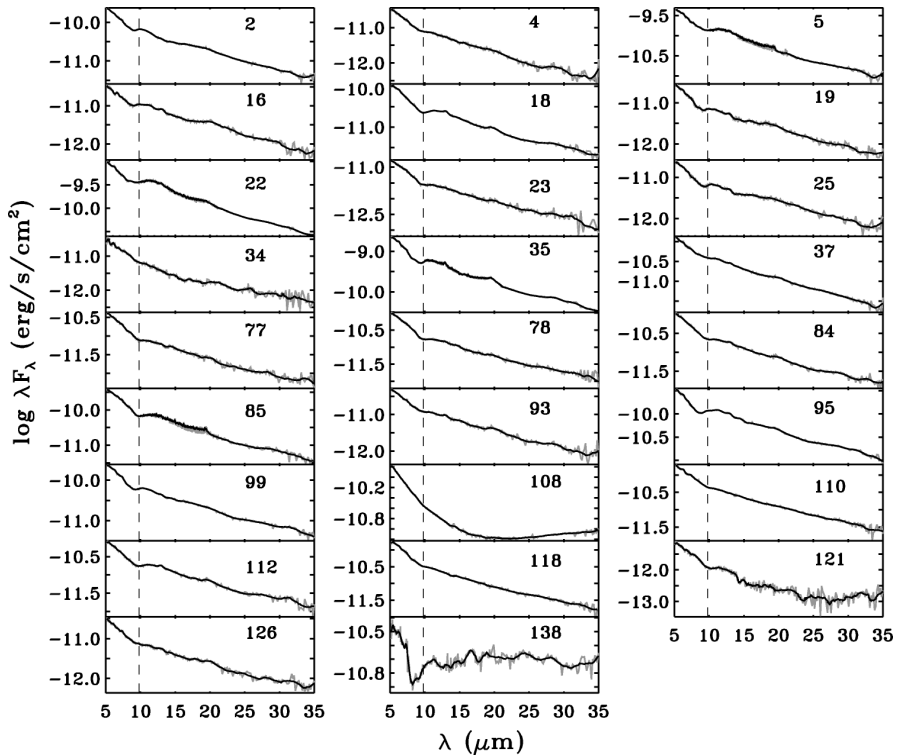
Figure A.1 − IRS spectra of the background stars toward Serpens with the characteristic 10 μm silicate absorption feature and falling SED. In gray are the original spectra, while in black a binned version is overplotted. The object number is indicated at the top right of each panel.

Besides these 18 objects, another 8 objects in this sample with falling mid-IR spectra show the 10 μm silicate feature in absorption (objects 19, 25, 37, 78, 95, 126 were not observed by Oliveira et al. 2009), leading to their classification as background stars. Alternatively, those eight objects could be highly extincted YSOs, with silicate features in absorption arising from such extinction. However, using the dense cloud dust properties, as in Section 4.3.3.5, an extinction of 10 mag would produce a $\tau_{9.7}$ of only 0.14 (see also Chiar et al. 2007). Since these objects do have silicate features in absorption, it is understood that they have high extinction (considerably higher than what is found for the cloud at their location). Thus, it is unlikely that they are actually highly extincted cloud members. Our working assumption is that these are background objects. These 26 spectra are shown in Figure A.1.

Figure A.2 – IRS spectra of the background galaxies toward Serpens, shown in rest-frame wavelength. The dashed lines indicate the rest-frame PAH features at 6.2, 7.7, 8.6, 11.2, 12.8, and 16.4 μm. The object number and z are indicated in each panel.
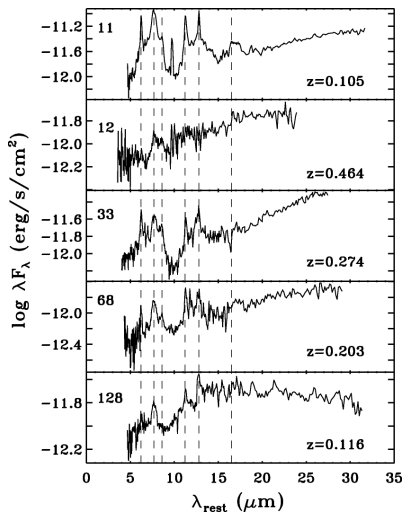
A.2   Background Galaxies

Five of the sources with clear PAH features show wavelength shifts in their line positions compared with galactic sources. These features thus allow us to identify them as background galaxies in this sample. PAHs are common features in most nearby galaxies with ongoing or recent star formation (Smith et al. 2007), and some contamination by background galaxies is expected (Papovich et al. 2004).

By identifying PAH features from their shape and pattern (Tielens 2008 and references therein), the observed wavelength ($\lambda_{\rm obs}$) can be related to the rest-frame wavelength ($\lambda_{\rm rest}$) of each feature through a redshift ($z = \frac{\lambda_{\rm obs}}{\lambda_{\rm rest}} - 1.0$). Between 3 (#12) and 5 (#11 and 68) PAH features are identified in each spectrum, and the redshift of each line is calculated. For a given object, the z values derived from the various lines agree within 2% and the mean of these values is taken as the redshift for that source. These five redshifted galaxies can be seen, in rest-frame wavelength, in Figure A.2.

Star-forming galaxies show strong correlations between the extinction-corrected Paschen α luminosity coming from H II regions and the luminosity at 24 μm due to the emission of dust heated by hot, young stars. Rieke et al. (2009) obtained power-law fits to the relation between the star formation rate (SFR) and the observed 24 μm flux densities ($f_{24,obs}$), parameterized with respect to z to take into account the fact that the rest-frame wavelengths sampled change with redshift (Equation 14 in their paper). In order to estimate the infrared luminosity (L(TIR)), we use their best-fit relations between the (rest) 24 μm luminosity, L(TIR) and SFR (Eqs. 11 and 25).

We have calculated SFRs[2] and $L(\mathrm{TIR})$ for the five background galaxies contaminating this sample. These results can be found in Table A.1. $L(\mathrm{TIR})$ ranges from a few times 10^{11} to a few times 10^{12} $L_\odot$, indicating that these galaxies are typical so-called luminous infrared galaxies (LIRGs, $L(\mathrm{TIR}) > 10^{11}$ $L_\odot$), while two are ultra-luminous (ULIRGs, $L(\mathrm{TIR}) > 10^{12}$ $L_\odot$). The latter are a class of heavily obscured galaxies having enormous instantaneous SFRs that are often associated with merging galaxies (Sanders & Mirabel 1996). These galaxies are very rare locally and become more common at high redshift. Their space density rises by about a factor of 10 from $z = 0$ to $z \sim 0.5$ (Magnelli et al. 2009), consistent with the relatively high redshifts found ($z \sim 0.3 - 0.5$). Furthermore, due to its high SFR and the empirical correlation between the infrared and radio emission from starburst galaxies (Condon 1992), the ULIRG #12 at $z = 0.46$ can be identified with a previously unidentified radio source in the NRAO VLA Sky Survey (NVSS J182817+001604, Condon et al. 1998).

The inferred SFRs range between 11 and 731 $\mathrm{M_\odot\ yr^{-1}}$, compared to a Milky Way SFR of about 3–5 $\mathrm{M_\odot\ yr^{-1}}$ (Prantzos & Aubert 1995, and references therein). For further reference, the SFR of Serpens is 5.7×10^{-5} $\mathrm{M_\odot\ yr^{-1}}$ (Evans et al. 2009). Even though the star formation observed in those galaxies is due to high mass star-forming regions such as Orion, the high SFRs in the LIRGs and ULIRGs found are equivalent to $10^5 - 10^7$ molecular clouds such as Serpens!

A.3   High Ionization Object

One of the objects, #17 (SSTc2dJ18282720+0044450), in this sample presents very strong emission lines that do not seem compatible with YSOs. Figure A.3 shows a blow-up of the spectrum, identifying the high ionization lines at $z = 0$. The source itself is highly reddened, being barely detected in IRAC1 (3.5 μm) but very prominent in MIPS1 (24 μm), with a 3–24 μm slope of 1.82. Two types of galactic objects show such high excitation lines: dusty planetary nebulae and supernova remnants. The IRS spectrum of this object (#17) resembles those of shocked ejecta of supernova remnants, as in Sandstrom et al. (2009) and Ghavamian et al. (2009) and that of planetary nebulae such as LMC 78, shown in Bernard-Salas et al. (2009).

The spectrum also shows PAH emission at 6.2, 7.7, 11.2, and 12.8 μm. Optical and near-IR spectra are necessary to confirm the nature of this object.

---

[2]The SFRs correspond to an IMF according to Chabrier (2003).
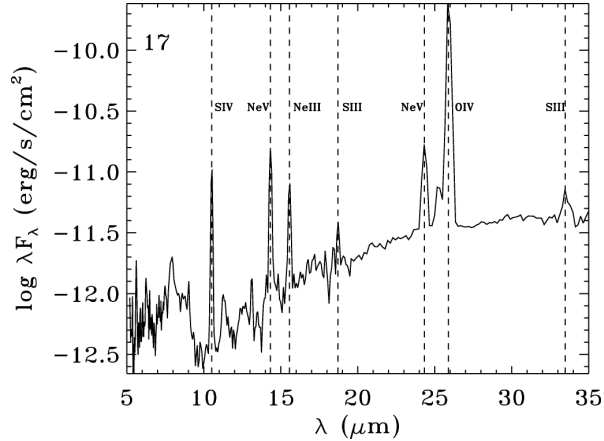
Figure A.3 – IRS spectra of the planetary nebula candidate (#17) found among this sample, presenting high ionization lines.

Table A.1 – Characteristics of the Background Galaxies

No.	z	24μm (Jy)	SFR (M$_\odot$ yr^{-1})	L(TIR) ($L_\odot$)	Type
11	0.1051	0.01800	16	1.5×10^{11}	LIRG
12[a]	0.4637	0.00893	731	4.8×10^{12}	ULIRG
33	0.2742	0.01490	217	1.6×10^{12}	ULIRG
68	0.2032	0.00909	47	4.0×10^{11}	LIRG
128	0.1164	0.01010	11	1.1×10^{11}	LIRG

[a] NVSS J182817+001604.

5

VLT/X-shooter Spectroscopy of a Dusty Planetary Nebula Discovered with Spitzer/IRS

As part of a mid-infrared spectroscopic survey of young stars with the *Spitzer Space Telescope*, an unclassified red emission line object was discovered. Based on its high ionization state indicated by the *Spitzer* spectrum, this object could either be a dusty Supernova Remnant (SNR) or a Planetary Nebula (PN). In this research note, the object is classified and the available spectroscopic data are presented to the community for further analysis. UV/optical/NIR spectra were obtained during the science verification run of the VLT/X-shooter. A large number of emission lines are identified allowing the determination of the nature of this object. The presence of strong, narrow ($\Delta v \sim 8 - 74$ km s^{-1}) emission lines, combined with very low line ratios of, e.g., [N II]/Hα and [S II]/Hα show that the object is a Planetary Nebula (PN) that lies at an undetermined distance behind the Serpens Molecular Cloud. This illustrates the potential of X-shooter as an efficient tool for constraining the nature of faint sources with unknown spectral properties or colors.

Isa Oliveira, Roderik A. Overzier, Klaus M. Pontoppidan, Ewine F. van Dishoeck,
and Loredana Spezzi

5.1   Introduction

As part of a program with the InfraRed Spectrograph (IRS, Houck et al. 2004) onboard the *Spitzer Space Telescope* (SST, Werner et al. 2004) aimed at characterizing the circumstellar disks of a flux-limited sample of infrared-excess young stellar objects (YSOs) in the Serpens Molecular Cloud ($\alpha_{J2000}=18^h29^m49^s$, $\delta_{J2000}=+01^d14^m48^s$), an interesting object of unknown nature was discovered (SSTc2dJ18282720+0044450, or #17 in Oliveira et al. 2010, hereafter OL17). The very bright, high ionization emission lines seen in the mid-IR spectrum of this object are not consistent with it being a YSO.

Two types of galactic objects show such high excitation lines: dusty planetary nebulae (PNe, Bernard-Salas et al. 2009; Stanghellini et al. 2007; Guiles et al. 2007) and supernova remnants (SNRs, Sandstrom et al. 2009; Ghavamian et al. 2009). SNRs typically show very broad emission lines, produced by the high velocity shock waves (Fesen et al. 1985; Fesen & Hurford 1996; Stupar et al. 2007). PNe, on the other hand, are characterized by narrow emission lines arising from the low velocity expanding outer shells (Balick & Frank 2002; Górny et al. 2009). Both classes of objects have been extensively studied by several authors, although just a few are so dusty that they were initially discovered only at mid-infrared wavelengths. To distinguish between these two possibilities, further spectroscopy on OL17 was needed.

In this research note, we present the original IRS spectrum (§ 5.2) as well as follow-up VLT/X-shooter spectra obtained as part of the instrument science verification phase (§ 5.3) and report on our identification of this object as a PN (§ 5.4).

5.2   *Spitzer*/IRS Data

The IRS spectrum of OL17 ($\alpha_{J2000}=18^h28^m27.2^s$, $\delta_{J2000}=+00^d44^m45^s$) is presented in Figure 5.1. The data were obtained as part of the SST Cycle 3 program (GO3 30223, PI: Pontoppidan) in the low-resolution module ($R = \lambda/\Delta\lambda = 50 - 100$; Short Low [SL], 5.2 – 14.5 μm and Long Low [LL], 14.0 – 38.0 μm). See Oliveira et al. (2010) for further details on the program and the procedures for data reduction.

The spectrum is dominated by strong [O IV] emission[1] at 25.89 μm, and is accompanied by other prominent high ionization lines: [Ar III] (8.99 μm), [S IV] (10.51 μm), [Ar V] (13.07 μm), [Ne V] (14.32, 24.32 μm), [Ne III] (15.56 μm), and [S III] (18.71 μm, 33.48 μm). The equivalent width (EW) of these lines, calculated from Gaussian fits, as well as the lines fluxes are given in Table 5.1. Furthermore, the spectrum shows clear evidence for polycyclic aromatic hydrocarbon (PAH) emission (most notably at 6.2, 7.7, 11.2, and 12.8 μm). This emission most likely comes from a shell of dusty material that surrounds, and is illuminated by, the central object.

Because OL17 lies along the line of sight towards the Serpens Molecular Cloud,

---

[1]In principle, the [O IV] may suffer from contamination by [Fe II] at the resolution of the LL module, but this is ruled out in this case following our conclusion that this object is a PN and given that [Fe II] is relatively weak in such objects.
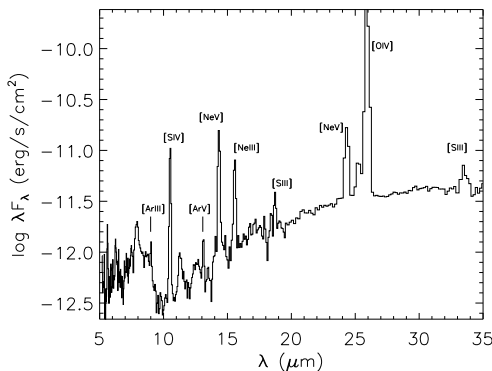
Figure 5.1 − IRS spectrum of OL17, a PN/SNR candidate found among the sample from Oliveira et al. (2010). The [O IV] line (25.89 μm) clearly dominates the spectrum.
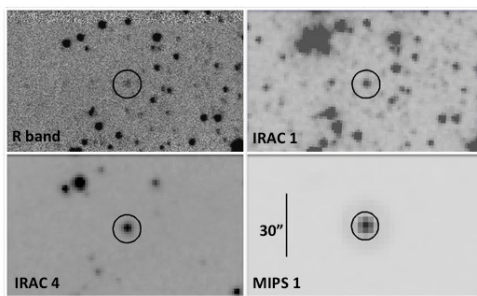
Figure 5.2 − Optical and infrared images showing the INT/WFC *R*-band (*top-left*), IRAC1 (*top-right*), IRAC4 (*bottom-left*) and MIPS1 (*bottom-right*). All three images display the same field of view and a length scale of 30″ is shown for reference.

it is appreciably extincted due to foreground material ($A_V \sim 6.0$ mag). It has weak detections in both the *R*-band and IRAC1 band (3.5 μm), but is very prominent in the MIPS1 band (24 μm). It has a 3–24 μm slope ($\frac{d \log(\lambda F_\lambda)}{d \log(\lambda)}$) of $\approx$1.8. As shown in Fig. 5.1, the MIPS1 band is dominated by the very strong [O IV] emission line. This explains why this object appeared so red in the infrared color-magnitude diagrams, leading to the original misclassification of the source as an YSO. The optical *R*-band image (taken with the Wide Field Camera (WFC) on the Isaac Newton Telescope (INT, Spezzi et al. 2010), the IRAC1 (Harvey et al. 2006) and MIPS1 (Harvey et al. 2007a) images are shown in Figure 5.2 (see Table 5.2 for the photometry in different bands).

5.3   X-shooter Data

X-shooter (D'Odorico et al. 2006) is a unique multi-wavelength (300-2480 nm) medium resolution ($R = 4000 - 14000$) spectrograph on the Cassegrain focus of UT2 on the Very Large Telescope (VLT). It consists of 3 independent arms that give simultaneous spectra long-ward of the atmospheric cutoff in the UV ('UVB' arm), optical ('VIS' arm) and near-infrared ('NIR' arm). The data[2] presented here were obtained as part of the X-shooter 2nd science verification phase (SV2), during September–October 2009 (60.A-9416(A), PI: Oliveira). The total amount of time awarded was 1 hr, during which integrations of 2760, 2560 and 2880s were obtained with the UVB, VIS and NIR arms, respectively. The observations were performed using the $1'' \times 12''$ slit in 'nodding-on-slit' mode to perform adequate background subtraction in the near-infrared. The spectral resolving powers achieved in this setup were $\approx$5100 in UVB and NIR and $\approx$8800 in VIS. The raw science data consist of images containing highly curved, multi-order, two-dimensional spectra that need to be rectified, wavelength calibrated and merged using an input model configuration that describes the X-shooter spectral format. Data reduction was performed using an internal release of the X-shooter data calibration pipeline version 0.9.4 (Andrea Modigliani, private communication), together with the 'com4' reference calibration data.

The extracted one-dimensional spectra are shown in Figure 5.3, and show many strong, narrow emission lines especially in the optical and NIR. These spectra were extracted using an aperture with a length of $\sim 5''$ in order to include most of the extended emission seen along the slit (see top panel of Figure 5.4 for the two-dimensional spectrum). Since OL17 is seen through a dense molecular cloud, it is very faint. These exposures therefore allowed the detection of the brightest emission lines, but not the continuum. Although the spectra were not flux calibrated, the analysis below makes use of line ratios involving lines that are closely spaced in wavelength, and not affected by strong telluric absorption bands.

The main lines identified, and their EWs are listed in Table 5.3. The EWs were calculated by fitting the lines and a possible continuum using a Gaussian profile and should be considered (3σ) lower limits, as the continuum was not detected at a sufficient signal-to-noise in these observations. It is interesting to note that the faintness of the continuum as inferred from the optical spectrum implies that the object detected in the R-band image shown in the top-left panel of Fig. 5.2 must consist almost entirely of Hα line emission.

5.4   Results

According to Fesen et al. (1985), the main quantitative criterion used to distinguish SNRs from PNe is the strength of the [S II] ($\lambda\lambda$6717, 6731 Å) emission lines relative to that of Hα. That is, [S II]/H$\alpha > 0.4$ for typical SNRs (Matonick & Fesen 1997; Blair & Long 2004). Furthermore, SNRs typically have very strong [N II] ($\lambda\lambda$6548,

---

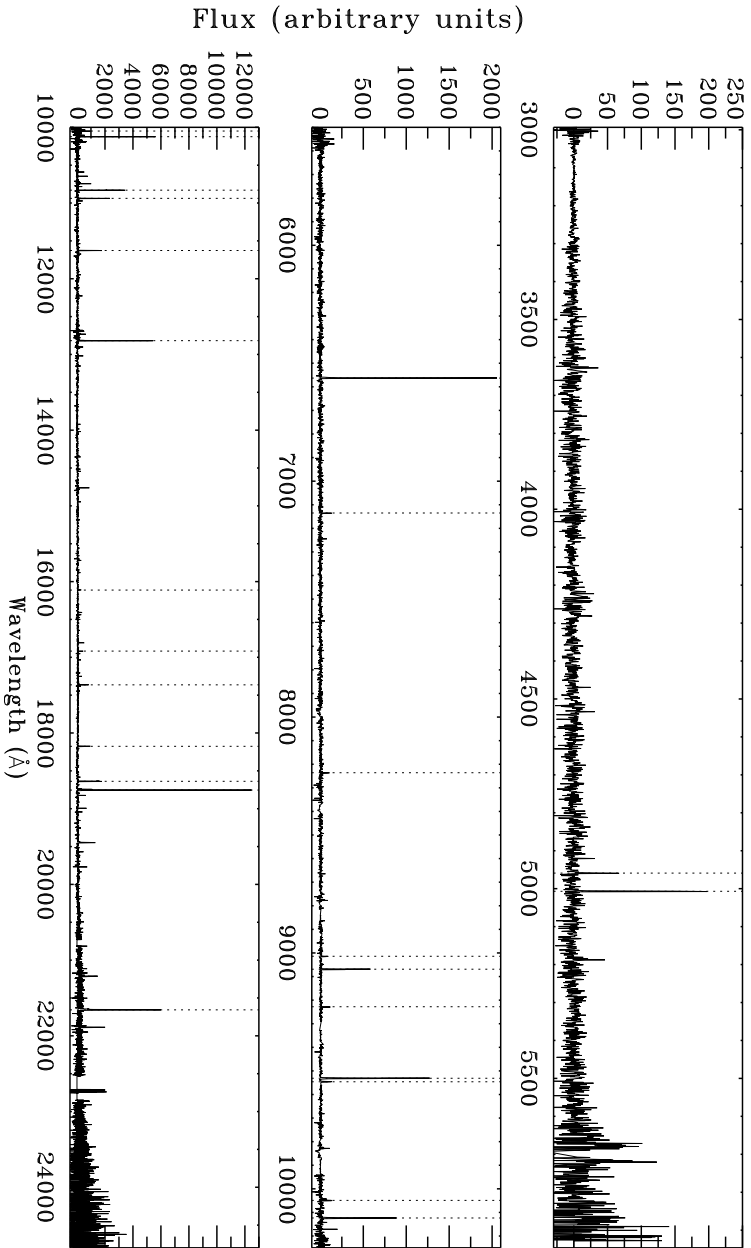[2]Program ID 60.A-9416(A)

Figure 5.3 – X-shooter spectra of OL17. Panels show the one-dimensional spectra extracted from the UV/blue (*top*), the visible (*middle*), and the near-infrared (*bottom*) arms. Dotted lines mark the major emission lines tabulated in Table 5.3.
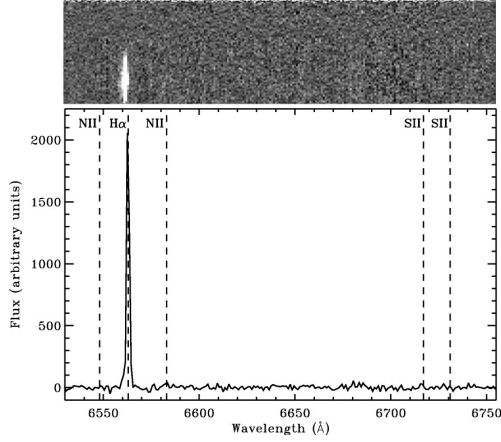
Figure 5.4 − A zoom-in of the optical spectrum covering Hα and the [N II] and [S II] line doublets. The weakness of [N II] and [S II] relative to Hα indicate that this object is a PN and not a SNR (see § 5.4 for details). The top panel shows the two-dimensional spectrum at corresponding wavelengths (white pixels indicate large, positive pixel values). The slit height measures 12″, while the spatial extent of the resolved Hα is about 6″.

6583 Å) emission. Figure 5.4 shows a zoom of the X-shooter/VIS spectrum in the wavelength range covering Hα and the [N II] and [S II] doublets as labelled. It is clearly seen that the [N II] and [S II] lines are not detected, while Hα is very strong. Upper limits for the undetected lines were derived, yielding a flux ratio of [N II]/Hα ∼ [S II]/Hα ≤ 0.06 (3σ). This value is well below the value of 0.4 quoted above as the lower threshold for SNRs.

Furthermore, SNRs have broad, high velocity ($\Delta v \geq 300$ km s^{-1}) emission lines, while PNe show much narrower lines. This criterion was used by Fesen & Milisavljevic (2010) to classify the Spitzer source J222557+601148, previously believed to be a young galactic SNR (Morris et al. 2006), as a PN. As it can be seen in Figure 5.5 for a selection of lines in all 3 X-shooter arms, the typical FWHM for lines seen in these data are <15–74 km s^{-1} (deconvolved for instrumental resolutions of FWHM 59 in UVB/NIR and 34 km s^{-1} in VIS). The low velocity of the lines, combined with the low ratio of [S II]/Hα ≤ 0.06 allow the conclusion that OL17 is a PN and not a SNR.

The electron density (n_e) can be derived from the ratio between the [S III] lines at 33.48 and 18.71 μm in the IRS spectrum, using the method of Herter et al. (1982). The ratio of [S III]λ33.48/18.71∼ 1.9 yields an electron density of ∼1–100 cm^{-3} (Rubin 1989), where the large range is due to the fact that we are in the regime where the line ratio is least sensitive to the density. However, we should note that the line at 33.47μm appears to be twice as broad as that at 18.71μm (possibly due to a data artifact). If we conservatively estimate that ∼ 50% of the flux in this line is indeed due to contamination, the [S III] 33.47/18.71 ratio would yield a density of order 1000 cm^{-3}, more typical of PNe. In any case, we note that unlike the intensity ratios
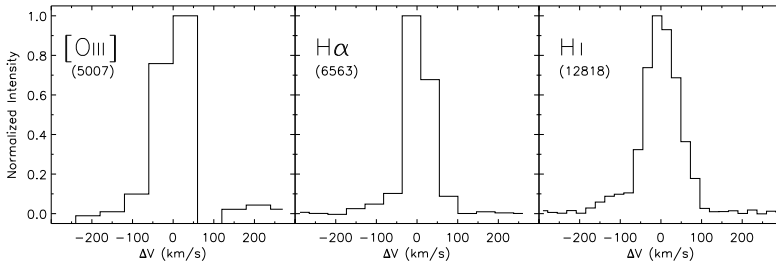
Figure 5.5 – A sample of the narrow emission lines present in the X-shooter spectra: [O III] (*left*) at 5007 Å, Hα (*middle*) and H I (Paβ, *right*) at 12818 Å.

of [NII]/Ha and [S II]/Hα, n_e is a rather poor diagnostic for discriminating between SNRs and PNe as both span a similarly large range in density (Sabbadin et al. 1977; Riesgo & López 2005).

While the distance to this PN cannot be determined without knowing its intrinsic size, its angular extent of ≈6″ (determined from the extent of Hα in the two-dimensional spectrum) and the large extinction it experiences in the bluer parts of the spectrum suggest that this PN must lie at a distance of at least several kpc, i.e., firmly behind the Serpens Molecular Cloud (distance of ∼415 pc, Dzib et al. 2010).

We summarize as follows:

1. The *Spitzer*/IRS spectrum of SSTc2dJ18282720+0044450 from Oliveira et al. (2010) shows strong high ionization emission lines, compatible with both Planetary Nebulae and Supernova Remnants, one of only a handful such objects identified in the mid-IR to date.
2. High quality VLT/X-shooter spectra, obtained during the science verification run, show a wealth of narrow emission lines in the UV/blue, optical and near-IR arm data, illustrating the enormous potential of X-shooter as a diagnostic tool for optically faint sources discovered at other wavelengths.
3. The optical line ratios are compatible with PNe and not with SNRs: the low values measured for the line ratio [S II]/Hα, one of the main diagnostic criteria for distinguishing between the two types of objects, allows a straightforward classification of this object as a PN.
4. The PN interpretation is confirmed by the relative narrow (Δv ∼8–74 km s^{-1}) width of the emission lines seen throughout the spectra.
5. This previously unknown PN now has public, high-quality spectroscopic data covering a very large bandwidth ranging from 0.3 to 35 μm. We encourage the use of these data[3] by the community wishing to further study objects of this class.

---

[3]The data are publicly available through the data archives at ESO and the Spitzer Science Center:
`http://archive.eso.org/eso_archive_main.html`
`http://ssc.spitzer.caltech.edu/spitzerdataarchives/`

References

Balick, B., & Frank, A. 2002, ARA&A, 40, 439

Bernard-Salas, J., Peeters, E., Sloan, G. C., Gutenkunst, S., Matsuura, M., Tielens, A. G. G. M., Zijlstra, A. A., & Houck, J. R. 2009, ApJ, 699, 1541

Blair, W. P., & Long, K. S. 2004, ApJS, 155, 101

D'Odorico, S., et al. 2006, Proc. SPIE, 6269, 98

Dzib, S., Loinard, L., Mioduszewski, A. J., Boden, A. F., Rodríguez, L. F., & Torres, R. M. 2010, ApJ, 718, 610

Fesen, R. A., Blair, W. P., & Kirshner, R. P. 1985, ApJ, 292, 29

Fesen, R. A., & Hurford, A. P. 1996, ApJS, 106, 563

Fesen, R. A., & Milisavljevic, D. 2010, AJ, 139, 2595

Ghavamian, P., Raymond, J. C., Blair, W. P., Long, K. S., Tappe, A., Park, S., & Winkler, P. F. 2009, ApJ, 696, 1307

Górny, S. K., Chiappini, C., Stasińska, G., & Cuisinier, F. 2009, A&A, 500, 1089

Guiles, S., Bernard-Salas, J., Pottasch, S. R., & Roellig, T. L. 2007, ApJ, 660, 1282

Harvey, P. M., et al. 2006, ApJ, 644, 307

Harvey, P. M., et al. 2007, ApJ, 663, 1139

Herter, T., Briotta, D. A., Jr., Gull, G. E., Shure, M. A., & Houck, J. R. 1982, ApJ, 262, 164

Houck, J. R., et al. 2004, ApJS, 154, 18

Matonick, D. M., & Fesen, R. A. 1997, ApJS, 112, 49

Morris, P. W., Stolovy, S., Wachter, S., Noriega-Crespo, A., Pannuti, T. G., & Hoard, D. W. 2006, ApJ, 640, L179

Oliveira, I., et al. 2010, ApJ, 714, 778

Riesgo, H., & López, J. A. 2005, Rev. of Mex. Astron. and Astroph., 41, 57

Rubin, R. H. 1989, ApJS, 69, 897

Sabbadin, F., Minello, S., & Bianchini, A. 1977, A&A, 60, 147

Sandstrom, K. M., Bolatto, A. D., Stanimirović, S., van Loon, J. T., & Smith, J. D. T. 2009, ApJ, 696, 2138

Spezzi, L., Merin, B., Oliveira, I., van Dishoeck, E. F., & Brown, J. M. 2010, A&A, 513, A38

Stanghellini, L., García-Lario, P., García-Hernández, D. A., Perea-Calderón, J. V., Davies, J. E., Manchado, A., Villaver, E., & Shaw, R. A. 2007, ApJ, 671, 1669

Stupar, M., Parker, Q. A., Filipović, M. D., Frew, D. J., Bojičić, I., & Aschenbach, B. 2007, MNRAS, 381, 377

Werner, M. W., Gallagher, D. B., & Irace, W. R. 2004, Advances in Space Research, 34, 600

Table 5.1 – Emission lines identified in the IRS spectrum of OL17 (Figure 5.1).

λ (μm)	Line	EW (μm)	Flux (erg/s/cm^2)
8.99	[Ar III]	0.08	6.15×10^{-15}
10.51	[S IV]	2.91	1.26×10^{-13}
13.07	[Ar V]	0.14	6.89×10^{-15}
14.32	[Ne V]	3.23	1.88×10^{-13}
15.56	[Ne III]	1.11	8.30×10^{-14}
18.71	[S III]	0.23	2.03×10^{-14}
24.32	[Ne V]	1.45	1.92×10^{-13}
25.89	[O IV]	13.64	2.81×10^{-12}
33.48	[S III]	0.31	3.80×10^{-14}

Table 5.2 – Optical R-band magnitude and *Spitzer* IRAC/MIPS fluxes of OL17 (see also Figure 5.2).

R† (mag)	3.6 μm (mJy)	4.5 μm (mJy)	5.8 μm (mJy)	8.0 μm (mJy)	24.0 μm (mJy)
22.8	0.28	0.64	0.80	2.29	69.60

† From Spezzi et al. 2010.

Table 5.3 – Major emission lines identified in the X-shooter spectra (Figure 5.3). Equivalent widths (EW) given indicate (3σ) lower limits, due to the faintness of the continuum.

λ (Å)	Line	EW (Å)	λ (Å)	Line	EW (Å)
4959	[O III]	1.4	10831	He I	196.1
5007	[O III]	5.1	10938	H I	125.7
6563	Hα	47.1	11627	He II	100.4
7135	[Ar III]	2.6	12818	H I	290.5
8236	He II	2.9	16112	O I	21.9
9014	H I	2.4	16918	Al II	25.6
9069	[S III]	18.8	17364	Ne II	66.0
9229	H I	5.5	18176	Ne II	88.1
9531	[S III]	43.4	18638	Ne II	183.4
9546	H I	22.2	18754	N II	564.4
10049	H I	5.4	21657	Br γ	597.1
10123	He II	228.5			

6

On the Evolution of Dust Mineralogy: from Protoplanetary Disks to Planetary Systems

Mineralogical studies of silicate features emitted by dust grains in protoplanetary disks and Solar System bodies can shed light on the progress of planet formation. The significant fraction of crystalline material in comets, chondritic meteorites and interplanetary dust particles indicates a modification of the almost completely amorphous interstellar medium (ISM) dust from which they formed. The production of crystalline silicates, thus, must happen in protoplanetary disks, where dust evolves to build planets and planetesimals. Different scenarios have been proposed, but it is still unclear how and when this happens. This paper presents dust grain mineralogy (composition, crystallinity and grain size distribution) of a complete sample of protoplanetary disks in the young Serpens cluster. These results are compared to those in the young Taurus region and to sources that have retained their protoplanetary disks in the older Upper Scorpius and η Chamaeleontis stellar clusters, using the same analysis technique for all samples. This comparison allows an investigation of the grain mineralogy evolution with time for a total sample of 139 disks. The mean cluster age and disk fraction are used as indicators of the evolutionary stage of the different populations. Our results show that the disks in the different regions have similar distributions of mean grain sizes and crystallinity fractions ($\sim$10 – 20%) despite the spread in mean ages. Furthermore, there is no evidence of preferential grain sizes for any given disk geometry, nor for the mean cluster crystallinity fraction to increase with mean age in the 1 – 8 Myr range. The main implication is that a modest level of crystallinity is established in the disk surface early on ($\leq$ 1 Myr), reaching an equilibrium that is independent of what may be happening in the disk midplane. These results are discussed in the context of planet formation, in comparison with mineralogical results from small bodies in our own Solar System.

Isa Oliveira, Johan Olofsson, Klaus M. Pontoppidan, Ewine F. van Dishoeck,
Jean-Charles Augereau & Bruno Merín

6.1   Introduction

Protoplanetary disks originate from dense cloud material consisting of sub-μm sized, almost completely amorphous interstellar medium (ISM) dust grains (Beckwith et al. 2000; Li & Draine 2001; Kemper et al. 2004; Henning 2010). The dust and gas in these disks form the basic matter from which planets may form. At the same time, mineralogical studies of primitive solar system bodies suggest that a considerable fraction of the silicate grains in these objects are of crystalline nature (Wooden et al. 2007; Pontoppidan & Brearley 2010, and references therein). It is then naturally implied that the crystallinity fraction increases, through thermal and chemical modification of these solids during the general planet formation process, commonly referred to in the literature as "disk evolution".

As time passes, the small dust responsible for the infrared (IR) excess observed around young stars is subjected to different processes that affect, and will eventually determine how this progression will end. Planets and planetary systems have been observed around hundreds of stars other than the Sun, showing that this result is rather common (Udry & Santos 2007). IR observations have revealed a great number of *debris disks*, composed of large planetesimal rocks and smaller bodies, around a variety of stars spanning a large range in spectral types and ages (Rieke et al. 2005; Bryden et al. 2006; Su et al. 2006; Gautier et al. 2007; Carpenter et al. 2009). A few debris disks are known to harbor planets (e.g., β Pictoris and Fomalhaut, Lagrange et al. 2010; Kalas et al. 2008), although it is still unclear whether this is often true (Kóspál et al. 2009). The majority of main-sequence stars show no signs of planets or debris within the current observational limitations, however, indicating that the disks around such stars at the time of their formation have dissipated completely, leaving no dust behind to tell the story. Which processes are important and determinant for the aftermath of disk evolution are still under debate, and this topic is the subject of many theoretical and observational studies over the last decade, stimulated in large by recent IR and (sub-)millimeter facilities.

Specifically on the subject of the mineralogical composition, spectra from the ground and the *Infrared Space Observatory* gave the first clues of a potential link between crystalline material in protoplanetary disks and comets. A great similarity was noted between the spectra of the disk around the Herbig star HD 100546 and that of comet Hale-Bopp (Crovisier et al. 1997; Malfait et al. 1998). More recently, the InfraRed Spectrograph (IRS, $5 - 38$ μm, Houck et al. 2004) on-board the *Spitzer Space Telescope* allowed an unprecedented combination of high sensitivity and the ability to observe large numbers of disks, down to the brown dwarf limit. The shape of the silicate features probed by the IRS spectra at 10 and 20 μm is affected by the composition, size and structure of its emitting dust. Amorphous silicates show broad smooth mid-IR features, while the opacities of crystalline grains show sharp features due to their large-scale lattice arrangement, such that even small fractions of crystalline grains produce additional structure in the silicate features (Min et al. 2005; Bouwman et al. 2008; Juhász et al. 2009; Olofsson et al. 2010). Because most

protoplanetary disks are optically thick at optical and IR wavelengths, the silicate features observed in the mid-IR are generally emitted by dust in the optically thin disk surface only. To probe the disk midplane, observations at longer wavelengths are necessary. Additionally, the emission at 10 and 20 μm has been shown to arise from different grain populations, probing different radii (Kessler-Silacci et al. 2006; Olofsson et al. 2009, 2010). While the 10 μm feature probes a warmer dust population, at ≤ 1 AU for T Tauri stars, the dust emitting at 20 μm is colder, further out and deeper into the disk (Kessler-Silacci et al. 2007).

Two methods have been proposed to explain the formation of crystal grains: thermal annealing of amorphous grains or vaporization followed by gas-phase condensation. Both methods require high temperatures (above $\sim$1000 K, Fabian et al. 2000; Gail 2004) which is inconsistent with outer disk temperatures. However, crystalline grains have been observed in outer, as well as in inner disks (van Boekel et al. 2004). Large-scale radial mixing has been invoked to explain the presence of crystals at low temperatures in the outer disk (Bockelée-Morvan et al. 2000; Gail 2004; Ciesla 2009). A third proposed formation mechanism for crystal formation is that shock waves could locally heat amorphous silicates and crystallize them (Desch & Connolly 2002; Harker & Desch 2002).

From protoplanetary disks to comets, several authors have attempted to infer the dust composition from IRS spectra and laboratory data on amorphous and crystalline silicate dust, using a variety of analysis techniques. Whether for individual objects (Forrest et al. 2004; Merín et al. 2007; Pinte et al. 2008; Bouy et al. 2008), for mixed disk samples (Bouwman et al. 2001; Apai et al. 2005; van Boekel et al. 2005; Bouwman et al. 2008; Olofsson et al. 2009, 2010; Juhász et al. 2010), or systematic studies of the disk population of a given star-forming region (Sicilia-Aguilar et al. 2009; Watson et al. 2009; Sargent et al. 2009), it has been shown that a significant mass fraction of the dust in those disks must be in crystalline form. However, the many studies dealing with the mineralogical composition of dust to date focus on a specific region or object, failing to investigate the hypothesis that the crystallinity fraction is a measure of the evolutionary stage of a region. That is, no study in the literature has yet investigated an increase of crystallinity fraction with cluster age.

Mineralogical studies of Solar System bodies show a range of crystallinity fractions. Evidence from primitive chondrites shows that the abundance of crystalline silicate material varies from nearly nothing up to $20 - 30$ % (e.g. Acfer 094 and ALH77307, Pontoppidan & Brearley 2010 and references therein). Oort cloud comets, with long periods and large distances from the Sun, have inferred crystallinity fractions up to $60 - 80$ % (e.g. Hale-Bopp, Wooden et al. 1999, 2007). Jupiter-family, or short period comets, have lower fractions, up to $\sim$35 % (e.g. 9P/Tempel 1, Harvey et al. 2007b; 81P/Wild 2, Zolensky et al. 2006). This discrepancy in fractions points to the existence of a radial dependence in crystallinity fraction in the protoplanetary disk around the young Sun (Harker et al. 2005). It is important to note that those values are model dependent, and the use of large amorphous grains ($10 - 100$ μm) can lead to systematically lower crystalline fractions (Harker et al. 2002). This is evident for

Hale-Bopp, where Min et al. (2005) find a much lower fraction ($\sim$7.5 %) than other authors, using a distribution of amorphous grain sizes up to 100 μm. What is clear is that even within the discrepancies, the crystallinity fractions derived for Solar System bodies are appreciably higher than those derived for the ISM dust ($< 2\%$, Kemper et al. 2004). Recent *Spitzer* data indicate further similarities between crystalline silicate features seen in comets or asteroids with those seen in some debris disks around solar mass stars (Beichman et al. 2006; Lisse et al. 2007, 2008). One proposed explanation is that the observed spectral features in the disk result from the catastrophic break-up of a single large body (a 'super comet') which creates the small dust particles needed for detection. At the even earlier protoplanetary disk stage, there is limited observational evidence for radial gradients in crystallinity from mid-infrared interferometry data, with higher crystallinity fractions found closer to the young stars (van Boekel et al. 2004; Schegerer et al. 2008). All of this suggests that the crystallization occurs early in the disk evolution and is then incorporated into larger solid bodies.

Besides dust composition, the evolution of grain sizes is an essential indicator of disk evolution. The initially sub-μm size ISM grains must grow astounding 14–15 orders of magnitude in diameter if they are to form planets. If grains were to grow orderly and steadily, theoretical calculations predict disks to have fully dissipated their small grains within $\sim 10^5$ years (Weidenschilling 1980; Dullemond & Dominik 2005). The fact that many disks a few Myr old are observed to have small grains (Hernández et al. 2008) poses a serious problem for the paradigm that grain growth is a steady, monotonic process in disk evolution and planet formation. Additionally, small dust has been observed in the surface layers of disks in clusters of different ages and environments for hundreds of systems. The implications, as discussed most recently by Oliveira et al. (2010) and Olofsson et al. (2010), is that small grains must be replenished by fragmentation of bigger grains, and that an equilibrium between grain growth and fragmentation is established. Oliveira et al. (2010) have shown that this equilibrium is maintained over a few million years, as long as the disks are optically thick, and is independent of the population or environment studied.

In this paper we present a comprehensive study of the mineralogical composition of disks around stars in young star-forming regions (where most stars are still surrounded by optically thick disks) and older clusters (where the majority of disks has already dissipated). Correlating the results on mean size and composition of dust grains per region, obtained in a homogeneous way using the same methodology, with the properties of small bodies in our own Solar System can put constraints on some of the processes responsible for disk evolution and planet formation. The Serpens Molecular Cloud, whose complete flux-limited YSO population has been observed by the IRS instrument (Oliveira et al. 2010), is used as a prototype of a young star-forming region, together with Taurus, the best studied region to date. The sources that have retained their protoplanetary disks in the η Chamaeleontis and Upper Scorpius clusters are used to probe the mineralogy in the older bin of disk evolution.

Section 6.2 describes the YSO samples in the 4 regions mentioned. The *Spitzer* IRS observations and reduction are explained. The spectral decomposition method B2C

(Olofsson et al. 2010) is briefly introduced in § 6.3, and its results for individual and mean cluster grain sizes and composition are shown in § 6.4. In § 6.5 the results are discussed in the context of time evolution. There we demonstrate that no evolution is seen in either mean grain sizes or crystallinity fractions as clusters evolve from ∼1 to 8 Myr. The implications for disk formation and dissipation, and planet formation are discussed. In § 6.6 we present our conclusions.

6.2   Spitzer IRS Data

The four regions presented here were chosen due to the availability of complete sets of IRS spectra of their IR-excess sources, while spanning a wide range of stellar characteristics, environment, mean ages and disk fractions (the disk fraction of Serpens is still unknown, see Table 6.1).

The IRS spectra of a complete flux-limited sample of young stellar objects (YSO) in the Serpens Molecular Cloud have been presented by Oliveira et al. (2010), based on program ID #30223 (PI: Pontoppidan). As detailed there, the spectra were extracted from the basic calibration data (BCD) using the reduction pipeline from the Spitzer Legacy Program "From Molecular Cores to Planet-Forming Disks" (c2d, Lahuis et al. 2006). A similarly large YSO sample in the Taurus star-forming region has been presented by Furlan et al. (2006). IRS spectra of all 18 members of the η Chamaeleontis cluster were first shown by Sicilia-Aguilar et al. (2009), while the spectra of 26 out of the 35 IR-excess sources in the Upper Scorpius OB association were shown by Dahm & Carpenter (2009) (the remaining 9 objects were not known at the time the observations were proposed). For the latter 3 regions, the post-BCD data were downloaded from the SSC pipeline (version S18.4) and then extracted with the Spitzer IRS Custom Extraction software (SPICE, version 2.3) using the batch generic template for point sources. As a test, the IRS spectra of the YSOs in Serpens were also reduced using SPICE to ensure that both pipelines produce nearly identical results. On visual inspection, no discrepancies were found between the results from the two pipelines, all objects showed the exact same features in both spectra. The similarity in outputs is such that the effects on the spectral decomposition results are within the cited error bars.

Since the spectral decomposition method applied here aims to reproduce the silicate emission from dust particles in circumstellar disks, the sample has been limited to spectra that show clear silicate features. The few sources with PAH emission have been excluded from the sample. PAH sources amount to less than 8% in low-mass star-forming regions (Geers et al. 2006; Oliveira et al. 2010). Furthermore, spectra with very low signal-to-noise ratios (S/N) are excluded from the analysed sample in order to guarantee the quality of the results. In addition, for objects #114 and 137 in Serpens, and 04370+2559 and V955Tau in Taurus the warm component fit contributes to most of the spectrum, leaving very low fluxes to be fitted by the cold component. This produces large uncertainties in the cold component fit, and they are therefore not further used in the analysis. The low S/N objects rejected amount to less than

10 % of each of the Serpens and Taurus samples, so the statistical results derived here should not be affected by this removal. The final sample of 139 sources analysed is composed of 60 objects in Serpens, 66 in Taurus, 9 objects in Upper Scorpius, and 4 in η Chamaeleontis. The statistical uncertainties of the spectra were estimated as explained in Olofsson et al. (2009).

The great majority of the objects studied here are low-mass stars (spectral types K and M, see Tables A.1 and A.2). The study of mineralogical evolution across stellar mass is not the focus of this paper. Such a study would require a separate paper, in which the same techniques are used for low- and intermediate-mass stars. Thus, the statistical results derived in the following sections concern T Tauri stars, and not necessarily apply to intermediate-mass Herbig Ae/Be stars.

6.3 Spectral Decomposition and the B2C Method

In order to reproduce the observed IRS spectra of these circumstellar disks the B2C decomposition method, explained in detail and tested extensively in Olofsson et al. (2010), is applied. Two dust grain populations, or components, at different temperatures (warm and cold) are used in the method, in addition to a continuum emission. The warm component reproduces the 10 μm feature, while the cold component reproduces the non-negligible residuals at longer wavelengths, over the full spectral range (see Figure 6.1). Each component, warm and cold, is the combination of five different dust species and three grain sizes for amorphous silicates or two grain sizes for crystalline silicates.
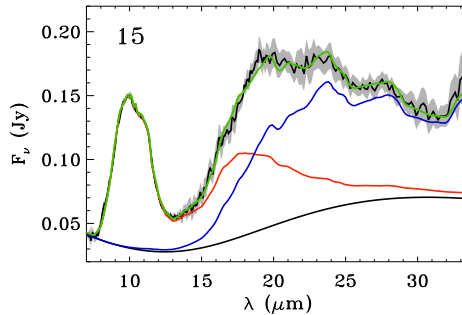
Figure 6.1 – Example of the B2C modeling for object #15 in Serpens. The down-most black line is the estimated continuum for this source. The dark gray line is the fit to the warm component (fitting well the 10 μm feature) and the black line is the fit to the cold component (contributing mostly to longer wavelengths). The light gray line is the final fit to the entire spectrum. The original spectrum is shown in black with its uncertainties in light grey. (A color version of this figure is available in the online journal)

The three amorphous species are silicates of olivine stoichiometry ($MgFeSiO_4$), silicates of pyroxene stoichiometry ($MgFeSiO_6$), and silica (SiO_2). The two crystalline species are both Mg-rich end members of the pyroxene and olivine groups, enstatite

(MgSiO$_3$) and forsterite (Mg$_2$SiO$_4$). As further explained in Olofsson et al. (2010), the theoretical opacities of the amorphous species are computed assuming homogeneous spheres (Mie theory), while those for the crystalline species use the distribution of hollow spheres (DHS, Min et al. 2005) theory so that irregularly shaped particles can be simulated.

In addition, the three grain sizes used are 0.1, 1.5 and 6.0 μm, representing well the spectroscopic behaviour of very small, intermediate-sized and large grains. For the crystalline species, however, the code is limited to only 2 grain sizes (0.1 and 1.5 μm). This restriction is imposed because large crystalline grains are highly degenerate with large amorphous grains (as can be seen in Figure 1 of Olofsson et al. 2010), and because the production of large 6.0 μm pure crystals is not expected via thermal annealing (Gail 2004).

The B2C method itself consists of three steps. First, the continuum is estimated and subtracted from the observed spectrum. The adopted continuum is built by using a power-law plus a black-body at temperature T_{cont}. The power-law represents the mid-IR tail of emission from the star and inner disk rim. The black-body is designed to contribute at longer wavelengths, and is therefore constrained to be less than 150 K. Each dust component is then fitted separately to the continuum-subtracted spectrum.

The second step is to fit the warm component to reproduce the 10 μm silicate feature between $\sim$7.5 and 13.5 μm. This is done by summing up the 13 mass absorption coefficients ($N_{\mathrm{species}} = 5$, $N_{\mathrm{sizes}} = 3$ or 2, for amorphous and crystalline species, respectively), multiplied by a black-body $B_\nu(T_{\mathrm{w}})$ at a given warm temperature T_{w}.

The third step is to fit the residuals, mostly at longer wavelengths, over the entire spectral range (5 – 35 μm). This is done in a similar manner, for a given cold temperature T_{c}. The final fit is a sum of the three fits described, as can be seen in Figure 6.1. The entire fitting process is based on a Bayesian analysis, combined with a Monte Carlo Markov chain, in order to randomly explore the space of free parameters. The resulting mean mass-average grain size is the sum of all sizes fitted, each size being weighted by their corresponding masses, as:

$$\langle a_{\mathrm{warm/cold}} \rangle = \left(\sum_{j=1}^{N_{\mathrm{sizes}}} a_j \sum_{i=1}^{N_{\mathrm{species}}} M_{\mathrm{w/c},i}^j \right) \times \left(\sum_{j=1}^{N_{\mathrm{sizes}}} \sum_{i=1}^{N_{\mathrm{species}}} M_{\mathrm{w/c},i}^j \right)^{-1} \qquad (6.1)$$

where $a_1 = 0.1\,\mu$m (small grains), $a_2 = 1.5\,\mu$m (intermediate-sized grains) and $a_3 = 6\,\mu$m (large grains). Further details and tests of the B2C procedure can be found in Olofsson et al. (2010). That paper also demonstrates that the procedure is robust for statistical samples, and that the relative comparisons between samples, which are the focus of this paper, should not suffer from the assumptions that enter in the procedure. The robustness of the procedure is evaluated by fitting synthetic spectra, and is discussed in detail in their Appendix A. The influence of the continuum estimate is also discussed, especially for the cold component for both grain sizes and crystallinity fractions, and it is shown that prescriptions that do not use large 6 μm grains (which are, to some degree, degenerate with the continuum) give fits that are not so good.

For the amorphous grains, the B2C procedure uses the Mie scattering theory to compute mass absorption coefficients. However, Min et al. (2007) found that they could best reproduce the extinction profile toward the galactic center using the DHS scattering theory, with a maximum filling factor of 0.7. The most striking difference between Mie and DHS mass absorption coefficients is seen for the O–Si–O bending mode around 20 μm. Here we investigate the influence of the use of DHS instead of Mie for amorphous grain with an olivine or pyroxene stoichiometry. We conducted tests on a sub-sample of 30 objects (15 in Serpens and 15 in Taurus). The conclusion of such tests is that it has a small influence on the quantities we discuss in this study. For the warm component of the 30 objects, we find a change in the mean crystallinity fraction of -1.6% (the mean crystallinity for this sub-sample using DHS is 9.3% versus 10.9% using Mie), which is in the range of uncertainties claimed in this study. We also computed the mean slope of grain size distributions to gauge the effect of using DHS on grain sizes. On average, the grain size distribution indices are steeper by $\sim$0.2 (with a mean slope of -3.01 for this sub-sample using DHS versus -2.80 using Mie). Therefore, our main conclusions are preserved for the warm component. Concerning the cold component, the inferred crystallinity fraction using DHS is 22.5% versus 15.1% with Mie, a mean increase of 7.4%. For the mean slope of grain size distributions, a negligible decrease is found (-3.07 using DHS versus -3.01 for Mie). Again, the differences found are within our significant errors for the cold component and do not change any of our conclusions.

It is important to note that the S/N generally degrades at longer wavelengths when compared to shorter wavelengths. The lower S/N reflect on the cold component fits and will most likely result in larger uncertainties. We evaluate that the fits to the cold component are reliable and add important information on the dust mineralogy (albeit with larger uncertainties) and thus those results are included in the following discussion.

6.4   Results

The IRS spectra of the 139 YSOs with IR excess discussed in § 6.2 were fitted with the B2C spectral decomposition procedure. The relative abundances derived for all objects are shown in Appendix A. The S/N drops considerably for the long wavelength module of some of the objects studied (including all objects in Upper Scorpius and η Chamaeleontis). For this reason, the cold component could not be satisfactorily fitted and no results for this component are presented for these sources (see Appendix A).

Due to the large number of objects, these results allow statistical studies on both the mineralogy and size distribution of the grains that compose the optically thin surface layers of disks in each cluster studied. The mean abundances of each species per region are presented in Table 6.2, where it can be seen that the majority of the dust studied is of amorphous form. In Table 6.3 the mean mass-average grain sizes and crystallinity fractions per region are shown. Mean sizes are in the range $1-3$ μm, without significant difference between regions. These results are discussed in detail

in the following sections.

It is important to note that the comparison of results derived here for the different regions is valid because the same method, with exact same species, is used for all sources. The comparison of samples analyzed in distinct ways can lead to differences in results that do not correspond to real differences in composition. Nevertheless, in § 6.4.5 the results presented here are compared to literature results for the same objects, when available, with generally good agreement.

6.4.1   Grain Sizes

The mean mass-averaged grain sizes for the warm ($\langle a_{\mathrm{warm}} \rangle$) and cold ($\langle a_{\mathrm{cold}} \rangle$) components are shown in Figure 6.2, for Serpens and Taurus (for the objects in Upper Sco and η Cha no results for the cold component are not available, see Appendix A). It is seen that the two clouds overlap greatly, and that the grain sizes derived from the different temperature components do not seem to correlate. To quantify this correlation, a Kendall τ correlation coefficient can be computed together with its associated probability P (between 0 and 1). $\tau = 1(-1)$ defines a perfect correlation (anti-correlation), and $\tau = 0$ means that the datasets are completely independent. A small P, on the other hand, testifies to how tight the correlation is. For the warm and cold mean mass-averaged grain sizes for both clouds, τ is found to be 0.14, with $P = 0.07$. This lack of correlation indicates that different processes are likely responsible for regulating the size distribution at different radii (Olofsson et al. 2010).
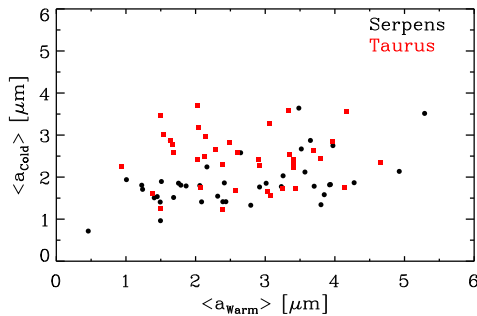
Figure 6.2 – Mass-averaged mean grain sizes for the warm ($\langle a_{\mathrm{warm}} \rangle$) and cold ($\langle a_{\mathrm{cold}} \rangle$) components. Black dots are the objects in Serpens, and gray squares are the objects in Taurus. (A color version of this figure is available in the online journal)

Although the average grain size in the warm component is bigger than that in the cold component within a given star-forming region, as shown in Table 6.3, this difference is mostly not significant. However, Figures 6.2 and 6.3 clearly show a difference between the range of grain sizes spanned in both components, with $\langle a_{\mathrm{cold}} \rangle$ never reaching near the biggest grain size modeled (6.0 μm) for any object. A possible explanation for larger grains at smaller radii, suggested by Sargent et al. (2009), is

that grains coagulate faster in the inner disk where dynamical timescales are shorter. However as discussed by Oliveira et al. (2010) and in § 6.5.1, the mean dust size at the disk surface is not regulated by grain growth alone, but also by fragmentation and vertical mix. This means that faster coagulation at smaller radii cannot be uniquely responsible for bigger grains in the inner disk. Future modeling should try to understand this difference in mean grain sizes observed.
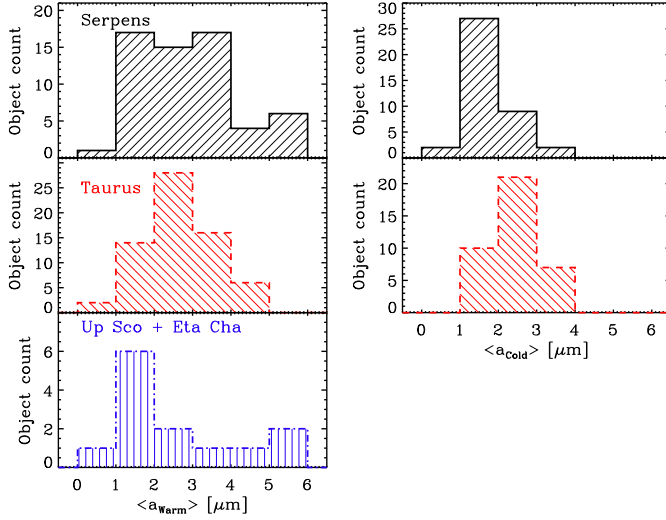
Figure 6.3 – Distribution of mass-averaged mean grain sizes for the warm ($\langle a_{\mathrm{warm}} \rangle$, left panel) and cold ($\langle a_{\mathrm{cold}} \rangle$, right panel) components. Due to the low number statistics, the objects in Upper Sco and η Cha have been merged together as an older cluster. (A color version of this figure is available in the online journal)

Furthermore, Serpens and Taurus occupy an indistinguishable locus in Figure 6.2, explicitly seen in Figure 6.3. A two sample Kolmogorov-Smirnov test (KS-test) was performed and the results show that the null hypothesis that the two distributions come from the same parent population cannot be rejected to any significance (14%). The older regions, although lacking statistical significance, show a distribution of mass-average grain sizes in the same range probed by the young star-forming regions (Figure 6.3). This supports the evidence that the size distribution of the dust in the surface layers of disks is statistically the same independent of the population studied (Oliveira et al. 2010).

The results here confirm those from Olofsson et al. (2010) that the mean differential grain size distributions slope for the three grain sizes considered are shallower than the reference MRN differential size distribution ($\alpha = $ -3.5). The mean grain size distributions slopes (α) for each region can be found in Table 6.3.

6.4.2   Disk Geometry

The amount of IR-excess in a disk is directly related to its geometry (Kenyon & Hartmann 1987; Meeus et al. 2001; Dullemond et al. 2001). Specifically using the IRS spectra, disk geometry can be inferred from the flux ratio between 30 and 13 μm (F_{30}/F_{13}, Brown et al. 2007; Oliveira et al. 2010; Merín et al. 2010). A flared geometry ($1.5 \lesssim F_{30}/F_{13} \lesssim 5$), with considerable IR excess and small dust, allows the uppermost dust layers to intercept stellar light at both the inner and outer disk. For flat disks ($F_{30}/F_{13} \lesssim 1.5$) with little IR excess, only the inner disk can easily intercept the stellar radiation as the outer disk is shadowed. Moreover, cold or transitional disks are interesting objects that present inner dust gaps or holes, producing a region with little or no near-IR excess ($5 \lesssim F_{30}/F_{13} \lesssim 15$). It is interesting to explore the effect of disk geometry on both the mean mass-average grain sizes and crystallinity fractions of the disks studied.
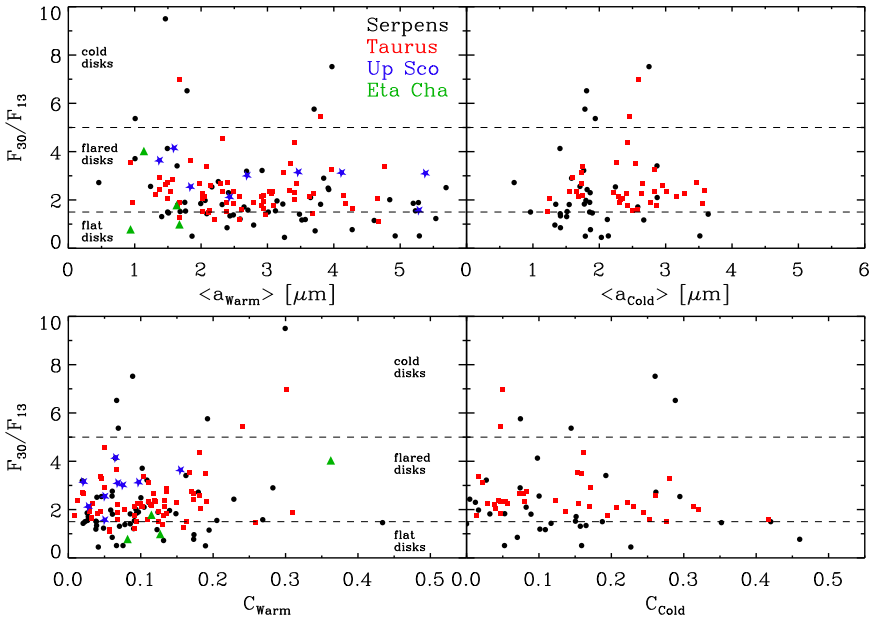
Figure 6.4 – Top: Flaring index F_{30}/F_{13}, used as a proxy for disk geometry, versus warm (left) and cold (right) mass-averaged mean grain sizes. Bottom: F_{30}/F_{13} versus warm (left) and cold (right) crystallinity fractions. The YSOs in Serpens (black dots), Taurus (gray squares), Upper Sco (gray stars), and η Cha (gray triangles) are compared. (A color version of this figure is available in the online journal)

Figure 6.4 shows F_{30}/F_{13} as a proxy for disk geometry compared with the mean mass-averaged grain sizes and crystallinity fractions for both components and all regions studied here. No preferential grain size (correlation coefficient $\tau = -0.14$, $P = 0.02$, and $\tau = 0.07$, $P = 0.33$ for warm and cold components, respectively) nor
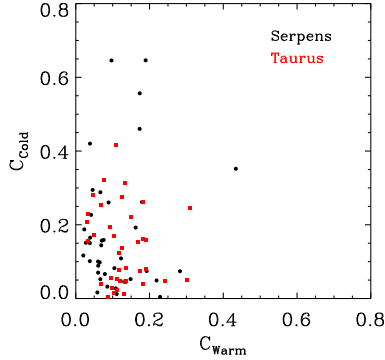
Figure 6.5 – Crystalline fraction of the warm and cold components in Serpens (black dots) and Taurus (gray squares). (A color version of this figure is available in the online journal)

crystallinity fraction ($\tau = 0.09$, $P = 0.10$ for the warm, and $\tau = -0.19$, $P = 0.01$ for the cold component) is apparent for any given disk geometry. Similar scatter plots result for the mean mass-average grains sizes for only amorphous ($\tau = -0.12$, $P = 0.08$ for the warm, and $\tau = 0.13$, $P = 0.11$ for the cold component), or only crystalline grains ($\tau = 0.08$, $P = 0.17$ for the warm, and $\tau = -0.13$, $P = 0.10$ for the cold component). Furthermore, no clear separation is seen between the different regions studied. The statistically relevant samples in Serpens and Taurus define a locus where the majority of the objects is located in each plot, which is followed by the lower number statistics for older regions. Figure 6.4 therefore shows not only that grain size and crystallinity fraction are not a function of disk geometry, but also that younger and older regions show similar distributions of those two parameters.

6.4.3 Crystallinity Fraction

The crystallinity fractions derived from the warm and cold components (C_{Warm} and C_{Cold}, respectively) for Serpens and Taurus are show in Figure 6.5. No strong trend of warm and cold crystallinity fractions increasing together is seen ($\tau = 0.10$, with $P = 0.10$ for the entire sample). This fact implies that, if an unique process is responsible for the crystallization of dust at all radii, this process is not occurring at the same rate in the innermost regions as further out in the disk. This is opposite to the conclusion of Watson et al. (2009), who derive a correlation between inner and outer disk crystallinity from the simultaneous presence of the 11.3 and 33 μm features. The opacities of the crystalline species are more complex than those two features alone, making the analysis here more complete than that of Watson et al. (2009). Our finding that the fraction of crystalline material in disk surfaces varies with radius can constrain some of the mechanisms for formation and distribution of crystals.

A wider spread in crystallinity fraction is observed for the cold component than
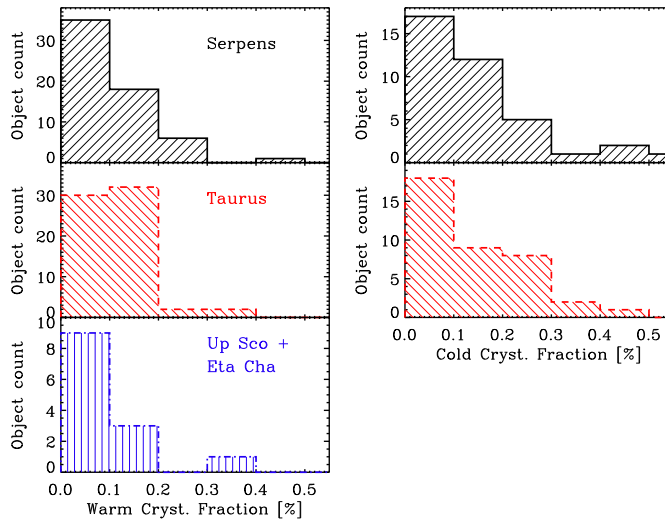
Figure 6.6 – Distribution of crystalline fractions for Serpens (top), Taurus (middle), and Upper Sco and η Cha combined (bottom). Similar distributions and the same range of fractions are seen for all clusters. (A color version of this figure is available in the online journal)

for the warm component (Figure 6.6), which is reflected in the mean crystallinity fractions for each sample (Table 6.3). This discrepancy could be real, or an artifact due to the signal-to-noise ratio (S/N) being frequently lower at longer wavelengths (cold component) than that at shorter wavelengths (warm component), introducing a larger scatter. The difference in Serpens is more significant ($\langle C_{\mathrm{warm}} \rangle \simeq 11.0\%$ and $\langle C_{\mathrm{cold}} \rangle \simeq 17.5\%$). The left panel of Figure 6.7 shows the cumulative fractions as functions of crystallinity fractions. Despite small differences between the warm (red line) and cold (blue line) components, the two cumulative fractions have similar behavior. If this difference is true, there is a small fraction of T Tauri disks with a higher cold (outer) than warm (inner) crystallinity fraction. This finding contrasts with that derived by van Boekel et al. (2004) for the disks around 3 Herbig stars. Their spatially resolved observations infer higher crystallinity fractions in the inner than in the outer disks, albeit based on only 10 μm data. A larger sample of objects with good S/N including both 10 and 20 μm data is needed to better constrain this point. In addition, Figure 6.6 shows that younger and older clusters have similar distributions of crystallinity fractions.

As discussed by many authors, both the grain size and the degree of crystallinity affect the silicate features, therefore it is interesting to search for trends between these two parameters. In Figure 6.8, the mass-average grain sizes are compared to the crystallinity fraction for both warm (left panel) and cold (right panel) components. No obvious trends are seen in either component, neither any separation between regions. This result supports the discussion of Olofsson et al. (2010) that whatever processes
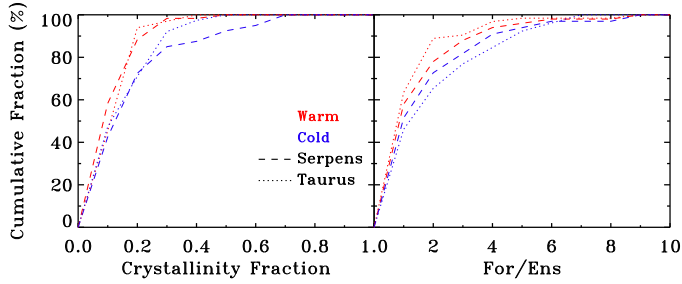
Figure 6.7 – Left: Cumulative fractions of the crystallinity fractions, for Serpens (dashed line) and Taurus (dotted line). Right: Cumulative fraction of the ration between the forsterite and enstatite fractions, for Serpens (dashed line) and Taurus (dotted line). The warm component is shown in light gray while the cold component is dark gray. (A color version of this figure is available in the online journal)

govern the mean grain size and the crystallinity in disks, they are independent from each other.
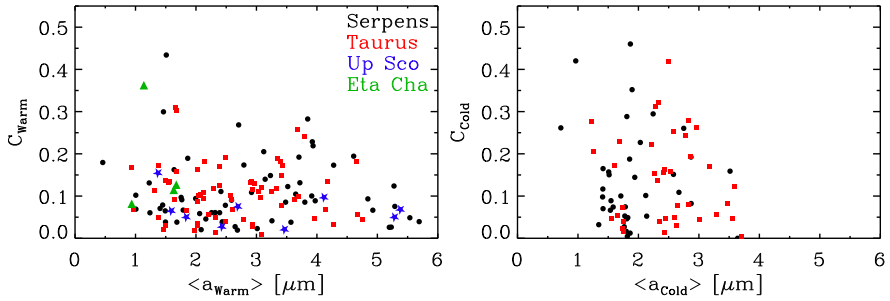
Figure 6.8 – Mass-averaged mean grain sizes versus the crystalline fraction for Serpens (black dots), Taurus (gray squares), Upper Sco (gray stars), and η Cha (gray triangles). (A color version of this figure is available in the online journal)

6.4.3.1   Enstatite vs. Forsterite

The disk models of Gail (2004) consider chemical equilibrium of a mixture of solid and gas at high temperatures, allowing radial mixing of material. These models predict a predominance of forsterite in the innermost regions of the disk, while enstatite dominates at lower temperatures (being converted from forsterite). From the observational point of view, data on disks around T Tauri (Bouwman et al. 2008) and Herbig Ae/Be stars (Juhász et al. 2010) have shown the opposite trend: enstatite is more concentrated in the inner disk, while forsterite dominates the colder, outer disk region. Bouwman et al. (2008) interpret this result as a radial dependence of the species formation mechanisms, or a non-equilibrium of the conditions under which

the species formed, contrary to the models assumptions.

For the regions presented in this study, it can be seen in Table 6.2 for mean cluster values and in Tables A.1 and A.2 for individual objects that the results derived from this study generally follow those of Bouwman et al. (2008), with more enstatite in the warm component and, to a lesser extent, more forsterite in the cold component. The right panel of Figure 6.7 illustrates this for the cumulative fraction of the forsterite over enstatite ratios for individuals disks. However, this trend is not very significant given the uncertainties.

6.4.4   The Silicate Strength-Shape Relation

A correlation between the shape and the strength of the 10 μm silicate feature from disks has been discussed extensively in the literature (van Boekel et al. 2003; Kessler-Silacci et al. 2006; Olofsson et al. 2009; Pascucci et al. 2009; Oliveira et al. 2010; Olofsson et al. 2010). Synthetic 10 μm features generated for different grain sizes and compositions have been shown to fit well with observations, yielding grain size as the important parameter responsible for such a relationship. The degree of crystallinity of the dust also plays a role on the shape of this feature. However, as clearly shown for EX Lup (Ábrahám et al. 2009), and supported by models (Min et al. 2008; Olofsson et al. 2009), an increase in crystallinity fraction does not change the strength of the feature, even though its shape does change. Crystallinity is then understood as responsible for the scatter in the strength-shape relationship, and not the relationship itself. As a result, the strength and shape of the 10 μm silicate feature yield the typical size of the grains in the upper layers of the disk at a few AU from the star (Kessler-Silacci et al. 2007). The top panel of Figure 6.9 shows the results for Serpens, Taurus, Upper Sco and η Cha. The bottom panel presents the median values per region, indicating the 15 – 85 percentile ranges of the distributions. Overlaid are the models of Olofsson et al. (2009) for different grain sizes (0.1 – 6.0 μm) generated for amorphous silicates of olivine and pyroxene stoichiometry, and a 50:50 mixture. The difference in mean ages does not correspond to a significant difference in mean grain sizes between the different regions.

With the mean grain sizes derived from the spectral decomposition, it is possible to further explore the validity of using the strength of the 10 μm silicate feature to trace the sizes of grains in the surfaces of disks. The left panel of Figure 6.10 shows the correlation between $\langle a_{\mathrm{warm}} \rangle$ and $S_{\mathrm{peak}}^{10\mu\mathrm{m}}$ for all 4 samples. The Kendall τ coefficient of -0.29, $P = 0.01$ supports the effectiveness of $S_{\mathrm{peak}}^{10\mu\mathrm{m}}$ as a proxy for grain sizes, with smaller values of $S_{\mathrm{peak}}^{10\mu\mathrm{m}}$ implying larger grain sizes.

On the other hand, it is also possible to test how the degree of crystallinity can influence the strength of the 10 μm silicate feature. The lack of correlation between C_{warm} and $S_{\mathrm{peak}}^{10\mu\mathrm{m}}$ (τ = -0.07, P = 0.14), shown in the right panel of Figure 6.10 for all samples, supports that the degree of crystallinity is not the dominant parameter setting the strength of the 10 μm silicate feature. These results argue against the results of Sargent et al. (2009) that find a high crystallinity fraction and small grains
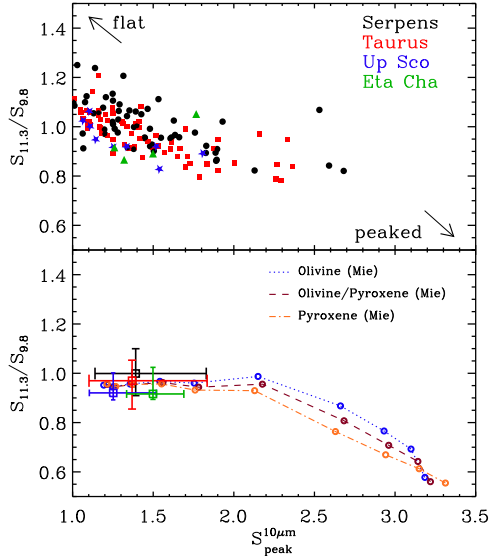
Figure 6.9 – Top: The ratio of normalized fluxes at 11.3 to 9.8 μm ($S_{11.3}/S_{9.8}$) is plotted against the peak at 10 μm ($S_{\mathrm{peak}}^{10\mu\mathrm{m}}$) for Serpens (black dots), Taurus (gray squares), Upper Scorpius (gray stars), η Chamaeleontis (gray triangles). Bottom: Squares show the median values and crosses indicate the 15 – 85 percentile ranges of the distributions (top panel). Colored curves are derived from theoretical opacities for different mixtures by Olofsson et al. (2009). The open circles correspond to different grain sizes, from left to right 6.25, 5.2, 4.3, 3.25, 2.7, 2.0, 1.5, 1.25, 1.0 and 0.1 μm. (A color version of this figure is available in the online journal)
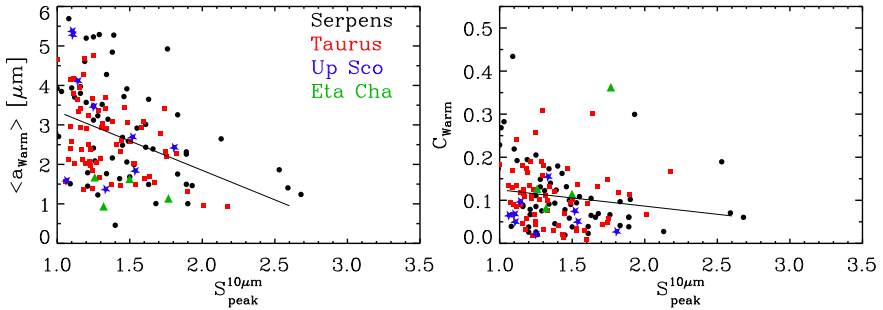
Figure 6.10 – Left panel: Strength of the 10 μm silicate feature ($S_{\mathrm{peak}}^{10\mu\mathrm{m}}$) versus the mass-averaged mean grain size for the warm component. Right panel: Strength of the 10 μm silicate feature versus crystalline fraction for the warm component. The best fit relationships are shown for reference. Symbols as in Figure 6.9. (A color version of this figure is available in the online journal)

fitting low strengths of the 10 μm silicate feature. Although it may be possible to fit a few spectra with a certain prescription, a good model should be able to explain

the robust relationship between the strength and shape of the 10 μm silicate feature observed for large numbers of disks. Despite the many processes able to change the shape or the strength of this feature, only grain size has so far demonstrated capability to explain the observed trend. Our conclusion is that $S_{\mathrm{peak}}^{10\mu m}$ and dust sizes are appropriately correlated.

6.4.5 Comparison with Other Studies

Dust composition results are available in the literature for the disks in Taurus and η Cha (see Table 6.4 for an overview). Sicilia-Aguilar et al. (2009) present their analysis in η Cha considering the same 5 dust species and three grain sizes (enstatite in their model is the only species for which only the 2 smaller grain sizes are considered), but for a distribution of temperatures derived using the Two Layer Temperature Distribution (TLTD, Juhász et al. 2009) decomposition procedure. For the same 4 objects, their mean amorphous fraction is 80.1 $\pm$ 9.3 %. This result is consistent with the 82.8 $\pm$ 12.9 % mean amorphous fraction found here. The mean crystalline fractions derived are 18.4 $\pm$ 10.7 % with TLTD and 17.1 $\pm$ 12.8 % derived here.

Sargent et al. (2009) present their decomposition procedure for 65 YSOs in Taurus. This method also takes into consideration a warm and a cold temperature, and makes use of two amorphous species (olivine and pyroxene) with two grain sizes (small and large), and 3 crystalline species (enstatite, forsterite and crystalline silica) of a single size. Their mean warm amorphous fraction is 82.9 $\pm$ 19.3 % and warm crystalline fraction is 17.1 $\pm$ 19.3 %, while here the derived fractions are 89.0 $\pm$ 6.6 % and 10.9 $\pm$ 6.6 % for the warm amorphous and crystalline fractions, respectively. For the cold component, Sargent et al. (2009) derive a mean cold amorphous fraction of 77.3 $\pm$ 19.9 % and cold crystalline fraction of 22.6 $\pm$ 19.9 %, while here the values are 85.9 $\pm$ 10.6 % and 13.9 $\pm$ 10.5 %, respectively. The consistently lower amorphous (higher crystalline) fractions found by Sargent et al. (2009) could be a result of their choice to use silica in crystalline rather than amorphous form (as used here).

6.5   Discussion

6.5.1   Dust Characteristics

Section 6.4 has shown that the disk populations in the four regions presented here, young and older, have very similar distributions in the two main dust parameters: grain size and composition. The large number of objects in the two young regions studied occupy a region in parameter space of either grain size or crystallinity fraction that is also populated by the small number of older disks. The grain sizes derived for the cold component never reach the biggest grain size modeled (6 μm), different from the warm component results that span the entire range in sizes. The crystallinity fraction does not seem to be correlated with mean grain size, warm or cold. Whatever processes are responsible for the crystallization of the initially amorphous grains, they should not only be independent from the processes that govern the grain size distribu-

tion, but they should also be able to work on bigger amorphous grains. Alternatively, the crystalline lattice should be able to keep itself regular during the coagulation of small crystalline dust to create big crystalline grains. The correlation between the strength of the 10 μm feature and the mean grain size in disk surfaces, combined with the lack of correlation between crystallinity fraction and $S_{\mathrm{peak}}^{10\mu\mathrm{m}}$, supports the wide usage of $S_{\mathrm{peak}}^{10\mu\mathrm{m}}$ as a proxy for dust size in literature (van Boekel et al. 2003; Kessler-Silacci et al. 2006; Pascucci et al. 2009).

Bouwman et al. (2008) found a strong correlation between disk geometry and the strength of the 10 μm silicate feature for a very small sample of T Tauri stars (7 disks), which points to flatter disks having shallower 10 μm features (i.e., big grains in the disk surface). Using results from similar decomposition procedures, Olofsson et al. (2010) and Juhász et al. (2010) confirm this trend for larger samples of T Tauri (58 disks) and Herbig Ae/Be stars (45 disks), respectively. Those trends are much weaker than that found by Bouwman et al. (2008), showing a larger spread. For the current even larger sample (139 disks), no significant trend is seen, indicating that the earlier small sample trends may have been affected by a few outliers. This result is similar to that found by Oliveira et al. (2010) for a large YSO sample (~ 200 objects) using the strength of the 10 μm silicate feature as a proxy for grain size (Figure 14 in that paper). As discussed by Oliveira et al., the models of sedimentation only of Dullemond & Dominik (2008) expect a strong correlation of larger grains in flatter disks that is not seen. This means that sedimentation alone cannot be responsible for the distribution of mean grain sizes in the upper layers of protoplanetary disks around T Tauri stars. Furthermore, the lack of correlation between crystallinity fraction and disk geometry is not in support of the results of Watson et al. (2009) and Sargent et al. (2009), who find a link between increasing crystallinity fraction and dust sedimentation.

As discussed in Oliveira et al. (2010) for Serpens and Taurus, and confirmed by the addition of considerably older samples, there is no clear difference in the mean grain sizes in the disk surfaces with mean cluster age, which can be seen in Figure 6.11. This evidence supports the discussion in that paper that the dust population observed in the disk surface cannot be a result of a progressive, monotonic change of state from small amorphous grains, to large, more crystalline grains, or 'grain growth and processing'. The fact that the distribution of grain sizes in the upper layers of disks does not change with cluster age implies that an equilibrium of the processes of dust growth and fragmentation must exist, which also supports the existence of small grains in disks that are millions of years old whereas dust growth is a rapid process (Weidenschilling 1980; Dullemond & Dominik 2005). That small dust is still seen in disks in older regions like Upper Sco and η Cha argues that this equilibrium of processes is maintained for millions of years, as long as the disks are optically thick, but independent of them having a flared or flatter geometry.

Figure 6.11 – Left: Mean mass-average grain sizes vs. disk fraction. Serpens is not included because its disk fraction is not yet known. Filled circles represent mean warm grain sizes, and open triangles represent mean cold grain sizes. Error bars for the mean mass-average grain sizes are estimated using a Monte Carlo approach, sampling the errors of the individual objects. Right: Mean grain sizes vs. mean cluster age. Filled symbols represent results for the warm component, while open symbols represent the cold component. The black points are YSOs in Serpens, gray squares in Taurus, gray stars in Upper Sco and gray triangles in η Cha. (A color version of this figure is available in the online journal)

6.5.2   Evolution of Crystallinity with Time?

Literature studies of disk fractions of different YSO clusters with different mean ages show a trend of decreasing disk fraction, i.e. disks dissipating with time, over some few millions of years (Haisch et al. 2001; Hernández et al. 2008). This decrease is clearly confirmed by the lower fraction of disks still present in the older regions studied here (Upper Sco and η Cha). According to current planet formation theories, if giant planets are to be formed from gas rich disks, the optically thin, gas-poor disks in those older regions should already harbor (proto-)planets. Considering the evidence from small bodies in our own Solar System that suggest considerably higher crystallinity fractions than ISM dust (see Wooden et al. 2007 and Pontoppidan & Brearley 2010 for reviews of latest results), a crystallinity increase must occur.

In Figure 6.12, the mean crystallinity fraction per region is plotted against two evolutionary parameters: disk fraction (left) and mean age (right). Within the spread in individual fractions it is seen that, just as for grain sizes, there is no strong evidence of an increase of crystallinity fraction with either evolutionary parameter. This implies that there is no evolution in grain sizes or crystallinity fraction for the dust in the surface of disks over cluster ages in the range $1-8$ Myr, as probed by the observations presented here. Essentially, there is no change in these two parameters until the disks disperse. Starting from the assumption that initially the dust in protoplanetary disks is of ISM origin (sub-μm in size and almost completely amorphous), it appears that a modest level of crystallinity is established in the disk surface early in the evolution ($\leq$ 1 Myr) and then reaches some sort of steady state, irrespective of what is taking place in the disk midplane. Thus, the dust in the upper layers of disks does not seem to be a good tracer of the evolution that is taking place in the disk interior, where dust is
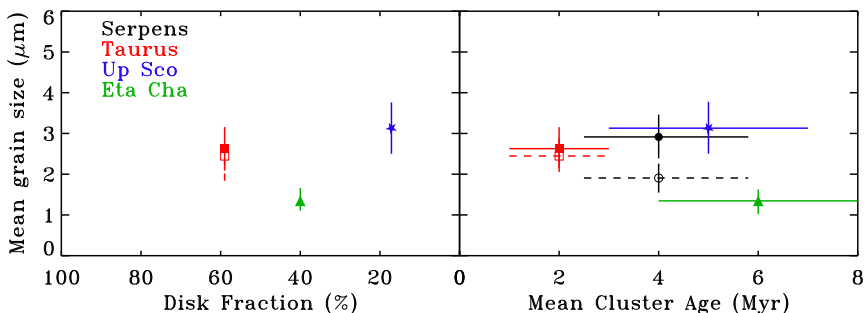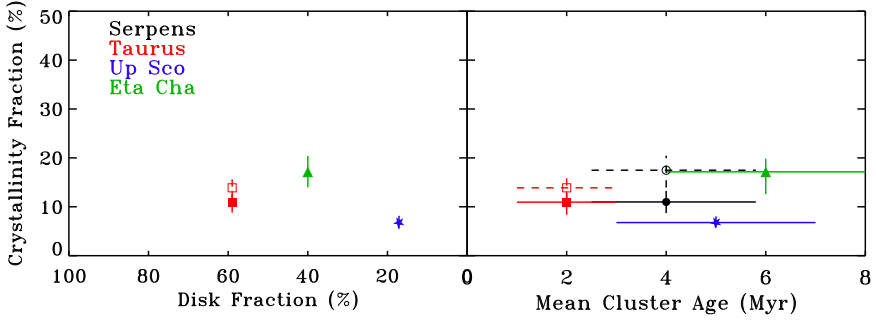
Figure 6.12 – Left: Crystallinity fraction vs. disk fraction. Serpens is not included because its disk fraction is not yet known. Filled circles represent mean warm crystallinity, and open triangles represent mean cold crystallinity. Uncertainty for crystallinity fractions are estimated using a Monte Carlo approach, sampling the errors of the individual objects. Right: Crystallinity fraction vs. mean cluster age. Filled symbols represent results for the warm component, while open symbols represent the cold component. The black points are YSOs in Serpens, gray squares in Taurus, gray stars in Upper Sco and gray triangles in η Cha. (A color version of this figure is available in the online journal)

growing further for the formation of planetesimals and planets, at many times higher crystallinity fractions, to be consistent with evidence from Solar system bodies.

If this is the case, within 1 Myr this surface dust must be crystallized to the observed fraction ($\sim$10 – 20 %). This result puts constraints on the formation of circumstellar disks. One possibility is that this crystallization of the dust in disks mostly occurs during the embedded phase. In this early stage of star formation, where large quantities of material are still accreting towards the protostar, a fraction of the infalling material comes very close to the protostar and is heated to temperatures >800 K before it moves outwards in the disk. Alternatively, accretion shocks or episodic heating events could be responsible for thermally annealing the dust in the disk surface.

The 2-D models of Visser & Dullemond (2010) treat the radial evolution of crystals in time. According to these models, 100 % of the dust in the inner disk ($\leq$ 1 AU) is crystallized within 1 Myr. With time, the inner disk crystalline fraction drops as the disk spreads, and crystalline material is transported to outer parts of the disk. These models can help explain the rapid crystallization required to account for our results. However, the models do show a decrease in inner disk ($\leq$ 1 AU) crystallinity fraction with time, which is not supported by our results. Since these models do not discriminate on vertical structure, but rather present crystallinity fractions that are integrated over all heights at a given radius, this decrease in crystallinity fraction is not necessarily connected to the surface of the disk. Thus the decrease in crystallinity fraction with time found in the models of Visser & Dullemond (2010) could be explained as a decrease in crystallinity fraction just in the disk midplane where the bulk of the mass resides, but not in the surface layers, as our data indicate. That would

imply that radial mixing of these crystals is more efficient than vertical mixing, which is responsible for the crystallinity fraction decrease in the disk midplane.

According to the models of Ciesla (2007) for outward transport of high temperature materials, variations in radial transport dynamics with height produce vertical gradients in the crystalline fractions, such that the upper layers of the disk will have lower crystallinity fractions than the midplane population. If that is the case, the observations discussed here, which probe the disk surface only, lead to lower limits on the real crystalline fraction of disk midplanes. In this scenario, planets (and comets) forming in the disk midplane would have higher crystalline abundances than those derived here for the disk surfaces, which are compatible with what has been observed in our Solar System. However, this model does not make predictions for the time evolution of the systems. Combining the vertical and radial mixing processes with evolutionary models such as those of Visser & Dullemond (2010) are needed to investigate whether older and younger disks could still show the same distribution of crystallinity fractions in the upper layers of disks, as observed here.

6.6   Conclusions

This paper presents the spectral decomposition of Spitzer/IRS spectra using the B2C decomposition model of Olofsson et al. (2010). Mineralogical compositions and size distributions of dust grains in the surface layers of protoplanetary disks are derived for 139 YSOs belonging to four young star clusters using the same method.

Serpens and Taurus are used as prototypes of young regions, where most stars are still surrounded by disks, while Upper Sco and η Cha represent the older bin of disk evolution, where a large fraction of the disks have already dissipated but some massive protoplanetary disks are left. The large number of objects analyzed allows statistical results that point to the main processes that affect the grain size distribution and composition of dust in protoplanetary disks. Furthermore, the usage of the same analysis method for regions of different mean ages allow a study of evolution of the dust parameters with time.

Our large sample does not show a preferential grain size or crystallinity fraction with disk geometry, contrary to earlier analyses based on smaller samples. Also, younger and older regions have very similar distributions. The difference between mean mass-averaged grain sizes for the warm and cold components of a given star-forming region is small, however a considerable difference is seen between the ranges of grain sizes spanned in both components. The cold mass-averaged grain sizes never reach the biggest size modelled (6 μm) while the warm mass-averaged grain sizes span the entire range of sizes modeled. The crystallinity fractions derived for inner (warm) and outer (cold) disks are typically $10 - 20\%$, and not correlated. The cold crystallinity fraction shows a larger spread than the warm. No strong difference is seen between the overall mean warm and cold crystallinity fraction. Within the crystalline dust population, more enstatite is found in the warm component and more forsterite in the cold component. The differences are not very significant, however.

The results of the spectral decomposition support the usage of the strength of the 10 μm silicate feature ($S_{\text{peak}}^{10\mu\text{m}}$) as a proxy of the mean grain size of dust in the disk surface. This is supported by the correlation between $S_{\text{peak}}^{10\mu\text{m}}$ and mean grain size and lack of correlation with the mean crystallinity.

Mean cluster ages and disk fractions are used as indicators of the evolutionary stage of the different populations. Our results show that the different regions have similar distributions of mean grain sizes and crystallinity fractions regardless of the spread in mean ages of 1 – 8 Myr. Thus, despite the fact that the majority of disks dissipate within a few Myr, the surface dust properties do not depend on age for those disks that have not yet dissipated in the 1 – 8 Myr range. This points to a rapid change in the composition and crystallinity of the dust in the early stages (≤ 1 Myr) that is maintained essentially until the disks dissipate.

References

Ábrahám, P., et al. 2009, Nature, 459, 224

Apai, D., Pascucci, I., Bouwman, J., Natta, A., Henning, T., & Dullemond, C. P. 2005, Science, 310, 834

Beckwith, S. V. W., Henning, T., & Nakagawa, Y. 2000, Protostars and Planets IV, 533

Beichman, C. A., et al. 2006, ApJ, 639, 1166

Blaauw, A. 1978, Problems of Physics and Evolution of the Universe, 101

Bockelée-Morvan, D., et al. 2000, A&A, 353, 1101

Bouwman, J., Meeus, G., de Koter, A., Hony, S., Dominik, C., & Waters, L. B. F. M. 2001, A&A, 375, 950

Bouwman, J., et al. 2008, ApJ, 683, 479

Bouy, H., et al. 2008, A&A, 486, 877

Brown, J. M., et al. 2007, ApJ, 664, L107

Bryden, G., et al. 2006, ApJ, 636, 1098

Carpenter, J. M., Mamajek, E. E., Hillenbrand, L. A., & Meyer, M. R. 2006, ApJ, 651, L49

Carpenter, J. M., et al. 2009, ApJS, 181, 197

Ciesla, F. J. 2007, Science, 318, 613

Ciesla, F. J. 2009, Icarus, 200, 655

Crovisier, J., Leech, K., Bockelee-Morvan, D., Brooke, T. Y., Hanner, M. S., Altieri, B., Keller, H. U., & Lellouch, E. 1997, Science, 275, 1904

Dahm, S. E., & Carpenter, J. M. 2009, AJ, 137, 4024

Desch, S. J., & Connolly, H. C., Jr. 2002, Meteoritics and Planetary Science, 37, 183

de Zeeuw, P. T., Hoogerwerf, R., de Bruijne, J. H. J., Brown, A. G. A., & Blaauw, A. 1999, AJ, 117, 354

Dullemond, C. P., Dominik, C., & Natta, A. 2001, ApJ, 560, 957

Dullemond, C. P., & Dominik, C. 2005, A&A, 434, 971

Dullemond, C. P., & Dominik, C. 2008, A&A, 487, 205

Dzib, S., Loinard, L., Mioduszewski, A. J., Boden, A. F., Rodríguez, L. F., & Torres, R. M. 2010, ApJ, 718, 610

Fabian, D., Jäger, C., Henning, T., Dorschner, J., & Mutschke, H. 2000, A&A, 364, 282

Forrest, W. J., et al. 2004, ApJS, 154, 443

Furlan, E., et al. 2006, ApJS, 165, 568

Gail, H.-P. 2004, A&A, 413, 571

Gautier, T. N., III, et al. 2007, ApJ, 667, 527

Geers, V. C., et al. 2006, A&A, 459, 545

Haisch, K. E., Jr., Lada, E. A., & Lada, C. J. 2001, ApJ, 553, L153

Harker, D. E., & Desch, S. J. 2002, ApJ, 565, L109

Harker, D. E., Wooden, D. H., Woodward, C. E., & Lisse, C. M. 2002, ApJ, 580, 579

Harker, D. E., Woodward, C. E., & Wooden, D. H. 2005, Science, 310, 278

Harker, D. E., Woodward, C. E., Wooden, D. H., Fisher, R. S., & Trujillo, C. A. 2007, Icarus, 190, 432

Hartmann, L., Ballesteros-Paredes, J., & Bergin, E. A. 2001, ApJ, 562, 852

Henning, T. 2010, ARA&A, 48, 21

Hernández, J., Hartmann, L., Calvet, N., Jeffries, R. D., Gutermuth, R., Muzerolle, J., & Stauffer, J. 2008, ApJ, 686, 1195

Houck, J. R., et al. 2004, ApJS, 154, 18

Juhász, A., Henning, T., Bouwman, J., Dullemond, C. P., Pascucci, I., & Apai, D. 2009, ApJ, 695, 1024

Juhász, A., et al. 2010, ApJ, 721, 431

Kalas, P., et al. 2008, Science, 322, 1345

Kemper, F., Vriend, W. J., & Tielens, A. G. G. M. 2004, ApJ, 609, 826

Kenyon, S. J., & Hartmann, L. 1987, ApJ, 323, 714

Kenyon, S. J., Dobrzycka, D., & Hartmann, L. 1994, AJ, 108, 1872

Kessler-Silacci, J., et al. 2006, ApJ, 639, 275

Kessler-Silacci, J. E., et al. 2007, ApJ, 659, 680

Kóspál, Á., Ardila, D. R., Moór, A., & Ábrahám, P. 2009, ApJ, 700, L73

Lagrange, A.-M., et al. 2010, Science, 329, 57

Lahuis, F., Kessler-Silacci, J. E., Evans, N. J., I., et al. 2006, c2d Spectroscopy Explanatory Supplement, Tech. rep., Pasadena: Spitzer Science Center

Li, A., & Draine, B. T. 2001, ApJ, 550, L213

Lisse, C. M., Kraemer, K. E., Nuth, J. A., Li, A., & Joswiak, D. 2007, Icarus, 187, 69

Lisse, C. M., Chen, C. H., Wyatt, M. C., & Morlok, A. 2008, ApJ, 673, 1106

Luhman, K. L., & Steeghs, D. 2004, ApJ, 609, 917

Luhman, K. L., Allen, P. R., Espaillat, C., Hartmann, L., & Calvet, N. 2010, ApJS, 186, 111

Malfait, K., Waelkens, C., Waters, L. B. F. M., Vandenbussche, B., Huygen, E., & de Graauw, M. S. 1998, A&A, 332, L25x

Mamajek, E. E., Lawson, W. A., & Feigelson, E. D. 1999, ApJ, 516, L77

Megeath, S. T., Hartmann, L., Luhman, K. L., & Fazio, G. G. 2005, ApJ, 634, L113

Meeus, G., Waters, L. B. F. M., Bouwman, J., van den Ancker, M. E., Waelkens, C., & Malfait, K. 2001, A&A, 365, 476

Merín, B., et al. 2007, ApJ, 661, 361

Merín, B., et al. 2010, ApJ, 718, 1200

Min, M., Hovenier, J. W., & de Koter, A. 2005, A&A, 432, 909

Min, M., Hovenier, J. W., de Koter, A., Waters, L. B. F. M., & Dominik, C. 2005, Icarus, 179, 158

Min, M., Waters, L. B. F. M., de Koter, A., Hovenier, J. W., Keller, L. P., & Markwick-Kemper, F. 2007, A&A, 462, 667

Min, M., Hovenier, J. W., Waters, L. B. F. M., & de Koter, A. 2008, A&A, 489, 135

Oliveira, I., et al. 2009, ApJ, 691, 672

Oliveira, I., et al. 2010, ApJ, 714, 778

Olofsson, J., et al. 2009, A&A, 507, 327

Olofsson, J., Augereau, J.-C., van Dishoeck, E. F., Merín, B., Grosso, N., Ménard, F., Blake, G. A., & Monin, J.-L. 2010, A&A, 520, A39

Pascucci, I., Apai, D., Luhman, K., Henning, T., Bouwman, J., Meyer, M. R., Lahuis, F., & Natta, A. 2009, ApJ, 696, 143

Pinte, C., et al. 2008, A&A, 489, 633

Pontoppidan, K. M., & Brearley, A. J. 2010, Protoplanetary Dust: Astrophysical and Cosmochemical Perspectives, 191

Rieke, G. H., et al. 2005, ApJ, 620, 1010

Sargent, B. A., et al. 2009, ApJS, 182, 477

Sicilia-Aguilar, A., et al. 2009, ApJ, 701, 1188

Schegerer, A. A., Wolf, S., Ratzka, T., & Leinert, C. 2008, A&A, 478, 779

Straizys, V., Cernis, K. & Bartasiute, S. 1996, Baltic Astron., 5, 125

Su, K. Y. L., et al. 2006, ApJ, 653, 675

Udry, S., & Santos, N. C. 2007, ARA&A, 45, 397

van Boekel, R., Waters, L. B. F. M., Dominik, C., Bouwman, J., de Koter, A., Dullemond, C. P., & Paresce, F. 2003, A&A, 400, L21

van Boekel, R., et al. 2004, Nature, 432, 479

van Boekel, R., Min, M., Waters, L. B. F. M., de Koter, A., Dominik, C., van den Ancker, M. E., & Bouwman, J. 2005, A&A, 437, 189

Visser, R., & Dullemond, C. P. 2010, A&A, 519, A28

Watson, D. M., et al. 2009, ApJS, 180, 84

Weidenschilling, S. J. 1980, Icarus, 44, 172

Wooden, D. H., Harker, D. E., Woodward, C. E., Butner, H. M., Koike, C., Witteborn, F. C., & McMurtry, C. W. 1999, ApJ, 517, 1034

Wooden, D., Desch, S., Harker, D., Gail, H.-P., & Keller, L. 2007, Protostars and Planets V, 815

Zolensky, M. E., et al. 2006, Science, 314, 1735

Table 6.1 – Characteristics of the star-forming regions presented in this work.

Region	Dist (pc)	Mean Age (Myr)	Disk Fraction	Ref.
Serpens	259–415	2–6	–	1, 2
Taurus	140	∼2	∼60%	3, 4, 5
Up Sco	145	∼5	∼17%	6, 7, 8
η Cha	97	∼6	∼40%	9, 10, 11

References: **1**: The distance to Serpens is still under debate, different methods yield distances ranging from 259 (Straizys et al. 1996) to 415 pc (Dzib et al. 2010); **2**: From Oliveira et al. (2009), using $d = 259$ pc; **3**: From Kenyon et al. (1994); **4**: From Hartmann et al. (2001); **5**: From Luhman et al. (2010); **6**: From de Zeeuw et al. (1999); **7**: From Blaauw (1978); **8**: From Carpenter et al. (2006); **9**: From Mamajek et al. (1999); **10**: From Luhman & Steeghs (2004); **11**: From Megeath et al. (2005).

Table 6.2 – B2C mean composition of each star-forming region.

Region	Oli/Pyr[a]	Silica	Forsterite	Enstatite
		Warm	Component	
Serpens	81.3±11.7%	7.8±6.5%	5.8±4.9%	5.2±4.9%
Taurus	79.4±9.4%	9.6±7.0%	4.4±3.3%	6.5±4.5%
Up Sco	89.7±4.7%	3.5±3.4%	2.6±1.1%	4.1±3.1%
η Cha	75.0±13.4%	7.8±4.6%	6.8±4.0%	10.3±9.8%
		Cold	Component	
Serpens	68.0±20.1%	14.4±12.3%	9.5±9.5%	8.0±8.0%
Taurus	64.7±14.3%	21.3±11.4%	8.6±8.6%	5.3±5.3%

[a] Amorphous olivine and pyroxene combined.

Table 6.3 – B2C mean grain size and crystallinity parameters for each star-forming region.

Region	Number	$\langle a_{\mathrm{warm}} \rangle$ μm	$\langle a_{\mathrm{cold}} \rangle$ μm	$\langle \alpha_{\mathrm{warm}} \rangle$	$\langle \alpha_{\mathrm{cold}} \rangle$	$\langle C_{\mathrm{warm}} \rangle$ %	$\langle C_{\mathrm{cold}} \rangle$ %
Serpens	60	2.9±1.3	1.9±0.6	-2.75±0.39	-3.16±0.18	11.0±6.9	17.5±12.4
Taurus	66	2.6±0.9	2.4±0.6	-2.83±0.31	-3.02±0.15	10.9±5.6	13.9±10.1
Up Sco	9	3.1±1.5	–	-3.33±0.18	–	6.8±3.3	–
η Cha	4	1.3±0.4	–	-2.71±0.39	–	17.1±10.6	–

Table 6.4 – Comparison of mean mineralogical results from this study with literature studies.

Region	This	work	Literature	
	Amorphous	Crystalline	Amorphous	Crystalline
		Warm	Component	
Taurus	89.0±6.6 %	10.9±6.6 %	82.9±19.3 %	17.1±19.3 % [a]
η Cha	82.8±12.9 %	17.1±12.8 %	80.1±9.3 %	18.4±10.7 % [b]
		Cold	Component	
Taurus	85.9±10.6 %	13.9±10.5 %	77.3±19.9 %	22.6±19.9 % [a]

[a] Sargent et al. (2009); [b] Sicilia-Aguilar et al. (2009)

A. Relative Abundances of Species

The relative abundances, as resulting from the B2C compositional fitting (§ 6.3) to the IRS spectra of protoplanetary disks in Serpens, Taurus, Upper Sco and η Cha are shown in Tables A.1 and A.2. Since the opacities of amorphous olivine and pyroxene are degenerate, the abundances of these two species have been added into one, marked 'Oli/Pyr' in the Tables. Furthermore, 'Sil' designates the amorphous silica, and the crystalline enstatite and forsterite are marked as 'Ens' and 'For', respectively. In the tables, the first line of a given object corresponds to the results of the fit to the warm component and the second line to the results of the cold component. For some objects (20 in Serpens, 28 in Taurus, all in Upper Sco and η Cha), the S/N drops considerably at longer wavelengths and the results of the procedure are no longer reliable. For these sources, the cold component could not be fitted satisfactorily and, in Tables A.1 and A.2, only the warm component results are shown.

ID	SpT	Oli/Pyr[a] % (0.1 μm)	Ens % (0.1 μm)	For % (0.1 μm)	Sil % (0.1 μm)
Serpens					
1	K2	$29.7^{+10.7}_{-15.3}$	$1.0^{+2.0}_{-0.4}$	$2.6^{+2.6}_{-1.4}$	$0.1^{+0.9}_{-0.0}$
...		$38.4^{+14.5}_{-15.8}$	$0.0^{+1.6}_{-0.0}$	$8.7^{+5.5}_{-3.6}$	$1.2^{+3.0}_{-0.0}$
3	M0	$26.5^{+15.9}_{-7.3}$	$0.0^{+2.4}_{-0.0}$	$0.9^{+3.5}_{-0.4}$	$0.0^{+1.7}_{-0.0}$
...		$27.3^{+33.7}_{-8.6}$	$0.0^{+10.5}_{-0.0}$	$10.2^{+19.1}_{-4.9}$	$0.0^{+16.3}_{-4.0}$
6	K5	$25.4^{+4.5}_{-6.0}$	$0.0^{+0.7}_{-0.0}$	$0.8^{+1.1}_{-0.0}$	$0.0^{+0.3}_{-0.0}$
...		$6.4^{+3.8}_{-3.3}$	$4.1^{+2.1}_{-2.3}$	$5.1^{+3.4}_{-0.0}$	$0.5^{+1.1}_{-0.0}$
7	M0	$3.7^{+3.1}_{-0.9}$	$0.0^{+2.9}_{-0.0}$	$0.8^{+4.3}_{-0.0}$	$0.0^{+0.9}_{-0.0}$
...		$0.0^{+3.4}_{-0.5}$	$7.2^{+4.9}_{-6.9}$	$8.1^{+5.3}_{-6.9}$	$14.1^{+8.3}_{-11.5}$
9	–	$58.3^{+10.9}_{-8.8}$	$0.0^{+1.4}_{-0.0}$	$0.5^{+1.1}_{-0.0}$	$0.0^{+0.7}_{-0.0}$
...		$24.5^{+16.3}_{-14.5}$	$0.0^{+3.5}_{-0.0}$	$14.4^{+13.9}_{-9.8}$	$16.9^{+24.0}_{-15.0}$
10	–	$1.9^{+5.9}_{-0.6}$	$0.0^{+2.5}_{-0.0}$	$2.3^{+2.1}_{-0.7}$	$4.3^{+2.4}_{-1.4}$
...		$37.4^{+29.1}_{-9.4}$	$2.0^{+10.1}_{-0.0}$	$0.0^{+9.2}_{-0.0}$	$0.0^{+19.4}_{-0.0}$
14	M2	$11.1^{+46.8}_{-0.0}$	$0.0^{+6.0}_{-0.0}$	$3.0^{+7.1}_{-0.0}$	$0.0^{+6.9}_{-0.0}$
15	–	$35.6^{+12.5}_{-7.0}$	$0.2^{+1.5}_{-0.0}$	$2.9^{+1.6}_{-1.3}$	$0.0^{+0.6}_{-0.0}$
...		$36.3^{+10.4}_{-12.9}$	$2.4^{+1.8}_{-1.6}$	$2.2^{+3.5}_{-0.0}$	$1.1^{+2.8}_{-0.9}$
21	–	$2.2^{+5.0}_{-0.0}$	$0.0^{+1.6}_{-0.0}$	$2.7^{+3.7}_{-0.0}$	$0.1^{+3.6}_{-0.0}$
...		$33.0^{+18.1}_{-20.7}$	$1.6^{+5.2}_{-0.0}$	$0.0^{+2.3}_{-0.0}$	$1.3^{+11.9}_{-0.0}$
29	M2	$1.4^{+6.4}_{-0.0}$	$0.0^{+3.1}_{-0.0}$	$1.6^{+7.8}_{-0.0}$	$2.7^{+6.6}_{-0.0}$
30	M1	$0.0^{+9.7}_{-0.0}$	$0.1^{+4.4}_{-0.0}$	$3.4^{+4.6}_{-1.2}$	$4.5^{+6.8}_{-0.2}$
...		$10.3^{+51.7}_{-13.8}$	$1.7^{+15.4}_{-3.2}$	$5.5^{+14.1}_{-4.3}$	$8.1^{+21.6}_{-6.3}$
31	–	$1.2^{+0.8}_{-0.0}$	$0.0^{+0.8}_{-0.0}$	$0.8^{+0.5}_{-0.0}$	$0.0^{+1.0}_{-0.0}$
...		$21.8^{+5.3}_{-4.9}$	$2.4^{+1.6}_{-0.0}$	$0.0^{+0.7}_{-0.0}$	$16.7^{+8.7}_{-7.9}$
36	K5	$22.3^{+5.2}_{-6.2}$	$0.9^{+1.6}_{-0.0}$	$0.6^{+1.3}_{-0.0}$	$0.0^{+0.8}_{-0.0}$
...		$37.4^{+11.0}_{-15.4}$	$0.0^{+3.9}_{-0.0}$	$1.6^{+2.7}_{-1.0}$	$2.9^{+8.6}_{-2.5}$

ID	SpT	Oli/Pyr[a] % (0.1 μm)	Ens % (0.1 μm)	For % (0.1 μm)	Sil % (0.1 μm)
40	M7	$0.0^{+8.3}_{-0.0}$	$0.0^{+8.4}_{-0.0}$	$2.9^{+4.4}_{-0.8}$	$10.9^{+4.6}_{-4.1}$
...		$24.2^{+15.5}_{-18.3}$	$16.6^{+11.2}_{-8.4}$	$3.1^{+16.4}_{-0.0}$	$0.0^{+4.8}_{-0.0}$
41	K2	$0.0^{+18.9}_{-0.0}$	$6.3^{+19.1}_{-0.0}$	$3.9^{+16.0}_{-0.0}$	$0.8^{+8.6}_{-0.0}$
43	M0.5	$0.0^{+13.0}_{-0.0}$	$0.0^{+4.0}_{-0.0}$	$4.2^{+5.7}_{-0.0}$	$4.6^{+6.1}_{-0.0}$
48	M5.5	$7.0^{+17.5}_{-0.1}$	$0.1^{+8.4}_{-0.0}$	$2.0^{+10.2}_{-0.0}$	$0.6^{+3.0}_{-0.6}$
...		$46.0^{+23.9}_{-40.6}$	$5.1^{+10.9}_{-3.3}$	$2.5^{+10.5}_{-1.1}$	$0.3^{+21.3}_{-2.3}$
53	M2.5	$0.0^{+36.7}_{-0.0}$	$5.0^{+26.6}_{-0.0}$	$5.4^{+18.5}_{-0.0}$	$5.9^{+20.1}_{-0.0}$
55	K2	$16.9^{+11.3}_{-4.0}$	$1.6^{+2.7}_{-0.9}$	$2.3^{+2.5}_{-0.0}$	$0.0^{+1.1}_{-0.0}$
...		$27.7^{+81.3}_{-23.1}$	$4.8^{+36.6}_{-1.1}$	$21.5^{+34.7}_{-14.2}$	$0.0^{+22.9}_{-0.0}$
56	–	$7.8^{+8.3}_{-2.0}$	$1.7^{+1.9}_{-0.8}$	$2.5^{+2.4}_{-0.0}$	$1.1^{+3.4}_{-0.0}$
...		$44.4^{+22.2}_{-17.0}$	$1.6^{+5.1}_{-1.0}$	$0.0^{+6.4}_{-0.0}$	$2.2^{+21.1}_{-0.0}$
57	–	$2.2^{+22.8}_{-0.0}$	$0.0^{+9.1}_{-0.0}$	$5.7^{+7.2}_{-1.1}$	$3.0^{+3.2}_{-1.4}$
...		$23.0^{+76.9}_{-5.8}$	$0.0^{+79.5}_{-0.0}$	$14.4^{+46.6}_{-10.4}$	$0.7^{+131.2}_{-0.0}$
58	K7	$6.6^{+3.2}_{-0.5}$	$0.0^{+1.0}_{-0.0}$	$0.6^{+1.1}_{-0.0}$	$1.2^{+0.7}_{-0.0}$
...		$32.2^{+16.8}_{-16.4}$	$3.2^{+15.6}_{-0.0}$	$0.0^{+3.7}_{-0.0}$	$0.0^{+7.2}_{-0.0}$
60	M0.5	$0.0^{+10.1}_{-0.0}$	$9.8^{+23.2}_{-0.0}$	$5.2^{+11.8}_{-0.0}$	$0.0^{+3.9}_{-0.0}$
61	M0	$12.2^{+7.2}_{-0.0}$	$0.0^{+0.6}_{-0.0}$	$1.8^{+1.3}_{-0.0}$	$0.0^{+1.1}_{-0.0}$
...		$38.2^{+3.7}_{-7.6}$	$0.0^{+0.8}_{-0.0}$	$0.1^{+0.9}_{-0.0}$	$0.6^{+1.7}_{-0.0}$
65	–	$0.0^{+2.7}_{-0.0}$	$0.0^{+2.0}_{-0.0}$	$6.0^{+2.6}_{-2.5}$	$0.0^{+1.0}_{-0.0}$
...		$54.9^{+56.6}_{-19.1}$	$0.1^{+7.9}_{-0.0}$	$0.0^{+6.3}_{-0.0}$	$8.8^{+16.2}_{-6.6}$
66	K5	$2.1^{+8.1}_{-0.0}$	$0.0^{+1.6}_{-0.0}$	$0.1^{+1.5}_{-0.0}$	$0.8^{+2.4}_{-0.0}$
...		$33.5^{+10.5}_{-16.5}$	$3.9^{+16.1}_{-0.0}$	$4.2^{+14.3}_{-0.0}$	$0.0^{+4.9}_{-0.0}$
71	M3	$6.4^{+28.2}_{-0.0}$	$0.0^{+1.8}_{-0.0}$	$2.3^{+6.8}_{-0.0}$	$0.8^{+8.7}_{-0.0}$
74	–	$0.0^{+5.1}_{-0.0}$	$0.0^{+1.7}_{-0.0}$	$6.3^{+3.7}_{-2.8}$	$13.4^{+4.8}_{-6.3}$
...		$50.7^{+33.8}_{-19.5}$	$0.1^{+11.1}_{-0.0}$	$0.1^{+6.4}_{-0.0}$	$0.0^{+29.4}_{-0.0}$
75	–	$0.0^{+72.5}_{-0.0}$	$0.0^{+10.2}_{-0.0}$	$4.1^{+28.5}_{-0.0}$	$0.1^{+20.2}_{-0.0}$
76	M1	$5.3^{+9.6}_{-3.4}$	$0.0^{+2.8}_{-0.0}$	$2.6^{+3.3}_{-0.0}$	$1.9^{+3.1}_{-0.0}$
...		$41.8^{+17.5}_{-23.6}$	$3.6^{+4.5}_{-1.9}$	$0.0^{+3.3}_{-0.0}$	$0.0^{+2.8}_{-0.0}$
80	–	$0.3^{+1.2}_{-0.0}$	$0.0^{+0.2}_{-0.0}$	$1.2^{+0.5}_{-0.0}$	$0.0^{+0.4}_{-0.0}$
...		$6.4^{+50.4}_{-0.0}$	$8.3^{+29.8}_{-0.0}$	$0.6^{+12.4}_{-0.0}$	$7.4^{+34.2}_{-0.0}$
81	M5	$10.7^{+2.8}_{-0.0}$	$0.0^{+0.8}_{-0.0}$	$0.0^{+0.4}_{-0.0}$	$4.3^{+1.2}_{-0.0}$
...		$45.4^{+6.2}_{-5.1}$	$0.0^{+1.1}_{-0.0}$	$0.0^{+0.4}_{-0.0}$	$0.0^{+1.5}_{-0.0}$
86	M5.5	$15.7^{+3.1}_{-1.7}$	$0.0^{+0.5}_{-0.0}$	$0.8^{+0.7}_{-0.0}$	$0.0^{+0.2}_{-0.0}$
...		$26.7^{+83.1}_{-0.0}$	$12.2^{+28.5}_{-0.0}$	$0.0^{+38.4}_{-0.0}$	$1.9^{+14.8}_{-0.0}$
88	M0.5	$0.0^{+5.0}_{-0.0}$	$0.0^{+1.0}_{-0.0}$	$8.6^{+4.4}_{-0.0}$	$0.0^{+0.4}_{-0.0}$
...		$6.0^{+30.9}_{-10.0}$	$0.7^{+37.8}_{-9.0}$	$33.3^{+22.2}_{-13.7}$	$6.0^{+31.7}_{-9.2}$
89	K5	$0.0^{+0.7}_{-0.0}$	$0.0^{+0.2}_{-0.0}$	$2.6^{+1.6}_{-1.0}$	$1.6^{+0.7}_{-0.0}$
90	–	$26.0^{+20.9}_{-12.1}$	$0.0^{+4.1}_{-0.1}$	$3.0^{+4.4}_{-1.6}$	$0.0^{+2.7}_{-0.0}$
...		$31.1^{+65.4}_{-0.0}$	$7.5^{+13.4}_{-1.4}$	$8.5^{+51.3}_{-0.0}$	$0.7^{+21.3}_{-0.0}$
92	M0	$1.1^{+9.7}_{-0.0}$	$0.0^{+0.9}_{-0.0}$	$4.8^{+4.8}_{-0.0}$	$2.3^{+5.3}_{-0.1}$
...		$19.6^{+9.7}_{-7.1}$	$0.8^{+3.4}_{-0.0}$	$0.2^{+9.0}_{-0.0}$	$3.0^{+4.6}_{-0.0}$

ID	SpT	Oli/Pyr[a] % (0.1 μm)	Ens % (0.1 μm)	For % (0.1 μm)	Sil % (0.1 μm)
96	M1	$18.2^{+8.7}_{-11.8}$	$2.6^{+3.8}_{-2.0}$	$2.8^{+4.6}_{-1.6}$	$0.0^{+5.9}_{-0.0}$
100	–	$0.0^{+29.3}_{-0.0}$	$0.0^{+12.0}_{-0.0}$	$2.8^{+42.3}_{-0.0}$	$0.5^{+35.5}_{-0.0}$
101	–	$24.1^{+26.6}_{-6.9}$	$0.0^{+4.1}_{-0.0}$	$2.0^{+3.2}_{-1.4}$	$1.0^{+4.2}_{-0.0}$
...		$48.0^{+7.1}_{-19.8}$	$0.0^{+2.7}_{-0.1}$	$0.2^{+2.7}_{-0.0}$	$2.5^{+3.1}_{-1.9}$
103	–	$0.0^{+0.9}_{-0.0}$	$0.0^{+0.3}_{-0.0}$	$2.4^{+0.6}_{-0.0}$	$3.2^{+0.9}_{-0.0}$
...		$11.0^{+3.7}_{-9.1}$	$5.8^{+4.2}_{-2.7}$	$0.0^{+3.9}_{-0.0}$	$5.8^{+3.3}_{-1.8}$
104	–	$1.6^{+14.7}_{-1.1}$	$0.9^{+6.1}_{-0.2}$	$3.7^{+5.2}_{-2.3}$	$4.3^{+4.1}_{-1.8}$
106	M3	$0.0^{+16.0}_{-0.0}$	$5.1^{+23.7}_{-0.0}$	$4.0^{+17.1}_{-0.0}$	$5.7^{+34.2}_{-0.0}$
113	K7	$0.0^{+1.2}_{-0.0}$	$0.0^{+0.7}_{-0.0}$	$3.3^{+1.7}_{-0.5}$	$4.4^{+1.3}_{-1.9}$
...		$36.9^{+19.9}_{-14.1}$	$2.1^{+8.1}_{-0.0}$	$3.6^{+4.2}_{-1.4}$	$0.0^{+2.6}_{-0.0}$
114	F9	$0.4^{+5.3}_{-0.0}$	$0.0^{+0.5}_{-0.0}$	$2.8^{+1.2}_{-1.1}$	$0.1^{+0.8}_{-0.0}$
115	M0.5	$3.5^{+6.8}_{-2.2}$	$0.4^{+1.2}_{-0.2}$	$1.5^{+1.5}_{-0.0}$	$0.6^{+1.2}_{-0.0}$
117	K2	$74.6^{+32.8}_{-31.9}$	$1.4^{+3.6}_{-0.0}$	$5.9^{+2.1}_{-4.1}$	$0.0^{+1.6}_{-0.0}$
...		$37.9^{+14.9}_{-15.7}$	$6.3^{+5.5}_{-4.7}$	$19.0^{+9.2}_{-9.9}$	$6.1^{+5.3}_{-4.1}$
119	K7	$0.0^{+11.2}_{-0.0}$	$0.7^{+23.7}_{-0.0}$	$1.1^{+17.4}_{-0.0}$	$1.9^{+31.6}_{-0.0}$
122	M0	$30.7^{+3.5}_{-30.4}$	$0.0^{+7.8}_{-0.0}$	$1.4^{+10.5}_{-0.0}$	$0.0^{+7.1}_{-0.0}$
...		$25.3^{+38.5}_{-12.9}$	$0.2^{+7.5}_{-0.6}$	$5.5^{+19.7}_{-0.0}$	$22.7^{+36.9}_{-14.1}$
123	M0	$42.0^{+65.0}_{-19.7}$	$0.7^{+3.3}_{-0.0}$	$5.4^{+2.7}_{-3.7}$	$0.0^{+1.4}_{-0.0}$
125	M0	$4.9^{+13.0}_{-0.0}$	$0.0^{+3.3}_{-0.0}$	$2.3^{+2.5}_{-1.6}$	$0.0^{+1.9}_{-0.0}$
...		$31.0^{+10.3}_{-20.4}$	$11.6^{+1.5}_{-12.8}$	$0.0^{+0.9}_{-2.6}$	$0.0^{+2.5}_{-0.0}$
127	M2	$1.5^{+2.9}_{-0.0}$	$3.4^{+1.2}_{-2.6}$	$0.0^{+2.0}_{-0.0}$	$0.9^{+1.9}_{-0.4}$
129	–	$0.2^{+2.4}_{-0.0}$	$0.0^{+0.8}_{-0.0}$	$0.9^{+1.7}_{-0.0}$	$0.0^{+1.3}_{-0.0}$
137	–	$40.7^{+10.3}_{-12.0}$	$0.8^{+6.0}_{-0.0}$	$0.9^{+2.9}_{-0.0}$	$0.0^{+2.3}_{-0.0}$
142	M4	$0.7^{+6.3}_{-0.0}$	$0.5^{+2.4}_{-0.0}$	$2.6^{+2.3}_{-1.1}$	$1.3^{+2.9}_{-0.2}$
144	–	$0.0^{+5.3}_{-0.0}$	$0.0^{+2.1}_{-0.0}$	$6.1^{+1.6}_{-1.3}$	$4.4^{+2.6}_{-1.9}$
...		$23.3^{+91.2}_{-9.5}$	$22.1^{+33.3}_{-11.6}$	$10.9^{+26.9}_{-9.9}$	$0.0^{+41.9}_{-0.0}$
146	M4	$6.8^{+2.7}_{-1.1}$	$0.0^{+0.6}_{-0.0}$	$4.4^{+1.2}_{-1.6}$	$2.2^{+1.1}_{-1.1}$
...		$17.2^{+6.3}_{-2.6}$	$0.0^{+4.2}_{-0.0}$	$0.0^{+3.8}_{-0.0}$	$0.0^{+4.7}_{-0.0}$
147	–	$0.0^{+4.5}_{-0.0}$	$0.0^{+2.9}_{-0.0}$	$3.3^{+2.8}_{-1.3}$	$1.3^{+1.6}_{-0.9}$
148	K7	$7.4^{+15.4}_{-0.0}$	$2.5^{+2.7}_{-1.3}$	$3.5^{+3.4}_{-0.8}$	$0.0^{+1.0}_{-0.0}$
...		$3.8^{+36.6}_{-0.0}$	$17.8^{+16.9}_{-8.3}$	$30.8^{+24.5}_{-11.4}$	$1.9^{+10.7}_{-0.0}$
149	M0	$37.8^{+22.2}_{-13.3}$	$0.7^{+2.9}_{-0.0}$	$1.4^{+2.8}_{-0.9}$	$0.0^{+1.6}_{-0.0}$
...		$41.7^{+24.7}_{-28.1}$	$0.0^{+5.5}_{-0.0}$	$4.1^{+10.3}_{-1.5}$	$4.4^{+8.6}_{-3.6}$
Taurus					
04108+2910	M0	$0.1^{+0.4}_{-0.0}$	$0.5^{+1.4}_{-0.0}$	$2.9^{+1.2}_{-1.0}$	$0.0^{+0.8}_{-0.0}$
...		$13.2^{+9.3}_{-5.6}$	$0.1^{+6.5}_{-0.0}$	$4.0^{+10.8}_{-0.0}$	$0.0^{+9.9}_{-0.0}$
04200+2759	–	$4.7^{+1.5}_{-2.4}$	$0.1^{+2.2}_{-0.0}$	$0.4^{+1.2}_{-0.0}$	$0.0^{+0.9}_{-0.0}$
...		$14.3^{+11.5}_{-7.3}$	$1.2^{+4.5}_{-7.9}$	$4.2^{+5.1}_{-3.6}$	$3.8^{+8.2}_{-7.2}$
04216+2603	M1	$43.9^{+15.3}_{-22.8}$	$1.8^{+5.4}_{-0.7}$	$2.1^{+3.0}_{-1.0}$	$0.0^{+2.2}_{-0.0}$
...		$18.6^{+27.5}_{-9.0}$	$0.1^{+16.8}_{-0.0}$	$13.2^{+31.5}_{-10.7}$	$1.8^{+40.3}_{-8.2}$
04303+2240	–	$2.4^{+9.1}_{-0.0}$	$0.0^{+1.7}_{-0.0}$	$2.7^{+3.6}_{-0.0}$	$0.0^{+0.7}_{-0.0}$

ID	SpT	Oli/Pyr[a] % (0.1 μm)	Ens % (0.1 μm)	For % (0.1 μm)	Sil % (0.1 μm)
04370+2559	–	$3.1^{+7.3}_{-0.0}$	$1.2^{+2.3}_{-0.0}$	$0.7^{+1.5}_{-0.0}$	$0.0^{+0.4}_{-0.0}$
04385+2550	M0	$16.2^{+2.3}_{-7.9}$	$0.8^{+1.3}_{-0.5}$	$1.0^{+1.9}_{-0.0}$	$0.0^{+0.7}_{-0.0}$
$\cdots$		$13.2^{+11.7}_{-0.0}$	$0.0^{+2.2}_{-0.0}$	$1.6^{+3.3}_{-0.0}$	$5.7^{+11.4}_{-0.0}$
AATau	K7	$12.5^{+10.1}_{-0.6}$	$0.4^{+1.0}_{-0.0}$	$1.4^{+1.4}_{-0.7}$	$0.0^{+0.7}_{-0.0}$
$\cdots$		$2.6^{+19.7}_{-0.0}$	$19.2^{+15.3}_{-0.0}$	$0.0^{+24.2}_{-0.0}$	$18.3^{+22.4}_{-0.0}$
BPTau	K7	$29.9^{+5.4}_{-7.9}$	$1.1^{+0.9}_{-0.6}$	$1.0^{+1.3}_{-0.0}$	$0.0^{+0.3}_{-0.0}$
CITau	K7	$2.3^{+5.6}_{-0.0}$	$0.0^{+0.3}_{-0.0}$	$2.1^{+1.0}_{-0.0}$	$0.0^{+0.9}_{-0.0}$
$\cdots$		$14.8^{+12.4}_{-7.1}$	$0.3^{+1.5}_{-0.0}$	$3.5^{+10.3}_{-0.0}$	$7.5^{+9.9}_{-0.0}$
CWTau	K3	$8.2^{+1.9}_{-2.3}$	$1.0^{+0.7}_{-0.0}$	$1.0^{+1.5}_{-0.0}$	$0.2^{+2.4}_{-0.0}$
CoKuTau3	M1	$3.3^{+6.8}_{-0.5}$	$0.0^{+1.0}_{-0.0}$	$2.7^{+1.6}_{-1.4}$	$0.0^{+0.3}_{-0.0}$
$\cdots$		$15.2^{+9.6}_{-6.0}$	$5.3^{+10.2}_{-0.0}$	$3.8^{+1.9}_{-2.7}$	$0.2^{+4.6}_{-0.0}$
CoKuTau4	M1.5	$24.5^{+3.5}_{-17.1}$	$0.0^{+2.7}_{-0.0}$	$1.0^{+2.2}_{-0.0}$	$0.0^{+1.0}_{-0.0}$
$\cdots$		$13.4^{+8.4}_{-5.4}$	$0.3^{+1.3}_{-0.6}$	$0.0^{+1.4}_{-0.7}$	$13.5^{+9.1}_{-6.3}$
DDTau	M3	$10.6^{+4.7}_{-2.7}$	$2.6^{+3.8}_{-0.0}$	$2.5^{+2.6}_{-0.0}$	$0.0^{+1.4}_{-0.0}$
$\cdots$		$38.7^{+26.0}_{-23.6}$	$9.0^{+8.8}_{-6.1}$	$18.5^{+11.9}_{-8.6}$	$0.0^{+5.5}_{-0.0}$
DETau	M1	$11.0^{+6.9}_{-2.4}$	$0.4^{+1.7}_{-0.0}$	$3.3^{+2.5}_{-0.0}$	$0.0^{+0.6}_{-0.0}$
$\cdots$		$51.2^{+22.1}_{-24.7}$	$0.3^{+6.2}_{-0.0}$	$4.4^{+6.9}_{-0.0}$	$0.7^{+10.2}_{-0.0}$
DFTau	M0.5	$0.6^{+8.0}_{-0.0}$	$0.2^{+2.3}_{-0.0}$	$1.8^{+2.1}_{-0.0}$	$0.3^{+3.1}_{-0.0}$
DHTau	M2	$2.3^{+2.1}_{-0.3}$	$1.8^{+1.8}_{-0.8}$	$5.4^{+2.4}_{-1.2}$	$1.5^{+1.6}_{-0.9}$
$\cdots$		$32.0^{+16.2}_{-12.3}$	$2.5^{+6.0}_{-1.7}$	$3.4^{+8.5}_{-3.1}$	$0.0^{+5.6}_{-1.3}$
DKTau	M0	$13.0^{+3.8}_{-3.1}$	$0.6^{+0.9}_{-0.0}$	$1.9^{+1.3}_{-1.2}$	$3.3^{+1.3}_{-0.9}$
DLTau	K7	$0.1^{+5.6}_{-1.5}$	$0.0^{+1.1}_{-0.0}$	$3.0^{+2.3}_{-1.2}$	$5.0^{+3.5}_{-2.2}$
DMTau	M1	$4.1^{+13.6}_{-0.0}$	$0.0^{+1.8}_{-0.0}$	$4.7^{+2.3}_{-1.0}$	$0.0^{+1.2}_{-0.0}$
$\cdots$		$42.6^{+28.1}_{-17.1}$	$0.7^{+8.9}_{-0.0}$	$1.2^{+3.6}_{-0.0}$	$5.3^{+12.2}_{-4.8}$
DNTau	M0	$3.4^{+5.1}_{-0.0}$	$0.0^{+0.6}_{-0.0}$	$2.2^{+1.4}_{-0.6}$	$1.4^{+1.1}_{-0.9}$
$\cdots$		$33.7^{+39.1}_{-0.0}$	$0.2^{+9.1}_{-0.0}$	$0.0^{+18.1}_{-0.0}$	$0.0^{+7.6}_{-0.0}$
DOTau	M0	$1.2^{+8.4}_{-0.0}$	$0.0^{+3.8}_{-0.0}$	$1.6^{+2.7}_{-0.0}$	$0.3^{+4.0}_{-0.0}$
DPTau	M0.5	$35.1^{+13.7}_{-15.8}$	$0.0^{+1.5}_{-0.0}$	$1.1^{+1.9}_{-0.0}$	$0.0^{+1.6}_{-0.0}$
$\cdots$		$20.1^{+8.9}_{-8.0}$	$9.8^{+4.6}_{-5.1}$	$3.0^{+3.7}_{-2.1}$	$7.7^{+3.8}_{-3.8}$
DQTau	M0	$1.8^{+1.2}_{-1.3}$	$5.5^{+1.7}_{-1.4}$	$2.0^{+1.1}_{-0.7}$	$0.0^{+0.6}_{-0.0}$
$\cdots$		$14.4^{+12.0}_{-5.6}$	$0.1^{+8.7}_{-0.0}$	$0.0^{+8.0}_{-0.0}$	$0.0^{+3.3}_{-0.0}$
DRTau	K7	$25.0^{+5.8}_{-5.3}$	$0.0^{+0.7}_{-0.0}$	$1.0^{+1.5}_{-0.0}$	$0.0^{+0.6}_{-0.0}$
DSTau	K5	$35.9^{+7.1}_{-6.3}$	$0.8^{+2.9}_{-0.7}$	$2.8^{+2.3}_{-1.7}$	$0.2^{+1.2}_{-0.0}$
$\cdots$		$22.0^{+14.7}_{-10.3}$	$0.2^{+3.5}_{-1.8}$	$2.7^{+3.3}_{-1.8}$	$17.2^{+14.0}_{-9.7}$
F04147+2822	M4	$10.2^{+6.3}_{-0.0}$	$0.0^{+4.3}_{-0.0}$	$2.9^{+2.5}_{-0.0}$	$0.0^{+1.4}_{-0.0}$
F04192+2647	–	$3.4^{+12.4}_{-0.0}$	$0.1^{+0.8}_{-0.0}$	$3.6^{+1.7}_{-0.8}$	$0.0^{+0.7}_{-0.0}$
$\cdots$		$19.7^{+16.8}_{-7.4}$	$0.0^{+9.0}_{-1.6}$	$14.2^{+15.3}_{-7.1}$	$3.7^{+9.4}_{-4.5}$
F04262+2654	–	$0.0^{+1.0}_{-0.0}$	$2.1^{+2.0}_{-0.9}$	$0.0^{+1.2}_{-0.0}$	$3.9^{+2.8}_{-2.4}$
F04297+2246	–	$5.7^{+3.7}_{-1.3}$	$0.0^{+1.5}_{-0.0}$	$2.6^{+2.0}_{-1.5}$	$0.3^{+1.6}_{-0.0}$
$\cdots$		$24.7^{+61.7}_{-6.4}$	$3.5^{+15.1}_{-0.0}$	$0.1^{+32.3}_{-0.0}$	$0.0^{+17.6}_{-0.0}$
F04297+2246A	–	$6.0^{+4.4}_{-1.5}$	$3.6^{+1.8}_{-1.8}$	$3.1^{+1.0}_{-0.7}$	$0.0^{+0.9}_{-0.0}$

ID	SpT	Oli/Pyr[a] % (0.1 μm)	Ens % (0.1 μm)	For % (0.1 μm)	Sil % (0.1 μm)
...		$31.3^{+15.2}_{-10.4}$	$1.4^{+2.8}_{-0.0}$	$2.1^{+2.1}_{-0.0}$	$0.0^{+8.2}_{-0.0}$
F04570+2520	–	$2.9^{+11.6}_{-0.0}$	$0.1^{+1.7}_{-0.0}$	$0.1^{+3.9}_{-0.0}$	$0.0^{+2.9}_{-0.0}$
...		$0.1^{+4.1}_{-8.8}$	$0.0^{+1.8}_{-1.9}$	$0.0^{+9.0}_{-0.0}$	$40.0^{+8.3}_{-30.3}$
FMTau	M0	$56.0^{+14.4}_{-10.3}$	$0.0^{+2.4}_{-1.5}$	$2.1^{+2.6}_{-1.5}$	$0.0^{+1.7}_{-0.0}$
...		$25.0^{+46.8}_{-0.0}$	$2.4^{+23.7}_{-0.0}$	$3.5^{+4.5}_{-0.0}$	$1.2^{+17.8}_{-0.0}$
FNTau	M5	$11.3^{+3.5}_{-2.0}$	$4.5^{+2.7}_{-1.4}$	$2.7^{+2.0}_{-1.0}$	$0.1^{+2.0}_{-0.2}$
...		$10.6^{+52.1}_{-0.0}$	$9.3^{+29.6}_{-0.0}$	$12.6^{+37.1}_{-0.0}$	$0.0^{+22.9}_{-0.0}$
FOTau	M2	$12.4^{+6.8}_{-6.2}$	$0.0^{+4.2}_{-0.0}$	$2.5^{+6.5}_{-0.0}$	$0.2^{+3.3}_{-0.0}$
FPTau	M4	$25.8^{+9.3}_{-5.8}$	$3.7^{+2.6}_{-2.4}$	$0.9^{+1.6}_{-0.4}$	$0.0^{+2.4}_{-0.0}$
...		$8.6^{+8.4}_{-2.5}$	$7.2^{+6.1}_{-3.7}$	$2.4^{+2.7}_{-1.7}$	$10.1^{+6.6}_{-0.0}$
FQTau	M2	$17.9^{+15.3}_{-11.8}$	$1.0^{+7.1}_{-0.3}$	$0.4^{+3.3}_{-0.2}$	$5.2^{+7.0}_{-2.7}$
FSTau	M1	$32.5^{+10.9}_{-9.6}$	$1.6^{+3.0}_{-0.6}$	$0.3^{+1.4}_{-0.0}$	$1.3^{+1.7}_{-0.6}$
FTTau	c	$20.1^{+5.5}_{-3.9}$	$1.0^{+1.4}_{-0.8}$	$2.9^{+1.8}_{-1.5}$	$0.0^{+1.0}_{-0.0}$
...		$14.4^{+17.8}_{-0.0}$	$0.0^{+10.9}_{-0.0}$	$0.0^{+4.4}_{-0.0}$	$2.9^{+13.7}_{-0.0}$
FVTau	K5	$1.4^{+6.5}_{-0.0}$	$0.0^{+4.8}_{-0.0}$	$3.9^{+3.0}_{-0.0}$	$0.0^{+0.8}_{-0.0}$
FXTau	M1	$28.2^{+8.6}_{-5.6}$	$3.7^{+5.0}_{-0.0}$	$3.4^{+1.8}_{-1.6}$	$0.0^{+0.8}_{-0.0}$
...		$21.1^{+14.8}_{-3.5}$	$0.0^{+8.8}_{-0.0}$	$3.9^{+8.7}_{-0.0}$	$4.6^{+16.3}_{-0.0}$
FZTau	M0	$24.8^{+7.5}_{-10.9}$	$1.3^{+2.2}_{-0.0}$	$1.9^{+1.0}_{-0.9}$	$10.7^{+2.6}_{-2.6}$
GGTau	M0	$9.2^{+3.4}_{-3.7}$	$0.9^{+2.0}_{-0.0}$	$1.6^{+1.4}_{-0.0}$	$0.0^{+0.9}_{-0.0}$
GHTau	M2	$10.6^{+3.1}_{-3.9}$	$1.7^{+1.7}_{-0.9}$	$2.1^{+1.1}_{-1.3}$	$0.7^{+1.4}_{-0.7}$
...		$8.7^{+4.5}_{-4.5}$	$2.0^{+4.1}_{-2.4}$	$4.9^{+5.4}_{-4.4}$	$2.7^{+2.7}_{-2.3}$
GITau	K6	$35.6^{+10.0}_{-10.5}$	$0.4^{+3.0}_{-0.0}$	$1.4^{+1.3}_{-0.9}$	$0.0^{+0.6}_{-0.0}$
...		$16.0^{+10.5}_{-7.3}$	$8.4^{+5.7}_{-3.8}$	$11.1^{+6.0}_{-5.2}$	$1.9^{+5.1}_{-1.9}$
GKTau	K7	$64.5^{+7.3}_{-10.7}$	$0.0^{+0.9}_{-0.0}$	$3.1^{+1.5}_{-1.3}$	$0.0^{+0.7}_{-0.0}$
GMAur	K3	$37.3^{+9.4}_{-11.2}$	$0.0^{+3.2}_{-0.0}$	$3.1^{+2.8}_{-0.0}$	$0.0^{+1.3}_{-0.0}$
...		$15.7^{+29.0}_{-0.0}$	$0.7^{+5.5}_{-0.0}$	$0.4^{+29.4}_{-0.0}$	$17.3^{+33.6}_{-0.0}$
GOTau	M0	$12.0^{+6.5}_{-7.6}$	$0.0^{+4.8}_{-0.0}$	$3.4^{+2.8}_{-2.3}$	$0.1^{+2.0}_{-0.0}$
HKTau	M1	$1.0^{+2.9}_{-0.3}$	$0.4^{+2.0}_{-0.0}$	$1.8^{+1.3}_{-0.0}$	$0.1^{+1.1}_{-0.0}$
...		$19.5^{+29.6}_{-3.4}$	$5.3^{+10.3}_{-0.0}$	$1.3^{+8.8}_{-0.0}$	$11.1^{+54.3}_{-2.5}$
HNTau	K5	$13.9^{+6.7}_{-3.7}$	$0.0^{+0.4}_{-0.0}$	$0.8^{+0.7}_{-0.0}$	$0.0^{+0.4}_{-0.0}$
HOTau	M0.5	$10.8^{+3.7}_{-1.6}$	$0.7^{+1.0}_{-0.4}$	$2.0^{+2.6}_{-0.6}$	$0.0^{+0.7}_{-0.0}$
...		$38.3^{+19.0}_{-16.0}$	$0.0^{+1.2}_{-0.0}$	$1.6^{+4.0}_{-0.0}$	$0.0^{+2.7}_{-0.0}$
HPTau	K3	$57.4^{+10.9}_{-10.6}$	$0.0^{+0.8}_{-0.0}$	$1.0^{+1.0}_{-0.0}$	$0.0^{+0.9}_{-0.0}$
Haro6-37	K7	$11.4^{+13.5}_{-7.7}$	$0.0^{+1.6}_{-0.0}$	$3.4^{+2.2}_{-1.8}$	$3.0^{+2.9}_{-1.8}$
IPTau	M0	$28.0^{+9.2}_{-7.4}$	$0.8^{+2.4}_{-0.3}$	$2.5^{+1.4}_{-1.7}$	$0.0^{+0.5}_{-0.0}$
...		$17.0^{+8.1}_{-6.0}$	$0.2^{+7.4}_{-0.0}$	$1.7^{+5.7}_{-0.1}$	$8.2^{+5.6}_{-2.9}$
IQTau	M0.5	$17.3^{+4.1}_{-4.0}$	$0.0^{+1.4}_{-0.0}$	$2.0^{+1.7}_{-1.1}$	$0.0^{+0.9}_{-0.0}$
...		$24.3^{+8.9}_{-6.3}$	$0.0^{+1.2}_{-0.0}$	$0.7^{+2.7}_{-0.4}$	$1.6^{+3.1}_{-1.0}$
ISTau	K7	$0.0^{+4.1}_{-0.0}$	$0.0^{+3.3}_{-0.0}$	$6.8^{+2.9}_{-1.8}$	$11.6^{+3.8}_{-3.3}$
...		$3.0^{+24.8}_{-0.0}$	$0.0^{+31.7}_{-0.0}$	$10.4^{+55.5}_{-0.0}$	$6.8^{+66.0}_{-0.0}$
LkCa15	K5	$55.9^{+11.0}_{-15.1}$	$0.0^{+2.0}_{-0.0}$	$2.7^{+3.8}_{-0.0}$	$0.0^{+0.6}_{-0.0}$

ID	SpT	Oli/Pyr^a % (0.1 μm)	Ens % (0.1 μm)	For % (0.1 μm)	Sil % (0.1 μm)
...		$22.0^{+11.7}_{-8.4}$	$9.2^{+6.1}_{-6.1}$	$0.0^{+2.0}_{-0.0}$	$10.2^{+7.4}_{-5.8}$
RWAur	K3	$26.1^{+9.0}_{-9.6}$	$0.3^{+1.0}_{-0.0}$	$1.5^{+2.1}_{-0.0}$	$0.0^{+0.5}_{-0.0}$
RYTau	G1	$6.5^{+3.8}_{-1.8}$	$8.4^{+1.7}_{-2.7}$	$1.1^{+0.8}_{-0.6}$	$8.0^{+1.7}_{-1.5}$
SUAur	G1	$20.2^{+5.0}_{-5.4}$	$0.0^{+0.6}_{-0.0}$	$1.3^{+1.0}_{-0.9}$	$0.0^{+0.6}_{-0.0}$
UYAur	K7	$19.9^{+6.4}_{-6.8}$	$0.1^{+2.6}_{-0.0}$	$0.0^{+1.3}_{-0.0}$	$0.0^{+1.9}_{-0.0}$
V710Tau	M1	$27.7^{+14.5}_{-19.2}$	$0.0^{+1.6}_{-0.0}$	$2.8^{+2.6}_{-1.8}$	$0.9^{+1.45}_{-0.6}$
V773Tau	K3	$26.2^{+24.6}_{-5.4}$	$3.8^{+5.9}_{-0.0}$	$1.3^{+2.3}_{-0.0}$	$0.0^{+1.8}_{-0.0}$
V836Tau	K7	$1.2^{+3.4}_{-0.0}$	$0.9^{+0.8}_{-0.6}$	$4.5^{+1.9}_{-0.8}$	$0.0^{+0.9}_{-0.0}$
...		$30.7^{+48.4}_{-8.9}$	$0.0^{+26.6}_{-0.0}$	$1.7^{+9.2}_{-0.0}$	$10.4^{+61.5}_{-0.0}$
V955Tau	K5	$0.0^{+1.3}_{-0.0}$	$0.0^{+0.9}_{-0.0}$	$6.3^{+2.5}_{-1.6}$	$10.7^{+3.1}_{-2.8}$
VYTau	M0	$2.5^{+13.5}_{-0.0}$	$0.0^{+12.4}_{-0.0}$	$3.3^{+16.1}_{-0.0}$	$0.0^{+8.4}_{-0.0}$
ZZTauIRS	M4.5	$16.0^{+6.3}_{-3.5}$	$0.7^{+3.0}_{-0.0}$	$0.7^{+2.2}_{-0.0}$	$0.1^{+1.2}_{-0.0}$
...		$16.1^{+8.6}_{-6.5}$	$0.0^{+2.0}_{-0.2}$	$8.1^{+6.9}_{-5.0}$	$6.0^{+4.7}_{-3.3}$
Upper Scorpius					
PBB2002 J160357.9	M2	$8.2^{+16.3}_{-2.1}$	$0.0^{+1.5}_{-0.0}$	$2.1^{+4.6}_{-0.2}$	$0.0^{+1.0}_{-0.0}$
PBB2002 J160823.2	K9	$2.4^{+6.2}_{-0.0}$	$0.0^{+5.3}_{-0.0}$	$3.8^{+6.2}_{-0.0}$	$0.0^{+1.1}_{-0.0}$
PBB2002 J160900.7	K9	$17.2^{+6.5}_{-4.5}$	$0.5^{+1.4}_{-0.0}$	$3.0^{+2.0}_{-1.6}$	$0.0^{+0.3}_{-0.0}$
PBB2002 J160959.4	M4	$17.7^{+31.6}_{-11.4}$	$0.0^{+2.7}_{-0.0}$	$4.8^{+3.8}_{-2.4}$	$0.5^{+2.5}_{-0.0}$
PBB2002 J161115.3	M1	$20.3^{+4.2}_{-12.7}$	$0.0^{+2.4}_{-0.0}$	$1.9^{+2.5}_{-1.4}$	$0.0^{+0.7}_{-0.0}$
PBB2002 J161420.2	M0	$6.5^{+1.4}_{-1.4}$	$0.0^{+0.5}_{-0.0}$	$1.4^{+0.9}_{-0.9}$	$0.0^{+0.3}_{-0.0}$
PZ99 J160357.6	K5	$0.0^{+3.1}_{-0.0}$	$0.0^{+2.8}_{-0.0}$	$2.8^{+5.1}_{-0.0}$	$0.0^{+3.2}_{-0.0}$
PZ99 J161411.0	K0	$0.0^{+2.0}_{-0.0}$	$0.0^{+4.0}_{-0.0}$	$1.1^{+2.1}_{-0.0}$	$1.4^{+4.4}_{-0.0}$
ScoPMS31	M0.5	$9.6^{+7.5}_{-11.3}$	$0.0^{+2.5}_{-0.0}$	$1.9^{+3.3}_{-1.8}$	$3.0^{+4.6}_{-1.6}$
η Chamaeleontis					
J0843	M3.4	$27.2^{+16.9}_{-11.0}$	$1.1^{+8.3}_{-0.0}$	$4.4^{+3.3}_{-0.0}$	$1.5^{+2.8}_{-0.0}$
RECX-5	M3.8	$36.1^{+23.4}_{-19.4}$	$0.0^{+2.9}_{-0.0}$	$12.3^{+8.7}_{-0.0}$	$0.3^{+14.8}_{-0.0}$
RECX-9	M4.4	$42.9^{+21.6}_{-34.1}$	$0.0^{+6.0}_{-0.0}$	$1.9^{+3.9}_{-1.0}$	$8.6^{+8.3}_{-6.7}$
RECX-11	K6.5	$36.9^{+18.1}_{-17.2}$	$1.4^{+3.4}_{-0.0}$	$3.4^{+8.4}_{-0.0}$	$2.6^{+4.2}_{-0.0}$

Table A.1 – Small dust composition derived using the "B2C" procedure.^{b}

^{a} Amorphous olivine and pyroxene combined.

^{b} For each object, the first line corresponds to the warm component abundances, while the second line corresponds to the cold component abundances, when available.

ID	Oli/Pyr[a] % (1.5 μm)	Ens % (1.5 μm)	For % (1.5 μm)	Sil % (1.5 μm)	Oli/Pyr[a] % (6.0 μm)	Sil % (6.0 μm)
Serpens						
1	$53.7^{+16.5}_{-23.0}$	$3.5^{+3.5}_{-2.4}$	$0.0^{+2.9}_{-0.0}$	$1.0^{+2.1}_{-0.0}$	$7.8^{+3.8}_{-0.0}$	$0.6^{+1.9}_{-0.0}$
...	$29.3^{+6.2}_{-15.3}$	$6.8^{+4.3}_{-2.8}$	$0.2^{+1.1}_{-0.0}$	$0.3^{+1.4}_{-0.0}$	$9.7^{+4.7}_{-4.4}$	$5.5^{+1.4}_{-1.6}$
3	$43.9^{+19.8}_{-18.6}$	$0.2^{+4.1}_{-0.2}$	$2.7^{+3.8}_{-2.1}$	$0.0^{+2.9}_{-0.0}$	$15.7^{+3.2}_{-2.8}$	$0.0^{+1.0}_{-0.0}$
...	$32.9^{+34.1}_{-9.9}$	$4.9^{+19.2}_{-5.5}$	$0.0^{+13.9}_{-2.9}$	$12.7^{+22.5}_{-5.6}$	$10.2^{+7.4}_{-4.7}$	$1.8^{+2.2}_{-0.6}$
6	$38.2^{+11.6}_{-7.4}$	$1.0^{+1.4}_{-0.0}$	$1.0^{+1.4}_{-0.0}$	$0.0^{+1.4}_{-0.0}$	$28.8^{+4.5}_{-5.0}$	$4.8^{+3.6}_{-1.8}$
...	$46.1^{+19.8}_{-20.3}$	$4.7^{+6.2}_{-0.0}$	$1.2^{+2.3}_{-0.0}$	$2.7^{+4.4}_{-0.0}$	$25.4^{+8.6}_{-7.6}$	$3.7^{+2.2}_{-0.0}$
7	$75.6^{+26.0}_{-23.9}$	$0.0^{+5.6}_{-0.1}$	$3.7^{+4.7}_{-3.0}$	$0.0^{+5.1}_{-0.0}$	$0.0^{+9.8}_{-0.0}$	$16.1^{+4.4}_{-13.7}$
...	$6.0^{+7.7}_{-6.0}$	$14.1^{+8.8}_{-11.7}$	$0.0^{+3.0}_{-0.1}$	$24.7^{+14.3}_{-19.7}$	$25.6^{+14.0}_{-13.9}$	$0.0^{+3.5}_{-2.6}$
9	$27.4^{+5.7}_{-7.2}$	$3.8^{+2.4}_{-2.1}$	$2.5^{+1.5}_{-2.0}$	$0.0^{+1.3}_{-0.0}$	$3.6^{+4.1}_{-0.0}$	$3.7^{+1.7}_{-0.0}$
...	$9.4^{+6.7}_{-6.1}$	$0.0^{+3.8}_{-0.8}$	$0.0^{+1.5}_{-0.0}$	$7.5^{+5.8}_{-5.2}$	$24.4^{+16.2}_{-14.3}$	$2.7^{+7.2}_{-3.2}$
10	$37.6^{+17.3}_{-16.8}$	$7.2^{+4.2}_{-3.5}$	$5.3^{+6.6}_{-2.9}$	$0.2^{+4.0}_{-0.0}$	$31.6^{+18.5}_{-8.3}$	$9.5^{+7.6}_{-4.4}$
...	$39.0^{+23.6}_{-10.3}$	$0.0^{+20.1}_{-0.0}$	$3.3^{+9.6}_{-1.3}$	$0.0^{+9.3}_{-0.0}$	$14.8^{+35.1}_{-1.2}$	$3.6^{+14.1}_{-0.5}$
14	$54.7^{+31.3}_{-20.3}$	$4.8^{+20.8}_{-0.0}$	$0.0^{+4.9}_{-0.0}$	$0.0^{+8.7}_{-0.0}$	$13.5^{+9.3}_{-5.8}$	$12.8^{+10.4}_{-4.0}$
15	$51.3^{+9.3}_{-16.1}$	$3.0^{+3.4}_{-1.5}$	$0.0^{+1.6}_{-0.0}$	$0.8^{+1.8}_{-0.0}$	$1.2^{+2.2}_{-0.0}$	$5.0^{+2.0}_{-0.5}$
...	$34.9^{+9.9}_{-12.2}$	$0.0^{+1.0}_{-0.0}$	$5.4^{+2.0}_{-2.1}$	$0.0^{+2.1}_{-0.6}$	$14.6^{+4.7}_{-4.6}$	$3.0^{+1.4}_{-1.9}$
21	$20.2^{+10.1}_{-12.9}$	$0.1^{+4.2}_{-0.0}$	$19.2^{+11.1}_{-9.1}$	$0.0^{+4.2}_{-0.0}$	$43.3^{+.6.5}_{-21.3}$	$12.3^{+8.6}_{-9.1}$
...	$42.5^{+22.6}_{-24.9}$	$2.7^{+14.8}_{-0.0}$	$0.5^{+3.8}_{-0.0}$	$0.0^{+14.2}_{-0.0}$	$9.6^{+8.7}_{-3.3}$	$8.7^{+5.2}_{-7.5}$
29	$71.0^{+26.0}_{-49.2}$	$0.0^{+9.3}_{-0.0}$	$4.4^{+9.4}_{-3.1}$	$0.0^{+7.9}_{-0.0}$	$13.0^{+6.4}_{-7.}$	$5.6^{+14.7}_{-3.1}$
30	$12.5^{+8.5}_{-6.4}$	$12.5^{+8.1}_{-3.4}$	$1.3^{+5.9}_{-0.8}$	$1.5^{+5.0}_{-0.0}$	$64.2^{+18.1}_{-47.0}$	$0.0^{+21.4}_{-0.0}$
...	$8.0^{+58.7}_{-19.4}$	$9.1^{+14.9}_{-5.1}$	$29.6^{+44.9}_{-24.3}$	$11.4^{+37.5}_{-10.3}$	$14.0^{+36.3}_{-2.3}$	$2.1^{+9.6}_{-2.3}$
31	$15.0^{+2.6}_{-1.5}$	$2.5^{+1.2}_{-0.0}$	$3.4^{+1.5}_{-0.0}$	$0.4^{+0.4}_{-0.0}$	$76.1^{+7.8}_{-5.4}$	$0.6^{+1.0}_{-0.0}$
...	$24.0^{+4.7}_{-4.0}$	$2.3^{+2.0}_{-0.0}$	$0.5^{+1.7}_{-0.0}$	$5.4^{+4.4}_{-2.6}$	$9.2^{+4.8}_{-5.2}$	$17.6^{+3.3}_{-4.7}$
36	$51.9^{+12.1}_{-12.3}$	$1.0^{+2.9}_{-0.6}$	$3.3^{+2.8}_{-2.5}$	$0.0^{+1.6}_{-0.0}$	$10.8^{+2.8}_{-2.6}$	$9.0^{+2.7}_{-4.8}$
...	$38.1^{+11.0}_{-14.3}$	$0.0^{+2.4}_{-0.0}$	$0.0^{+2.9}_{-0.0}$	$0.2^{+8.7}_{-0.0}$	$19.6^{+5.9}_{-7.7}$	$0.1^{+0.3}_{-1.4}$
40	$41.2^{+17.3}_{-25.0}$	$22.5^{+11.0}_{-8.8}$	$17.9^{+11.6}_{-7.4}$	$0.0^{+5.5}_{-0.0}$	$4.5^{+9.7}_{-0.2}$	$0.0^{+9.8}_{-0.0}$
...	$18.2^{+9.5}_{-13.8}$	$2.1^{+12.8}_{-1.9}$	$13.4^{+7.8}_{-9.8}$	$0.0^{+3.0}_{-0.0}$	$0.2^{+9.7}_{-0.0}$	$22.3^{+11.2}_{-12.6}$
41	$66.6^{+6.8}_{-58.2}$	$3.4^{+16.3}_{-0.0}$	$16.4^{+11.3}_{-8.6}$	$0.0^{+6.3}_{-0.0}$	$2.6^{+13.8}_{-0.0}$	$0.0^{+14.8}_{-0.0}$
43	$42.1^{+19.1}_{-27.0}$	$7.1^{+8.9}_{-5.1}$	$2.7^{+7.1}_{-2.0}$	$0.0^{+3.5}_{-0.0}$	$37.2^{+15.8}_{-19.3}$	$2.0^{+12.7}_{-0.0}$
48	$73.3^{+28.2}_{-35.2}$	$0.0^{+9.2}_{-0.0}$	$0.0^{+13.8}_{-0.1}$	$1.1^{+9.9}_{-0.7}$	$6.0^{+8.4}_{-2.1}$	$9.9^{+4.6}_{-6.9}$
...	$18.7^{+10.0}_{-17.6}$	$0.0^{+7.5}_{-0.1}$	$4.1^{+12.0}_{-3.5}$	$8.6^{+5.8}_{-8.1}$	$7.4^{+5.6}_{-4.7}$	$7.5^{+4.4}_{-6.6}$
53	$30.2^{+18.2}_{-14.6}$	$10.1^{+19.9}_{-5.8}$	$0.0^{+11.6}_{-0.0}$	$2.3^{+15.6}_{-0.7}$	$32.9^{+27.1}_{-6.7}$	$8.1^{+9.4}_{-5.3}$
55	$71.0^{+16.2}_{-26.2}$	$0.0^{+3.0}_{-0.0}$	$0.0^{+2.7}_{-0.0}$	$1.9^{+3.0}_{-0.0}$	$4.2^{+1.5}_{-0.8}$	$2.1^{+0.9}_{-0.7}$
...	$20.5^{+71.1}_{-20.0}$	$15.7^{+72.9}_{-9.9}$	$0.0^{+22.3}_{-0.1}$	$4.8^{+65.6}_{-4.2}$	$2.9^{+5.8}_{-1.6}$	$1.9^{+6.0}_{-1.8}$
56	$44.6^{+16.6}_{-28.5}$	$5.0^{+7.9}_{-2.7}$	$1.7^{+7.3}_{-0.5}$	$0.0^{+4.6}_{-0.0}$	$29.5^{+11.8}_{-11.8}$	$6.1^{+12.2}_{-0.1}$
...	$29.8^{+11.0}_{-12.0}$	$0.0^{+15.8}_{-0.0}$	$1.1^{+7.5}_{-0.0}$	$0.0^{+3.2}_{-0.0}$	$19.3^{+24.2}_{-7.9}$	$1.6^{+27.0}_{-0.0}$
57	$72.0^{+29.0}_{-40.9}$	$10.5^{+13.3}_{-6.6}$	$0.0^{+7.1}_{-0.0}$	$0.0^{+7.1}_{-0.0}$	$6.5^{+19.1}_{-0.0}$	$0.0^{+9.5}_{-0.0}$
...	$13.1^{+55.6}_{-4.8}$	$0.3^{+27.7}_{-0.0}$	$4.5^{+61.3}_{-0.0}$	$1.7^{+25.5}_{-4.5}$	$25.1^{+85.7}_{-3.7}$	$17.2^{+81.4}_{-5.0}$
58	$29.9^{+4.6}_{-6.7}$	$1.0^{+2.2}_{-0.7}$	$7.1^{+3.0}_{-2.1}$	$0.0^{+1.8}_{-0.0}$	$28.3^{+6.5}_{-11.5}$	$25.4^{+6.4}_{-8.7}$
...	$57.0^{+24.9}_{-36.3}$	$0.0^{+7.5}_{-0.0}$	$0.0^{+8.0}_{-0.0}$	$0.0^{+6.2}_{-0.0}$	$4.7^{+2.9}_{-1.4}$	$2.8^{+2.5}_{-0.0}$

ID	Oli/Pyr[a] % (1.5 μm)	Ens % (1.5 μm)	For % (1.5 μm)	Sil % (1.5 μm)	Oli/Pyr[a] % (6.0 μm)	Sil % (6.0 μm)
60	$41.7^{+31.4}_{-21.7}$	$8.5^{+13.1}_{-5.2}$	$3.3^{+14.0}_{-2.3}$	$0.0^{+13.7}_{-0.0}$	$4.9^{+14.8}_{-1.7}$	$26.5^{+17.0}_{-14.6}$
61	$52.1^{+11.9}_{-13.2}$	$3.1^{+5.1}_{-0.0}$	$6.2^{+3.6}_{-3.0}$	$0.0^{+2.4}_{-0.0}$	$11.3^{+4.2}_{-3.0}$	$13.3^{+1.8}_{-6.3}$
$\cdots$	$38.7^{+6.6}_{-6.3}$	$0.0^{+1.6}_{-0.0}$	$1.1^{+0.9}_{-0.6}$	$1.2^{+2.3}_{-0.1}$	$7.5^{+5.7}_{-0.0}$	$12.7^{+6.0}_{-2.4}$
65	$21.3^{+9.9}_{-16.6}$	$8.6^{+5.3}_{-5.4}$	$8.3^{+4.2}_{-3.2}$	$0.0^{+1.3}_{-2.7}$	$41.8^{+15.0}_{-22.4}$	$13.9^{+7.9}_{-10.4}$
$\cdots$	$6.2^{+9.7}_{-2.8}$	$0.3^{+9.6}_{-0.0}$	$0.0^{+4.0}_{-0.0}$	$2.7^{+3.8}_{-1.4}$	$8.5^{+28.2}_{-2.5}$	$18.4^{+20.9}_{-7.7}$
66	$46.5^{+15.4}_{-15.6}$	$0.8^{+5.1}_{-0.0}$	$2.9^{+5.0}_{-1.6}$	$0.0^{+2.3}_{-0.0}$	$38.2^{+18.7}_{-18.7}$	$8.7^{+8.2}_{-2.5}$
$\cdots$	$26.3^{+25.8}_{-8.9}$	$1.7^{+11.2}_{-0.0}$	$0.4^{+8.1}_{-0.0}$	$3.2^{+19.6}_{-0.0}$	$11.0^{+21.0}_{-0.0}$	$15.7^{+6.8}_{-8.1}$
71	$24.2^{+24.6}_{-11.4}$	$3.0^{+20.1}_{-0.3}$	$4.7^{+25.9}_{-0.0}$	$1.9^{+12.1}_{-0.5}$	$56.6^{+55.6}_{-10.9}$	$0.0^{+10.4}_{-0.0}$
74	$0.0^{+6.3}_{-0.0}$	$5.8^{+3.4}_{-3.0}$	$16.1^{+5.7}_{-0.0}$	$0.0^{+4.7}_{-0.0}$	$58.3^{+17.9}_{-31.2}$	$0.0^{+18.2}_{-0.0}$
$\cdots$	$24.2^{+26.5}_{-9.8}$	$1.8^{+23.4}_{-0.0}$	$5.4^{+31.1}_{-0.0}$	$0.0^{+12.8}_{-0.0}$	$9.9^{+22.5}_{-5.9}$	$7.8^{+23.4}_{-7.1}$
75	$15.0^{+>15.0}_{-0.0}$	$5.2^{+36.0}_{-0.0}$	$0.0^{+32.5}_{-0.0}$	$0.0^{+51.2}_{-0.0}$	$59.6^{+42.6}_{-33.4}$	$16.0^{+69.6}_{-0.0}$
76	$65.0^{+15.7}_{-29.6}$	$0.0^{+3.3}_{-0.0}$	$1.3^{+5.3}_{-0.0}$	$0.0^{+3.0}_{-0.0}$	$23.7^{+13.5}_{-3.9}$	$0.1^{+2.0}_{-0.0}$
$\cdots$	$29.6^{+12.4}_{-12.1}$	$0.0^{+3.3}_{-0.0}$	$12.9^{+7.2}_{-5.2}$	$0.0^{+2.1}_{-0.0}$	$12.2^{+5.9}_{-4.3}$	$0.0^{+2.1}_{-1.0}$
80	$7.5^{+2.0}_{-0.0}$	$3.2^{+1.3}_{-1.5}$	$3.1^{+1.0}_{-0.9}$	$0.0^{+0.6}_{-0.0}$	$84.7^{+8.2}_{-6.6}$	$0.0^{+1.1}_{-0.0}$
$\cdots$	$15.4^{+50.2}_{-0.0}$	$6.2^{+18.2}_{-0.0}$	$0.8^{+10.1}_{-0.0}$	$3.1^{+9.0}_{-0.0}$	$22.6^{+78.6}_{-0.0}$	$29.2^{+67.6}_{-0.0}$
81	$54.5^{+5.4}_{-3.7}$	$0.0^{+0.7}_{-0.0}$	$6.1^{+1.9}_{-2.0}$	$0.0^{+0.5}_{-0.0}$	$15.6^{+2.5}_{-2.7}$	$8.8^{+1.6}_{-1.2}$
$\cdots$	$31.4^{+8.3}_{-4.4}$	$7.0^{+2.4}_{-2.2}$	$0.0^{+0.3}_{-0.0}$	$4.0^{+2.3}_{-2.0}$	$7.7^{+1.0}_{-1.2}$	$4.5^{+0.7}_{-0.9}$
86	$36.0^{+3.4}_{-3.0}$	$0.0^{+0.2}_{-0.0}$	$3.3^{+1.1}_{-1.7}$	$0.0^{+0.2}_{-0.0}$	$44.1^{+4.2}_{-4.4}$	$0.1^{+0.7}_{-0.0}$
$\cdots$	$18.2^{+55.5}_{-0.0}$	$10.0^{+27.7}_{-0.0}$	$0.5^{+20.3}_{-0.0}$	$6.0^{+29.6}_{-0.0}$	$10.7^{+39.6}_{-0.0}$	$13.7^{+38.7}_{-0.0}$
88	$67.1^{+20.5}_{-17.3}$	$10.3^{+7.1}_{-5.0}$	$0.0^{+3.6}_{-0.0}$	$3.1^{+2.4}_{-2.0}$	$9.9^{+6.3}_{-1.8}$	$0.9^{+1.2}_{-0.6}$
$\cdots$	$2.1^{+21.3}_{-6.5}$	$0.0^{+7.7}_{-0.0}$	$30.6^{+29.1}_{-12.4}$	$0.6^{+9.9}_{-3.0}$	$17.6^{+32.8}_{-10.1}$	$3.1^{+11.2}_{-3.5}$
89	$0.0^{+0.7}_{-0.0}$	$0.0^{+0.6}_{-0.0}$	$1.4^{+0.9}_{-0.0}$	$0.0^{+0.6}_{-0.0}$	$94.4^{+18.8}_{-75.4}$	$0.0^{+3.7}_{-0.0}$
90	$49.1^{+24.7}_{-30.7}$	$3.7^{+9.5}_{-1.8}$	$0.0^{+10.1}_{-1.8}$	$2.8^{+5.5}_{-1.9}$	$5.4^{+16.4}_{-1.2}$	$10.0^{+12.9}_{-1.8}$
$\cdots$	$16.8^{+54.1}_{-0.0}$	$3.6^{+38.8}_{-0.0}$	$9.2^{+58.7}_{-0.0}$	$0.8^{+24.8}_{-0.0}$	$12.5^{+52.2}_{-0.0}$	$9.2^{+39.3}_{-0.0}$
92	$35.8^{+25.4}_{-8.5}$	$5.7^{+7.5}_{-2.1}$	$0.0^{+3.5}_{-0.0}$	$0.0^{+2.4}_{-0.0}$	$44.0^{+13.1}_{-15.9}$	$6.3^{+14.1}_{-2.4}$
$\cdots$	$31.2^{+9.3}_{-15.1}$	$0.4^{+6.5}_{-0.0}$	$6.8^{+3.8}_{-3.9}$	$0.0^{+10.0}_{-0.0}$	$37.9^{+19.4}_{-12.3}$	$0.0^{+12.6}_{-0.0}$
96	$56.5^{+23.3}_{-35.1}$	$3.8^{+12.9}_{-1.8}$	$0.0^{+15.2}_{-0.0}$	$3.0^{+9.2}_{-0.8}$	$7.4^{+6.7}_{-4.3}$	$5.8^{+10.1}_{-1.5}$
100	$1.2^{+88.8}_{-0.0}$	$9.5^{+81.9}_{-0.0}$	$0.0^{+34.1}_{-0.0}$	$1.1^{+106.2}_{-0.0}$	$81.8^{+47.3}_{-54.1}$	$3.1^{+11.6}_{-4.1}$
101	$60.2^{+22.6}_{-33.4}$	$1.9^{+8.8}_{-0.0}$	$2.6^{+7.5}_{-0.5}$	$0.0^{+5.3}_{-0.0}$	$6.6^{+10.1}_{-0.0}$	$1.6^{+5.2}_{-0.0}$
$\cdots$	$55.9^{+7.1}_{-11.9}$	$0.0^{+3.7}_{-0.0}$	$9.5^{+4.8}_{-6.1}$	$0.0^{+2.7}_{-0.0}$	$13.6^{+3.5}_{-7.2}$	$0.1^{+3.0}_{-0.0}$
103	$38.0^{+7.0}_{-5.0}$	$2.0^{+2.3}_{-1.2}$	$7.8^{+2.4}_{-2.1}$	$0.0^{+1.8}_{-0.0}$	$27.6^{+6.0}_{-5.5}$	$18.9^{+4.2}_{-4.1}$
$\cdots$	$35.1^{+18.1}_{-20.5}$	$0.0^{+6.3}_{-0.0}$	$5.1^{+5.6}_{-0.0}$	$4.2^{+9.0}_{-0.0}$	$15.7^{+8.5}_{-4.5}$	$17.3^{+2.3}_{-17.7}$
104	$70.4^{+35.4}_{-48.8}$	$4.7^{+12.4}_{-3.6}$	$0.0^{+10.2}_{-0.0}$	$0.0^{+6.1}_{-0.0}$	$14.2^{+17.3}_{-6.1}$	$0.1^{+14.8}_{-0.0}$
106	$0.1^{+24.9}_{-0.0}$	$10.0^{+21.9}_{-5.5}$	$0.3^{+10.7}_{-0.0}$	$1.1^{+15.6}_{-0.0}$	$73.7^{+19.9}_{-61.5}$	$0.0^{+20.7}_{-0.0}$
113	$24.9^{+12.9}_{-10.3}$	$10.3^{+4.9}_{-3.4}$	$5.8^{+5.2}_{-2.2}$	$0.0^{+2.0}_{-0.0}$	$42.5^{+13.4}_{-17.9}$	$8.8^{+7.0}_{-4.4}$
$\cdots$	$36.2^{+21.8}_{-13.5}$	$1.7^{+9.0}_{-0.0}$	$0.0^{+5.8}_{-0.0}$	$0.0^{+7.9}_{-0.0}$	$10.9^{+11.9}_{-1.3}$	$8.6^{+10.8}_{-4.2}$
114	$34.7^{+17.7}_{-12.5}$	$4.2^{+3.2}_{-2.8}$	$1.9^{+6.6}_{-0.6}$	$0.0^{+2.3}_{-0.0}$	$51.8^{+15.2}_{-17.1}$	$17.4^{+10.1}_{-5.2}$
115	$65.7^{+17.3}_{-48.2}$	$0.0^{+4.3}_{-0.0}$	$0.0^{+4.3}_{-0.0}$	$0.0^{+3.5}_{-0.0}$	$25.6^{+10.3}_{-14.5}$	$2.6^{+4.6}_{-0.9}$
117	$5.1^{+6.4}_{-0.2}$	$10.7^{+2.1}_{-3.2}$	$0.0^{+0.9}_{-0.0}$	$0.0^{+0.9}_{-0.0}$	$2.1^{+2.0}_{-0.0}$	$0.2^{+1.2}_{-0.0}$
$\cdots$	$23.6^{+14.9}_{-6.8}$	$0.8^{+2.1}_{-0.4}$	$0.0^{+6.8}_{-0.0}$	$2.3^{+3.9}_{-2.4}$	$2.4^{+2.8}_{-1.3}$	$1.7^{+2.2}_{-0.9}$
119	$11.1^{+56.7}_{-2.7}$	$0.2^{+25.1}_{-0.0}$	$0.6^{+41.3}_{-0.0}$	$0.3^{+33.6}_{-0.0}$	$84.0^{+58.6}_{-26.7}$	$0.0^{+96.2}_{-0.0}$
122	$52.6^{+10.1}_{-35.4}$	$6.4^{+15.0}_{-3.1}$	$0.0^{+10.0}_{-0.0}$	$0.0^{+4.4}_{-0.0}$	$1.7^{+17.3}_{-1.0}$	$7.1^{+14.6}_{-1.1}$

ID	Oli/Pyr[a] % (1.5 μm)	Ens % (1.5 μm)	For % (1.5 μm)	Sil % (1.5 μm)	Oli/Pyr[a] % (6.0 μm)	Sil % (6.0 μm)
$\cdots$	$27.8^{+39.9}_{-13.3}$	$0.9^{+11.2}_{-0.0}$	$0.0^{+14.3}_{-0.0}$	$0.0^{+10.5}_{-1.7}$	$11.8^{+13.6}_{-4.3}$	$5.7^{+18.0}_{-0.0}$
123	$41.2^{+11.7}_{-16.8}$	$4.1^{+6.4}_{-0.6}$	$0.0^{+4.2}_{-0.0}$	$2.7^{+3.7}_{-1.4}$	$4.0^{+6.8}_{-0.1}$	$0.0^{+0.5}_{-0.0}$
125	$56.9^{+11.9}_{-23.8}$	$0.0^{+5.0}_{-0.0}$	$0.0^{+7.2}_{-0.0}$	$0.0^{+4.4}_{-0.0}$	$30.8^{+6.4}_{-16.9}$	$5.0^{+11.2}_{-1.2}$
$\cdots$	$29.1^{+9.2}_{-13.7}$	$7.0^{+4.1}_{-5.2}$	$0.2^{+1.8}_{-0.0}$	$0.0^{+3.8}_{-0.0}$	$16.0^{+6.1}_{-7.7}$	$5.1^{+3.2}_{-3.1}$
127	$0.0^{+2.0}_{-0.0}$	$0.0^{+3.1}_{-0.0}$	$1.5^{+5.7}_{-0.0}$	$1.3^{+4.4}_{-0.5}$	$91.5^{+71.4}_{-21.7}$	$0.0^{+7.8}_{-0.0}$
129	$14.7^{+7.3}_{-4.2}$	$1.7^{+4.2}_{-0.0}$	$0.0^{+2.3}_{-0.0}$	$0.0^{+0.9}_{-0.0}$	$82.5^{+20.0}_{-55.0}$	$0.0^{+6.7}_{-0.0}$
137	$39.0^{+10.8}_{-19.2}$	$5.6^{+3.4}_{-4.2}$	$5.8^{+4.1}_{-3.6}$	$0.0^{+3.2}_{-0.0}$	$0.0^{+2.3}_{-0.0}$	$7.1^{+4.7}_{-2.1}$
142	$58.7^{+20.7}_{-33.8}$	$4.0^{+6.6}_{-2.6}$	$1.9^{+7.4}_{-0.0}$	$4.5^{+4.9}_{-2.7}$	$25.7^{+9.0}_{-10.1}$	$0.1^{+6.1}_{-0.0}$
144	$46.2^{+6.0}_{-23.0}$	$11.2^{+4.4}_{-3.3}$	$0.0^{+3.0}_{-0.0}$	$0.0^{+3.0}_{-0.0}$	$32.0^{+13.9}_{-7.4}$	$0.0^{+2.6}_{-0.0}$
$\cdots$	$7.3^{+21.8}_{-7.8}$	$10.5^{+20.1}_{-6.9}$	$12.1^{+10.9}_{-6.2}$	$0.0^{+22.2}_{-0.0}$	$8.3^{+19.9}_{-3.5}$	$5.5^{+14.3}_{-3.7}$
146	$34.1^{+4.5}_{-6.7}$	$0.0^{+1.1}_{-0.0}$	$4.1^{+3.0}_{-2.3}$	$0.0^{+1.3}_{-0.0}$	$32.6^{+8.3}_{-7.7}$	$15.6^{+2.9}_{-4.7}$
$\cdots$	$27.7^{+8.1}_{-8.0}$	$0.0^{+3.8}_{-0.0}$	$2.2^{+1.5}_{-0.0}$	$0.0^{+2.6}_{-0.0}$	$52.9^{+19.8}_{-10.5}$	$0.0^{+8.7}_{-0.0}$
147	$34.1^{+18.9}_{-10.9}$	$9.8^{+9.0}_{-4.6}$	$0.0^{+3.5}_{-0.6}$	$0.7^{+4.8}_{-0.0}$	$50.7^{+18.1}_{-41.6}$	$0.0^{+15.4}_{-0.0}$
148	$70.6^{+18.2}_{-49.9}$	$3.7^{+8.0}_{-2.0}$	$0.0^{+5.3}_{-0.0}$	$2.5^{+5.1}_{-0.0}$	$5.1^{+8.9}_{-0.0}$	$4.6^{+5.1}_{-1.1}$
$\cdots$	$2.0^{+13.4}_{-0.0}$	$10.9^{+16.2}_{-7.5}$	$5.0^{+17.7}_{-3.7}$	$2.9^{+21.5}_{-0.0}$	$24.7^{+18.4}_{-9.6}$	$0.1^{+4.7}_{-0.0}$
149	$24.1^{+10.8}_{-10.7}$	$3.9^{+5.5}_{-1.6}$	$0.0^{+2.3}_{-0.0}$	$1.3^{+2.6}_{-0.0}$	$30.1^{+11.2}_{-8.9}$	$0.4^{+8.8}_{-0.0}$
$\cdots$	$28.3^{+14.5}_{-21.1}$	$3.7^{+13.2}_{-0.5}$	$1.1^{+12.7}_{-0.1}$	$0.0^{+8.3}_{-0.0}$	$8.8^{+6.5}_{-1.2}$	$7.8^{+5.4}_{-1.9}$
Taurus						
04108+2910	$10.4^{+4.1}_{-6.1}$	$11.2^{+3.1}_{-4.7}$	$3.6^{+3.1}_{-1.6}$	$0.0^{+0.9}_{-0.0}$	$71.3^{+16.2}_{-29.0}$	$0.0^{+8.4}_{-0.0}$
$\cdots$	$58.5^{+22.3}_{-17.8}$	$0.0^{+8.0}_{-0.0}$	$0.0^{+7.8}_{-0.0}$	$0.0^{+45.4}_{-0.0}$	$12.9^{+15.9}_{-5.3}$	$11.4^{+7.1}_{-6.4}$
04200+2759	$48.4^{+14.7}_{-13.1}$	$7.9^{+6.2}_{-4.1}$	$2.8^{+5.3}_{-0.0}$	$0.0^{+2.5}_{-0.0}$	$19.6^{9.4}_{-5.6}$	$16.0^{+7.1}_{-11.1}$
$\cdots$	$58.6^{+32.2}_{-26.4}$	$0.0^{+9.8}_{-0.0}$	$0.0^{+18.6}_{-0.0}$	$7.2^{+31.8}_{-20.3}$	$10.3^{+7.3}_{-5.6}$	$0.4^{+2.6}_{-1.4}$
04216+2603	$18.9^{+17.6}_{-12.3}$	$6.4^{+1.7}_{-5.1}$	$0.0^{+2.5}_{-0.0}$	$0.0^{+2.8}_{-0.0}$	$27.1^{+9.7}_{-9.5}$	$0.0^{+9.3}_{-0.0}$
$\cdots$	$4.4^{+16.5}_{-5.1}$	$2.1^{+18.1}_{-3.1}$	$1.5^{+20.5}_{-0.0}$	$10.5^{+17.2}_{-5.9}$	$44.5^{+31.4}_{-17.3}$	$3.2^{+13.5}_{-4.3}$
04303+2240	$74.2^{+25.2}_{-17.9}$	$3.5^{+8.5}_{-0.0}$	$9.6^{+10.7}_{-6.3}$	$2.0^{+4.0}_{-0.4}$	$0.0^{+1.0}_{-0.0}$	$5.5^{+9.8}_{-0.0}$
04370+2559	$80.2^{+16.5}_{-33.6}$	$0.3^{+7.0}_{-0.0}$	$1.2^{+5.7}_{-0.0}$	$0.0^{+2.1}_{-0.0}$	$4.9^{+5.3}_{-0.0}$	$8.3^{+2.8}_{-2.3}$
04385+2550	$55.1^{+12.3}_{-12.6}$	$4.8^{+4.9}_{-3.0}$	$3.7^{+3.8}_{-0.0}$	$0.0^{+2.5}_{-0.0}$	$6.4^{+1.9}_{-1.7}$	$11.9^{+2.7}_{-6.2}$
$\cdots$	$47.7^{+34.5}_{-12.4}$	$0.0^{+16.4}_{-0.0}$	$0.0^{+9.1}_{-0.0}$	$19.9^{+39.6}_{-0.0}$	$8.1^{+5.0}_{-1.6}$	$3.9^{+6.0}_{-0.0}$
AATau	$30.6^{+7.5}_{-8.4}$	$3.4^{+2.6}_{-2.6}$	$2.6^{+3.3}_{-1.6}$	$2.1^{+2.6}_{-0.0}$	$45.7^{+13.6}_{-20.6}$	$1.3^{+5.3}_{-0.6}$
$\cdots$	$9.3^{+20.9}_{-0.0}$	$8.3^{+16.8}_{-0.0}$	$4.5^{+6.0}_{-0.0}$	$7.0^{+13.7}_{-0.0}$	$29.6^{+37.2}_{-0.0}$	$1.2^{+24.4}_{-0.0}$
BPTau	$25.4^{+5.6}_{-8.4}$	$0.8^{+1.1}_{-0.0}$	$0.0^{+0.8}_{-0.0}$	$0.0^{+0.5}_{-0.0}$	$31.6^{+6.8}_{-10.3}$	$10.3^{+2.9}_{-4.1}$
CITau	$51.8^{+10.5}_{-12.3}$	$4.6^{+6.6}_{-1.0}$	$2.8^{+3.7}_{-1.3}$	$0.1^{+1.5}_{-0.0}$	$17.8^{+13.8}_{-7.8}$	$18.7^{+5.1}_{-3.9}$
$\cdots$	$14.5^{+12.3}_{-4.3}$	$1.9^{+19.1}_{-0.0}$	$0.0^{+3.4}_{-0.0}$	$9.7^{+7.2}_{-5.8}$	$27.4^{+11.9}_{-11.2}$	$20.3^{+36.9}_{-6.0}$
CWTau	$23.5^{+10.5}_{-5.3}$	$1.2^{+3.5}_{-0.0}$	$0.0^{+1.1}_{-0.0}$	$0.0^{+0.8}_{-0.0}$	$46.4^{+9.9}_{-19.3}$	$18.5^{+7.4}_{-4.7}$
CoKuTau3	$63.5^{+15.4}_{-24.8}$	$3.7^{+4.5}_{-2.0}$	$0.4^{+3.2}_{-0.0}$	$0.0^{+2.0}_{-0.0}$	$26.0^{+8.3}_{-4.4}$	$0.3^{+4.4}_{-0.0}$
$\cdots$	$24.1^{+10.5}_{-8.6}$	$1.8^{+3.0}_{-0.0}$	$14.3^{+25.3}_{-4.3}$	$4.4^{+7.3}_{-2.8}$	$22.5^{+15.4}_{-10.1}$	$9.0^{+4.9}_{-4.9}$
CoKuTau4	$44.8^{+10.8}_{-12.1}$	$3.7^{+3.5}_{-1.4}$	$3.9^{+3.9}_{-2.8}$	$2.6^{+4.5}_{-2.3}$	$6.0^{+6.9}_{-0.6}$	$3.6^{+4.2}_{-7.1}$
$\cdots$	$5.8^{+4.0}_{-2.6}$	$0.0^{+0.7}_{-0.4}$	$0.1^{+0.7}_{-0.2}$	$9.5^{+6.4}_{-4.3}$	$53.9^{+26.6}_{-17.1}$	$3.5^{+5.3}_{-3.2}$
DDTau	$50.2^{+19.1}_{-24.5}$	$5.2^{+5.6}_{-3.0}$	$2.1^{+5.1}_{-1.6}$	$1.1^{+4.2}_{-0.6}$	$1.7^{+11.5}_{-0.3}$	$22.9^{+9.0}_{-9.0}$
$\cdots$	$16.1^{+9.4}_{-7.1}$	$0.1^{+1.1}_{-0.2}$	$0.0^{+2.2}_{-1.2}$	$0.2^{+3.9}_{-0.9}$	$14.5^{+4.7}_{-5.6}$	$0.0^{+1.1}_{-0.0}$
DETau	$37.3^{+6.9}_{-19.5}$	$7.2^{+3.8}_{-2.2}$	$1.1^{+3.2}_{-1.1}$	$0.0^{+1.4}_{-1.1}$	$31.3^{+6.3}_{-6.1}$	$8.5^{+5.4}_{-3.3}$
$\cdots$	$15.1^{+11.0}_{-4.2}$	$0.0^{+5.3}_{-0.0}$	$0.0^{+2.5}_{-0.0}$	$9.3^{+15.2}_{-0.0}$	$18.9^{+14.7}_{-5.2}$	$0.0^{+4.6}_{-0.0}$

ID	Oli/Pyr[a] % (1.5 μm)	Ens % (1.5 μm)	For % (1.5 μm)	Sil % (1.5 μm)	Oli/Pyr[a] % (6.0 μm)	Sil % (6.0 μm)
DFTau	$19.2^{+3.8}_{-7.8}$	$3.7^{+3.9}_{-0.0}$	$0.0^{+4.9}_{-0.0}$	$2.8^{+6.5}_{-0.0}$	$71.3^{+18.8}_{-17.4}$	$0.0^{+7.3}_{-0.0}$
DHTau	$29.6^{+9.8}_{-10.3}$	$11.9^{+5.6}_{-3.1}$	$0.0^{+2.2}_{-0.4}$	$1.1^{+2.2}_{-1.0}$	$44.6^{+17.1}_{-22.4}$	$0.0^{+9.9}_{-0.0}$
· · ·	$17.3^{+20.6}_{-11.8}$	$5.7^{+17.2}_{-5.9}$	$4.3^{+8.0}_{-3.2}$	$0.0^{+22.9}_{-7.3}$	$22.4^{+9.4}_{-8.0}$	$12.4^{+10.2}_{-7.4}$
DKTau	$54.6^{+10.1}_{-12.9}$	$3.1^{+2.7}_{-1.9}$	$0.0^{+1.2}_{-0.0}$	$1.8^{+1.8}_{-0.0}$	$17.2^{+3.1}_{-3.7}$	$4.2^{+1.4}_{-1.1}$
DLTau	$38.0^{+17.1}_{-25.0}$	$10.1^{+10.2}_{-5.6}$	$0.0^{+6.0}_{-0.0}$	$8.8^{+7.6}_{-4.7}$	$24.4^{+12.3}_{-8.5}$	$10.7^{+7.4}_{-4.7}$
DMTau	$18.0^{+8.5}_{-13.8}$	$16.6^{+6.6}_{-7.4}$	$2.8^{+5.4}_{-1.4}$	$0.0^{+2.1}_{-0.0}$	$36.8^{+14.4}_{-10.8}$	$17.0^{+8.3}_{-12.1}$
· · ·	$2.0^{+2.6}_{-1.0}$	$0.8^{+2.8}_{-0.0}$	$2.1^{+5.9}_{-0.0}$	$8.8^{+9.7}_{-4.7}$	$29.7^{+21.5}_{-10.3}$	$6.8^{+4.2}_{-5.0}$
DNTau	$27.6^{+11.4}_{-3.5}$	$3.1^{+2.7}_{-2.0}$	$1.4^{+1.9}_{-0.9}$	$0.0^{+2.1}_{-0.0}$	$43.8^{+23.9}_{-26.5}$	$17.0^{+13.5}_{-4.4}$
· · ·	$46.4^{+53.9}_{-0.0}$	$0.0^{+38.7}_{-0.0}$	$3.6^{+16.8}_{-0.0}$	$0.0^{+>1.0}_{-0.0}$	$3.2^{+11.2}_{-0.0}$	$12.9^{+32.7}_{-0.0}$
DOTau	$52.2^{+28.2}_{-9.1}$	$4.5^{+5.7}_{-0.0}$	$5.3^{+6.3}_{-0.0}$	$1.9^{+6.2}_{-0.0}$	$19.9^{+14.9}_{-7.5}$	$13.1^{+5.0}_{-4.6}$
DPTau	$50.7^{+27.5}_{-15.8}$	$0.3^{+2.8}_{-0.0}$	$1.5^{+4.0}_{-0.0}$	$0.0^{+1.8}_{-0.0}$	$0.2^{+1.6}_{-0.0}$	$11.0^{+5.6}_{-0.0}$
· · ·	$44.4^{+18.0}_{-23.3}$	$0.0^{+5.4}_{-0.0}$	$7.8^{+5.1}_{-3.8}$	$0.0^{+2.7}_{-0.3}$	$4.0^{+1.2}_{-1.0}$	$3.1^{+2.3}_{-0.0}$
DQTau	$20.6^{+6.8}_{-8.1}$	$6.0^{+3.1}_{-2.0}$	$0.0^{+1.4}_{-0.0}$	$1.7^{+2.8}_{-1.0}$	$62.3^{+22.9}_{-34.4}$	$0.0^{+5.8}_{-0.0}$
· · ·	$30.8^{+36.9}_{-14.5}$	$0.0^{+12.6}_{-0.0}$	$4.6^{+8.4}_{-3.1}$	$0.0^{+11.7}_{-0.2}$	$21.1^{+36.2}_{-10.5}$	$29.1^{+21.2}_{-11.9}$
DRTau	$31.6^{+9.3}_{-8.7}$	$0.6^{+1.5}_{-0.0}$	$1.6^{+2.1}_{-1.1}$	$0.0^{+1.0}_{-0.0}$	$20.4^{+9.9}_{-9.6}$	$19.8^{+6.4}_{-4.7}$
DSTau	$17.4^{+13.7}_{-4.1}$	$6.2^{+3.4}_{-3.1}$	$0.2^{+1.4}_{-0.0}$	$0.0^{+1.1}_{-0.0}$	$36.4^{+11.9}_{-10.5}$	$0.0^{+4.5}_{-0.0}$
· · ·	$13.4^{+10.9}_{-6.7}$	$20.1^{+17.0}_{-10.8}$	$0.1^{+3.6}_{-1.4}$	$7.0^{+7.3}_{-4.8}$	$11.0^{+7.6}_{-4.9}$	$6.3^{+6.0}_{-4.1}$
F04147+2822	$71.2^{+11.8}_{-25.9}$	$0.0^{+4.4}_{-0.0}$	$0.0^{+4.0}_{-0.0}$	$0.1^{+2.8}_{-0.0}$	$3.6^{+3.4}_{-0.1}$	$12.0^{+5.3}_{-3.4}$
F04192+2647	$49.0^{+10.0}_{-11.6}$	$8.7^{+3.6}_{-4.0}$	$0.9^{+3.3}_{-0.5}$	$0.7^{+4.2}_{-0.1}$	$21.5^{+11.8}_{-9.9}$	$12.1^{+4.2}_{-4.0}$
· · ·	$16.1^{+12.1}_{-6.0}$	$5.3^{+9.9}_{-3.2}$	$11.7^{+16.0}_{-7.1}$	$0.0^{+5.8}_{-0.0}$	$19.4^{+12.2}_{-7.1}$	$9.7^{+8.5}_{-4.8}$
F04262+2654	$53.7^{+59.3}_{-16.5}$	$14.9^{+14.3}_{-5.7}$	$0.0^{+8.6}_{-0.0}$	$3.7^{+9.6}_{-3.1}$	$19.1^{+12.1}_{-8.9}$	$2.6^{+7.6}_{-2.2}$
F04297+2246	$34.0^{+7.8}_{-16.4}$	$9.5^{+4.4}_{-2.9}$	$2.8^{+4.4}_{-1.9}$	$0.0^{+3.2}_{-0.0}$	$44.1^{+9.8}_{-26.1}$	$0.9^{+12.5}_{-1.0}$
· · ·	$22.8^{+66.2}_{-0.0}$	$0.0^{+26.4}_{-0.0}$	$18.7^{+18.5}_{-15.3}$	$5.4^{+35.6}_{-0.0}$	$21.3^{+29.8}_{-5.7}$	$3.5^{+23.3}_{-0.0}$
F04297+2246A	$45.9^{+9.6}_{-10.3}$	$9.0^{+2.9}_{-3.1}$	$3.4^{+3.0}_{-2.4}$	$2.9^{+2.3}_{-1.5}$	$23.9^{+4.1}_{-5.3}$	$2.1^{+8.0}_{-0.0}$
· · ·	$20.1^{+11.1}_{-9.1}$	$0.2^{+2.4}_{-0.0}$	$4.3^{+5.4}_{-0.0}$	$0.0^{+1.4}_{-0.0}$	$11.2^{+6.3}_{-5.2}$	$29.2^{+15.0}_{-15.7}$
F04570+2520	$64.1^{+24.3}_{-22.8}$	$5.8^{+6.2}_{-5.2}$	$6.6^{+6.4}_{-0.0}$	$0.0^{+4.7}_{-0.0}$	$20.5^{+11.0}_{-4.3}$	$0.0^{+3.2}_{-0.3}$
· · ·	$0.0^{+3.6}_{-0.9}$	$0.0^{+7.3}_{-0.0}$	$13.7^{+9.1}_{-13.9}$	$15.7^{+7.4}_{-12.3}$	$21.5^{+9.9}_{-17.6}$	$9.0^{+2.6}_{-7.4}$
FMTau	$12.4^{+2.5}_{-9.9}$	$8.2^{+3.2}_{-3.6}$	$3.3^{+6.0}_{-1.4}$	$0.0^{+1.5}_{-0.0}$	$13.0^{+5.8}_{-5.4}$	$5.0^{+7.4}_{-0.7}$
· · ·	$6.4^{+10.5}_{-0.0}$	$1.1^{+3.7}_{-0.0}$	$1.3^{+17.3}_{-0.0}$	$5.4^{+14.0}_{-0.0}$	$28.3^{+17.3}_{-9.4}$	$25.4^{+45.6}_{-7.9}$
FNTau	$47.1^{+7.4}_{-14.4}$	$10.9^{+5.0}_{-3.7}$	$0.1^{+3.9}_{-0.0}$	$3.2^{+3.2}_{-2.3}$	$20.1^{+2.7}_{-7.2}$	$0.0^{+14.5}_{-0.0}$
· · ·	$19.0^{+68.3}_{-0.0}$	$1.3^{+16.2}_{-0.0}$	$2.9^{+14.3}_{-0.0}$	$1.8^{+36.4}_{-0.0}$	$18.8^{+56.1}_{-0.0}$	$23.6^{+102.6}_{-0.0}$
FOTau	$20.6^{+10.7}_{-12.0}$	$6.6^{+10.5}_{-2.3}$	$0.0^{+5.4}_{-0.0}$	$5.6^{+13.5}_{-0.0}$	$52.1^{+23.4}_{-18.6}$	$0.0^{+19.4}_{-0.0}$
FPTau	$5.5^{+11.8}_{-3.6}$	$0.0^{+3.2}_{-0.2}$	$0.0^{+1.7}_{-0.0}$	$0.0^{+1.1}_{-0.0}$	$64.1^{+25.1}_{-20.7}$	$0.0^{+11.6}_{-1.1}$
· · ·	$6.3^{+5.5}_{-3.5}$	$15.5^{+11.9}_{-10.1}$	$2.8^{+1.8}_{-0.0}$	$8.5^{+9.4}_{-0.0}$	$33.5^{+18.2}_{-9.2}$	$5.0^{+4.6}_{-0.0}$
FQTau	$49.6^{+32.6}_{-28.2}$	$9.1^{+13.6}_{-4.1}$	$3.0^{+8.0}_{-2.4}$	$4.8^{+7.8}_{-3.0}$	$9.0^{+7.0}_{-3.6}$	$0.0^{+2.7}_{-0.0}$
FSTau	$42.6^{+11.4}_{-14.7}$	$0.0^{+2.1}_{-0.0}$	$0.0^{+2.2}_{-0.0}$	$0.0^{+2.5}_{-0.0}$	$17.0^{+5.8}_{-6.1}$	$4.6^{+5.2}_{-3.2}$
FTTau	$13.9^{+8.6}_{-3.6}$	$3.9^{+3.4}_{-1.6}$	$2.1^{+2.1}_{-1.4}$	$0.1^{+1.6}_{-0.0}$	$49.7^{+15.9}_{-27.4}$	$6.4^{+10.3}_{-3.6}$
· · ·	$48.8^{+22.9}_{-5.6}$	$0.0^{+23.7}_{-0.0}$	$2.9^{+11.9}_{-0.0}$	$0.5^{+35.3}_{-0.0}$	$12.0^{+30.6}_{-0.0}$	$18.6^{+15.1}_{-0.0}$
FVTau	$22.7^{+19.4}_{-0.0}$	$12.8^{+8.7}_{-7.2}$	$9.0^{+11.8}_{-0.0}$	$0.0^{+3.0}_{-0.0}$	$43.2^{+12.9}_{-13.5}$	$6.9^{+16.1}_{-0.0}$
FXTau	$46.5^{+10.5}_{-13.3}$	$6.3^{+4.2}_{-2.5}$	$0.0^{+2.1}_{-0.0}$	$0.0^{+1.6}_{-0.0}$	$4.0^{+3.6}_{-0.0}$	$8.0^{+2.6}_{-1.8}$
· · ·	$25.3^{+16.6}_{-8.6}$	$0.2^{+2.7}_{-0.0}$	$0.2^{+4.2}_{-0.0}$	$1.7^{+10.7}_{-0.0}$	$33.3^{+16.6}_{-14.1}$	$9.6^{+21.9}_{-0.0}$
FZTau	$19.1^{+10.8}_{-5.4}$	$4.4^{+2.3}_{-1.9}$	$1.5^{+2.2}_{-0.5}$	$0.0^{+2.8}_{-0.0}$	$25.0^{+6.4}_{-8.4}$	$11.1^{+4.0}_{-4.2}$

ID	Oli/Pyr[a] % (1.5 μm)	Ens % (1.5 μm)	For % (1.5 μm)	Sil % (1.5 μm)	Oli/Pyr[a] % (6.0 μm)	Sil % (6.0 μm)
GGTau	$54.2^{+15.5}_{-15.3}$	$0.0^{+2.1}_{-0.0}$	$1.9^{+2.8}_{-1.3}$	$0.0^{+1.1}_{-0.0}$	$16.5^{+4.7}_{-3.8}$	$15.7^{+4.9}_{-4.4}$
GHTau	$27.3^{+15.0}_{-11.6}$	$7.3^{+3.2}_{-4.0}$	$0.8^{+2.7}_{-0.8}$	$4.1^{+3.1}_{-2.9}$	$45.4^{+26.6}_{-14.6}$	$0.0^{+4.3}_{-0.0}$
$\cdots$	$11.5^{+8.2}_{-6.5}$	$4.4^{+1.8}_{-3.2}$	$1.0^{+1.8}_{-1.0}$	$12.6^{+10.3}_{-8.0}$	$32.4^{+19.8}_{-14.5}$	$19.7^{+18.4}_{-13.8}$
GITau	$39.3^{+14.0}_{-7.7}$	$5.7^{+2.6}_{-2.7}$	$1.6^{+2.0}_{-0.0}$	$1.0^{+1.8}_{-0.0}$	$6.4^{+1.8}_{-1.8}$	$8.4^{+2.9}_{-2.1}$
$\cdots$	$20.5^{+10.5}_{-7.6}$	$0.0^{+2.1}_{-0.0}$	$0.0^{+2.7}_{-0.0}$	$0.1^{+2.8}_{-0.0}$	$33.9^{+14.4}_{-12.7}$	$8.1^{+9.2}_{-4.9}$
GKTau	$18.0^{+3.5}_{-6.6}$	$3.7^{+0.8}_{-1.4}$	$0.0^{+0.7}_{-0.0}$	$1.7^{+0.9}_{-0.7}$	$7.3^{+1.8}_{-1.8}$	$1.8^{+0.8}_{-0.8}$
GMAur	$16.0^{+5.5}_{-4.1}$	$12.2^{+3.4}_{-4.2}$	$14.9^{+5.6}_{-0.0}$	$0.0^{+1.2}_{-0.0}$	$1.2^{+10.8}_{-0.0}$	$15.4^{+4.5}_{-6.7}$
$\cdots$	$9.6^{+14.1}_{-0.0}$	$3.8^{+20.4}_{-0.0}$	$0.0^{+8.6}_{-0.0}$	$17.4^{+17.6}_{-0.0}$	$33.6^{+32.2}_{-0.0}$	$1.3^{+14.1}_{-0.0}$
GOTau	$63.2^{+24.7}_{-37.8}$	$3.3^{+6.0}_{-5.3}$	$0.0^{+5.4}_{-0.0}$	$5.6^{+7.8}_{-4.8}$	$12.4^{+6.4}_{-5.3}$	$0.0^{+2.0}_{-0.0}$
HKTau	$37.5^{+6.1}_{-21.5}$	$7.7^{+2.8}_{-4.7}$	$8.2^{+4.0}_{-0.0}$	$0.0^{+3.3}_{-0.0}$	$18.6^{+8.1}_{-6.0}$	$24.8^{+4.5}_{-11.5}$
$\cdots$	$13.5^{+33.1}_{-3.4}$	$6.7^{+33.1}_{-0.0}$	$2.9^{+5.6}_{-0.0}$	$7.4^{+64.7}_{-0.0}$	$21.5^{+25.3}_{-6.3}$	$10.6^{+14.0}_{-6.4}$
HNTau	$45.5^{+12.1}_{-7.7}$	$0.0^{+1.3}_{-0.0}$	$0.0^{+1.3}_{-0.0}$	$0.0^{+1.3}_{-0.0}$	$22.9^{+4.8}_{-4.6}$	$16.8^{+4.5}_{-3.2}$
HOTau	$34.6^{+12.9}_{-8.6}$	$6.2^{+3.6}_{-3.9}$	$2.2^{+5.5}_{-0.0}$	$0.4^{+2.2}_{-0.0}$	$43.0^{+11.7}_{-17.1}$	$0.0^{+10.3}_{-0.0}$
$\cdots$	$37.6^{+23.2}_{-11.3}$	$0.4^{+5.9}_{-0.0}$	$0.3^{+2.0}_{-0.0}$	$4.2^{+7.1}_{-3.4}$	$8.3^{+7.0}_{-3.6}$	$9.3^{+3.2}_{-5.8}$
HPTau	$22.1^{+3.6}_{-4.9}$	$1.1^{+1.9}_{-0.0}$	$0.0^{+1.3}_{-0.0}$	$0.9^{+1.3}_{-0.0}$	$14.3^{+4.4}_{-2.3}$	$3.4^{+1.3}_{-1.3}$
Haro6-37	$45.0^{+16.2}_{-27.5}$	$10.4^{+5.8}_{-5.4}$	$2.6^{+4.5}_{-0.0}$	$7.0^{+6.5}_{-4.0}$	$17.2^{+12.2}_{-7.0}$	$0.0^{+7.1}_{-0.0}$
IPTau	$33.0^{+9.9}_{-7.5}$	$4.5^{+4.4}_{-2.4}$	$3.9^{+5.0}_{-2.5}$	$0.0^{+1.2}_{-0.0}$	$18.7^{+12.5}_{-8.3}$	$8.5^{+3.2}_{-4.1}$
$\cdots$	$19.3^{+18.2}_{-8.9}$	$4.2^{+18.2}_{-0.0}$	$1.8^{+9.0}_{-0.0}$	$13.7^{+8.5}_{-5.7}$	$32.3^{+11.1}_{-6.9}$	$1.7^{+12.0}_{-1.4}$
IQTau	$30.7^{+8.8}_{-8.7}$	$8.4^{+3.6}_{-2.4}$	$2.7^{+3.5}_{-1.4}$	$1.6^{+2.4}_{-0.9}$	$28.7^{+6.8}_{-11.3}$	$8.7^{+3.9}_{-3.8}$
$\cdots$	$43.9^{+14.6}_{-12.9}$	$0.0^{+4.6}_{-0.0}$	$0.6^{+3.1}_{-0.0}$	$0.0^{+6.5}_{-0.0}$	$14.7^{+9.1}_{-3.3}$	$14.1^{+12.4}_{-7.1}$
ISTau	$47.8^{+13.5}_{-16.1}$	$19.0^{+7.3}_{-5.2}$	$5.1^{+7.1}_{-4.2}$	$0.3^{+4.4}_{-0.0}$	$9.4^{+8.4}_{-3.0}$	$0.0^{+7.7}_{-0.0}$
$\cdots$	$26.5^{+42.8}_{-13.3}$	$0.0^{+76.9}_{-0.0}$	$14.0^{+97.4}_{-0.0}$	$4.7^{+66.6}_{-0.0}$	$26.9^{+67.9}_{-6.9}$	$7.6^{+47.0}_{-0.0}$
LkCa15	$21.6^{+11.5}_{-6.1}$	$7.7^{+2.7}_{-2.7}$	$6.3^{+3.5}_{-3.0}$	$0.0^{+0.6}_{-0.0}$	$4.8^{+2.7}_{-0.0}$	$0.8^{+3.1}_{-0.0}$
$\cdots$	$16.0^{+7.7}_{-6.8}$	$6.1^{+5.6}_{-3.6}$	$0.0^{+1.5}_{-0.0}$	$6.6^{+6.3}_{-4.9}$	$16.2^{+8.1}_{-6.9}$	$13.7^{+9.5}_{-7.0}$
RWAur	$39.0^{+9.1}_{-23.1}$	$2.3^{+3.9}_{-0.0}$	$0.0^{+1.8}_{-0.0}$	$0.0^{+1.5}_{-0.0}$	$12.4^{+3.3}_{-8.7}$	$18.3^{+6.7}_{-6.8}$
RYTau	$69.7^{+13.3}_{-10.2}$	$1.9^{+3.3}_{-0.0}$	$0.0^{+1.6}_{-0.0}$	$1.0^{+2.1}_{-0.0}$	$3.3^{+1.8}_{-1.1}$	$0.0^{+0.2}_{-0.0}$
SUAur	$49.7^{+8.5}_{-8.5}$	$1.2^{+1.8}_{-0.0}$	$2.4^{+3.3}_{-0.0}$	$0.0^{+0.6}_{-0.0}$	$3.9^{+1.9}_{-1.7}$	$21.3^{+3.1}_{-3.6}$
UYAur	$54.3^{+11.1}_{-13.1}$	$0.0^{+1.9}_{-0.0}$	$1.3^{+3.6}_{-0.0}$	$0.0^{+1.3}_{-0.0}$	$14.1^{+3.9}_{-6.2}$	$10.4^{+7.2}_{-0.0}$
V710Tau	$39.1^{+17.8}_{-28.1}$	$8.5^{+6.9}_{-5.0}$	$6.0^{+5.9}_{-3.5}$	$8.0^{+6.2}_{-4.6}$	$3.7^{+1.9}_{-1.8}$	$3.3^{+2.5}_{-1.3}$
V773Tau	$40.9^{+12.7}_{-17.2}$	$4.3^{+9.4}_{-0.0}$	$0.0^{+1.8}_{-0.0}$	$0.0^{+8.0}_{-0.0}$	$10.9^{+5.7}_{-3.8}$	$12.5^{+5.6}_{-6.3}$
V836Tau	$32.4^{+16.9}_{-14.5}$	$9.1^{+4.2}_{-3.3}$	$2.8^{+3.4}_{-1.9}$	$3.9^{+2.1}_{-2.8}$	$45.1^{+9.7}_{-35.6}$	$0.0^{+8.7}_{-0.0}$
$\cdots$	$32.6^{+52.5}_{-19.6}$	$3.9^{+23.7}_{-0.0}$	$1.7^{+12.2}_{-0.0}$	$0.5^{+24.0}_{-0.0}$	$17.0^{+30.6}_{-3.8}$	$1.5^{+3.7}_{-1.5}$
V955Tau	$59.3^{+15.0}_{-32.6}$	$4.6^{+5.8}_{-2.1}$	$0.0^{+3.0}_{-0.0}$	$0.0^{+2.9}_{-0.1}$	$11.9^{+4.7}_{-3.6}$	$7.2^{+6.7}_{-1.8}$
VYTau	$18.1^{+4.7}_{-8.2}$	$1.1^{+7.2}_{-0.1}$	$0.0^{+14.7}_{-0.0}$	$0.6^{+7.6}_{-0.0}$	$74.0^{+18.0}_{-47.6}$	$0.3^{+18.0}_{-0.0}$
ZZTauIRS	$76.1^{+12.9}_{-21.8}$	$0.3^{+4.3}_{-0.5}$	$3.3^{+4.8}_{-1.9}$	$0.0^{+2.9}_{-0.0}$	$0.0^{+1.6}_{-0.0}$	$2.8^{+7.3}_{-0.0}$
$\cdots$	$39.4^{+18.7}_{-15.4}$	$0.0^{+3.7}_{-0.4}$	$9.1^{+7.5}_{-5.2}$	$9.7^{+9.3}_{-6.1}$	$7.0^{+5.2}_{-3.5}$	$4.6^{+4.3}_{-2.9}$
Upper Scorpius						
PBB2002 J160357.9	$42.9^{+14.8}_{-24.5}$	$0.0^{+0.5}_{-4.5}$	$0.0^{+4.7}_{-0.0}$	$0.0^{+3.9}_{-0.0}$	$46.8^{+28.8}_{-32.4}$	$0.0^{+10.9}_{-0.0}$
PBB2002 J160823.2	$27.1^{+2.5}_{-24.1}$	$5.9^{+3.9}_{-3.6}$	$0.0^{+7.7}_{-0.0}$	$0.6^{+10.4}_{-0.0}$	$60.1^{+38.8}_{-22.7}$	$0.0^{+5.1}_{-0.1}$
PBB2002 J160900.7	$42.3^{+14.3}_{-17.3}$	$4.1^{+3.7}_{-2.4}$	$0.0^{+2.5}_{-0.0}$	$0.0^{+1.0}_{-0.0}$	$24.9^{+2.9}_{-16.8}$	$8.0^{+4.9}_{-4.0}$
PBB2002 J160959.4	$61.9^{+16.5}_{-50.2}$	$10.6^{+12.0}_{-8.1}$	$0.0^{+7.6}_{-0.0}$	$0.0^{+4.5}_{-0.0}$	$3.1^{+5.9}_{-0.9}$	$1.2^{+11.7}_{-0.2}$
PBB2002 J161115.3	$58.7^{+11.1}_{-26.8}$	$3.1^{+5.0}_{-2.0}$	$0.0^{+6.7}_{-0.0}$	$1.5^{+2.6}_{-0.4}$	$9.2^{+3.2}_{-4.6}$	$5.3^{+1.3}_{-4.9}$

ID	Oli/Pyr[a] % (1.5 μm)	Ens % (1.5 μm)	For % (1.5 μm)	Sil % (1.5 μm)	Oli/Pyr[a] % (6.0 μm)	Sil % (6.0 μm)
PBB2002 J161420.2	$67.7^{+7.9}_{-7.8}$	$0.6^{+0.9}_{-0.0}$	$0.8^{+1.2}_{-0.0}$	$0.0^{+0.4}_{-0.0}$	$15.2^{+2.8}_{-1.5}$	$7.9^{+1.3}_{-1.3}$
PZ99 J160357.6	$6.1^{+9.2}_{-0.0}$	$3.8^{+2.9}_{-0.0}$	$0.2^{+2.2}_{-0.0}$	$0.0^{+2.6}_{-0.0}$	$87.1^{+19.9}_{-46.7}$	$0.0^{+5.1}_{-0.0}$
PZ99 J161411.0	$8.8^{+4.7}_{-0.0}$	$3.9^{+3.5}_{-0.0}$	$0.0^{+1.4}_{-0.0}$	$0.0^{+4.1}_{-0.0}$	$84.8^{+8.6}_{-55.2}$	$0.0^{+3.0}_{-0.0}$
ScoPMS31	$72.4^{+39.8}_{-61.0}$	$4.6^{+10.7}_{-3.7}$	$0.0^{+9.0}_{-1.9}$	$1.9^{+9.2}_{-1.4}$	$6.6^{+4.2}_{-6.2}$	$0.0^{+1.5}_{-0.0}$
η Chamaeleontis						
J0843	$44.6^{+19.9}_{-21.9}$	$5.9^{+7.6}_{-0.0}$	$0.0^{+10.2}_{-0.0}$	$1.6^{+11.6}_{-0.0}$	$13.6^{+19.2}_{-0.0}$	$0.0^{+3.9}_{-0.0}$
RECX-5	$12.3^{+15.6}_{-3.5}$	$23.9^{+13.9}_{-0.0}$	$0.0^{+8.0}_{-0.0}$	$8.0^{+6.9}_{-3.3}$	$7.1^{+18.9}_{-0.0}$	$0.0^{+10.0}_{-0.0}$
RECX-9	$31.6^{+15.8}_{-24.2}$	$0.9^{+7.0}_{-0.0}$	$5.4^{+5.8}_{-3.2}$	$4.6^{+10.8}_{-2.1}$	$3.3^{+3.0}_{-1.1}$	$0.8^{+8.3}_{-0.0}$
RECX-11	$26.8^{+15.7}_{-14.4}$	$8.0^{+10.5}_{-0.0}$	$0.0^{+2.7}_{-0.0}$	$3.4^{+3.7}_{-1.9}$	$17.6^{+8.1}_{-6.6}$	$0.0^{+1.9}_{-0.0}$

Table A.2 – Intermediate and large dust composition derived using the "B2C" procedure.[b]

[a] Amorphous olivine and pyroxene combined.
[b] For each object, the first line corresponds to the warm component abundances, while the second line corresponds to the cold component abundances, when available.

7

Spectral Energy Distributions of the Young Stars with Disks in Serpens

We present the spectral energy distributions (SEDs) of the young stars surrounded by disks in the Serpens Molecular Cloud. The SEDs allow a correct separation between the stellar radiation from that re-emitted by the disks. Taking into account the distance of 415 pc, the distribution of ages is shifted to lower values, in the 1 – 3 Myr range, with a tail up to 10 Myr. The mass distribution varies between 0.2 and 1.2 $M_\odot$, with median mass of 0.7 $M_\odot$. The distribution of fractional disk luminosities resembles that of the young Taurus Molecular Cloud, with most disks consistent with passively irradiated disks. The actively accreting and non-accreting stars show very similar distributions in fractional disk luminosities, differing in the brighter tail. Comparison with a sample of Herbig Ae/Be stars shows that the T Tauri disks do not show the clear separation in fractional disk luminosities for different geometries as seen for disks around the more massive Herbig Ae/Be. Furthermore, the results for the mineralogy of the dust in the disk surface do not seem to be directly related to either stellar or disk characteristics.

Isa Oliveira, Bruno Merín, Ewine F. van Dishoeck, Klaus M. Pontoppidan
In preparation

7.1   Introduction

Protoplanetary disks are a natural consequence of the star formation process. They are created as a result of the conservation of angular momentum when a dense slowly rotating core in a molecular cloud collapses to form a star. From formation to dissipation, which takes a few million years, the disk is connected to its central star through magnetic field lines. During the evolution of the system (star+disk), material is accreted from the disk onto the star at the same time as material is blown away from the disk driven by winds and stellar radiation. For most disks, in which the central star is the main source of radiation (passive disks), the stellar radiation field defines and controls the temperature distribution throughout the disk.

There is evidence that the initial disk mass is a function of the stellar mass (Andrews & Williams 2005; Greaves & Rice 2010). In addition, different disk lifetimes have been suggested for stars of different masses, with disks around low-mass stars lasting longer (Carpenter et al. 2006; Kennedy & Kenyon 2009). If true, this evidence puts strong constraints on the number of planets, and of which type, could be formed in such disks. A great diversity in planetary systems is observed for the more than 500 exo-planets discovered to date (Udry & Santos 2007) and it is worth exploring whether the variety of planets is a consequence of the diversification in stars, and therefore their protoplanetary disks.

All these constraints point to a dependence and co-evolution of disks and their host stars. What happens to one will directly affect the other, and the best way to understand their evolution is to study them together, as a system. For this purpose, several authors have analyzed disks by studying the spectral energy distribution (SED) of the system. For young stars surrounded by disks, the SED is composed basically of the stellar radiation, which peaks at the visible/near-IR regime depending on the stellar effective temperature, and of the radiation re-processed and re-emitted by the dust in the disk. Due to the varying dust temperature with radius, the radiation emitted by the disk is concentrated in the infrared (IR) and millimeter (mm) regimes, which appears in the SED as an excess of radiation beyond that emitted by the star alone. Additionally, accretion of matter from the disk to the star is responsible for creating an excess of continuum radiation from hot gas, clearly seen in the ultra-violet (UV) regime, and strong emission lines. If the stellar characteristics are well known (T_{eff}, L_{star}, M_{star}), observations of the system in different wavelength regimes will directly inform about the disk, through the SED of the system. Indeed, SEDs have been used to probe disk characteristics (e.g., geometry, mass) by a great number of authors (e.g., Meeus et al. 2001; Furlan et al. 2006; Sicilia-Aguilar et al. 2009).

During the millions of years it takes for most disks to go from their initial composition of small dust grains coupled to the gas (therefore presenting an SED with a considerable amount of IR excess) to no disk (and therefore little or no IR-excess), different processes affect the dust. Besides material accreting from the disk into the star, and material being blown away from the disk, the dust inside the disk needs to stick together and grow, if it is to form planets. Combining theory, observations

and laboratory experiments, the initial growth from dust into pebbles and boulders is fairly well understood (Weidenschilling 1980; Dominik & Tielens 1997; Blum & Wurm 2008). The further growth is still under debate, and is a very active field in simulations of planet formation. In addition to growth, a change in dust composition has been observed. Crystallization of the originally amorphous interstellar medium grains is necessary to understand the high crystallinity fraction found in many comets and interplanetary dust grains (see Wooden et al. 2007 and Pontoppidan & Brearley 2010 for recent reviews).

Furthermore, protoplanetary disks around low-mass stars are divided in two categories, separating actively accreting (classical T Tauri stars, CTTS) and non-accreting (weak-line T Tauri stars, WTTS) stars (Cieza et al. 2007). Initially it was thought that WTTS were young stars no longer surrounded by disks, with the lack of a disk being the reason that no material is accreted onto the star. It is now understood that the WTTS class comprises some systems that do not show signs of accretion even though a disk is present, in addition to stars no longer surrounded by disks (i.e. no material to accrete onto the star). By the time the gas in the disk has dissipated, possible giant planets should already have formed, leaving an optically thin disk with no IR excess. Some older stars, however, are observed to have some IR excess even though the gas has already dissipated. Those systems are called debris disks, where the presence of small dust is understood to be produced in situ, likely from collisions between large bodies.

For low-mass stars, the stellar and disk characteristics cannot be easily separated as is the case for higher mass Herbig stars (e.g. Meeus et al. 2001), unless the stellar characteristics are well known. To date, such studies have mostly concentrated on low-mass stars in the Taurus Molecular Cloud (e.g. Kenyon & Hartmann 1987, 1995). Taurus has an isolated stellar population, different from the more clustered environments of other nearby star-forming regions. Additionally, Taurus has been studied in a wide range of wavelengths, from X-rays to radio, which allows an extensive characterization of its members that are still surrounded by disks, as well as the lower fraction of young stars ($\sim$40%) around which disks have already dissipated (e.g. Padgett et al. 1999; Andrews & Williams 2005; Güdel et al. 2007). To test whether the results for the Taurus population are valid for stars in other star-forming regions (of different mean ages and environments), we have engaged in a systematic study of stars and their disks in several of the nearby low-mass star-forming regions. One of those regions is the Serpens Molecular Cloud, an actively star-forming complex containing a substantial mass of molecular gas and young stars both clustered and in isolation.

This work presents the SEDs of the young stellar population of Serpens discovered by the *Spitzer Space Telescope* legacy program "From molecular cores to planet-forming disks" (c2d, Evans et al. 2003). The stellar and disk components of these systems have been well studied (Harvey et al. 2006, 2007a,b; Oliveira et al. 2009, 2010, 2011; Spezzi et al. 2010), providing the necessary ingredients for constructing their SEDs in § 7.2. Specifically, the data are presented in § 7.2.1, the procedure to

construct the SEDs is described in § 7.2.2. From the SEDs it is possible to separate the disk from the stellar radiation, and characterize the disks. Using the new distance estimate for the cloud ($d = 415$ pc, Dzib et al. 2010), an updated distribution of ages and masses is derived in § 7.2.3. The disk characteristics are discussed in § 7.3. With stars and disks well characterized, § 7.4 investigates to what extent they affect each other. Finally, the conclusions are presented in § 7.5.

7.2   Spectral Energy Distributions

7.2.1   Data

The Serpens Molecular Cloud has been imaged by *Spitzer* as part of the c2d program. The detected sources in the IRAC and MIPS band were published by Harvey et al. (2006) and Harvey et al. (2007a), respectively. By combining the data in all bands, Harvey et al. (2007b) could identify a red population classified as young stellar object candidates, which is interpreted as being due to emission from the disk. Due to the position of Serpens in the sky, close to the galactic plane, a higher contamination is expected from red background sources, and for this reason the YSOs identified are still candidates in the sample of Harvey et al. (2007b). Confirmation of their nature as young objects members of the cloud is necessary. This can be done through spectroscopy, but can also be achieved through photometry in more bands. The final catalog of Harvey et al. (2007b) is band-merged with the Two Micron All Sky Survey (2MASS), providing data at J, H, K_s (at 1.2, 1.6 and 2.2 μm, respectively), IRAC bands 1 through 4 (at 3.6, 4.5, 5.8 and 8.0 μm) and MIPS bands 1 and 2 (at 24 and 70 μm), when available.

Oliveira et al. (2010) describe the complete, flux-limited sample of young stellar objects in Serpens that is used in this work. The 115 objects comprise the entire young IR-excess population of Serpens that is brighter than 3 mJy at 8 μm (from the catalog of Harvey et al. 2007b). Of these 115 young objects, 21 are shown to be still embedded in a dusty envelope (thus showing a rising IR spectra, often with deep ice features, as can be seen in Figure 2 of Oliveira et al. 2010). The remaining 94 objects are classified as disk sources, and are the subject of this work. Oliveira et al. (2009) derived spectral types (and therefore also temperatures) from optical spectroscopy for 62% of the Serpens flux-limited disk sample (58 objects). The remaining 36 objects are too extincted and could not be detected using 4-meter class telescopes. These objects have spectral types derived from photometry alone, which is less reliable than derivations from spectroscopy.

In addition to the optical spectroscopy and near- and mid-IR photometric data, optical R-band photometry (at 6260 Å) is available (Spezzi et al. 2010). Although these observations covered exactly the same area of Serpens that was covered by the c2d *Spitzer* observations, the high extinction toward a few directions in Serpens makes it impossible for optical detection. That means that not all objects have optical photometric data available.

Furthermore, Oliveira et al. (2010) present *Spitzer* IRS mid-IR spectroscopy (5 – 35 μm) for this sample. These spectra cover the silicate bands at 10 and 20 μm that are emitted by the dust in the surface layers of optically thick protoplanetary disks. Information about the typical sizes and composition of the emitting dust can be obtained from fitting models to these silicate bands. Those results are presented in Oliveira et al. (2011).

7.2.2   Building the SEDs

The first step to build the SED of a given object is to determine the stellar emission. For each object, a NextGen stellar photosphere (Hauschildt et al. 1999) corresponding to the spectral type of said star is selected. This model photosphere is scaled to either the optical or the 2MASS J photometric point to account for the object's brightness. The observed photometric data are corrected for extinction from its visual extinction (R_V) using the Weingartner & Draine (2001) extinction law, with R_V = 5.5. For objects without A_V values derived from the optical spectroscopy, these values are estimated by the best fit of the optical/near-IR photometry to the NextGen photosphere, on a close visual inspection of the final result SEDs.

Figure 7.1 shows the SEDs constructed for the objects in the sample. No SEDs could be constructed for objects #42 and 94 due to the lack of either optical or 2MASS near-IR photometric detections. For the other sources, Figure 7.1 shows the NextGen model photosphere (dashed black line), observed photometry (open squares), dereddened photometry (filled circles) and IRS spectrum (thick blue line). When there is no detection for the MIPS2 band at 70 μm, an upper limit is indicated by a downward arrow. A notable difference in the amounts of IR radiation in excess of the stellar photosphere is evident. This translates into a diversity of disk geometries, as inferred by mid-IR data (Oliveira et al. 2010).

Once the SEDs are built, aided by the model photosphere for each object, it is possible to separate the radiation that is being emitted by the star from that re-emitted by the disk, which was not possible by simply looking at the system emission – the integration of the radiation emitted by the system at all wavelengths gives the brightness of the entire system. By integrating the scaled NextGen model photosphere, the stellar luminosity (L_{star}) can be directly obtained. If this value is subtracted from the emission of the entire system, the disk luminosity (L_{disk}) can be derived. These integrations take into consideration the distance to the star, besides the fluxes at different bands.

Similar procedures for constructing SEDs are being performed for a large number of systems in most of the nearby star-forming regions observed by *Spitzer* (L. Maud private communication). In that work, all young stellar objects observed by *Spitzer* for which the central star has been optically characterized in the literature (thus providing the input T_{eff} needed to construct the SEDs) are considered. This large database allows comparison between the disks in Serpens with those in other star-forming regions, of different mean ages and environments. Their results for Taurus,
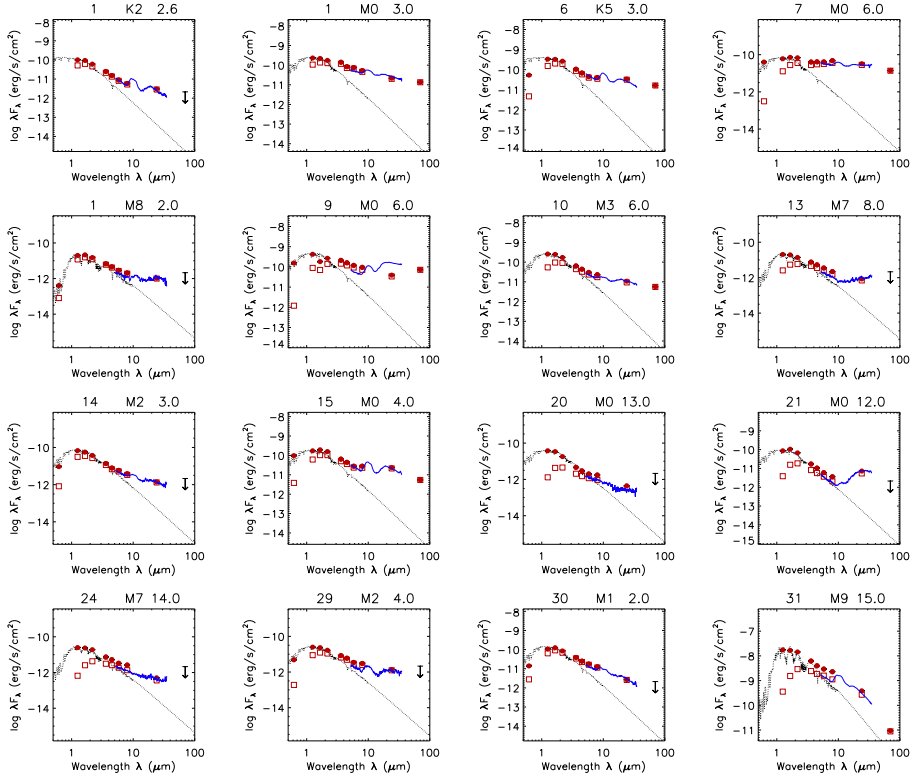
Figure 7.1 – SEDs of the young stellar population with disks of Serpens. Each SED has the corresponding object ID (as in Oliveira et al. 2010) on the top left. The solid black line indicates the NextGen stellar photosphere model for the spectral type indicated on the top of each plot. Open squares are the observed photometry while the solid circles are the dereddened photometry. The visual extinction of each object can be seen on the top right. The solid gray line is the object's IRS spectrum. Only 16 objects are shown here, the remaining 76 SEDs are shown in Appendix A.

Upper Scorpius and η Chamaeleontis will be used in this work in order to put Serpens in context.

In their derivation of stellar luminosities for the Serpens YSOs with optical spectroscopy, Oliveira et al. (2009) adopted a distance to Serpens of 259 ± 37 pc (Straizys et al. 1996, a discussion using $d = 193 \pm 13$ pc of Knude 2010 is included). However, since then the distance to the cloud has been revisited. Dzib et al. (2010) find a distance of 415 ± 15 pc to the Serpens Core from VLBA parallax observations. This new distance is used in this work. The errors in the derivation of L_{star} and L_{disk} are propagated from the errors in the distance, extinction ($\pm$ 2 mag) and in the spectral type determination.

7.2.3   Masses and Ages Revisited

The new stellar luminosities, derived for the distance of 415 pc, imply that the young stars in Serpens move in the Hertzsprung-Russell (HR) diagram. The physical HR diagram relates the effective temperature (T_{eff}) and luminosity of a star. Following Oliveira et al. (2009), T_{eff} is determined from the object's spectral type as follows: stars earlier than M0 follow the relationship of Kenyon & Hartmann (1995), while stars of later spectral type follow that of Luhman et al. (2003). The errors in temperature are translated directly from the errors in spectral types. With L_{star} and T_{eff} in hand, the objects can be placed in the HR diagram.

For young stellar objects, ages and masses can be derived by overlaying pre-main sequence (PMS) evolutionary tracks on the HR diagram, and comparing the position of an object to the isochrones and mass tracks, using the PMS models of Baraffe et al. (1998) and Siess et al. (2000). Due to the intrinsic physics and validation of parameters, the models of Baraffe et al. (1998) are used for stars with masses smaller than 1.4 $M_{\odot}$, while more massive stars are compared to the models of Siess et al. (2000). The new individual ages and masses are presented in Table A.1.

Figure 7.2 shows the distribution of masses and ages for the YSOs in Serpens. Compared to the results of Oliveira et al. (2009) for $d = 259$ pc, it is seen that the mass distribution does not change much, while the age distribution does. This is understood by looking at the isochrones and mass tracks of a given model (e.g. Figure 7 of Oliveira et al. 2009): for the temperature range of the stars in Serpens (mostly K- and M-type), mass tracks are almost vertical. This means that a change in luminosity due to the new distance hardly affects the inferred mass. From the isochrones, however, it can be noted that in general higher stellar luminosities (for this further distance) imply younger ages. Indeed, the median mass derived here is $\sim$0.7 $M_{\odot}$ and median age is $\sim$2.3 Myr, while Oliveira et al. (2009) found $\sim$0.7 $M_{\odot}$ and $\sim$5 Myr.
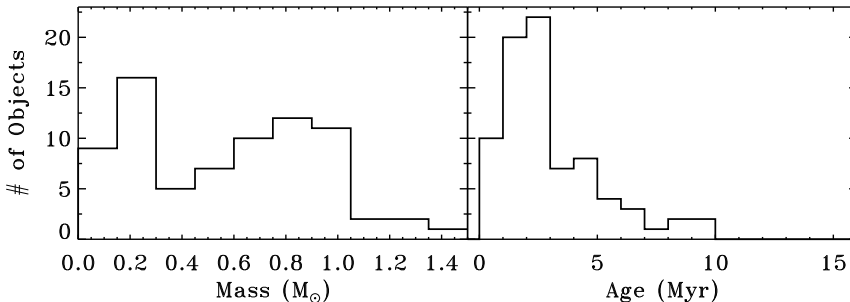

Figure 7.2 – Distribution of masses and ages of the young stellar objects in Serpens, assuming $d = 415$ pc.

7.2.4   Notes on Individual Objects

Since the quantity of data available for each object in this sample varies, not all SEDs produce good results or yield physical parameters. Objects 31, 62, 80, 81, 86 and 103 are found to be much too luminous, which is not consistent with them being members of Serpens. The degeneracy between spectral type and extinction for sources without optical spectra makes it difficult to establish good values for both parameters. Thus, they could not be placed in the HR diagram, and therefore no ages and masses could be determined. Confirmation of their spectral type, better extinction determination, and the addition of optical photometry is necessary to revisit these objects and precisely determine their stellar parameters.

Furthermore, a few objects (# 7, 40, 48, 54, 56, 59, 60, 65, 74, 88, 101, 117 and 129) show flat SEDs. This produces large disk luminosities that deserve attention. None of these objects show signs of being (close to) edge-on. Edge-on systems will indeed produce high disk luminosities, but will also produce other signatures (e.g. inability of fitting optical/near-IR photometry to its stellar photosphere, forbidden emission lines, etc; Merín et al. 2010), which is not the case of any for the high luminosity disks shown here. Most likely, those objects are in transition from stage I (embedded) to stage II (disks) or surrounded by a nebulosity, leading to their classification as flat sources.

Lastly, object 41 seems to have a mismatch in the 2MASS photometry, making the results unreliable. For all these objects, the addition of more data will help in understanding their nature and the derivation of accurate parameters.

7.3   Disk Properties

The construction of the SEDs allows to study the diversity of disks in the same region, most of which have ages with a narrow span around a few Myr (Figure 7.2). It is clear from the SEDs that different types of disks are present in Serpens, some with lots of IR excess, others almost entirely dissipated. This is even more clear by looking at the distribution of fractional disk luminosities ($L_{\rm disk}/L_{\rm star}$) for this sample, which is presented in Figure 7.3. Here, Serpens (solid black line) is compared to the equally young, yet very different in terms of cloud structure and environment, Taurus (dotted red line, Maud et al. in prep). The peak and distribution of these two samples are very similar, with the bulk of each population showing fairly bright disks ($L_{\rm disk}/L_{\rm star} \sim$ 0.1), the majority of which are consistent with passively irradiated disks ($L_{\rm disk}/L_{\rm star} \leq$ 0.25, Kenyon & Hartmann 1987). This is is agreement with studies of disk geometry as inferred from IR colors, which show a large fraction of disks to be flared, based on IR colors (Oliveira et al. 2010). These two findings support the idea that these two star-forming regions are similar in spite of their different environments and star formation rate, and a good probe of the young bin of disk evolution. That is, regions in which most stars are still surrounded by disks, and most disks are flared and optically thick (at optical and IR wavelengths).
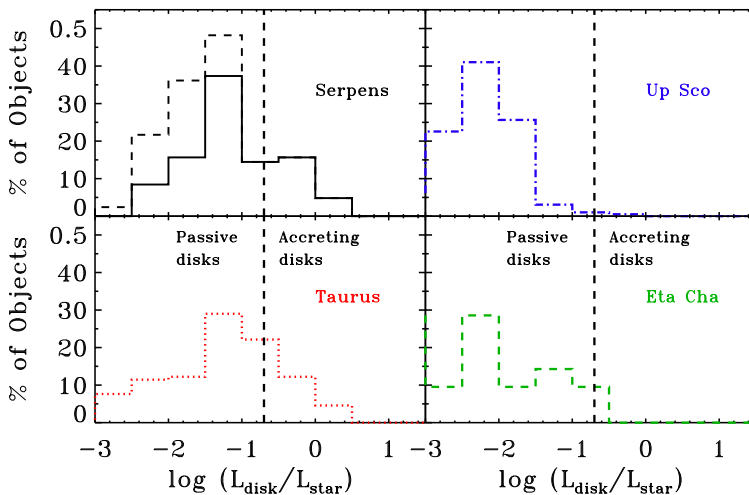
Figure 7.3 – Fractional disk luminosity (L_{disk}/L_{star}) derived for the objects in Serpens (top left), compared to those in Taurus (bottom left), Upper Scorpius (top right) and η Chamaeleontis (bottom right). The dashed line in the Serpens distribution accounts for completeness (see text for details). The boundary for accreting vs. passive disks is put at $L_{disk}/L_{star} \sim 0.2$. Thus "accreting disks" does not refer to the information on accretion rates derived from Hα.

Furthermore, Figure 7.3 shows the distribution of L_{disk}/L_{star} in the Upper Scorpius and η Chamaeleontis clusters for the entire samples (consisting of objects with IR-excess and those that have little or no excess, Maud et al. in prep). These older regions are known to have lower disk fractions (Hernández et al. 2008), meaning that most of the member stars have already fully dissipated their disks. Figure 7.3 clearly shows this difference in relation to the young Serpens and Taurus clouds, with distributions that peak (and spread) at considerably lower disk luminosities. The vertical dotted lines roughly separate luminosity ratios that can be explained by different mechanisms: accretion disks ($L_{disk}/L_{star} > 0.2$, Kenyon & Hartmann 1987) and passive disks. "Debris"-like disks are considerably fainter ($L_{disk}/L_{star} < 0.001$).

It is important to note that the L_{disk}/L_{star} distributions in Taurus, Upper Sco and η Cha are fairly complete. That is, for these well studied regions information on the entire young star population is available whether or not the source has IR excess (down to the brown dwarf limit, which ensures completeness for the results derived here for T Tauri stars). Taurus indeed has a brighter disk population than Upper Sco and η Cha. The Serpens sample presented here, on the other hand, is flux-limited and selected based on IR excess. That means that, by definition of the selection criteria, stars without disks and with disks fainter than 3 mJy at 8 μm are not part of the sample and therefore not shown in Figure 7.3. A conservative calculation of the fractional disk luminosity of the 88 missed sources (considering a flux lower than 3 mJy at 8 μm) was performed and is shown on top of the distribution of Serpens in

Figure 7.3 for reference.

Due to the selection criteria, the disk population missed in Serpens should be fainter than that presented here. Harvey et al. (2007b) identified a population of 235 IR-excess sources in Serpens, called YSO candidates. 147 of the original sample were further studied with the IRS spectrograph onboard *Spitzer*, comprising the sample presented here. This means that about 88 potential young stars with disks are missing. Considering the $\sim$20 % contamination fraction of background sources in the direction of Serpens (due to its low galactic latitude), conservatively about 70 of these 88 should be young stars that were missed, and which should populate the left part of Figure 7.3. These missed sources could account for the difference between Serpens and Taurus in the faintest bin of $L_{\mathrm{disk}}/L_{\mathrm{star}}$ in Figure 7.3, but should not be able to shift the peak of the $L_{\mathrm{disk}}/L_{\mathrm{star}}$ distribution for Serpens.

Serpens has not been as well explored in the literature as Taurus or Upper Sco and η Cha, since it suffers from high extinction and is not amongst the closest star-forming regions. Data covering a wide range of wavelengths exists but have not yet been published. Specifically, because this new young population in Serpens has been discovered from IR colors, young stars no longer surrounded by disks (class III) are, by definition, missed in the selection criteria for cloud membership. For this reason, the fraction of young stars that are surrounded by disks, determined for instance by combining IR and X-ray observations, is still unknown. However, the agreement in disk distribution with Taurus (as seen in Figure 7.3 and in Oliveira et al. 2010) and difference with Upper Scorpius and η Chamaeleontis could hint that the disk fraction in Serpens must be of the order of that in Taurus.

Figure 7.4 shows an additional comparison of the disks in Serpens with a sample of weak-line T Tauri stars (WTTS, Cieza et al. 2007) and a sample of debris disks (Chen et al. 2005). Oliveira et al. (2009) derived mass accretion rates based on the width at 10% of peak intensity of the Hα line, covered by their optical spectra. As previously noted, that sample is smaller than that presented here, due to the non-detection of the faintest objects in their optical spectroscopy program. It can be seen in Figure 7.4 that $L_{\mathrm{disk}}/L_{\mathrm{star}}$ of the accreting and non-accreting stars in Serpens (solid and dot-dashed black lines, respectively) overlap with the WTTSs (dotted red line). The Serpens population and the WTTSs differ in the distribution tails. The WTTS sample has a faint tail that reaches the faint debris disks population (dashed blue line), while the Serpens population shows a bright tail population.

Specifically comparing the accreting and non-accreting sub-samples in Serpens, the two classes overlap greatly, except at the brighter end of the distribution, dominated by accreting objects. This is more clearly seen by looking at the mean fractional disk luminosity $\langle L_{\mathrm{disk}}/L_{\mathrm{star}}\rangle$ which is 0.21 and 0.11 for accreting and non-accreting objects, respectively. The median fractional disk luminosity $\langle L_{\mathrm{disk}}/L_{\mathrm{star}}\rangle$ for the entire population of Serpens is 0.20.
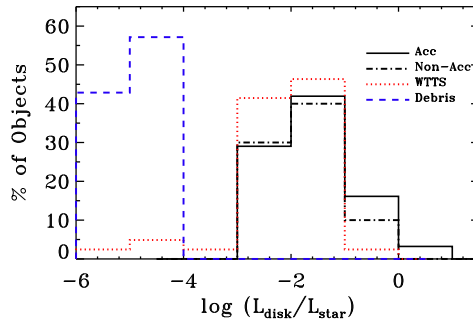
Figure 7.4 – Fractional disk luminosity (L_{disk}/L_{star}) derived for the accreting stars (based on Hα data, solid black line) and non-accreting stars (dot-dashed black line) in Serpens, compared to a sample of weak-lined T Tauri stars (WTTS, dotted gray line, Cieza et al. 2007) and a sample of debris disks (Debris, dashed gray line, Chen et al. 2005).

7.3.1 Comparison with Herbig Ae/Be Stars

Meeus et al. (2001) found that the disks around higher mass Herbig Ae/Be stars can be divided into two groups, according to the disk geometry: group I comprises sources with considerable IR excess, associated with a flared geometry; group II consists of little IR excess, associated with a geometrically thin midplane, shadowed by the puffed-up disk inner rim. Meeus et al. (2001) showed that the distributions of fractional disk luminosities for the two groups are different, with mean of 0.52 for group I and 0.17 for group II.

Figure 7.5 compares the two groups of Herbig Ae/Be stars with the young stars in Serpens, separated in disk geometry according to the ratio between the fluxes at 30 and 13 μm (F_{30}/F_{13}, Oliveira et al. 2010). It is seen that the geometry separation between flared and flat disks at $F_{30}/F_{13} = 1.5$ for T Tauri stars is not reflected with an accompanying separation in L_{disk}/L_{star}, which is the case for group I and II of the Herbig Ae/Be stars (dotted red and dashed blue lines, respectively). Although both the flared and flat disks span the same range, the peaks of the distributions are different, yielding distinctive median fractional disk luminosities: $\langle L_{disk}/L_{star} \rangle$ is 0.21 for the flared disks and 0.17 for flat disks.

It can be noted from Figure 7.5 that the great majority of disks around Herbig Ae/Be stars are concentrated in a narrow range of fractional disk luminosities, right at the border between disks dominated by accretion luminosity and passively irradiated disks, showing a bimodal distribution for group I and II. The T Tauri stars, on the other hand, span a much wider range of L_{disk}/L_{star}. In the center of the figure, the peaks of the distribution for flared and flat disks around T Tauri stars are not so different from those of group I and II of Herbig Ae/Be stars, albeit with greater overlap. The most striking difference between T Tauri and Herbig Ae/Be stars are both tails of the distribution. The lack of relatively very faint and very bright disks
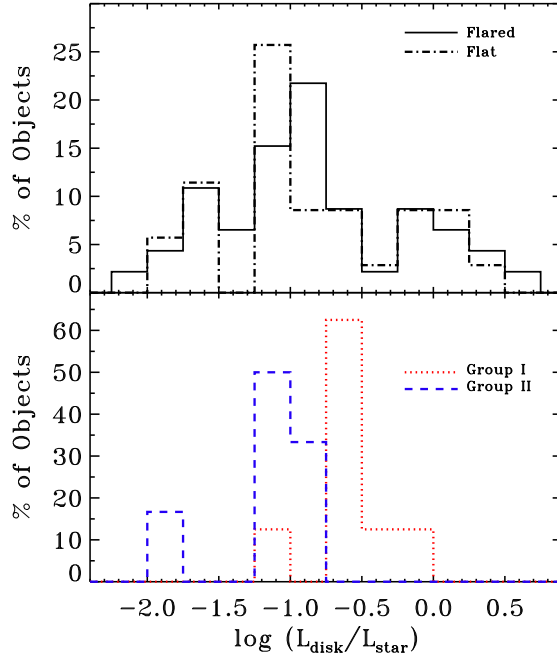
Figure 7.5 $-$ $L_{\rm disk}/L_{\rm star}$ derived for the flared (solid black line) and flat (dot-dashed black line) disks in Serpens (top), compared to the sample of Herbig Ae/Be of Meeus et al. (2001) (bottom). Objects belonging to group I (flared, dotted gray line) and group II (self-shadowed, dashed gray line) are shown separately.

around Herbig Ae/Be stars could be a bias effect due to the considerably lower number of such disks observed, when compared to their lower mass counterparts. Another possibility is that indeed disks around higher mass stars evolve faster. That would mean that the relatively very bright phase of disk evolution happens when the disks are still embedded in a gaseous envelope and consequently not visible, while the lack of the faint end of the distribution would imply on a very fast evolution from flat disks to no disks at all, being only visible again in the debris stage.

7.4   Connection Between Stars and Disks

While the late-type (K and M) population of Serpens spans a wide variety in disk shapes, the early-type (A, F and G) stars catch the attention. Two of the 9 early-type stars (#52 and 114) are surrounded by so-called cold disks, i.e. disks depleted of warm dust close to the star but otherwise massive (Oliveira et al. 2010; Merín et al. 2010). The majority, however, show very little IR excess (#70, 80, 98, 120, 131, 139, and 145) consistent with a transition from class II to class III. Assuming the stars in

Serpens are coeval, this result supports the idea that disks around more massive stars evolve on faster timescales.

Figure 7.6 shows the stellar luminosity related to the fractional disk luminosity for the sample in Serpens (black points), Taurus (red points), Upper Sco (blue points), and η Cha (green points). Horizontal dotted lines separate stellar luminosities of Herbig Ae/Be stars (earlier than F0), T Tauri stars (down to M7) and brown dwarfs (below M7), while the vertical lines roughly separate accreting from passive disks, as in Figure 7.3. It can be seen that the few Herbig Ae stars in Serpens follow the locus of $L_{\mathrm{disk}}/L_{\mathrm{star}}$ established by the larger sample of Herbig Ae/Be stars by Meeus et al. (2001), not occupying either tail of the distribution.
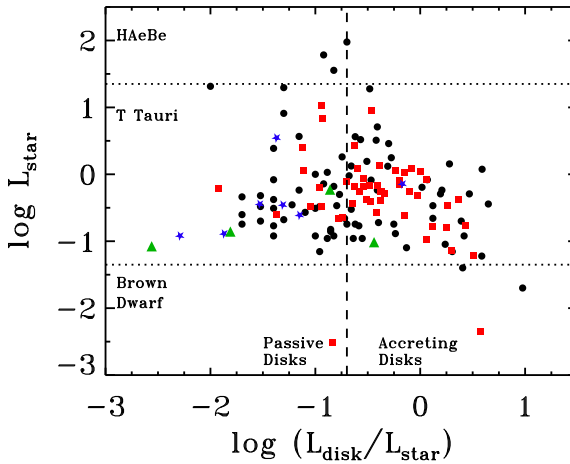

Figure 7.6 – Fractional disk luminosity ($L_{\mathrm{disk}}/L_{\mathrm{star}}$) versus the stellar luminosity (L_{star}) derived for the objects in Serpens (black circles), compared to the objects in Taurus (gray squares), in Upper Sco (gray stars), and in η Cha (gray triangles).

Besides the stellar and disk characteristics given in § 7.2, Oliveira et al. (2011) present the dust mineralogy and mean grain sizes in the surface of disks around the stars in Serpens, together with those disks in Taurus, Upper Sco and η Cha, obtained using the exact same procedure. Those results, combined with the analysis of their SEDs by Maud et al., allow the comparison of different disk and dust characteristics for all 4 regions.

Figures 7.7, 7.8 and 7.9 relate the stellar and disk fractional luminosities and mass accretion rate, respectively, with the results from the B2C decomposition method (Olofsson et al. 2010) on the mineralogy of the dust in the upper layers of these disks. In those figures, the two upper panels show the mean mass-average grain size and the two lower panels show the mean crystallinity fraction of the dust. The two left panels are the results for the warm component close to the stars, while the right panels show the results for the cold components, further away and deeper into the disk. The low
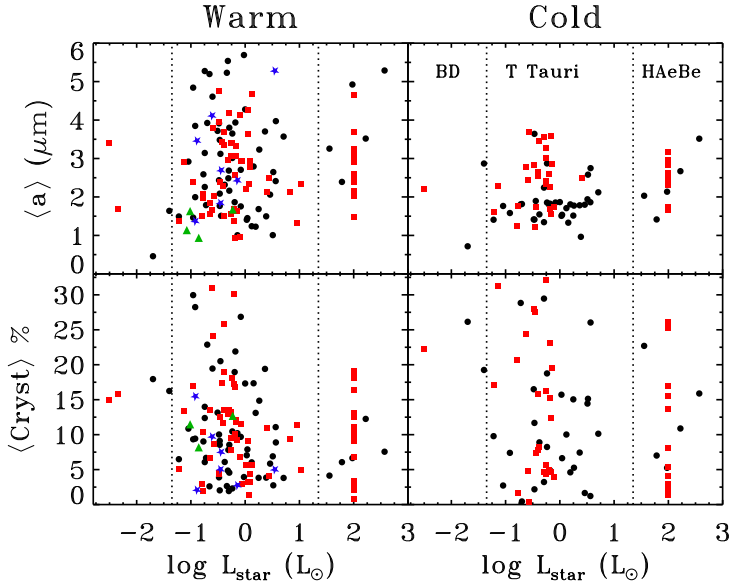
Figure 7.7 – Dust mineralogy versus the stellar luminosity (L_{star}) derived for the objects in Serpens (black circles), compared to the objects in Taurus (gray squares), in Upper Sco (gray stars), and in η Cha (gray triangles).

number of Herbig Ae/Be stars and brown dwarfs in this sample do not allow a study across the stellar mass regime.

No strong correlations are seen in either Figures 7.7, 7.8 or 7.9, pointing to no direct cause-effect relationships between either stellar or disk fractional luminosity and the dominant grain size or crystallinity fraction of the surface dust in a disk. The results from Figure 7.8 differ from those for Herbig Ae/Be stars (Meeus et al. 2001), which find a correlation between the mean grain size in the disk surface (as derived from the silicate features) and the geometry of the disk. Their study of a small number of disks (14 objects) argues that as the disk becomes flat (transitioning from group I into group II, and therefore decreasing L_{disk}/L_{star}, as they interpret), small dust grains are removed from the disk surface (by coagulation into bigger grains or blown away by the stellar radiation), which yields larger dominating grain sizes for flatter disks. Their results are supported by a less steep sub-mm slope for group II sources than for group I. Acke et al. (2004) studied the mm slope of a sample of 26 Herbig Ae/Be stars and found a correlation between this parameter and the geometry of the disk. It is important to note, however, that the mm data probe the entire dust population and do not say anything about the size of the dust in the disk surface, as is discussed here. Acke et al. (2004) suggest a geometry evolution from flared to self-shadowed with a concurrent evolution of the size of grains in the disk. Furthermore, similar results as those of Meeus et al. (2001) are found for T Tauri stars by Bouwman
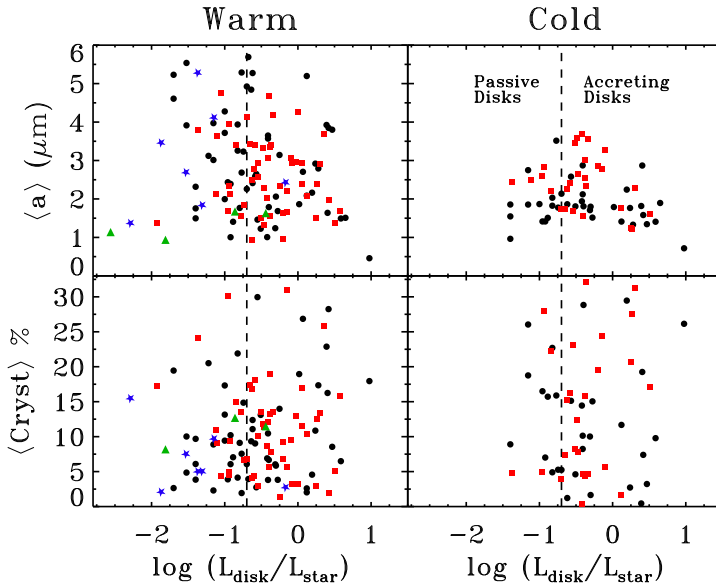
Figure 7.8 – Dust mineralogy versus the fractional disk luminosity ($L_{\mathrm{disk}}/L_{\mathrm{star}}$) derived for the objects in Serpens (black circles), compared to the objects in Taurus (gray squares), in Upper Sco (gray stars), and in η Cha (gray triangles).

et al. (2008), albeit for a very small number of objects (7 systems).

As discussed in Oliveira et al. (2010, 2011) for large samples of T Tauri stars, the dust population in the disk surface is not the result of grain growth alone, but also fragmentation of bigger grains that re-populate the small bin of grain sizes. This argument explains the presence of small grains in the disk surfaces of disks in all geometries (and even debris disks).

In addition to stellar and disk fractional luminosities and mass accretion rate, other stellar and disk parameters (such as stellar mass, disk colors and slopes) were investigated in relation to the mineralogical results. Similar to Figures 7.7, 7.8 and 7.9, no strong correlation was found for any combination of parameters. The lack of direct correlations between the stellar and disk characteristics shown above presents itself as a strong argument for the non-direct relationship of stellar and disk characteristics, in the range of parameters (time, mass, environment) probed by the objects presented here. That is, no direct causal relationship between stellar and disk characteristics is seen for T Tauri stars within a few Myr ($\sim$1 – 8 Myr). From the data presented here it is not possible to say whether any relationship could arise from studying in the same manner larger samples, that span a wider range in the parameters mentioned. Indeed, the few relationships claimed in the literature cover a large parameter space. For example, Sicilia-Aguilar et al. (2010) only found a trend of mass accretion rate decreasing over a range of dozens of millions of years, with a large spread at all ages.
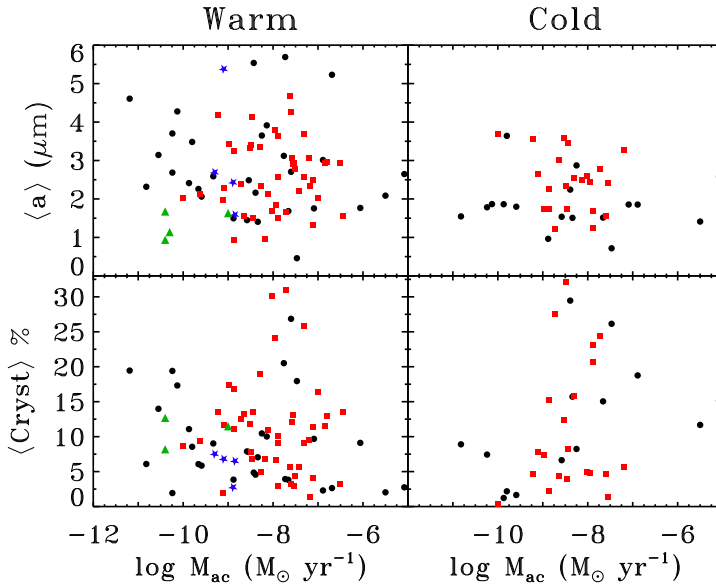
Figure 7.9 – Dust mineralogy versus the mass accretion rate of the objects in Serpens (black circles), compared to the objects in Taurus (gray squares), in Upper Sco (gray stars), and in η Cha (gray triangles).

Looking at a narrow age bin, no such relationship could be found. The same is true for the dependence of disk dispersal timescale on stellar mass found by Kennedy & Kenyon (2009). It will be interesting in the future to have a similar analysis as presented here (for stellar and disk characteristics, plus dust mineralogy) probing a wider range in stellar mass and in time, reaching the debris disk population.

7.5 Conclusions

We have studied the population of young stars still surrounded by disks in the Serpens Molecular Cloud. Aided by spectroscopic characterization of the central sources of star+disk system combined with IR photometry, spectral energy distributions of the objects could be constructed. The SEDs allow a correct separation between the radiation emitted by the central stars from that re-emitted by its surrounding disk.

The SEDs of Serpens show a considerable spread in IR excess. This implies the presence of disks with different geometries and in different stages of dissipation around stars that are nearly coeval, indicating that time is not the dominant parameter in the evolution of protoplanetary disks. The distribution of disk to star luminosity as a function of the stellar luminosity shows a trend in which lower mass stars have relatively brighter disks, consistent with evidence in the literature that disks around lower mass stars have generally longer lifetimes.

Adopting the new distance of 415 pc for Serpens, higher stellar luminosities are found than previously inferred by Oliveira et al. (2009). The higher luminosities, in turn, combined with pre-main sequence evolutionary models, allude to a distribution of ages that is younger than that found by Oliveira et al. (2009). The great majority of young stars in Serpens are in the 1 – 3 Myr range, with median age of $\sim$2.3 Myr. This result supports the disk observational evidence that Serpens joins the Taurus Molecular Cloud in probing the young bin of disk evolution, in spite of the different environment and star formation rates.

The distribution of fractional disk luminosity of the objects in Serpens also resembles closely that in Taurus, both of which are very different from those in the older regions Upper Scorpius and η Chamaeleontis, where most disks have already dissipated. Furthermore, the majority of the Serpens population is consistent with passively reprocessing disks. When comparing the actively accreting and non-accreting stars of Serpens (based on Hα data), the main difference seen is at the bright tail of the fractional disk luminosity, dominated by accreting stars.

The disks around T Tauri stars in Serpens are compared to those around Herbig Ae/Be stars (Meeus et al. 2001). It is found that the clear separation in fractional disk luminosity for different disk geometries (flared vs. flat) seen for Herbig Ae/Be stars is not as apparent for T Tauri stars. The disks around Herbig Ae/Be present a very narrow range of $L_{\rm disk}/L_{\rm star}$, concentrated around the border between disks dominated by accretion luminosity and passively irradiated disks, while the disks around T Tauri stars span a wider range on fractional disk luminosity. The absence of the tail distributions for Herbig Ae/Be could be due a faster evolution of these disks, or a bias effect due to the lower number of disks observed around those higher mass stars.

The stellar and disk characteristics are combined with dust mineralogy results delivered for the same regions by Oliveira et al. (2011). By combining all these data, the effect of stellar and disk characteristics on the surface dust of disks are studied. No strong correlations are found, suggesting that the many processes taking place in disks somehow conspire in such complicated ways that make it difficult to isolate the effect of each process/parameter.

References

Acke, B., van den Ancker, M. E., Dullemond, C. P., van Boekel, R., & Waters, L. B. F. M. 2004, A&A, 422, 621

Andrews, S. M., & Williams, J. P. 2005, ApJ, 631, 1134

Baraffe, I., Chabrier, G., Allard, F., & Hauschildt, P. H. 1998, A&A, 337, 403

Blum, J., & Wurm, G. 2008, ARA&A, 46, 21

Bouwman, J., et al. 2008, ApJ, 683, 479

Carpenter, J. M., Mamajek, E. E., Hillenbrand, L. A., & Meyer, M. R. 2006, ApJ, 651, L49

Chen, C. H., et al. 2005, ApJ, 634, 1372

Chiang, E. I., & Goldreich, P. 1997, ApJ, 490, 368

Cieza, L., et al. 2007, ApJ, 667, 308

Dominik, C., & Tielens, A. G. G. M. 1997, ApJ, 480, 647

Dullemond, C. P., & Dominik, C. 2004, A&A, 417, 159

Dzib, S., Loinard, L., Mioduszewski, A. J., Boden, A. F., Rodríguez, L. F., & Torres, R. M. 2010, ApJ, 718, 610

Evans, N. J., II, et al. 2003, PASP, 115, 965

Furlan, E., et al. 2006, ApJS, 165, 568

Güdel, M., et al. 2007, A&A, 468, 353

Greaves, J. S., & Rice, W. K. M. 2010, MNRAS, 407, 1981

Harvey, P. M., et al. 2006, ApJ, 644, 307

Harvey, P. M., et al. 2007, ApJ, 663, 1139

Harvey, P., Merín, B., Huard, T. L., Rebull, L. M., Chapman, N., Evans, N. J., II, & Myers, P. C. 2007, ApJ, 663, 1149

Hauschildt, P. H., Allard, F., Ferguson, J., Baron, E., & Alexander, D. R. 1999, ApJ, 525, 871

Hernández, J., Hartmann, L., Calvet, N., Jeffries, R. D., Gutermuth, R., Muzerolle, J., & Stauffer, J. 2008, ApJ, 686, 1195

Kennedy, G. M., & Kenyon, S. J. 2009, ApJ, 695, 1210

Kenyon, S. J., & Hartmann, L. 1987, ApJ, 323, 714

Kenyon, S. J., & Hartmann, L. 1995, ApJS, 101, 117

Knude, J. 2010, arXiv:1006.3676

Luhman, K. L., Stauffer, J. R., Muench, A. A., Rieke, G. H., Lada, E. A., Bouvier, J., & Lada, C. J. 2003, ApJ, 593, 1093

Maud, L. in preparation

Meeus, G., Waters, L. B. F. M., Bouwman, J., van den Ancker, M. E., Waelkens, C., & Malfait, K. 2001, A&A, 365, 476

Merín, B., et al. 2010, ApJ, 718, 1200

Oliveira, I., et al. 2009, ApJ, 691, 672

Oliveira, I., et al. 2010, ApJ, 714, 778

Oliveira, I., et al. 2011, accepted by ApJ

Olofsson, J., Augereau, J.-C., van Dishoeck, E. F., Merín, B., Grosso, N., Ménard, F., Blake, G. A., & Monin, J.-L. 2010, A&A, 520, A39

Padgett, D. L., Brandner, W., Stapelfeldt, K. R., Strom, S. E., Terebey, S., & Koerner, D. 1999, AJ, 117, 1490

Pontoppidan, K. M., & Brearley, A. J. 2010, Protoplanetary Dust: Astrophysical and Cosmochemical Perspectives, 191

Sicilia-Aguilar, A., et al. 2009, ApJ, 701, 1188

Sicilia-Aguilar, A., Henning, T., & Hartmann, L. W. 2010, ApJ, 710, 597

Siess, L., Dufour, E., & Forestini, M. 2000, A&A, 358, 593

Spezzi, L., Merin, B., Oliveira, I., van Dishoeck, E. F., & Brown, J. M. 2010, A&A, 513, A38

Straizys, V., Cernis, K. & Bartasiute, S. 1996, Baltic Astron., 5, 125

Strom, S. E., Strom, K. M., & Grasdalen, G. L. 1975, ARA&A, 13, 187

Udry, S., & Santos, N. C. 2007, ARA&A, 45, 397

Weidenschilling, S. J. 1980, Icarus, 44, 172

Weingartner, J. C., & Draine, B. T. 2001, ApJ, 548, 296

Wooden, D., Desch, S., Harker, D., Gail, H.-P., & Keller, L. 2007, Protostars and Planets V, 815

A. The Remaining SEDs
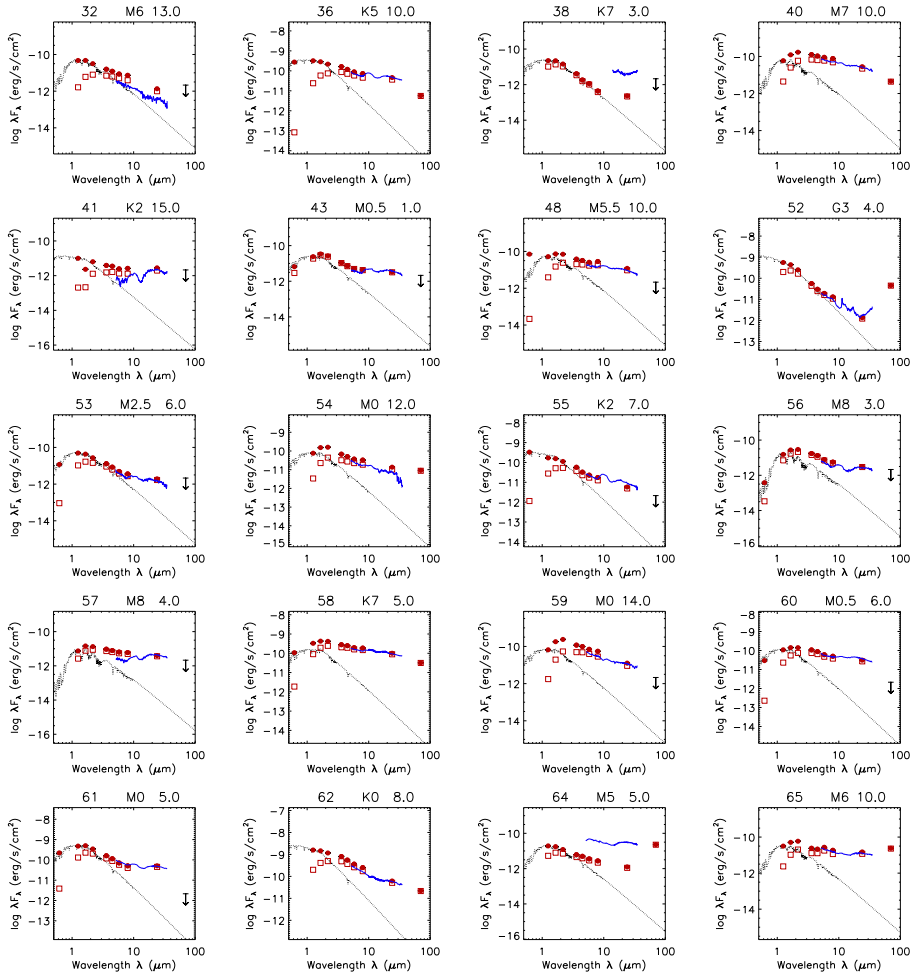
Figure A.1 – SEDs of the young stellar population with disks of Serpens. Each SED has the corresponding object ID (as in Oliveira et al. 2010) on the top left. The solid black line indicates the NextGen stellar photosphere model for the spectral type indicated on the top of each plot. Open squares are the observed photometry while the solid circles are the dereddened photometry. The visual extinction of each object can be seen on the top right. The solid gray line is the object's IRS spectrum.

Figure A.2 − SEDs, continued.

Figure A.3 − SEDs, continued.

Figure A.4 − SEDs, continued.

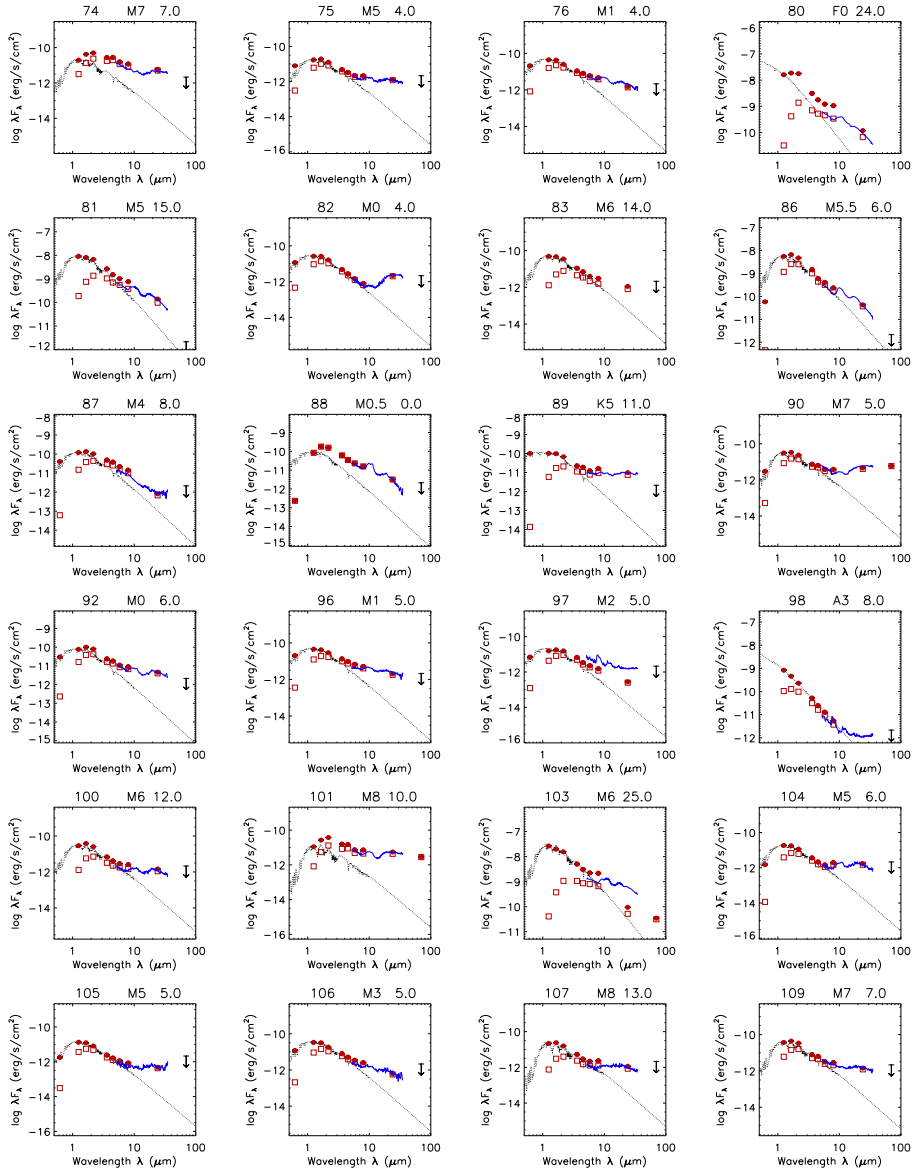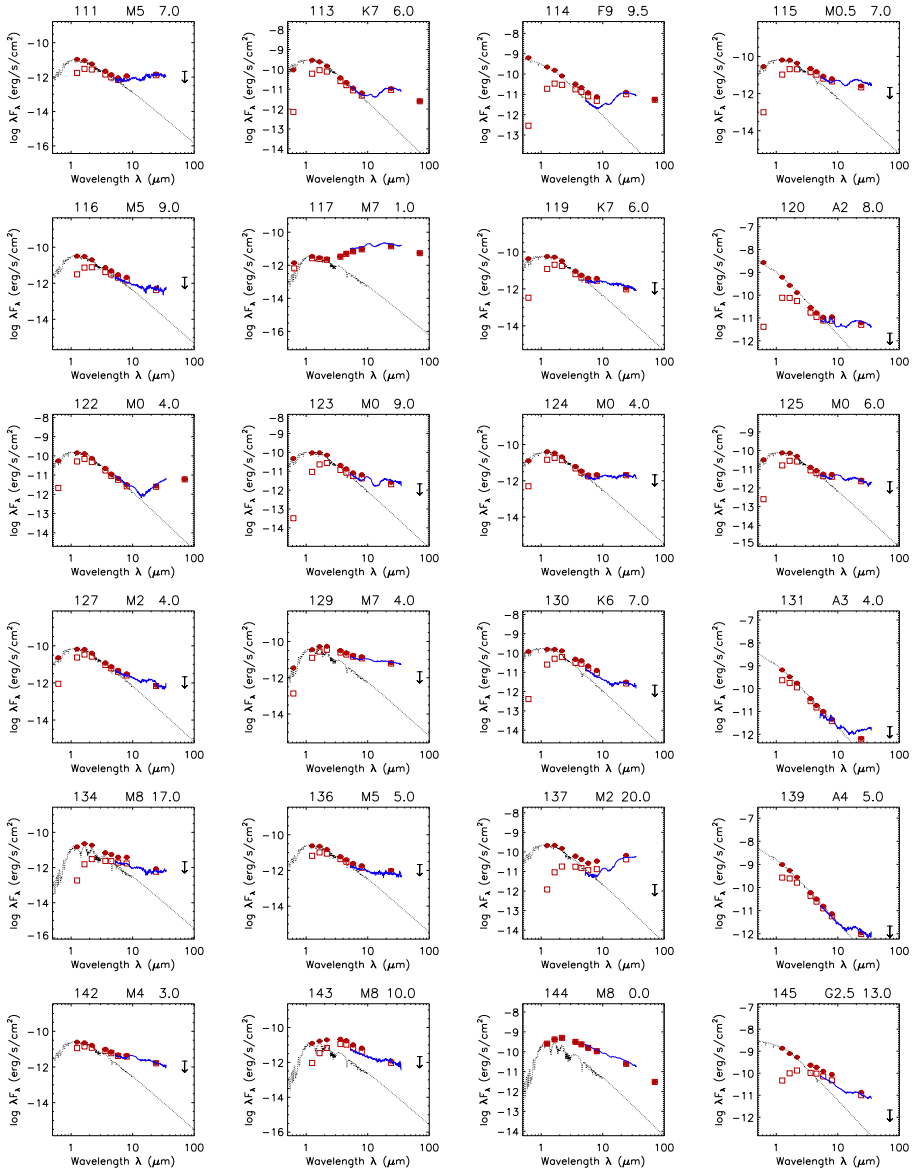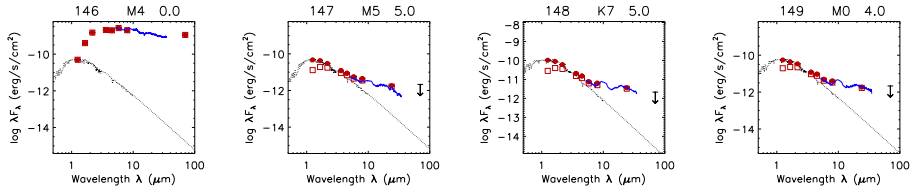| ID[a]	SpType	T_{eff} (K)	L_{star} (L$_\odot$)	L_{disk} (L$_\odot$)	A_V	Age (Myr)	Mass (M$_\odot$)	Accr?
1	K2	4900^{+610}_{-450}	$1.07^{+0.88}_{-0.52}$	$0.13^{+0.14}_{-0.14}$	2.6	$10.86^{+16.99}_{-7.04}$	$1.27^{+0.31}_{-0.31}$	yes
3	M0	3850^{+120}_{-80}	$1.77^{+1.55}_{-0.84}$	$0.53^{+0.94}_{-0.94}$	3.0	$0.50^{+1.40}_{-0.50}$	$1.04^{+0.18}_{-0.10}$	yes
6	K5	4350^{+330}_{-340}	$3.30^{+1.79}_{-1.17}$	$0.27^{+0.89}_{-0.89}$	3.0	$2.37^{+0.30}_{-0.30}$	$1.48^{+0.27}_{-0.27}$	yes
7	M0	3850^{+120}_{-80}	$0.51^{+2.36}_{-0.42}$	$1.56^{+0.80}_{-0.80}$	6.0	$4.36^{+47.24}_{-4.36}$	$0.88^{+0.28}_{-0.24}$	yes
8[b]	M8	2640^{+450}_{-207}	$0.11^{+0.09}_{-0.05}$	$0.13^{+0.01}_{-0.01}$	2.0	$0.78^{+0.78}_{-0.78}$	$0.12^{+0.12}_{-0.12}$	–
9[b]	M0	3850^{+190}_{-220}	$3.23^{+2.82}_{-1.53}$	$0.38^{+1.22}_{-1.22}$	6.0	$0.56^{+0.56}_{-0.56}$	$1.03^{+1.03}_{-1.03}$	–
10[b]	M3	3470^{+220}_{-260}	$1.82^{+1.59}_{-0.87}$	$0.18^{+0.32}_{-0.32}$	6.0	$0.44^{+0.44}_{-0.44}$	$0.68^{+0.68}_{-0.68}$	–
13[b]	M7	2940^{+340}_{-390}	$0.12^{+0.10}_{-0.06}$	$0.15^{+0.02}_{-0.02}$	8.0	$2.54^{+2.54}_{-2.54}$	$0.24^{+0.24}_{-0.24}$	–
14	M2	3580^{+250}_{-230}	$0.49^{+0.43}_{-0.23}$	$0.00^{+0.00}_{-0.00}$	3.0	$2.27^{+3.45}_{-1.50}$	$0.63^{+0.28}_{-0.19}$	yes
15[b]	M0	3850^{+190}_{-220}	$1.32^{+1.15}_{-0.63}$	$0.49^{+0.64}_{-0.64}$	4.0	$1.01^{+1.74}_{-1.01}$	$0.98^{+0.16}_{-0.18}$	–
20[b]	M0	3850^{+190}_{-220}	$0.29^{+0.25}_{-0.14}$	$0.05^{+0.01}_{-0.00}$	13.0	$9.06^{+14.45}_{-5.16}$	$0.81^{+0.08}_{-0.25}$	–
21[b]	M0	3850^{+190}_{-220}	$0.66^{+0.58}_{-0.32}$	$0.15^{+0.10}_{-0.10}$	12.0	$2.89^{+4.58}_{-1.74}$	$0.91^{+0.14}_{-0.26}$	–
24[b]	M7	2940^{+340}_{-390}	$0.15^{+0.13}_{-0.07}$	$0.14^{+0.02}_{-0.02}$	14.0	$2.06^{+2.06}_{-2.06}$	$0.24^{+0.24}_{-0.24}$	–
29	M2	3580^{+320}_{-360}	$0.18^{+0.16}_{-0.09}$	$0.20^{+0.04}_{-0.04}$	4.0	$8.13^{+18.42}_{-6.50}$	$0.56^{+0.23}_{-0.32}$	yes
30	M1	3720^{+150}_{-120}	$1.00^{+0.53}_{-0.36}$	$0.10^{+0.10}_{-0.10}$	2.0	$1.18^{+1.13}_{-0.74}$	$0.83^{+0.18}_{-0.10}$	yes
31[b]	M9	2510^{+440}_{-107}	$94.77^{+75.01}_{-47.21}$	$0.20^{+18.94}_{-18.94}$	15.0			–
32[b]	M6	3050^{+370}_{-360}	$0.30^{+0.25}_{-0.14}$	$0.22^{+0.06}_{-0.06}$	13.0	$1.73^{+1.73}_{-1.73}$	$0.38^{+0.38}_{-0.38}$	–
36	K5	4350^{+680}_{-480}	$2.88^{+1.56}_{-1.02}$	$0.50^{+1.43}_{-1.43}$	10.0	$1.20^{+4.56}_{-1.20}$	$1.21^{+0.50}_{-0.66}$	yes
38[b]	K7	4060^{+350}_{-80}	$0.18^{+0.16}_{-0.09}$	$0.02^{+0.00}_{-0.00}$	3.0	$21.77^{+39.11}_{-13.85}$	$0.72^{+0.02}_{-0.11}$	–
40	M7	2940^{+570}_{-507}	$0.36^{+0.30}_{-0.17}$	$4.46^{+1.61}_{-1.61}$	10.0	$2.03^{+2.03}_{-2.03}$	$0.48^{+0.48}_{-0.48}$	no
41	K2	4900^{+610}_{-450}	$0.11^{+0.09}_{-0.05}$	$0.28^{+0.03}_{-0.03}$	15.0			no
43	M0.5	3785^{+225}_{-380}	$0.18^{+0.16}_{-0.09}$	$0.56^{+0.10}_{-0.10}$	1.0	$18.20^{+25.92}_{-15.10}$	$0.75^{+0.08}_{-0.37}$	no
48	M5.5	3145^{+425}_{-525}	$0.34^{+0.29}_{-0.16}$	$1.32^{+0.44}_{-0.44}$	10.0	$1.58^{+1.07}_{-1.07}$	$0.33^{+0.19}_{-0.19}$	yes
52	G3	5830^{+400}_{-230}	$8.14^{+6.40}_{-4.07}$	$0.05^{+0.43}_{-0.43}$	4.0	$6.93^{+6.33}_{-2.63}$	$1.82^{+0.39}_{-0.38}$	no
53	M2.5	3525^{+385}_{-355}	$0.35^{+0.31}_{-0.17}$	$0.06^{+0.02}_{-0.02}$	6.0	$2.34^{+6.84}_{-2.34}$	$0.50^{+0.41}_{-0.36}$	yes
54[b]	M0	3850^{+190}_{-220}	$0.58^{+0.51}_{-0.28}$	$1.61^{+0.94}_{-0.94}$	12.0	$3.44^{+5.18}_{-1.97}$	$0.90^{+0.14}_{-0.26}$	–
55	K2	4900^{+450}_{-210}	$2.44^{+10.94}_{-2.03}$	$0.04^{+0.09}_{-0.09}$	7.0	$4.02^{+36.50}_{-4.02}$	$1.68^{+1.13}_{-0.80}$	yes
56[b]	M8	2640^{+450}_{-207}	$0.09^{+0.07}_{-0.04}$	$1.73^{+0.15}_{-0.15}$	3.0	$1.27^{+1.27}_{-1.27}$	$0.12^{+0.12}_{-0.12}$	–
57[b]	M8	2640^{+450}_{-207}	$0.04^{+0.03}_{-0.02}$	$2.54^{+0.11}_{-0.11}$	4.0	$2.94^{+2.94}_{-2.94}$	$0.11^{+0.11}_{-0.11}$	–
58	K7	4060^{+350}_{-80}	$1.19^{+5.48}_{-0.98}$	$3.89^{+4.62}_{-4.62}$	5.0	$2.31^{+24.92}_{-2.31}$	$1.14^{+0.25}_{-0.14}$	yes
59[b]	M0	3850^{+190}_{-220}	$0.51^{+0.44}_{-0.24}$	$2.94^{+1.49}_{-1.49}$	14.0	$4.42^{+5.41}_{-2.58}$	$0.87^{+0.14}_{-0.26}$	–
60	M0.5	3785^{+50}_{-80}	$0.83^{+0.73}_{-0.40}$	$1.17^{+0.97}_{-0.97}$	6.0	$2.20^{+3.35}_{-1.51}$	$0.93^{+0.08}_{-0.10}$	yes
61	M0	3850^{+120}_{-80}	$3.65^{+3.19}_{-1.73}$	$0.24^{+0.87}_{-0.87}$	5.0	$0.40^{+0.40}_{-0.40}$	$1.05^{+1.05}_{-1.05}$	yes
62	K0	5250^{+630}_{-1140}	$18.94^{+15.34}_{-9.34}$	$0.33^{+6.16}_{-6.16}$	8.0			no
64[b]	M5	3240^{+270}_{-260}	$0.13^{+0.11}_{-0.06}$	$0.58^{+0.08}_{-0.08}$	5.0	$2.05^{+5.19}_{-2.05}$	$0.21^{+0.21}_{-0.11}$	–
65[b]	M6	3050^{+370}_{-360}	$0.20^{+0.17}_{-0.10}$	$2.46^{+0.49}_{-0.49}$	10.0	$1.48^{+1.11}_{-1.11}$	$0.23^{+0.12}_{-0.12}$	–
66	K5	4350^{+330}_{-340}	$5.11^{+4.35}_{-2.46}$	$0.39^{+1.99}_{-1.99}$	7.0	$1.64^{+0.17}_{-0.17}$	$1.56^{+0.35}_{-0.35}$	yes
69[b]	M5	3240^{+270}_{-260}	$0.23^{+0.20}_{-0.11}$	$0.00^{+0.00}_{-0.00}$	11.0	$0.77^{+2.22}_{-0.77}$	$0.21^{+0.23}_{-0.07}$	–
70	A3	8720^{+720}_{-775}	$20.64^{+15.11}_{-10.63}$	$0.01^{+0.22}_{-0.22}$	3.0	$8.18^{+70.19}_{-8.18}$	$2.10^{+0.38}_{-0.21}$	no
71	M3	3470^{+80}_{-130}	$0.33^{+0.29}_{-0.16}$	$0.03^{+0.01}_{-0.01}$	4.0	$2.48^{+3.15}_{-1.37}$	$0.49^{+0.09}_{-0.11}$	yes
74[b]	M7	2940^{+340}_{-390}	$0.12^{+0.10}_{-0.06}$	$2.62^{+0.31}_{-0.31}$	7.0	$2.66^{+2.66}_{-2.66}$	$0.24^{+0.24}_{-0.24}$	–
75[b]	M5	3240^{+270}_{-260}	$0.11^{+0.10}_{-0.05}$	$0.23^{+0.03}_{-0.03}$	4.0	$2.33^{+5.95}_{-2.33}$	$0.21^{+0.21}_{-0.11}$	–
76	M1	3720^{+150}_{-120}	$0.33^{+0.29}_{-0.16}$	$0.11^{+0.04}_{-0.04}$	4.0	$5.66^{+7.09}_{-3.29}$	$0.71^{+0.16}_{-0.14}$	no
80[b]	F0	7200^{+380}_{-310}	$370.99^{+288.34}_{-86.29}$	$0.17^{+62.16}_{-62.16}$	24.0			–
81	M5	3240^{+520}_{-690}	$60.77^{+52.31}_{-29.09}$	$0.12^{+7.38}_{-7.38}$	15.0			–
82	M0	3850^{+190}_{-220}	$0.20^{+0.18}_{-0.10}$	$0.03^{+0.01}_{-0.01}$	4.0	$15.80^{+21.23}_{-9.13}$	$0.76^{+0.08}_{-0.22}$	yes
83[b]	M6	3050^{+370}_{-360}	$0.31^{+0.26}_{-0.15}$	$0.04^{+0.01}_{-0.01}$	14.0	$1.64^{+1.64}_{-1.64}$	$0.38^{+0.38}_{-0.38}$	–
86	M5.5	3145^{+270}_{-160}	$35.78^{+30.57}_{-17.19}$	$0.15^{+5.50}_{-5.50}$	6.0			–
87	M4	3370^{+320}_{-460}	$0.82^{+0.72}_{-0.39}$	$0.34^{+0.28}_{-0.28}$	8.0	$1.43^{+0.24}_{-0.24}$	$0.64^{+0.19}_{-0.19}$	no
88	M0.5	3785^{+155}_{-275}	$0.64^{+0.56}_{-0.31}$	$1.04^{+0.67}_{-0.67}$	0.0	$2.98^{+4.76}_{-1.80}$	$0.91^{+0.12}_{-0.30}$	no
89	K5	4350^{+850}_{-550}	$0.95^{+0.81}_{-0.46}$	$0.21^{+0.20}_{-0.20}$	11.0	$5.11^{+21.66}_{-3.76}$	$1.18^{+0.02}_{-0.62}$	yes
90[b]	M7	2940^{+680}_{-507}	$0.19^{+0.16}_{-0.09}$	$0.40^{+0.08}_{-0.08}$	5.0	$7.34^{+7.34}_{-7.34}$	$0.54^{+0.54}_{-0.54}$	–
92	M0	3850^{+120}_{-80}	$0.58^{+0.51}_{-0.28}$	$0.39^{+0.23}_{-0.23}$	6.0	$3.40^{+5.17}_{-1.95}$	$0.90^{+0.10}_{-0.10}$	yes
96	M1	3720^{+150}_{-120}	$0.34^{+0.30}_{-0.16}$	$0.16^{+0.06}_{-0.06}$	5.0	$5.51^{+6.80}_{-3.19}$	$0.72^{+0.16}_{-0.14}$	yes
97	M2	3580^{+250}_{-230}	$0.14^{+0.08}_{-0.05}$	$0.14^{+0.02}_{-0.02}$	5.0	$10.11^{+18.68}_{-6.67}$	$0.55^{+0.19}_{-0.22}$	no
98	A3	8720^{+3100}_{-1220}	$32.48^{+23.78}_{-16.72}$	$0.00^{+0.12}_{-0.12}$	8.0	$4.99^{+7.78}_{-1.68}$	$2.42^{+0.45}_{-0.44}$	no
100[b]	M6	3050^{+370}_{-360}	$0.18^{+0.15}_{-0.09}$	$0.24^{+0.04}_{-0.04}$	12.0	$1.61^{+1.15}_{-1.15}$	$0.22^{+0.12}_{-0.12}$	–

ID[a]	SpType	T_{eff} (K)	L_{star} ($L_\odot$)	L_{disk} ($L_\odot$)	A_V	Age (Myr)	Mass ($M_\odot$)	Accr?
101[b]	M8	2640^{+450}_{-207}	$0.06^{+0.05}_{-0.03}$	$3.86^{+0.24}_{-0.24}$	10.0	$2.02^{+2.02}_{-2.02}$	$0.12^{+0.12}_{-0.12}$	–
103[b]	M6	3050^{+370}_{-400}	$166.68^{+141.01}_{-80.49}$	$0.06^{+0.69}_{-0.00}$	25.0			–
104[b]	M5	3240^{+270}_{-260}	$0.12^{+0.11}_{-0.06}$	$0.10^{+0.01}_{-0.01}$	6.0	$2.16^{+5.49}_{-2.16}$	$0.21^{+0.21}_{-0.11}$	–
105[b]	M5	3240^{+270}_{-260}	$0.09^{+0.05}_{-0.03}$	$0.00^{+0.00}_{-0.00}$	5.0	$2.91^{+7.96}_{-2.91}$	$0.21^{+0.20}_{-0.12}$	–
106	M3	3470^{+80}_{-130}	$0.25^{+0.13}_{-0.09}$	$0.02^{+0.01}_{-0.01}$	5.0	$3.10^{+3.20}_{-1.02}$	$0.47^{+0.08}_{-0.11}$	no
107[b]	M8	2640^{+450}_{-207}	$0.12^{+0.10}_{-0.06}$	$0.04^{+0.01}_{-0.01}$	13.0	$0.63^{+0.63}_{-0.63}$	$0.12^{+0.12}_{-0.12}$	–
109[b]	M7	2940^{+340}_{-390}	$0.22^{+0.19}_{-0.11}$	$0.19^{+0.04}_{-0.04}$	7.0	$1.16^{+1.16}_{-1.16}$	$0.25^{+0.25}_{-0.25}$	–
111[b]	M5	3240^{+270}_{-260}	$0.07^{+0.04}_{-0.02}$	$0.11^{+0.01}_{-0.01}$	7.0	$4.26^{+13.41}_{-4.26}$	$0.20^{+0.20}_{-0.11}$	–
113	K7	4060^{+350}_{-80}	$2.32^{+2.02}_{-1.11}$	$0.03^{+0.08}_{-0.00}$	6.0	$0.68^{+1.66}_{-0.13}$	$0.13^{+0.91}_{-0.22}$	yes
114	F9	6115^{+390}_{-400}	$3.68^{+2.87}_{-1.84}$	$0.07^{+0.24}_{-0.24}$	9.5	$14.29^{+17.38}_{-14.15}$	$116.38^{+1.39}_{-0.18}$	no
115	M0.5	3785^{+155}_{-275}	$0.50^{+0.43}_{-0.24}$	$0.17^{+0.09}_{-0.09}$	7.0	$4.58^{+5.47}_{-2.84}$	$0.87^{+0.12}_{-0.31}$	no
116[b]	M5	3240^{+270}_{-260}	$0.21^{+0.18}_{-0.10}$	$0.05^{+0.01}_{-0.01}$	9.0	$0.93^{+2.29}_{-0.93}$	$0.21^{+0.22}_{-0.08}$	–
117[b]	M7	2940^{+680}_{-507}	$0.02^{+0.02}_{-0.01}$	$9.47^{+0.20}_{-0.20}$	1.0	$3.14^{+4.07}_{-3.14}$	$0.06^{+0.73}_{-0.00}$	yes
119	K7	4060^{+350}_{-80}	$0.46^{+0.40}_{-0.22}$	$0.02^{+0.01}_{-0.01}$	6.0	$4.86^{+9.08}_{-2.33}$	$0.73^{+0.27}_{-0.09}$	yes
120	A2	8970^{+520}_{-540}	$25.13^{+18.67}_{-12.86}$	$0.00^{+0.06}_{-0.00}$	8.0	$6.69^{+2.10}_{-6.69}$	$2.24^{+0.35}_{-0.29}$	no
122	M0	3850^{+155}_{-150}	$1.10^{+0.96}_{-0.52}$	$0.03^{+0.03}_{-0.00}$	4.0	$1.43^{+2.03}_{-1.12}$	$0.96^{+0.15}_{-0.16}$	yes
123	M0	3850^{+120}_{-80}	$0.72^{+0.63}_{-0.34}$	$0.12^{+0.09}_{-0.09}$	9.0	$2.63^{+4.10}_{-1.66}$	$0.92^{+0.12}_{-0.10}$	no
124	M0	3850^{+155}_{-150}	$0.27^{+0.15}_{-0.10}$	$0.08^{+0.02}_{-0.02}$	4.0	$9.68^{+10.12}_{-3.71}$	$0.81^{+0.06}_{-0.17}$	no
125	M0	3850^{+120}_{-80}	$0.58^{+0.51}_{-0.28}$	$0.07^{+0.04}_{-0.04}$	6.0	$3.45^{+5.18}_{-1.98}$	$0.90^{+0.10}_{-0.10}$	yes
127	M2	3580^{+120}_{-130}	$0.48^{+0.42}_{-0.23}$	$0.03^{+0.02}_{-0.02}$	4.0	$2.35^{+3.15}_{-1.46}$	$0.63^{+0.15}_{-0.12}$	yes
129[b]	M7	2940^{+340}_{-390}	$0.22^{+0.18}_{-0.11}$	$1.32^{+0.29}_{-0.29}$	4.0	$1.23^{+1.23}_{-1.23}$	$0.25^{+0.25}_{-0.25}$	–
130	K6	4205^{+150}_{-140}	$1.33^{+1.15}_{-0.64}$	$0.22^{+0.30}_{-0.30}$	7.0	$2.16^{+2.43}_{-2.16}$	$0.91^{+0.22}_{-0.16}$	yes
131	A3	8720^{+720}_{-775}	$25.57^{+18.72}_{-13.16}$	$0.00^{+0.02}_{-0.02}$	4.0	$6.49^{+2.08}_{-6.49}$	$2.23^{+0.37}_{-0.30}$	no
134[b]	M8	2640^{+450}_{-207}	$0.08^{+0.07}_{-0.04}$	$0.74^{+0.06}_{-0.06}$	17.0	$1.30^{+1.30}_{-1.30}$	$0.12^{+0.12}_{-0.12}$	–
136[b]	M5	3240^{+270}_{-260}	$0.17^{+0.09}_{-0.06}$	$0.04^{+0.01}_{-0.01}$	5.0	$1.44^{+3.61}_{-1.44}$	$0.21^{+0.22}_{-0.10}$	–
137[b]	M2	3580^{+250}_{-230}	$1.56^{+1.36}_{-0.74}$	$0.31^{+0.48}_{-0.48}$	20.0	$1.01^{+0.06}_{-0.06}$	$0.89^{+0.18}_{-0.18}$	–
139	A4	8460^{+1120}_{-820}	$33.71^{+24.87}_{-17.30}$	$0.00^{+0.14}_{-0.14}$	5.0	$4.77^{+4.60}_{-1.79}$	$2.43^{+0.39}_{-0.45}$	no
142	M4	3370^{+180}_{-350}	$0.17^{+0.09}_{-0.06}$	$0.26^{+0.05}_{-0.05}$	3.0	$3.05^{+4.84}_{-3.05}$	$0.36^{+0.18}_{-0.23}$	yes
143[b]	M8	2640^{+450}_{-207}	$0.07^{+0.06}_{-0.03}$	$2.02^{+0.14}_{-0.14}$	10.0	$1.76^{+1.76}_{-1.76}$	$0.12^{+0.12}_{-0.12}$	–
144[b]	M8	2640^{+450}_{-207}	$1.43^{+1.16}_{-0.70}$	$1.90^{+2.71}_{-2.71}$	0.0			–
145	G2.5	5845^{+230}_{-30}	$19.73^{+15.51}_{-9.86}$	$0.05^{+1.01}_{-1.01}$	13.0	$3.19^{+2.66}_{-0.89}$	$2.47^{+0.44}_{-0.52}$	no
146	M4	3370^{+180}_{-350}	$0.34^{+0.30}_{-0.16}$	$89.13^{+30.44}_{-30.44}$	0.0	$1.65^{+1.39}_{-1.65}$	$0.42^{+0.16}_{-0.26}$	yes
147[b]	M5	3240^{+270}_{-260}	$0.31^{+0.27}_{-0.15}$	$0.10^{+0.03}_{-0.03}$	5.0	$0.37^{+1.98}_{-0.37}$	$0.20^{+0.26}_{-0.05}$	–
148	K7	4060^{+350}_{-80}	$0.83^{+0.72}_{-0.40}$	$0.04^{+0.03}_{-0.03}$	5.0	$2.58^{+2.87}_{-1.48}$	$0.70^{+0.42}_{-0.08}$	yes
149	M0	3850^{+190}_{-220}	$0.42^{+0.37}_{-0.20}$	$0.04^{+0.02}_{-0.02}$	4.0	$5.82^{+7.72}_{-3.47}$	$0.85^{+0.14}_{-0.26}$	yes

Table A.1 – Stellar and Disk Parameters in Serpens

[a] As in Oliveira et al. (2010).
[b] Spectral types from photometry.

Nederlandse Samenvatting

Inleiding

Metingen van de kosmische achtergrondstraling gedaan met de Wilkinson Microwave Anisotropy Probe (WMAP) hebben aangetoond dat het heelal ongeveer 14 miljard jaar geleden is ontstaan. De moderne kosmologie heeft verder laten zien dat het heelal grotendeels 'donker' was gedurende de eerste miljard jaar van zijn bestaan. In deze fase bestond materie in het heelal voornamelijk uit elektronen en geioniseerd waterstof. De eerste sterren vormden waarschijnlijk pas na de eerste paar honderd miljoen jaar. Naarmate het heelal afkoelde en enorme massa's neutraal waterstofgas samenklonterden, kwam de kosmische sterrenfabriek echter goed op gang en werden de eerste sterrenstelsels gevormd. Vandaag de dag bevat het waarneembare heelal zo'n 10^{21} (1 *triljard*) sterren! De ontwikkeling van sterren bepaalt grotendeels hoe sterrenstelsels eruit zien. Tevens bepaalt het hoe de meeste elementen zwaarder dan waterstof gevormd werden ten gevolge van de chemische evolutie die diep binnenin de sterren plaatsvindt. Oorspronkelijk bestonden deze elementen slechts uit waterstof, helium en kleine hoeveelheden lithium, beryllium en boor. Zwaardere elementen zoals zuurstof, koolstof en stikstof bestonden nog niet.

Sterren worden geboren, ontwikkelen zich (ze evolueren) en sterven. Ze ontstaan grofweg wanneer een wolk van molekulair gas inelkaarstort. De nieuwe sterren ontwikkelen zich daarna op verschillende manieren afhankelijk van hun beginmassa's. Tijdens deze evolutie vindt kernfusie plaats die lichtere elementen omzet in zwaardere elementen. Op deze wijze produceren sterren de energie die nodig is om te voorkomen dat de ster ten gevolge van zijn eigen zwaartekracht ineenstort. De sterren veranderen verder vaak van massa (door in- of uitstroom van materie), van afmeting (groter of kleiner) en helderheid (bijvoorbeeld door een verandering in de thermo-nucleaire reacties in de kern van de ster, of door stof). Sterren kunnen vormen in isolatie, maar veel vaker worden ze gevormd als onderdeel van kleine of grote groepen. Wanneer een ster al zijn nucleaire brandstof verbruikt heeft kan de stralingsdruk van binnenuit in de ster de druk van de zwaartekracht niet meer compenseren. Een onontkoombare kettingreactie is het gevolg die uiteindelijk zal leiden tot de dood van de ster. Sterren van gemiddelde massa (zoals de zon) stoten hun buitenste laag van gas af en veranderen in een zogenaamde "planetaire nevel". Zwaardere sterren eindigen in krachtige explosies: supernova's. Tijdens deze explosies worden nieuw geproduceerde elementen, die uiteindelijk nodig zijn voor de stofdeeltjes waar planeten uit betaan (zoals silicium, zuurstof, koolstof, magnesium en ijzer), terug in de ruimte geblazen. Daar

worden deze deeltjes opgenomen in het "interstellaire medium" (ISM), de ijle ruimte tussen de sterren. Dit verrijkte ISM levert vervolgens het materiaal aan voor de produktie van een volgende generatie van sterren, hun bijbehorende planetenstelsels, en in het geval van de aarde zelfs levende organismen.

Een populaire theorie claimt dat de explosie van een supernova in ons eigen Melkwegstelsel ten grondslag ligt aan het ontstaan van een jonge Zon omgeven door een proto-planetaire schijf, zo'n viereneenhalf miljard jaar geleden. Het materiaal in deze zogenoemde "oernevel" vormde uiteindelijk de Zon, acht planeten (Mercurius, Venus, Aarde, Mars, Jupiter, Saturnus, Uranus en Neptunus) en talrijke kleinere hemellichamen (denk aan dwergplaneten zoals Pluto, kometen en asteroïden). De structuur en samenstelling van deze hemellichamen bevatten informatie over hoe zij precies zijn ontstaan, maar vele details over dit ontstaansproces zijn nog onbekend.

Dit proefschrift beschrijft de ontwikkeling van jonge sterren en hun proto-planetaire schijven en de evolutie van de stofdeeltjes waaruit die schijven bestaan. Deze studie beslaat dus de eerste fase van de ontwikkeling van planeten zoals die in ons eigen zonnestelsel.

Het Ontstaan van Sterren met Lage Massa

Het meest voorkomende type sterren zijn sterren met een relatief lage massa (een massa vergelijkbaar met ongeveer de helft van die van onze zon, of $\sim$0.5 $M_\odot$). Deze sterren domineren de gehele sterpopulatie in sterrenstelsels, zowel in hun aantal als in hun totale massa. De sterren vormen uit vrij dichte concentraties van interstellair gas en stof, "molekulaire wolken" genaamd. De totale hoeveelheid stof in deze wolken beslaat ongeveer 1% van hun totale massa. Dit stof bestaat voornamelijk uit amorfe silicaten en koolstofdeeltjes met een doorsnede van kleiner dan een micrometer ($<$1 μm). De stofwolken zijn grotendeels ondoorzichtig in het visuele golflengtegebied vanwege hun hoge extinctie (absorptie van licht door stofdeeltjes). Op langere golflengten zoals het infrarood zijn ze echter transparant.

Stervorming vindt plaats wanneer een deel van een wolk voldoende afkoelt en een voldoende hoge gasdichtheid bereikt ten gevolge van de samentrekking door zijn eigen zwaartekracht. Gedurende dit proces wordt zwaartekrachtsenergie omgezet in bewegingsenergie wat er toe leidt dat gasdeeltjes met hoge snelheden tegen elkaar botsen. Zo neemt de temperatuur van de ster-in-wording en zijn omgeving toe. Deze thermische druk helpt ook om de naar binnen gerichte druk van de zwaartekracht te compenseren zodat de wolk niet verder ineenstort. Als de temperatuur in het centrum zo hoog is dat er kernfusie plaatsvindt is een nieuwe ster, omgeven door een roterende schijf van gas en stof, geboren. Op den duur lossen de restanten van de oernevel rondom de ster op. De jonge ster en zijn stofschijf zijn nu zichtbaar. Deze fase staat bekend als de "T-Tauri" fase. Vanaf deze fase is de evolutie van de stofschijf gekoppeld aan die van de ster.
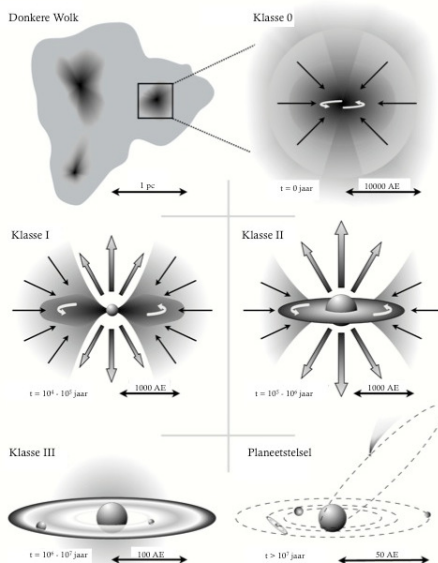
Figuur 1 – Het ontstaan van een ster met lage massa. Linksboven: Kernen met een relatief hoge gasdichtheid vormen in een molekulaire wolk. Rechtsboven: Een kern stort ineen onder de invloed van zijn eigen zwaartekracht. Links-midden: De restanten het omhulsel rondom de proto lossen op, en bipolaire straal-stromen ("jets") zorgen voor een afname van het impulsmoment van het systeem. Rechts-midden: De nieuwe ster en zijn circumstellaire schijf worden zichtbaar. Links-onder: Als het resterende gas verstrooid wordt hebben de reuze-planeten zich al gevormd. Rechts-onder: De schijf is volledig opgelost. Het nieuwe zonnestelsel is nu zichtbaar.

Eigenschappen van Sterren

Voordat men de structuur en de evolutie van protoplanetaire schijven en hoe deze in verband staan met de centrale ster kan onderzoeken, moet men ook de eigenschappen van de centrale ster kunnen bepalen. Sterren stralen als een zogenaamd "zwart lichaam" met een karakteristieke temperatuur die afhangt van de massa van de ster. De zwarte-lichaamstraling van zware sterren is het sterkst op ultraviolette en optische golflengten. De straling van sterren met een lagere massa is sterker op langere golflengten (optisch en nabij-infrarood). Het optimale golflengtegebied om de T-Tauri sterren, die een relatief lage massa hebben, te bestuderen is dus het optisch/nabij-infrarood.

Aan de hand van optische spectra van een verzameling van representatieve sterren waarvan de temperatuur nauwkeurig bepaald is kan men een aantal karakteristieke spectrale eigenschappen definiëren die vervolgens gebruikt kunnen worden om de temperaturen van andere, willekeurige sterren gemakkelijk te bepalen. Behalve de temperatuur, geven optische spectraalwaarnemingen ook informatie over de zwaarte-

kracht aan het oppervlak van de ster, de rotatiesnelheid, en het metaalgehalte. Deze eigenschappen zijn het beste te bestuderen met behulp van spectroscopische waarnemingen met gemiddelde tot hoge resolutie (het vermogen om kleine details in spectra van elkaar te onderscheiden). Als de afstand tot de ster bekend is, kan de helderheid van de ster rechtstreeks afgeleid worden door middel van fluxmetingen in verschillende golflengte-banden. De massa, straal en leeftijd kunnen bepaald worden aan de hand van een vergelijking met stermodellen. De afleiding van dit soort cruciale eigenschappen van sterren is het onderwerp van twee hoofdstukken in dit proefschrift.

Protoplanetaire Schijven en het Ontstaan van Planeten

De herkomst van planeten is nauw verbonden met de evolutie van de protoplanetaire schijven waaruit zij worden gevormd. Echter, de details over hoe deze schijven zich precies ontwikkelen vanuit een samenstelling van kleine stofdeeltjes en gas in de beginfase, tot complexe planeetstelsels in de eindfase, zijn nog onbekend. We zien schijven rond bijna alle jonge sterren, terwijl de meeste oudere hoofdreekssterren geen schijven meer hebben. Dit bewijst dat de schijven evolueren, ofwel door de verwijdering van hun stof en gas, ofwel door het omzetten van stof en gas in grotere lichamen (planeten, asteroiden, kometen).

Eigenschappen van de Schijven

Het materiaal waar de protoplanetaire schijf uit bestaat, staat bloot aan de straling van de centrale ster. Het stof in de schijf absorbeert een gedeelte van deze straling, en zet deze om in straling op langere golflengten. Het belangrijkste bewijs voor het bestaan van protoplanetaire schijven rond vele jonge sterren wordt - weliswaar indirect - geleverd door de waarneming van overmatige straling op infrarode en submillimeter golflengten welke niet van de ster zelf afkomstig is. Directe plaatjes van deze stofschijven kunnen met de huidige sterrenkundige observatoria alleen van de paar meest nabije schijven gemaakt worden. Het bestaan van stofschijven rond de meeste andere sterren wordt dus vaak indirect afgeleid door te zoeken naar de karakteristieke overmatige straling in het infrarood.

De aardatmosfeer absorbeert een groot deel van het licht op infrarode golflengte. Ruimteteleskopen met een grote gevoeligheid voor infrarood licht bieden uitkomst. Veel van de meetgegevens in dit proefschrift zijn dan ook gedaan met de *Spitzer Ruimteteleskoop*. Deze teleskoop is in 2003 gelanceerd en werkte met volle capaciteit tot de zomer van 2009. Hierna was de voorraad helium waarmee de teleskoop gekoeld werd uitgeput en eindigde het "cryogene" (gekoelde) gedeelte van de ruimtemissie. Tijdens dit schrijven produceert Spitzer nog steeds meetgegevens in beperkte capaciteit in de zogenaamde "warme missie". Spitzer heeft drie instrumenten aan boord. IRAC maakt opnamen op golflengten van 3.6, 4.5, 5.8 en 8 micrometer en MIPS op 24, 70 and 160 micrometer. IRS, tenslotte, doet spectraalwaarnemingen op 5–40 micrometer. Deze drie instrumenten zijn belangrijk voor het onderzoek naar protoplanetaire schijven, omdat deze verschillende golflengtegebieden bij uitstek gebruikt

kunnen worden om de verschillende onderdelen van protoplanetaire stofschijven te onderzoeken.
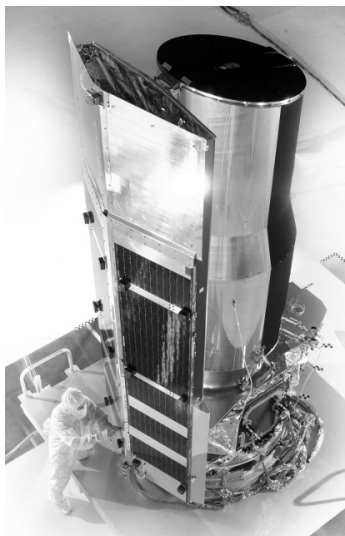
Figuur 2 – De Spitzer Ruimteteleskoop (Credit: NASA).

De emissie op korte infrarode golflengten is over het algemeen afkomstig van het warme oppervlak en de binnenrand van de stofschijf. De emissie dieper in de schijf is afkomstig van kouder stof en is de dominante stralingsbron op de langere, ver-infrarood en millimeter golflengten. Als één of meerdere van deze componenten boven- of ondergemiddeld in een stofschijf aanwezig zijn heeft dat duidelijke gevolgen voor het waargenomen spectrum. Hoe groter de overmaat aan infrarode straling, bijvoor-beeld, hoe wijder de schijf ten opzichte van het middenvlak uitloopt. Een schijf met relatief weinig gas en stof zal ook weinig overmaat aan infrarood licht laten zien. Ook leidt de aanwezigheid van openingen in de schijf tot specifieke kenmerken in het spectrum. Omdat deze openingen vertaald kunnen worden naar een gebrek aan kleine stofdeeltjes, zullen zij minder emissie op korte infrarode golflengten tot gevolg hebben. Behalve continuum straling, bevat het spectrum van een stofschijf ook een aantal specifieke kenmerken zoals veroorzaakt worden door de zogenaamde polycy-clische aromatische koolwaterstoffen (PAHs) of van silicaten (op 10 en 20 μm, dus in het golflengtebereik van de Spitzer/IRS). Deze kenmerken kunnen gebruikt wor-den om bepaalde fysische en chemische processen die van invloed zijn op het stof te bestuderen. Dit is het onderwerp van twee hoofdstukken in dit proefschrift.

Processen die van Invloed zijn op de Schijf

De evolutie van een schijf wordt bepaald door de combinatie van interne en externe processen. De centrale ster, de belangrijkste energiebron van het systeem, heeft directe invloed op de verspreiding van stof en gas in de schijf. Sterwinden kunnen massa van de schijf wegblazen. Energetische, ultraviolette en röntgen fotonen afkomstig van de centrale of een andere nabijgelegen ster, kunnen het schijfoppervlak verhitten en zo massa-verlies bewerkstelligen door de thermische druk. Dit proces, foto-evaporatie genaamd, is samen met de evolutie van de viscositeit van de schijven een efficiënt mechanisme om het materiaal waaruit de schijf bestaat verder te verspreiden. Terwijl materiaal de schijf verlaat, kan een gedeelte worden opgeslokt door de centrale ster. Het centrale gedeelte van de schijf staat namelijk sterk onder de invloed van het magneetveld van de ster, wat ervoor zorgt dat materie langs de magnetische veldlijnen vanaf de schijf naar de ster verplaatst wordt. Dit accretieproces produceert hoge temperatuur optische en UV continuum straling en heldere emissielijnen waarvan de Hα waterstoflijn de helderste is.

Behalve deze externe processen wijzen theorie, waarnemingen en laboratoriumexperimenten ook op het bestaan van processen die van invloed zijn op het stof en de structuur binnen in de schijf. Door de hoge materiedichtheid van de schijf botsen de deeltjes en klontert het stof. Naarmate de stofdeeltjes groeien, bewegen ze onder de invloed van de zwaartekracht naar het middenvlak van de schijf. Dit schept dan een omgeving met een nog hogere dichtheid, waar deeltjes makkelijker kunnen uitgroeien tot lichamen van ruwweg 1 kilometer in doorsnee: de planetesimalen. Deze processen beschrijven dus het eerste stadium van het ontstaan van planeten. Observationeel gezien komt de klontering van deeltjes in essentie overeen met het verdwijnen van de stof component. Dit wordt gekenmerkt door een afplatting van de stofschijf en een vermindering van de overmaat aan infrarood licht die zo typerend is voor de jonge stofschijven.

"Puin-schijven" bestaan uit grote planetesimale stenen en kleinere lichamen die gegroeid zijn door de vele botsingen tussen planetesimalen. Deze puin-schijven worden zowel rond geëvolueerde als rond jonge sterren gevonden. Het is aannemelijk dat deze fase volgt op die van de protoplanetaire schijf, wanneer al het gas verdwenen is.

Het Ontstaan van Planeten

Het is nog grotendeels onbekend hoe het ontwikkelingsproces van planetesimalen tot planeten verloopt. Het onderzoek naar dit vraagstuk wordt met name bemoeilijkt door het feit dat objecten met afmetingen van 10 cm tot 100 km niet direct waargenomen kunnen worden. Er zijn twee modellen die de vorming van planeten (objecten met afmetingen van duizenden kilometers) mogelijk kunnen verklaren. In het "kern-aanwas model" neemt men aan dat objecten met een grootte van een kilometer verder groeien door middel van klontering, net zoals dat voor kleine stofdeeltjes plaatsvindt. De zwaartekrachts-interactie tussen de planetesimalen leidt tot samensmeltingen en de vorming van een kern van zware elementen. Als de kern massief genoeg is trekt
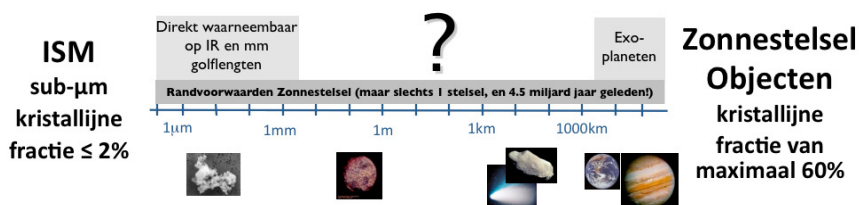
Figuur 3 − Het planeetvormingsproces, zoals dat ook in ons Zonnestelsel heeft plaatsgevonden, impliceert een enorme groei van zeer kleine, amorfe stofdeeltjes met diameters van kleiner dan een micrometer (links) tot zeer grote, planeetachtige objecten met diameters van duizenden kilometers (rechts). Hoe dit zeer complexe proces precies verloopt is onbekend.

zijn zwaartekrachtsveld grote hoeveelheden gasdeeltjes aan en zo ontstaat een gasreus. In het tweede model, het zogenaamde "schijf-instabiliteits model" daarentegen, wordt aangenomen dat de protoplanetaire schijf fragmenteert wat leidt tot een populatie van grote klonten die vervolgens ineenkrimpen en planeten vormen, analoog aan het proces van ster-vorming in moleculaire wolken. Het kern-accretie model wordt momenteel door de meeste theoreten ondersteund, maar de theorieën achter beide modellen hebben zowel goede eigenschappen als tekortkomingen. Een probleem met het kern-accretie model is dat de tijdsduur waarin de eerste kern gevormd wordt mogelijk langer is dan die waarin het gas uit de schijf verdwenen is. Een probleem met het schijf-instabiliteitsmodel is dat het mogelijk alleen werkt voor schijven die veel zwaarder zijn dan de huidige waarnemingen aangeven.

Het Zonnestelsel en Exoplaneten

Steeds vaker worden er planeten rond andere sterren gevonden. Van honderden sterren is nu bekend dat zij worden omgeven door één of meerdere planeten. Planetenstelsels beperken zich dus niet tot ons zonnestelsel alleen. De eigenschappen van al deze waargenomen planetenstelsels zijn vaak verschillend. Het is nog onbekend waar deze diversiteit vandaan komt, maar het heeft waarschijnlijk iets te maken met hun ontstaansproces. Planeten en planetenstelsels lijken een natuurlijk gevolg te zijn van de evolutie van de stofschijven. Echter, niet rond alle typen sterren leidt de stofschijf tot de vorming van planeten: de meeste hoofdreekssterren bijvoorbeeld lijken volgens de huidige waarnemingen niet te zijn omgeven door planeten of ander materiaal. Dit duidt erop dat de stofschijven rond deze sterren volledig zijn opgelost.

De baanbrekende ontdekking van de eerste planeet in omloop rond een andere ster dan de Zon (de ster 51 Peg), nu zo'n 15 jaar geleden, heeft er toe geleid dat er nu ongeveer 500 exoplaneten bekend zijn. Deze grote verzameling van exoplaneten, die men kan zien als de ultieme eindprodukten van de evolutie van de protoplanetaire schijven beschreven in dit proefschrift, bevat een enorme bron van informatie. De verdelingen van planeetmassa's en andere parameters die hun banen rond de centrale ster bepalen zijn bijvoorbeeld erg belangrijk voor het testen van modellen die het

ontstaan van planeten beschrijven.

Er is echter maar één planetenstelsel waarvan we de precieze details over de bewegingen en de samenstelling van haar leden echt goed kunnen bestuderen: ons eigen zonnestelsel. Het zonnestelsel bevat een grote hoeveelheid aan objecten die het oermateriaal waaruit het vroege zonnestelsel bestond geconserveerd hebben gedurende de laatste 4.5 miljard jaar. Analyse van de samenstellingen en mineralogische eigenschappen van deze chondritische meteorieten, interplanetaire stofdeeltjes, en kometen wijst op bepaalde fysische en chemische processen die van groot belang waren gedurende de eerste fase van de evolutie van de protoplanetaire schijf. Het onderzoek naar deze eerste fase van de evolutie, die samenhangt met de fase waarin de planeten nog volop in ontwikkeling waren, is een cruciaal onderzoeksterrein binnen de sterrenkunde en het onderwerp van Hoofdstuk 6 van dit proefschrift.

De Diversiteit van Protoplanetaire Schijven en hun Evolutie

De lancering van de Spitzer Ruimteteleskoop was een belangrijke mijlpaal in de studie van (proto-)stellaire schijven. Alhoewel dit soort objecten al eerder waren bestudeerd met onder andere de ISO telescoop, heeft de gevoeligheid en snelheid waarmee Spitzer zijn metingen uitvoert het mogelijk gemaakt om grote aantallen schijven nauwkeurig te analyseren. Gecombineerd met nieuwe waarnemingen op ultraviolette, visuele en submillimeter golflengten heeft dit ertoe geleid dat een groot aantal nieuwe soorten schijven in verschillende stadia van hun evolutie konden worden ontdekt en bestudeerd.

Voordat het Spitzer project begon, was onze kennis over de stofschijven vrij beperkt en gebaseerd op relatief kleine aantallen objecten. De modellen die beschrijven hoe de evolutie van stofschijf tot planeten tot stand komt waren dan ook veelal gebaseerd op de aanname dat de eigenschappen van de helderste (en dus de makkelijkst waarneembare) schijven representatief zijn voor de gehele schijfpopulatie. Ook werden gegevens over ons eigen zonnestelsel gebruikt, als mede het empirische bewijs dat stofschijven verdwenen zijn rond sterren met leeftijden van een paar miljoen jaar. Het algemene beeld van de evolutie van de stofschijven was dan ook dat de schijven gestaag evolueren doordat het schijfmateriaal naar de ster toe valt, doordat het oplost ten gevolge van het stralingsveld van de ster, of door het samenklonteren van steeds grotere stofdeeltjes.

Het ontstaan van reuze-planeten wordt voor een belangrijk deel bepaald door de leeftijd van het gasvormige gedeelte van de schijf. Dit gas is moeilijk waarneembaar, maar kan toch indirect bestudeerd worden omdat het vaak samengaat met kleine stofdeeltjes die makkelijker waarneembaar zijn. De levensduur van de schijf wordt vaak afgeleid uit de overmaat aan infrarood licht. Het referentiepunt dat gebruikt wordt om te bepalen in welke fase van evolutie een bepaalde stellaire schijf zich bevindt is de leeftijd van de ster. Verschillende onderzoeken hebben laten zien dat de fractie van sterren met een stofschijf afneemt naar mate de gemiddelde leeftijd van een groep sterren hoger wordt. Dit betekent dat de leeftijd van de ster dus een belangrijke

parameter is. Na 6 tot 8 miljoen jaar hebben minder dan 10% van de sterren nog een stofschijf. Tijd is echter niet de enige parameter waar de evolutie van de schijf door bepaald wordt. In zowel jonge (rond de 1 miljoen jaar) als in oude groepen (rond de 7 miljoen jaar) bestaat er een grote diversiteit aan de overmaat van infrarood licht wat samenhangt met de aanwezigheid van verschillende hoeveelheden stof. Het is niet precies duidelijk waarom sommige schijven na 1 of 2 miljoen jaar verdwenen zijn, terwijl andere wel tot 10 miljoen jaar kunnen bestaan.

Mogelijk zijn vele andere factoren belangrijk voor het evolutieproces van protoplanetaire stofschijven. Zo is het bijvoorbeeld bekend dat de leeftijden van schijven afhangen van de massa van de centrale ster; mogelijk hangt dit samen met een snellere verspreiding van het stof in de schijven rond zwaardere sterren. Jonge sterren vertonen een grote variatie in oppervlaktetemperatuur, helderheid en massa's. Omdat gedurende de protoplanetaire fase de schijven en sterren nauw met elkaar verbonden zijn, is het goed mogelijk dat de variatie in deze stereigenschappen zich ook in de eigenschappen van hun omringende materie weerspiegelt. Het is echter nog niet bekend welke processen precies verantwoordelijk zijn voor de tijdsduur waarop protoplanetaire schijven verdwijnen.

Protoplanetaire schijven - de kraamkamers van planeten - bieden een buitengewone kans om het proces van planeetvorming te onderzoeken. Om de verschillende factoren die bijdragen aan dit proces vast te stellen, zijn systematische studies van grote aantallen protoplanetaire schijven nodig. We weten inmiddels dat het evolutieproces heel verschillend kan verlopen voor verschillende protoplanetaire schijven. Het is echter nog steeds een mysterie welke verschillende paden mogelijk zijn en door wat die bepaald worden.

Dit Proefschrift

Dit proefschrift beschrijft een representatief onderzoek naar jonge, lage-massa sterren en hun stofschijven in een aantal nabijgelegen stervormingsgebieden. Dit onderzoek is gedaan met optische en infrarode telescopen, waarmee de evolutie van het stof in proto-planetaire schijven nauwkeurig onderzocht kan worden. Het volledige sterschijf systeem wordt onderzocht: de eigenschappen van de sterren en hun invloed op de evolutie van de schijven, en de veranderingen die het stof ondergaat. Het onderzoek is gebaseerd op statistisch relevante samples. De indeling van dit proefschrift is als volgt:

Hoofdstuk 2 – In dit hoofdstuk wordt een optisch, spectroscopisch onderzoek gepresenteerd teneinde de eigenschappen te bepalen van de nieuwe populatie jonge sterren die ontdekt is in de moleculaire wolk "Serpens". De spectraaltypen, en dus de effectieve temperaturen, worden bepaald aan de hand van de sterspectra. Vervolgens worden deze gecombineerd met optische en infrarode fotometrische waarnemingen en wordt de absolute helderheid van de sterren (en dus hun positie in het Hertzsprung-Russell diagram) bepaald. De verontreiniging van het sample door achtergrond-objecten (sterren en sterrenstelsels) is vrij hoog (25%), wat aantoont dat

men voorzichtig moet zijn met het selekteren van jonge stellaire objecten (YSOs) op grond van infrarood kleuren in wolken op lage galactische breedte. Met behulp van sterevolutie-modellen worden leeftijden gevonden voor de sterren in de wolk van 2 tot 6 miljoen jaar en massa's van 0.2 tot 1.2 keer de massa van de Zon (onder de aanname dat de Serpens wolk op een afstand van 259 parsec staat). Uit metingen van de Hα spectraallijn wordt verder afgeleid hoeveel materie er per jaar vanaf de schijf naar de ster toe stroomt. De resultaten laten zien dat dit in meer dan de helft van de sterren een substantiële hoeveelheid is.

Hoofdstuk 3 – In dit Hoofdstuk brengen we, in navolging van Hoofdstuk 2, verslag uit van een optische spectroskopische studie in de "Lupus" wolken. Van een sample van jonge stellaire objecten worden de spectraaltypen bepaald. De sample bestaat voor ongeveer 90% uit relatief koele, laat-type M sterren. Met behulp van sterevolutie-modellen wordt een gemiddelde leeftijd gevonden van 2 miljoen jaar en een massa van slechts 0.2 zonsmassa's. De Hα lijn geeft snelheden voor de materie-aanwas die karakteristiek zijn voor T Tauri sterren.

Hoofdstuk 4 – Dit Hoofdstuk beschrijft een omvangrijke studie naar een groot, representatief sample van spectra van jonge sterren in Serpens, waargenomen met de Spitzer IRS. De spectra worden geclassificeerd. In overeenstemming met het resultaat van Hoofdstuk 2 wordt aangetoond dat de achtergrondpopulatie bestaat uit sterren op een onbepaalde afstand achter de wolk, veel verder weg gelegen sterrenstelsels (te herkennen aan roodverschoven PAHs in hun spectra), en een ongeïdentificeerd object met spectraallijnen met een hoge ionisatie-graad. De verzameling van bona fide jonge stellaire objecten omvat 115 objecten, waarvan 18% uit objecten met een omhulsel ("klasse 1" objecten) en 82% uit schijven bestaat ("klasse 2" en "klasse 3" objecten"). De geometrie van de binnenschijf wordt bepaald op grond van de verhouding van de intensiteit gemeten op 30 en 13 μm. Omdat de silicaatstructuren op 10 en 20 μm sterk afhankelijk zijn van de afmeting van de stofdeeltjes door welke ze geproduceerd worden, gebruiken we deze banden om de typische afmetingen te schatten. We vinden een populatie van kleine stofkorrels aan het oppervlak van de schijven, die niet afhangt van de geometrie van de binnenschijf, of van het feit of de schijven voorkomen in sterren in een geclusterde of in een geïsoleerde omgeving. De resultaten gevonden voor Serpens worden vergeleken met die voor de jonge populatie in de veelbestudeerde Taurus wolk, en met het gehele c2d IRS sample bestaande uit jonge stellaire objecten verspreid over de hele hemel. Ondanks het feit dat deze twee andere populaties andere karakteristieke leeftijden en ster-vormingsomgevingen peilen, zijn de resultaten hetzelfde als gevonden voor Serpens. Dit toont aan dat de stofpopulatie aan het schijfoppervlak tot stand komt door een evenwicht tussen de groei en de fragmentatie van stofdeeltjes, onafhankelijk van hun omgeving. Dit evenwicht wordt in stand gehouden zolang de schijven ondoorzichtig zijn op optische en infrarode golflengten.

Hoofdstuk 5 – Hier wordt het hoge-ionisatie achtergrondobject OL17 dat werd ontdekt in Hoofdstuk 4 nader bestudeerd. We gebruiken de Very Large Telescope met de nieuwe X-shooter spectrograaf om nieuwe spectra te verkrijgen. De drie kanalen

van de X-shooter in het ultraviolet-blauw, optisch, en nabij-infrarood bestrijken vele emissielijnen die gebruikt worden om de eigenschappen van het object te onderzoeken. Smalle emissielijnen en lage verhoudingen van [N II]/Hα en [S II]/Hα tonen aan dat OL17 een nieuw ontdekte, stofrijke, planetaire nevel is.

Hoofdstuk 6 – Dit Hoofdstuk beschrijft details over de mineralogie van stofkorrels aan het oppervlak van stofschijven in vier clusters. Deze vier clusters zijn de jonge Serpens en Taurus wolken die het onderwerp waren van Hoofdstuk 4, en de "Upper Scorpius" en "η Chamaeleontis" clusters die door hun hogere leeftijd een latere fase in de evolutie van stofschijven representeren. De analyse is voor alle vier de wolken op dezelfde manier uitgevoerd zodat de resultaten goed te vergelijken zijn. In alle vier gebieden zijn de verdelingen die de afmetingen en mate van kristalliniteit van de stofkorrels beschrijven nagenoeg hetzelfde, terwijl de gemiddelde leeftijd en het aantal sterren met een stofschijf van wolk tot wolk verschillen. Dit betekent dat er een snelle fase in de evolutie plaatsvindt van rond de 1 miljoen jaar of minder waarna een evenwicht in deze eigenschappen bereikt wordt totdat de schijf oplost.

Hoofdstuk 7 – In dit Hoofdstuk gebruiken we de eigenschappen van de sterren en schijven afgeleid in de voorgaande Hoofdstukken om de spectrale energieverdeling (SED) van jonge sterren met schijven in Serpens te bepalen. Deze SEDs maken het mogelijk om de straling afkomstig van de ster en de schijf nauwkeurig van elkaar te onderscheiden. Samen met de meest recente afstandsbepaling voor Serpens (415 pc) vinden we dat de karakteristieke leeftijden rond de 1 tot 3 miljoen jaar liggen. De verdelingen van de fracties van de helderheid die afkomstig is van de schijf (verge-leken met de totale helderheid afkomstig van de ster én de schijf) zijn vergelijkbaar voor Serpens en Taurus. Ook zijn de meeste schijven consistent met het scenario van passieve bestraling. In tegenstelling tot de meer massieve Herbig Ae/Be sterren wordt geen aanmerkelijk verschil gevonden tussen de fractionele schijfhelderheden in brede en platte schijven rond T Tauri sterren. Tenslotte vinden we dat in onze grote sample, de mineralogische eigenschappen van het stof aan het schijfoppervlak niet direct gecorreleerd zijn aan de eigenschappen van de sterren òf die van de schijven.

Conclusies

Elk hoofdstuk wordt afgesloten met een reeks conclusies gebaseerd op de bestudeerde data. De belangrijkste van de conclusies uit dit proefschrift zijn:

- Serpens en Lupus zijn allebei jonge stervormings-gebieden met een mediane leeftijd rond de anderhalf tot drie miljoen jaar (onder de aanname dat de afstand tot Serpens 415 in plaats van 259 parsec is). Alhoewel de verdelingen van de leeftijden van de sterren in deze twee wolken vergelijkbaar zijn, geldt dat niet voor hun massa's. De sterren in Serpens bestaan uit G-, K-, en M-type sterren en de massa's liggen tussen 0.2 en 1.2 zonsmassa's, met een mediaan rond de 0.8 zonsmassa's. Deze verdeling is vergelijkbaar met die van Taurus. Lupus bestaat echter bijna in het geheel uit lage massa M-type sterren, met een gemiddelde massa rond de 0.2 zonsmassa's. Deze verdeling is vergelijkbaar met die gezien

in de jonge stervormings-gebieden Chamaeleon 1 en IC 348. Het verschil in de massa-verdelingen in deze diverse gebieden wijst mogelijk op een kleine variatie in de (over het algemeen genomen universele) functie die de beginmassa's van nieuwe sterren beschrijft (de "IMF").

- Voor zowel jonge clusters met een leeftijd van rond de 1 miljoen jaar, als voor oude clusters met een leeftijd van rond de 7–8 miljoen jaar, is de verdeling van afmetingen van de stofdeeltjes aan het schijfoppervlak statistisch gezien gelijkwaardig. Dit betekent dat het stof ook onderheving is aan een destructief botsingsproces, behalve groei door klontering. Het evenwicht tussen deze twee processen kan alleen verklaard worden als zij gedurende miljoenen jaren in stand wordt gehouden tot het moment waarop de schijf verdwenen is.

- De mineralogische samenstelling van het stof is gemiddeld genomen hetzelfde in alle gebieden. De kristallijne fractie is vrij hoog (ongeveer 10 tot 20%) en wordt vrij vroeg bepaald aan het schijfoppervlak, binnen ongeveer 1 miljoen jaar. Een evenwicht wordt bereikt onafhankelijk van wat er gebeurt in het middenvlak van de schijf, waar de planeten mogelijk gevormd worden.

Resumo em Português

Restrições Observacionais
na Evolução da Poeira
em Discos Protoplanetários

De acordo com dados do telescópio WMAP (Sonda Wilkinson de Anisotropia no Microondas, na sigla em inglês), o universo veio a existir aproximadamente 13.7 bilhões de anos atrás. A cosmologia moderna sugere que o universo permaneceu um lugar escuro grande parte de seus primeiros bilhões de anos, a "era opaca". Durante este tempo, o universo consistia de matéria escura, assim como nuvens de gás hidrogênio neutro e pouco mais. As primeiras estrelas não se formaram até centenas de milhões de anos se passarem. No entanto, uma vez que a máquina cósmica de fazer estrelas se iniciou, agitou bolas gigantes de gás em muitas estrelas, que formaram as primeiras galáxias. É estimado que o universo contenha 10^{21} (isto é, um sextilhão) estrelas. Formação estelar é o principal mecanismo que controla a estrutura visível das galáxias, e a formação de elementos pesados no universo com o tempo. Originalmente, os únicos elementos eram hidrogênio, hélio e traços de lítio, berílio e bóron. Elementos mais pesados não existiam ainda.

Estrelas nascem, evoluem, envelhecem, e eventualmente morrem. Em termos simples, elas nascem do colapso de uma nuvem molecular, e podem evoluir diferentemente durante sua vida, dependendo de suas massas. Durante sua evolução, uma estrela queima elementos leves em elementos mais pesados através de fusão nuclear, então produzindo a energia necessária para balancear a pressão gravitacional e manter-se viva. Durante o curso de sua evolução, estrelas mudam de massa (através de acreção ou perda de massa), de tamanho (expansão ou contração) e de luminosidade (por mudanças de reações termonucleares em seus núcleos). Estrelas podem ser sozinhas e isoladas ou, muito comumente, viver em sistemas multíplos. Quando a estrela esgota seu combustível nuclear, sua pressão de radiação já não pode equilibrar sua gravidade, iniciando uma cadeia de processos irreversíveis que eventualmente conduzem à sua morte. Estrelas de baixa massa ejetam seus envelopes gasosos e tornam-se visíveis as nebulosas planetárias, enquanto estrelas massivas explodem como supernovas. Elementos pesados recém sintetizados (incluindo Si, O, C, Mg and Fe, que compõem as partículas de poeira das quais planetas eventualmente podem formar-se) são portanto lançadas ao espaço, onde se misturarão com o meio interestelar (MI). Este MI enriquecido posteriormente fornece material para as próximas gerações de es-

trelas, eventualmente levando à criação de sistemas planetários onde vida no universo tornou-se possível.

Na nossa Via Láctea, uma teoria bastante popular sugere que a explosão de uma supernova provocou a formação do nosso Sol e seu disco protoplanetário, cerca de 4.6 bilhões de anos atrás. Oito planetas (Mercúrio, Vênus, Terra, Marte, Júpiter, Saturno, Urano e Netuno) e incontáveis objetos menores (como planetas anões, cometas e asteróides) foram formados a partir do material nesta névoa pré-solar.

Esta tese se concentra na interação entre a estrela jovem e seu disco protoplanetário, na evolução das partículas de poeira que compõem o disco protoplanetário ao redor da estrela jovem e, portanto, nos primeiros estágios da formação de planetas como os que compõem nosso próprio Sistema Solar.

Formação de Estrelas de Baixa Massa

O tipo mais comum de objectos estelares são estrelas de baixa massa ($\sim0.5\ M_\odot$), que dominam em número e massa total. Estrelas de baixa massa formam-se dentro de concentrações relativamente densas de gás e poeira interestelar conhecidas como nuvens moleculares, com a poeira compondo ~1 % da massa da nuvem. Acredita-se que esta poeira seja muito pequena em tamanho (menos de 1 micrômetro) e composta de grãos à base de carbono e silicato, quase completamente amorfos. Essas regiões mais densas são opacas à luz visível devido à sua alta extinção, porém translúcidas a comprimentos de onda maiores (por exemplo, infravermelho).

A formação estelar inicia-se quando uma região na nuvem esfria-se e atinge uma densidade de matéria suficientemente alta, começando a desmoronar sob sua própria gravidade. Energia gravitacional é transformada em energia cinética durante a queda, acelerando partículas de gás que se agitam, aumentando então a temperatura da estrela que se forma, e suas imediações. Como resultado, pressão térmica se acumula, o que serve de suporte à estrutura da nuvem, evitando adicionais contrações. Finalmente, o fragmento de nuvem colapsa em um núcleo central rodeado por um disco rotativo de material, ambos envoltos por um envelope gasoso que ainda está contraindo em direção ao centro. Com tempo o envelope se dissipa, tornando a estrela e seu disco visíveis em comprimentos de onda ópticos. Esta fase é conhecida como a fase "T Tauri". Porque estrelas e discos estão conectados, eles evoluem juntos e vão afetar um ao outro.

Propriedades Estelares

Para estudar a estrutura e evolução de discos protoplanetários, e como estes se conectam à estrela central, é de maior importância ser capaz de determinar propriedades estelares. Uma estrela de determinada temperatura emite radiação aproximadamente como um corpo negro de mesma temperatura. Radiação emitida por estrelas massivas é máxima em comprimentos de onda mais curtos (ultra-violeta/visível) que a radiação emitida por estrelas de baixa massa (visível/infravermelho próximo). Con-
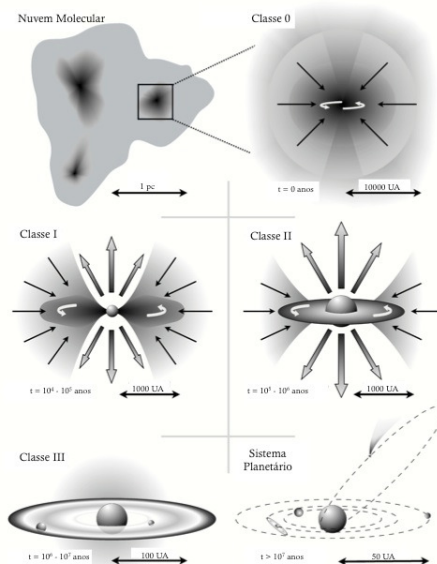
Figura 1 – Ilustração do cenário para a formação de estrelas de baixa massa. A formação de núcleos densos em nuvens moleculares é ilustrada no painel superior esquerdo, enquanto o painel superior direito mostra o colapso do núcleo sob a influência de sua própria gravidade. Ao mesmo tempo que o envelope começa a dissipar-se, a estrela em formação ejeta material por seus pólos removendo momento angular (painel central esquerdo), até que a recém-formada estrela e seus disco protoplanetário tornam-se visíveis (painel central direito). Enquanto o gás que compõe o disco se dissipa, planeta gigantes gasosos, como Júpiter e Saturno, já devem ter se formado (painel inferior esquerdo). No momento em que o disco inteiro se dissipou, o possível sistema planetário ao redor desta estrela deve ter se formado completamente (painel inferior direito).

sequentemente, o regime visível/infravermelho próximo é a faixa de comprimento de onda ideal para observar estrelas de baixa massa, do tipo T Tauri.

Ao estudar os espectros ópticos de estrelas de diferentes temperaturas é possível identificar bandas espectrais que são sensíveis à temperatura da estrelas. A presença ou absência destas bandas é utilizada para determinar a temperatura efetiva de uma estrela. Além da temperatura, a análise do espectro óptico de uma estrela também permite a determinação de sua gravidade superficial, sua velocidade de rotação, e sua metalicidade (isto é, sua composição química). Essas quantidades, no entanto, são determinadas com exatidão apenas com espectros de média e alta resolução, enquanto temperaturas são facilmente derivadas de espectros de baixa resolução. Se a distância à estrela é conhecida, sua luminosidade pode ser obtida diretamente através de medições de fluxo em differentes comprimentos de onda. A massa, o raio e a idade de uma estrela podem ser estimadas com base em modelos de evolução estelar. A derivação de parâmetros estelares é o tema de dois capítulos desta tese.

Discos Protoplanetários e Formação de Planetas

A origem de planetas está naturalmente ligada à evolução dos discos protoplanetários a partir dos quais os planetas se formam. No entanto, os detalhes de como exatamente os discos evoluem, a partir de sua composição inicial de pequenos grãos de poeira acoplados ao gás em sistemas planetários complexos, ainda não são compreendidos. Embora praticamente todas as estrelas jovens possuam discos protoplanetários, a maioria das estrelas mais velhas (que estão na sequência principal) não mostram nenhum sinal de estarem rodeadas por discos. Esta restrição implica que os discos devem evoluir, seja pela dispersão da poeira e do gás, seja pela construção de corpos maiores como planetas.

Propriedades de Discos

O material sólido que compõe um disco protoplanetário é exposto à radiação da estrela no centro do disco. A poeira, além de absorver parte da radiação, também re-processa e re-emite parte dela. Na verdade, a principal indicação observacional da existência de discos protoplanetários é a observação de um excesso de radiação (emitida pela poeira no disco) que não poderia ser atribuídos à estrela somente. Fazendo uso dos telescópios disponíveis hoje, só é possível observar diretamente (obter uma imagem) os discos ao redor de estrelas bem próximas. Portanto, a existência de discos é frequentemente inferida indiretamente a partir da existência de um excesso de radiação infravermelha (grão pequenos de poeira como os que compõe discos protoplanetários emitem mais eficientemente no infravermelho) em uma estrela.

A atmosfera terrestre absorve a maior parte da luz no regime infravermelho (felizmente para nós humanos), e então observações neste regime são quase impossíveis para telescópios na Terra. Por esta razão, muito esforço foi colocado no lançamento de telescópios espaciais no regime infravermelho. A grande maioria dos dados apresentados nesta tese foram obtidos utilizando o *Telescópio Espacial Spitzer*. *Spitzer* foi lançado em 2003 e operou em plena capacidade até o meio de 2009, quando sua missão criogênica (isto é, em baixa temperatura) terminou. Ao gastar todo o gás de hélio que mantinha o telescópio refrigerado, *Spitzer* continua a produzir dados em sua "missão morna", embora somente em dois filtros. Originalmente, o telescópio é composto de três instrumentos: duas câmaras de imagem, IRAC (com 4 filtros) e MIPS (com 3 filtros), e um espectrógrafo, IRS. Os comprimentos de onda no infravermelho em que *Spitzer* observa são utilizados para investigar regiões distintas dos discos protoplanetários, dando indicações da estrutura e composição dos discos desde bastante perto da estrela, até aproximadamente metade de sua extensão. Para obter informação sobre as regiões do disco mais distantes da estrela central é preciso estudá-los em comprimento de ondas ainda mais longos (milímetro e radio).

A morna superfície do disco e o aro interior (que interceptam a radiação estelar diretamente) são responsáveis pela emissão de radiação nos comprimentos de onda mais curtos do infravermelho. As camadas mais profundas (uma população mais fria por não interceptar radiação estelar diretamente) emitem radiação mais eficientemente em
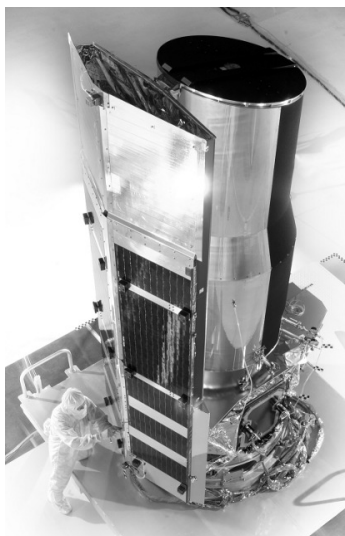
Figura 2 – O Telescópio Espacial Spitzer, antes de seu lançamento (crédito: NASA).

comprimentos de onda mais longos. A partir desta compreensão básica, torna-se claro quais seriam os resultados de suprimir ou aumentar qualquer um desses componentes. Por exemplo, um disco composto de muita poeira em toda sua extensão vai emitir muito excesso de radiação. Um disco empobrecido de poeira e gás (que foi acrescido à estrela, foi expelido por sua radiação, ou coagulou para formar corpos maiores) vai apresentar pouco ou nenhum excesso de radiação sobre a radiação estelar. Além disso, a presença de um buraco no disco produz uma assinatura bastante peculiar na radiação emitida pelo sistema (estrela + disco), por não apresentar a radiação que seria emitida pela poeira que não está presente no buraco. Ademais, a poeira emite bandas epsecíficas no infravermelho como hidrocarbonetos policíclicos aromáticos (HAPs) e silicatos (centrados em 10 e 20 μm). Esses silicatos são bastante proeminentes e são usados em dois capítulos desta tese para investigar os processos químicos e físicos que afetam a poeira nas camadas superficiais do disco.

- **Processos que Afetam Discos**

A evolução de discos protoplanetários é uma combinação de fatores externos e internos. Sendo a principal fonte de radiação do sistema, a estrela central afeta a dispersão do disco diretamente. Ventos estelares podem varrer e remover parte do material do disco. Além disso, os fótons de raios ultra-violeta e raios-X emitidos pela estrela central (ou por uma estrela massiva nas proximidades) esquentam a superfície do disco e podem causar uma pressão térmica que pode remover massa do disco. Esse processo é chamado *fotoevaporação* e, em combinação com a evolução viscosa do disco, tem sido demonstrado ser um mecanismo muito eficaz para a dispersão de

discos. Ao mesmo tempo em que material é expelido do disco, acreção de material do disco para a estrela continua. A parte interna do disco é interrompida pelo campo magnético da estrela, resultando em acreção através da magnetosfera estelar, na qual material do disco é canalizado ao longo das linhas do campo magnético para dentro da estrela. Esse transporte de material produz excesso de emissão de contínuo nos regimes óptico e ultra-violeta e intensas linhas de emissão, a mais forte delas é Hα.

Além dos processos externos descritos acima, estudos teóricos, observacionais e laboratoriais apontam para processos que afetam a poeira dentro dos discos e, consequentemente, também a estrutura do disco. A alta densidade do disco facilita colisões entre partículas de poeira, que podem coagular em partículas maiores. À medida que as partículas crescem, gravidade as puxa em direção ao plano médio do disco, tornando-o um ambiente ainda mais denso e, portanto, mais propenso a um maior crescimento das partículas em corpos de tamanhos de até alguns kilometros. Esses corpos são chamados *planetesimais*. Essas etapas são os estágios iniciais da formação de um planeta. Observacionalmente, coagulação de partículas é equivalente à remoção do componente 'poeira', manifestando-se como um achatamento do disco e uma diminuição do excesso de radiação infravermelha de um disco.

Discos de detritos (debris em inglês), compostos por planetesimais, grandes rochas e uma população de poeira que é produzida por colisões de planetesimais, têm sido encontrados ao redor de estrelas jovens e evoluídas. É entendido que esta fase siga a fase de disco protoplanetário, quando o gás não está mais presente.
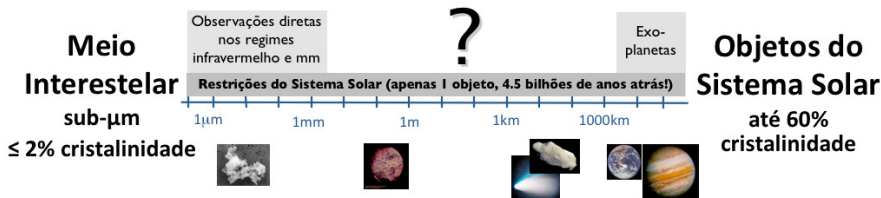

Figura 3 – O processo de formação planetária significa uma imensa modificação da matéria: de pequena e amorfa poeira (esquerda) a objetos que compõe um sistema planetário como o Sistema Solar, milhares de kilometros em diâmetro e extremamente complexos (direita).

Formação Planetária

O crescimento além de planetesimais para formar planetas ainda não é bem entendido. Para tornar as coisas ainda mais complicadas, objetos com tamanhos entre centímetro e alguns milhares de metros em diâmetro não podem ser observados diretamente. Dois modelos diferentes foram introduzidos na literatura para explicar a formação de planetas (milhares de kilometros em diâmetro). O modelo de *acreção de núcleo* sugere que o crescimento para diâmetros acima de kilometro acontece de maneira semelhante a como a coagulação funciona para partículas pequenas. Planetesimais

interagem gravitacionalmente, aglutinando-se para formar um núcleo de elementos pesados (como o núcleo da Terra). Uma vez que esse núcleo é grande e massivo o suficiente, seu campo gravitacional captura gás presente no disco protoplanetário para formar um planeta gigante gasoso (como Júpiter). Alternativamente, o modelo de *instabilidade do disco* sugere que partes mais densas se formam pela fragmentação do disco. Estes aglomerados contraem-se gravitacionalmente para formar planetas, da mesma maneira que estrelas se formam pelo colapso de um núcleo denso numa nuvem molecular (como descrito na ágina 204). Embora o modelo de acreção de núcleo seja favorecido pela maioria dos teóricos, ambos os modelos tem vantagens e problemas. Simulações de formação de planetas e observações ainda não são suficientes para determinar extamente como planetas se formam.

O Sistema Solar e Exo-planetas

Observações de um número crescente de estrelas têm demonstrado que o Sistema Solar não é único, e que planetas e sistemas planetários vêm em uma variedade de formas. A origem desta variedade ainda é incerta, mas deve estar ligada ao processo de formação destes sistemas. Planetas e sistemas planetários parecem ser um resultado bastante comum da evolução de discos, uma vez que planetas já foram observados ao redor de centenas de estrelas além do Sol. A formação de planetas, no entanto, não parece ser o único resultado da evolução do disco. A maioria das estrelas mais evoluídas não mostram sinais de serem rodeadas por planetas ou corpos menores, dentro das atuais limitações observacionais. Isso significa que os discos ao redor dessas estrelas quando elas eram jovens se dissiparam completamente, sem deixar nem uma poeirinha para contar a estória.

Desde a descoberta do primeiro planeta ao redor de uma estrela além do Sol, a estrela *51 Peg*, cerca de 15 anos atrás, os aproximadamente 500 exo-planetas (planetas fora do Sistema Solar) já descobertos formam um poderoso banco de dados desse possível produto final da evolução de discos protoplanetários. A distribuição de massas desses planetas, além de suas posições em relação às suas estrelas centrais oferecem restrições observacionais adicionais para os modelos de formação planetária.

Adicionalmente, apenas um sistema planetário (o nosso próprio Sistema Solar) pode ser estudade ao nível de detalhe necessário para fornecer informações confiáveis sobra a dinâmica e a composição de seus constituintes. Notavelmente, nosso Sistema Solar contém uma coleção de objetos que preservaram de forma praticamente inalterada o material que compôs o Sistema Solar primitivo mais de 4.5 bilhões de anos atrás. Análises de meteoritos e partículas de poeira interplanetária, assim como observações de cometas, revelaram sua estrutura e mineralogia, apontando para importantes processos físicos e químicos que ocorreram durante a evolução inicial do disco protoplanetário em torno do jovem Sol. A procura por pistas sobre como e quando tais alterações ocorrem na fase inicial de discos protoplanetários, quando os planetas ainda estão se formando, é um campo de pesquisa muito ativo, e assunto do capítulo 6 desta tese.

Diversidade e Evolução de Discos

O lançamento do telescópio *Spitzer* representou um passo importante no estudo de discos protoplanetários. Embora muitos discos tenham sido observados com sucesso por telescópios terrestres e espacias (por exemplo, o *Observatório Espacial no Infravermelho*, ISO na sigla em inglês), a sensibilidade para detectar objetos pouco brilhantes e a capacidade de mapear muitos objetos do telescópio *Spitzer* permitiu a observação de um número extremamente grande de sistemas. Graças às amostras de discos estatisticamente relevantes observadas por *Spitzer* (complementadas por dados em outros regimes como ultra-violeta e óptico), uma variedade até então desconhecida de estruturas e tempo de vida de discos foi revelada.

Antes de *Spitzer*, a compreensão global da evolução de discos era bastante baseada em evidências de um pequeno número de objetos. Assim, os modelos de evolução de discos e de formação planetária eram derivados de: i) extrapolação das características dos discos mais brilhantes como universais; ii) evidência do nosso Sistema Solar, e da 'névoa solar' a partir do qual se originou; iii) evidências observacionais de que discos se dissipam em alguns milhões de anos. A visão pré-*Spitzer* dominante era de que discos evoluíam constantemente com o tempo, com material caindo em direção à estrela, sendo dissipado pela radiação estelar ou coagulando em partículas maiores e maiores, que são atraídas gravitacionalmente para o plano médio do disco.

Um dos parâmetros mais importantes para a formação de planetas gigantes é o tempo de vida do disco gasoso. No entanto, como poeira pequena se acopla bem ao gás (como minúsculas partículas de tabaco se acoplam bem à fumaça do cigarro) e uma vez que a poeira é muito mais fácil de ser observada, o tempo de vida do disco geralmente se refere ao tempo em que se observa uma estrela possuir excesso de radiação no infravermelho (atribuído à presença de poeira). O relógio de discos é a idade da estrela central, uma vez que estrelas e discos nasceram juntos. Utilizando a idade média de um bando de estrelas e medindo o excesso de radiação infravermelha das estrelas do bando, diversos cientistas mostraram que a fração de estrelas rodeadas por discos diminui progressivamente com a idade média, concuindo que o tempo é um parâmetro essencial na evolução de discos: em 6 – 8 milhões de anos menos de 10% das estrelas ainda possuem discos em um certo bando. Embora este fato apresente o tempo como um parâmetro importante, ele não é o único. Dentro um bando de determindade idade (seja um bando jovem, de 1 milhão de anos, ou um bando velho, de 7 milhões de anos), uma grande diversidade em excesso de radiação infravermelha (e portanto de quantidade de poeira ainda presente no disco) é observado. Ainda não está claro porque alguns discos se dissipam completamente em 1 ou 2 milhões de anos, enquato outros podem viver até 10 milhões de anos.

Têm sido sugerido que muitos outros parâmetros podem desempenhar um papel importante na evolução de discos. Por exemplo, há evidências de tempos de vida diferentes para estrelas de diferentes massas (com mais rápida dispersão de discos ao redor de estrelas massivas). Uma diversidade de temperaturas, luminosidades e massas estelares é conhecida e estudada há décadas. De fato, uma vez que estrelas

e discos são conectados, é bastante improvável que diferenças nas fontes centrais não sejam refletidas na matéria que as envolve. No entanto, até hoje nenhuma forte evidência foi encontrada a respeito de que processos são determinantes na definição da escala de tempo em que um disco vai se dissipar.

Como o local de nascimento de planetas, os discos protoplanetários ricos em gás têm o potencial para responder muitas das questões relacionadas com a formação planetária. Amostragens estatísticas de discos protplanetários são necessários para identificar as condições ambientais e inciais dos discos, bem como os principais processos que afetam a evolução da poeira e controlam o resultado da evolução de discos. Tornou-se claro que nem todos os discos evoluem da mesma maneira, porém quais caminhos diferentes são possíveis, e por que, ainda é um mistério.

Esta Tese

Esta tese apresenta estudos imparciais de estrelas jovens de baixa massa e seus discos de poeira nas regiões de formação estelar mais próximas, usando telescópios nos regimes óptico e infravermelho para investigar a evolução da poeira em discos protoplanetários. A tese aborda o sistema estrela-disco completo: as características estelares e seus efeitos sobre a evolução, bem como as mudanças que ocorrem na poeira, fazendo uso de amostras estatisticamente relevantes. A estrutura desta tese é a seguinte:

Capítulo 2 – Neste capítulo um levantamento esprectroscópico óptico concebido para caracterizar a nova população estelar jovem descoberta na Nuvem Molecular Serpens é apresentado. Tipos espectrais, e portanto temperaturas efetivas, são derivados dos espectros. Combinando com fotometria óptica e infravermelha, luminosidades estelares são calculadas, o que permite a colocação destas estrelas no diagrama H-R. Uma alta contaminncação (25%) de objetos de fundo (estrelas e galáxias) é encontrada, elevando o cuidado ao usar cores infravermelhas para identificar objetos estelares jovens em nuvens de baixa latitude. Auxiliado por modelos de evolução estelar, idades na faixa de 2 – 6 milhões de anos e massas de 0.2 – 1.2 massas solares são inferidos para as estrelas pertencentes à nuvem, se a distância de 259 pc é considerada. Além disso, as taxas de acreção de massa em direção às estrelas são estimadas a partir da largura a 10% da intensidade do pico da linha de emissão Hα, mostrando que um pouco mais da metade da amostra (57%) mostra acreção ativa.

Capítulo 3 – Aqui nós relatamos um programa de epsectroscopia óptica semelhante ao do capítulo 2, mas realizado nas Nuvens Lúpus. Uma amostra de estrelas jovens previamente selecionadas é investigada, e tipos espectrais são determinados. A amostra é constituída principalmente de estrelas mais frias, de tipo M (90%). De acordo com modelos evolucionários teóricos sobrepostos ao diagrama H-R constuído para a amostra, a população tem aproximadamente 2 milhões de anos, com uma massa média de apenas 0.2 massas solares. A linha de emissão Hα indica uma distribuição de taxas de acreção de massa típicas de estrelas T Tauri.

Capítulo 4 – Este capítulo apresenta uma amostra completa, limitada por fluxo, de espectros *Spitzer* IRS no infravermelho médio (5–35 μm) da população estelar

jovem de Serpens, como estudada no capítulo 2. Os espectros são apresentados e classificados. Em concordância com as conclusões do capítulo 2, a população de fundo é caracterizada como estrelas de fundo (devido à inclinação espectral e bandas de silicato em absorção), galáxias de fundo (com HAPs transladados para o vermelho) e um objeto de alta ionização de natureza desconhecida. Os verdadeiros objetos estelares jovens somam em 115, incluindo estrelas ainda cercadas por um envelope (classe I, 18%) e discos (classes II e III, 82%). A geometria da parte interna do disco é inferida a partir da taxa de fluxo entre 30 and 13 micrômetros. As bandas de silicato em 10 e 20 micrômetros são fortemente afetadas pelo tamanho da poeira que as emite e, portanto, são usadas para identificar o tamanho da poeira. Uma população de poeira pequena nas camadas superficiais dos disco é observada sempre, independente da geometria, ou de a estrela estar numa região mais populosa ou mais isolada. Além disso, os resultados em Serpens são comparados com os da população jovem na região de Taurus, a região de formação estelar mais bem estudada até hoje, e com os resultados da amostra c2d IRS, que contém estrelas em distintas regiões. Os resultados em Serpens são bastante similares aos resultados destas duas populações de idades médias e ambientes diferentes. Este resultado implica que a população de poeira na superfície dos discos é o resultado de um equilíbrio entre a coagulação de partículas e sua fragmentação, independente do ambiente. Este equilíbrio é mantido enquanto os discos existem.

Capítulo 5 – O objeto de alta ionização descoberto no capítulo 4, OL17, é estudado aqui. Espectros adicionais foram obitidos com o novo instrumento X-shooter, que fica no Very Large Telescope (VLT, no Chile). A ampla gama de comprimento de onda alcançada pelos três braços deste instrumento (no ultra-violeta, visível, e infravermelho) abrange várias importantes linha de emissão que são usadas para determinar a natureza do objeto. Estreitas linha de emissão, combinadas com baixas razões das linhas [N II]/Hα e [S II]/Hα, mostram que o objeto é uma nova nebulosa planetária.

Capítulo 6 – Este capítulo apresenta a mineralogia dos grãos de poeira na superfície do disco para quatro grupos para os quais existem estudos completos com espectros IRS: os jovens Serpens e Taurus apresentados no capítulo 4, bem como as regiões mais velhas Upper Scorpius e η Chamaeleontis. A análise dos dados foi feita com as mesmas técnicas, permitindo a comparação direta dos resultados. Uma distribuição similar de tamanhos médios de grão e frações de cristalinidade é observada para as quatro regiões, apesar de idades médias diferentes e distintas frações de disco. A ampla diferença em idades médias ($\sim$1–8 milhões de anos) e geometrias de disco, sem acompanhamento da evolução das propriedades da poeira na superfície do disco, aponta para uma rápida mudança acontecendo ($\leq$1 milhão de anos), e que um equilíbrio é mantido de tal forma que as propriedades dos discos são estatisticamente as mesmas até a dissipação dos mesmos.

Capítulo 7 – Este capítulo faz uso das características das estrelas e discos derivados nos capítulos anteriores na construção de distribuições espectrais de energia (SED na sigla em ingês) para as estrelas jovens com discos em Serpens. As SEDs permitem

uma correta separação entre a radiação emitida pela estrela e aquela re-emitida pelo disco. Tendo em conta a nova distância à Serpens (415 pc), uma distribuição etária mais jovem é encontrada para a nuvem, concentrada entre 1 e 3 milhões de anos. A distribuição de luminosidades fracionárias de disco (i.e., luminosidade do disco em relação à luminosidade estelar) da população de Serpens se assemelha àquela da jovem Taurus, com a maioria dos discos compatíveis com discos passivamente irradiados. Em termos de geometria, não há separação clara em luminosidade fracionária de disco entre discos grandes e discos quase já dissipados, como é o caso dos discos ao redor de estrelas mais massivas, chamadas Herbig Ae/Be. Além disso, a mineralogia da poeira na superfície dos discos não parece correlacionar diretamente com quaisquer parâmetros estelares ou de disco para a grande amostra estudada.

Cada capítulo termina apresentando suas conclusões, deduzidas a partis dos dados ali apresentados. Em geral, as principais conclusões desta tese são:

- Separando a contaminação de fontes de fundo, Serpens e Lúpus são regiões jovens, com idades entre 1.5 – 3 milhões de anos (considerando a distância à Serpens sendo 415 ao invés de 259 pc). Embora a distribuição de idades seja muito semelhante, a distribuição de massas não é. Serpens é composta majoritariamente de estrelas de tipo K e M, espalhando-se entre 0.2 e 1.2 massas solares, com valor médio em torno de 0.7 massas solares. Esta distribuição é muito semelhante à da população de estrelas jovens em Taurus. Lúpus, no entanto, é quase totalmente composta de estrelas de muito baixa massa, de tipo M, com a maioria das estrelas tendo massa de 0.2 massas solares. Esta distribuição é bastante semelhante à das regiões de formação de estrelas jovens Chamaeleon I e IC 348. Essa diferença na distribuição de massas sugere alguns pequenos desvios de uma possível função de massa inicial universal.

- Para qualquer determinada região, seja ela uma região jovem de 1 milhão de anos ou velha, de 7 – 8 milhões de anos, a distribuição dos tamanhos de poeira dominantes na superfície dos discos é estatisticamente a mesma. Isto implica que, além de coagulação e do crescimento, esta poeira também é o resultado de processos colisionais destrutivos. Um equilíbrio desses dois processos deve ser mantido por milhões de anos, enquanto o disco existe, para explicar a mesma distribuição observada.

- A composição mineralógica da poeira é em média a mesma para todas as regiões estudadas. Um nível considerável de cristalinidade ($\sim$10 – 20 %) deve ser estabelecido na superfície do disco no início de sua evolução ($\leq$1 milhão de anos), alcançando um equilíbrio que é independente do que possa estar acontecendo no plano médio do disco, onde planetas pode ester se formando.

Curriculum Vitæ

I was born in the midst of winter in Teresópolis (Brazil) to join my brother Gabriel in completing the world of our parents, Marcia & Hercules. 17 years later, after finishing high school (ensino médio) at Colégio Salesiano Santa Rosa, I started the B.Sc. in Physics at the Federal University of Rio de Janeiro (UFRJ). Alongside the classes, I soon started my Astrophysics career with an undergraduate research project at the National Observatory (ON), also in Rio de Janeiro. Working under the supervision of Dr. Ramiro de la Reza, I studied the metallicity of post-T Tauri stars in young associations, a project that was motivated by the high metallicity of planet-host stars.

After graduating from UFRJ, I moved to Baltimore (USA). There I was a research assistant at the Johns Hopkins University (JHU) for 1.5 years. At JHU I worked with Dr. Luciana Bianchi on the stellar population of the Large Magellanic Cloud with data from the outstanding Hubble Space Telescope (HST). Living in Baltimore was one of the greatest experiences of my life! There I became a grown-up. Following Baltimore, I moved to Leiden, where I completed my M.Sc. in Astrophysics in record time! For my Master project, I worked under the direct supervision of Dr. Bruno Merín characterizing the newly discovered young stellar population of the Serpens Molecular Cloud. During this time I had the opportunity to collect data at the William Herschel Telescope and the Telescopio Nazionale Galileo, both in La Palma (Spain).

I obtained my Master degree in February 2007 and was ready to start as a Ph.D. student. As such, I moved to Pasadena (USA), where I attended the California Institute for Technology (Caltech) for my entire first year. Combined with visits in the following years, I stayed in Pasadena almost as long as I did in Leiden during the 4 years of the program (complemented by many work trips and conferences abroad). In Leiden I was a teaching assistant to the 'Data Mining' course by Dr. Jarle Brinchmann, and the 'Star Formation and Origin of Solar Systems' course by Prof. Ewine van Dishoeck. I also had the amazing opportunity of supervising the research projects of two master students: Annelies Mortier and Margriet van der Laan.

During these 4 years I was fortunate to visit the Very Large Telescope (VLT, in Chile) twice and made several work visits to many great astronomy institutes spread across Europe: the Max-Planck Institut für Extraterrestrische Physik (MPE, in Germany), the European Space Research and Technology Center (ESTEC, in the Netherlands), the European Southern Observatory (ESO, in Germany), the Max-Planck Institut für Astronomie (MPIA, in Germany), the European Space Astron-

omy Center (ESAC, in Spain) and the Laboratoire d'Astrophysique de Grenoble (in France). A great part of this thesis is based on observations with the superb *Spitzer Space Telescope*. Although (unfortunately) one cannot visit this telescope to collect data, the incredible amount of IRS spectra I have reduced and analyzed during my thesis, in addition to hundreds of optical spectra, has transformed me into an avid spectroscopist. The results of these projects are presented in this thesis, most of which have also appeared as separate publications in *The Astrophysical Journal* and *Astronomy & Astrophysics.*

I have presented the results achieved during these 4 years at several international conferences and schools: Gainesville, Baltimore, Pasadena and New York (USA), Leiden (the Netherlands), El Escorial (Spain), Rio de Janeiro (Brazil), and Garching (Germany). Furthermore, noting that a greater interaction between specialists in stars, in protoplanetary disks, and in exo-planets was lacking, I worked to establish an environment where this interaction could be furnished. This became the 2009 EARA workshop at the Lorentz Center in Leiden, entitled "From Disks to Planets: Learning from Starlight", that I co-organized.

You could say I'm a lucky girl, huh? This upcoming fall I will continue my research in astrophysics as the Harlan J. Smith Postdoctoral Fellow at the University of Texas at Austin (USA).

Publications

Refereed Papers

1. *Young Stellar Objects in the Lupus Molecular Clouds* (Chapter 3)
   Annelies Mortier, **Isa Oliveira** & Ewine F. van Dishoeck; submitted to the
   Monthly Notices of the Royal Astronomical Society
2. *Ruling Out Unresolved Binaries in 5 Transitional Disks – VLT/NACO Deep
   2.12 and 1.75 µm Narrow-band Imaging*
   Sílvia Vicente, Bruno Merín, Hervé Bouy, Markus Hartung, Nuria Huélamo,
   Étienne Artigau, Jean-Charles Augereau, Ewine van Dishoeck, Johan Olofsson,
   Isa Oliveira, Timo Prusti; submitted to Astronomy & Astrophysics
3. *On the Evolution of Dust Mineralogy, From Protoplaneatry Disks to Planetary
   Systems* (Chapter 6)
   Isa Oliveira, Johan Olofsson, Klaus M. Pontoppidan, Ewine F. van Dishoeck,
   Bruno Merín & Jean-Charles Augereau; The Astrophysical Journal, in press
4. *VLT/X-shooter Spectroscopy of a Dusty Planetary Nebula Discovered with Spitzer/IRS*
   (Chapter 5)
   Isa Oliveira, Roderik A. Overzier, Klaus M. Pontoppidan, Ewine F. van Dishoeck
   & Loredana Spezzi; 2011, Astronomy & Astrophysics, 526, 41
5. *A Spitzer Survey of Protoplanetary Disk Dust in the Young Serpens Cloud: How
   do Dust Characteristics Evolve with Time?* (Chapter 4)
   Isa Oliveira, Klaus M. Pontoppidan, Bruno Merín, Ewine F. van Dishoeck,
   Fred Lahuis, Vincent C. Geers, Jes K. Jørgensen, Johan Olofsson, Jean-Charles
   Augereau, Joanna M. Brown; 2010, The Astrophysical Journal, 714, 778
6. *A Spitzer c2d Legacy Survey to Identify and Characterize Disks with Inner Dust
   Holes*
   Bruno Merín, Joanna M. Brown, **Isa Oliveira**, Gregory J. Herczeg, Ewine F.
   van Dishoeck, Sandrine Bottinelli, Neal J. Evans II, Lucas Cieza, Loredana
   Spezzi, Juan M. Alcalá, Paul M. Harvey, Geoffrey A. Blake, Amelia Bayo,
   Vincent C. Geers, Fred Lahuis, Timo Prusti, Jean-Charles Augereau, Johan
   Olofsson, Frederick M. Walter, Kuenly Chiu; 2010, The Astrophysical Journal,
   718, 1200
7. *A Deep Optical/Near-Infrared Catalogue of Serpens*
   L. Spezzi, B. Merín, **I. Oliveira**, E.F. van Dishoeck, J.M. Brown, 2010, Astron-
   omy & Astrophysics, 513, 38

8. *c2d Spitzer-IRS Spectra of Disks Around T Tauri Stars. IV. Crystalline Silicates*
J. Olofsson, J.-C. Augereau, E.F. van Dischoeck, B. Merín, F. Lahuis, J. Kessler-Silacci, C.P. Dullemond, **I. Oliveira**, G.A. Blake, A.C.A. Boogert, J.M. Brown, N.J. Evans II, V.C. Geers, C. Knez, J.- L. Monin, K.M. Pontoppidan; 2009, Astronomy & Astrophysics, 507, 327

9. *Optical Spectroscopy of a New Young Stellar Population in the Serpens Molecular Cloud* (Chapter 2)
Isa Oliveira, Bruno Merín, Klaus M. Pontoppidan, Ewine F. van Dishoeck, Roderik A. Overzier, Jesús Hernández, Aurora Sicilia-Aguilar, Carlos Eiroa, Benjamin Montesinos; 2008, The Astrophysical Journal, 691, 672

10. *The Young Population of the Chamaeleon II Dark Cloud*
Loredana Spezzi, Juan M. Alcalá, Elvira Covino, Antonio Frasca, Davide Gandolfi, **Isa Oliveira**, Nicholas Chapman, Neal J. Evans II, Tracy L. Huard, Jes K. Jørgensen, Bruno Merín, Karl R. Stapelfedt; 2008, The Astrophysical Journal, 680, 1295

11. *The Spitzer c2d Survey of Large, Nearby, Interstellar Clouds. X. The Chamaeleon II Pre-Main Sequence Population as Observed with IRAC and MIPS*
Juan M. Alcalá, Loredana Spezzi, Nicholas Chapman, Neal J. Evans II, Tracy L. Huard, Jes K. Jørgensen, Bruno Merín, Karl R. Stapelfedt, Elvira Covino, Antonio Frasca, Davide Gandolfi, **Isa Oliveira**; 2008, The Astrophysical Journal, 676, 427

12. *Lyman Break Galaxies, Lyα Emitters and a Radio Galaxy in a Protocluster at z = 4.1*
Roderik A. Overzier, R.J. Bouwens, N.J.G. Cross, B.P. Venemans, G.K. Miley, A.W. Zirm, N. Benítez, J.P. Blakeslee, D. Coe, R. Demarco, H.C. Ford, N.L. Homeier, G.D. Illingworth, J.D. Kurk, A.R. Martel, S. Mei, **I. Oliveira**, H.J.A. Röttgering, Z.I. Tsvetanov, W. Zheng; 2008, The Astrophysical Journal, 673, 143

13. *Spatial Separation of Small and Large Grains in the Transitional Disk Around the Young Star IRS 48*
V.C. Geers, K.M. Pontoppidan, E.F. van Dishoeck, C.P. Dullemond, J.-C. Augereau, B. Merín, **I. Oliveira**, J.W. Pel; 2007, Astronomy & Astrophysics, 469, 35

Conference Proceedings

1. *Evolution of Dust in Protoplanetary Disks*
I. Oliveira, K.M. Pontoppidan, B. Merín, E.F. van Dishoeck; Disks, Meteorites, Planetesimals, held July 24-25, 2010 in New York, NY. Lunar and Planetary Science Institute

2. *Evolution of Young Stars and Their Disks in Serpens*
Isa Oliveira, Bruno Merín, Klaus M. Pontoppidan, Ewine F. van Dishoeck; 2010, Highlights of Astronomy, Volume 15, p. 731-731, IAU GA Rio de Janeiro

Thesis Acknowledgments

Not everybody has the opportunities they deserve in life. Deserving or not, I am most grateful for the many opportunities I had that led me here. The places, situations and people I met in life had a great impact on who I became and, although impossible to mention them all, I will do my best to acknowledge such inspiration in these pages.

I am a text-book Brazilian: hard-worker and under-appreciated, informal, and a dreamer. I'm proud to carry this inheritance and the green (now blue) passport with me wherever in the world I go.

Ramiro de la Reza, my passion for science and what things mean are a reflection of your knowledge and enthusiasm, while holding my hands as I took my first scientific steps. I wish every young student would have such pleasure.

Bruno Merín, your enthusiasm is contagious! I was very lucky to catch it when times were hard. *Klaus Pontoppidan*, your uncompromising science ethics and hard work are an inspiration, even when you're too tough.

Irma Black, Dian Buchness, Sarah DeFusco and Nora Oshima: all the time I've spent at Caltech was pleasant because of your hard work, always with a smile. The food and drinks in the PS department on special occasions are just so friendly. *Tycho Bot*, you've saved my life. I hope there'll always be computer support for the Sterrewachters.

Thiago e Karín, Pasadena mom and dad, obrigada por tudo. *Miles, Jason, Jamerson*, you were the coolest housemates. I miss the party house we shared at Los Robles. *Yolande, John and Elaine* - I feel at home in Leiden and a lot has to do with you. Thanks *Karin* for the tip.

Annelies Mortier, Margriet van der Laan, you taught me to teach. Always so patient and hard working. Keep going girls!

My office-mates: *Herma Cuppen*, you were a mother so much before Jop was born. *Umut Yildiz*, keep standing up for yourself, but remember to always be kind. *Emily Tenenbaum*, your grace and coolness made you a great fit for this green office.

Jon & Stephen, we had so many fun lunches together these past 4 years!

I was never as popular as I was at JHU, those friendships are forever: *Oiwei Ivy Wong, Ricardo Demarco, Nick Cross, Miriam García, Boryana Efremova, Alin Tolea, Sundar Srinivasan, Valentin Stanev, Zhuohan Liang, Manuchehr Taghizadeh-Popp* – I miss having you all around.

Friends coming and going in the Sterrewacht: *Dominic Schnitzeler, Stijn Wuyts,*

Liesbeth Vermaas, Ned Taylor, Elisabetta Micellotta, Vincent Geers, Niruj Mohan Ramanujam, Freeke van de Voort, the Pink Elephant and the party-goers, I surely am forgetting people... I had a lot of fun in and around Leiden with you. *Daniel Harsono, Ruud Visser, Lars Kristensen* and the *astrochem* group: our many coffee breaks were very much fun. *Edith Fayolle*, you'll be queen bee!

Being part of a big group was a great experience for me. I've learned so much in the c2d group meetings and telecons, and owe great gratitude to *Jean-Charles Augereau, Loredana Spezzi, Neal Evans, Paul Harvey, Juan Alcalá, Joanna Brown, Geoff Blake, Greg Herczeg, Rachel Smith. Johan Olofsson*, I found in you a collaborator for life, from the first meeting in Heidelberg to our papers together, you've been such a good colleague.

Music is very important in my life, working on my behalf when gravity wanted to bring me down. *Tom, Chico, Marisa, Dave, Diana, and John* are old friends, keeping the spirits up. *Harriët van den Berg*, I was never your best student, but I had a lot of fun with the flute. *Simone Pormes*, great fun we had singing Bossa Nova. Cantando eu mando a tristeza embora...

My fellow Nederlands cursisten *Mickey, Christiane, Felice, Jon, Andrés*, amongst many, leraren *Joke, Els, René* – wat een avontuur hadden we! It should be forbidden to mock those who venture themselves in a foreign language.

Of course, I must acknowledge the brave men and women who study as long as I did, but dedicate their lives to save the lives of others. The fact that I can type this with my own two hands speaks for itself. May science continue to make people's lives better and longer.

Jeanne, Marnix, Natasja, Lianne, Finn en Ria, de steun van familie op slechts een korte treinreis afstand stelde mij op mijn gemak en maakte dat ik me altijd welkom voelde in dit land.

Marcia, Lola, Gabriel, Mara, Joel, Sylvia, Daniel, Cintia, Gustavo, Théo e João Gabriel: quem eu sou devo a vocês. Seu apoio, vocal ou silencioso, me dá a certeza de que nunca estou sozinha, onde quer no mundo que eu esteja. *Mãe*, você me ensinou a nunca desistir. *Hercules* estaria orgulhoso (de mim e de vocês). Juntos, não tem para ninguém – somos brasileiros e não desistimos nunca!

Roderik, my prince charming, you keep me where the light is!

Follow your dreams, search for your own opportunities and work hard, fulfil your duties, demand your rights, and have fun – life is happening right now.

"Eu nasci assim
Eu cresci assim
Eu sou mesmo assim
Vou ser sempre assim"

Dorival Caymmi